ADVANCES IN FILTER MINIATURIZATION AND DESIGN/ANALYSIS OF RF MEMS TUNABLE FILTERS

A Dissertation

by

VIKRAM SEKAR

Submitted to the Office of Graduate Studies of
Texas A&M University
in partial fulfillment of the requirements for the degree of

DOCTOR OF PHILOSOPHY

August 2011

Major Subject: Electrical Engineering

ADVANCES IN FILTER MINIATURIZATION AND DESIGN/ANALYSIS OF RF MEMS TUNABLE FILTERS

A Dissertation

by

VIKRAM SEKAR

Submitted to the Office of Graduate Studies of
Texas A&M University
in partial fulfillment of the requirements for the degree of

DOCTOR OF PHILOSOPHY

Approved by:

Chair of Committee,	Kamran Entesari
Committee Members,	Robert D. Nevels
	Laszlo B. Kish
	Debjyoti Banerjee
Head of Department,	Costas Georghiades

August 2011

Major Subject: Electrical Engineering

ABSTRACT

Advances in Filter Miniaturization and
Design/Analysis of RF MEMS Tunable Filters. (August 2011)
Vikram Sekar, B.E., Visveswariah Technological University;
M.S., Texas A&M University
Chair of Advisory Committee: Dr. Kamran Entesari

The main purpose of this dissertation was to address key issues in the design and analysis of RF/microwave filters for wireless applications. Since RF/microwave filters are one of the bulkiest parts of communication systems, their miniaturization is one of the most important technological challenges for the development of compact transceivers. In this work, novel miniaturization techniques were investigated for single-band, dual-band, ultra-wideband and tunable bandpass filters. In single-band filters, the use of cross-shaped fractals in half-mode substrate-integrated-waveguide bandpass filters resulted in a 37% size reduction. A compact bandpass filter that occupies an area of 0.315 mm^2 is implemented in 90-nm CMOS technology for 20 GHz applications. For dual-band filters, using half-mode substrate-integrated-waveguides resulted in a filter that is six times smaller than its full-mode counterpart. For ultra-wideband filters, using slow-wave capacitively-loaded coplanar-waveguides resulted in a filter with improved stopband performance and frequency notch, while being 25% smaller in size.

A major part of this work also dealt with the concept of 'hybrid' RF MEMS tunable filters where packaged, off-the-shelf RF MEMS switches were used to implement high-performance tunable filters using substrate-integrated-waveguide technology. These 'hybrid' filters are very easily fabricated compared to current state-of-the-art RF MEMS tunable filters because they do not require a clean-room facility. Both

the full-mode and half-mode substrate-integrated waveguide tunable filters reported in this work have the best Q-factors ($93-132$ and $75-140$, respectively) compared to any 'hybrid' RF MEMS tunable filter reported in current literature. Also, the half-mode substrate-integrated waveguide tunable filter is 2.5 times smaller than its full-mode counterpart while having similar performance.

This dissertation also presented detailed analytical and simulation-based studies of nonlinear noise phenomena induced by Brownian motion in all-pole RF MEMS tunable filters. Two independent mathematical methods are proposed to calculate phase noise in RF MEMS tunable filters: (1) pole-perturbation approach, and (2) admittance-approach. These methods are compared to each other and to harmonic balance noise simulations using the CAD-model of the RF MEMS switch. To account for the switch nonlinearity in the mathematical methods, a nonlinear nodal analysis technique for tunable filters is also presented. In summary, it is shown that output signal-to-noise ratio degradation due to Brownian motion is maximum for low fractional bandwidth, high order and high quality factor RF MEMS tunable filters.

Finally, a self-sustained microwave platform to detect the dielectric constant of organic liquids is presented in this dissertation. The main idea is to use a voltage-controlled negative-resistance oscillator whose frequency of oscillation varies according to the organic liquid under test. To make the system self-sustained, the oscillator is embedded in a frequency synthesizer system, which is then digitally interfaced to a computer for calculation of dielectric constant. Such a system has potential uses in a variety of applications in medicine, agriculture and pharmaceuticals.

To all my loved ones

ACKNOWLEDGMENTS

A significant number of years has passed since my childhood days of pretending to be a scientist by collecting bugs, mixing "chemicals" I obtained from my mother's kitchen and walking around with my father's oversized white shirt and work gloves. My make-believe ideas were often fueled by "Dexter's Laboratory", a popular cartoon series in the nineties, about a boy genius who performed advanced scientific experiments in his hidden laboratory only to be destroyed by his clumsy sister. Those were probably the early roots of my scientific inquiry. Nearly two decades have passed, and I now have a completed doctoral dissertation. I cannot help but feel the end of my student years draw near while realizing that I have only managed to amass a tiny speck of knowledge from the vast multitude of existing information. Although learning is a lifelong process, there are several people I am thankful to, who helped me get to where my childhood dreams were.

Among these people is my Ph.D. advisor, Prof. Kamran Entesari, whose guidance has helped me develop my scientific rigor, rational thought and ideas through my years of advanced technical learning. His advice on various aspects of time management, technical analysis and scientific vision has helped me build a strong foundation for the future, which will aid me for many years to come. I would also like to thank my doctoral committee members, Prof. Robert D. Nevels, Prof. Laszlo B. Kish and Prof. Debjyoti Banerjee for all their assistance during my PhD program. I also thank Prof. Samuel Palermo for all the technical advice he provided during the development of the microwave sensor. I would also like to thank my colleagues and friends at Texas A&M University, especially Dr. Mohamed El-Nozahi, Mr. Ahmed A. Helmy, Mr. Marcelino Armendariz, Mr. Felix O. Fernandez, Dr. Raghavendra Kulkarni, Mr. William J. Torke, Mr. Hajir Hedayati, Mr. Mohamed Elkholy, and Mr. Ming-yi Li

for their help with measurement, design, fabrication and other matters. I would also like to thank Ms. Tammy Carda in the electrical engineering office for taking care of all my paperwork related issues, and Ms. Claudia Samford for assisting me in travel preparations.

I would like to thank my parents and family for their unwavering support from the early school years all through graduate school, and for their reassurance in difficult times. Finally, I would like to thank my wife for supporting me through graduate school, putting up with my long work hours, and making sure my graphs looked 'pretty.'

TABLE OF CONTENTS

CHAPTER Page

I INTRODUCTION 1

A. Filter Miniaturization 5
B. RF MEMS Tunable Filters: Hybrid Approach and Noise Analysis 9
C. Overview 12

II NOVEL TECHNIQUES FOR FILTER MINIATURIZATION . . 15

A. Miniaturized UWB Bandpass Filters With Notch Using Slow Wave CPW Multiple Mode Resonators 16
1. Introduction 16
2. Initial UWB BPF 17
a. Slow-Wave CPW MMR 17
b. Stub-Loaded Transition with DGS Unit 19
c. Measurements 21
3. Slow-Wave UWB BPF with Notch 23
4. Conclusion 24
B. A K-Band Integrated Bandpass Filter in 90 nm CMOS Technology 26
1. Introduction 26
2. Filter Design 27
a. Technology 27
b. Meander-Line Inductor 28
c. Filter Topology and Implementation 30
d. Effect of Metal Filling 33
3. Measurement Results 33
4. Conclusion 35
C. Miniaturized Half-Mode Substrate Integrated Waveguide Bandpass Filters Using Cross-Shaped Fractals 36
1. Introduction 36
2. Design 37
a. Fractal HMSIW Resonators 37
b. Coupling 40
3. Fabrication and Measurement 43

CHAPTER Page

4. Conclusion 46
D. A Novel Compact Dual-Band Half-Mode Substrate Integrated Waveguide Bandpass Filter 47
1. Introduction 47
2. Filter Synthesis 48
a. Dual-Band Resonator 48
b. Methodology 49
3. Design and Implementation 51
4. Fabrication and Measurements 55
5. Conclusion 57

III SUBSTRATE INTEGRATED WAVEGUIDE RF MEMS TUNABLE FILTERS 58

A. Introduction 58
B. A 1.2—1.6-GHz Substrate Integrated Waveguide RF MEMS Tunable Filter 61
1. Tunable Resonator Structure 61
a. SIW Cavity 61
b. Tuning Mechanism 63
c. Packaged RF MEMS Switch 66
2. Tunable Resonator Design 67
a. Resonance Contours 67
b. External Quality Factor 72
c. Tunable Cavity Implementation 73
3. Filter Design 77
4. Fabrication and Measurement 79
a. Fabrication, Implementation and Biasing 79
b. Measurements 82
5. Spurious Suppression 85
6. Nonlinear Characterization 87
7. Conclusion 90
C. Half-Mode Substrate Integrated Waveguide RF MEMS Tunable Filters 91
1. Resonator Design 91
a. HMSIW Model 91
b. Tuning Mechanism 93
c. Tuning Network 95
d. Implementation 97

CHAPTER Page

2. Filter Design 101
a. Inter-Resonator Coupling 101
b. External Coupling 105
c. Complete Filter Simulation 108
3. Fabrication and Measurement 110
4. Conclusion 116

IV NONLINEARITY AND NOISE ANALYSIS OF ALL-POLE RF MEMS TUNABLE FILTERS 118

A. Introduction 118
B. Nonlinear Noise Analysis of RF MEMS Tunable Filters Using Harmonic Balance Simulation* 120
1. Brownian Motion Noise 120
2. RF MEMS Tunable Filter 121
3. Power Handling versus Bandwidth 124
4. Phase Noise 125
5. Higher Order Filters 131
6. Conclusion 136
C. Nonlinear Nodal Analysis of Tunable Microwave Filters . . 137
1. Introduction 137
2. Theory 138
3. Iterative Solution of Nonlinear Equations 140
4. Nonlinear Varactor Model 143
5. Case Study 144
a. Nonlinear Reactance Deviations 144
b. Peak Internal Voltage Distribution 145
c. Large Signal S-Parameters 145
6. Conclusion 149
D. Pole Perturbation Theory for Nonlinear Noise Analysis of RF MEMS Tunable Filters 150
1. Introduction 150
2. Perturbation Theory 151
a. Methodology 152
b. Prototype Perturbation 153
c. Pole Perturbation 154
d. Discussion 158
3. Nonlinear Noise Perturbation in RF MEMS Tunable Filters 158

CHAPTER Page

a. Nonlinear Analysis 159
b. Noise Analysis 160
c. Phase Noise Calculations 163
4. RF MEMS Tunable Filter Example 165
a. Design 165
b. Nonlinearity 168
c. Phase Noise 170
5. Filter Nonidealities 173
a. Resonator Q-factor 173
b. Nonideal Inverters 176
6. Signal-to-Noise Ratio Analysis 182
a. Basics 183
b. Results 185
c. Discussion 186
7. Conclusion 188
E. Unified Method of Nonlinear Noise Analysis Using the Method of Admittances 189
1. Introduction 189
2. Theory 189
3. Filter Example 192
4. Nonidealities 193
a. Resonator Q-Factor 193
b. Frequency-Dependence of J-Inverters 195
5. Conclusion 197

V A SELF-SUSTAINED MICROWAVE PLATFORM FOR DETECTION OF ORGANIC LIQUIDS 198

A. Introduction 198
B. Fundamental Theory 202
C. Oscillators for Dielectric Constant Measurement 205
1. Oscillator Design 205
a. Source Network 207
b. Gate Network 209
2. Response to Material Dielectric Constant 210
3. Effect of Material Loss 212
D. VCO Fabrication and Chemical Measurements 215
E. Development of the Frequency Synthesizer System 219
1. System Overview 220

CHAPTER Page

2. Functionality 220
3. Implementation 223
F. Fully Self-Sustained Chemical Measurements 227
1. Measurement Procedure 229
2. Sensitivity Analysis 230
3. Chemical Calibration and Detection 232
G. Conclusion 236

VI CONCLUSION AND FUTURE WORK 237

A. Conclusion 237
B. Future Work 240
1. Half-Mode Substrate Integrated Waveguide Diplexer . 240
2. Ku-Band Half-Mode Substrate Integrated Waveguide RF MEMS Tunable Filter 240
3. Experimental Verification of Nonlinear Noise in RF MEMS Tunable Filters 241
4. Self-Sustained Platform for Detection of Material Loss 242

REFERENCES 244

APPENDIX A 260

APPENDIX B 261

VITA 263

LIST OF FIGURES

FIGURE		Page
1	UWB spectrum mask for indoor hand-held devices.	2
2	Block diagram of a multi-band wireless transceiver using RF MEMS technology.	5
3	A substrate integrated waveguide formed by linear arrays of metallic via-holes drilled in a planar substrate to emulate waveguide walls.	6
4	Metal-contact RF MEMS switches developed by (a) Radant MEMS [40], (b) Omron Inc. [41], and (c) MIT Lincoln Laboratories [42]. . .	11
5	Three-dimensional view of the proposed UWB BPF with notch using slow-wave CPW multiple-mode resonator (MMR).	17
6	Slow-wave CPW MMR and its equivalent circuit model.	18
7	Variation of loaded-line characteristic impedances, $Z_{0,A/B}$, normalized to the unloaded characteristic impedance Z_{0U}, and the change of resonance frequency of the first three modes of the slow-wave CPW MMR against L_f.	20
8	(a) Stub-loaded transition with DGS unit, (b) improvement of upper rejection skirt as the length of open stubs is increased, and (c) spurious suppression due to one DGS unit placed at the input or output.	21
9	(a) Fabricated conventional and proposed UWB BPF prototypes, (b) simulated/measured S-parameters of the conventional and proposed UWB BPF, and (c) simulated/measured group delay of the proposed UWB BPF.	22

FIGURE Page

10 (a) Proposed bridge structure over the slow-wave CPW MMR for notch generation, (b) equivalent circuit model of the bridge, and (c) simulated response of Section B of CPW MMR with bridge and model parameters for various lengths of the bridge with W_b=0.2 mm, W_p=1 mm and d=0.6 mm. 23

11 (a) Fabricated UWB BPF with notch, and simulated/measured performance of the UWB BPF with notch—(b) S-parameters, (c) group delay. 25

12 Layer configuration of the lumped inductors and capacitors in IBM 90-nm CMOS process. 27

13 (a) Meander-line grounded inductor, (b) inductor equivalent circuit model, and (c) simulated inductance and quality factor vs. frequency using Sonnet. 29

14 (a) Photograph of the fabricated two-port meander-line coupled inductor structure in 90-nm CMOS process, and (b) resulting S-parameters from the circuit model and measurements. 29

15 (a) Schematic of the two-pole Chebyshev bandpass filter, (b) top view of the filter layout, (c) cross section 'AA', of the layout top view, and (d) cross section 'BB' of the layout top view. 31

16 (a) Bandpass filter layout with dense metal filling around the filter components, and (b) simulated filter response with and without metal filling using Sonnet. 32

17 (a) Photograph of the fabricated bandpass filter in IBM 90-nm CMOS process, and (b) simulated and measured S-parameters of the bandpass filter. 34

18 (a) Conventional HMSIW resonator (0th-iteration), (b) the 1st fractal iteration, and (c) the 2nd fractal iteration. 38

19 Simulated S_{21}-parameters for various fractal iterations of the HMSIW resonator. 39

FIGURE Page

20 Inductive input/output J-inverter for the (a) 0th-iteration, (b) 1st-iteration, and (c) 2nd-iteration, and (d) variation of Q_{ext} with h_{io} for various fractal iterations. 40

21 Capacitive inter-resonator J-inverter for the (a) 0th-iteration, (b) 1st-iteration, and (c) 2nd-iteration, and (d) variation of k_{12} with L_c for various fractal iterations. 42

22 Photographs of the fabricated filter prototypes. 43

23 Comparison between simulated and measured S-parameters for (a) 0-th iteration, (b) 1st-iteration, and (c) 2nd-iteration HMSIW bandpass filters. 44

24 A dual-band inverter coupled resonator. 49

25 (a) Generalized nth-order bandpass filter with ideal admittance inverters, and (b) equivalent lowpass prototype network. 49

26 Synthesized response of the dual-band Chebyshev filter. 52

27 Geometrical structure of the proposed dual-band Chebyshev HM-SIW BPF. 52

28 (a) Photograph of the fabricated filter prototype, (b) measured and simulated filter response, and (c) filter response up to 3.2 GHz. . 56

29 (a) Top view of the tunable SIW cavity using packaged RF MEMS switches, (b) $A-A'$ cross section of the tuning cavity, (c) top view of the tuning element employing an RF MEMS switch package, two tuning posts and a top via, and (d) $B-B'$ cross section of the tuning element. 62

30 (a) Photograph and structure of the packaged SPDT RF MEMS switch, (b) side view of the SPST switch, (c) schematic of the SPDT switch, and (d) measured S-parameters of the MEMS switch. . 65

31 Surface current distribution on the tuning post and vector magnetic field distribution within the cavity resonator at resonance frequency, when tuning post P is (a) disconnected, (b) connected. . . 68

FIGURE Page

32 Magnitude of electric field distribution in the cavity at resonance frequency, for various locations of tuning post; (a) disconnected post P near cavity center, and connected (b) post P near cavity center, (c) post Q near output port, (d) post R near input port, and (e) post S away from ports and cavity center. 69

33 (a) Simulated magnitude of S_{21} for the tuning post configurations in Fig. 32, and (b) resonance contours for a single tuning post within the cavity. 71

34 Normalized variation of external quality factor for various locations of the tuning post with respect to (a) input port, and (b) output port. 73

35 (a) A tunable SIW resonator employing six tuning posts controlled by three SPDT RF MEMS switch packages, and (b) coarse tuning states obtained using only tuning posts ABCD. 74

36 Simulated resonant frequency of the SIW cavity for different tuning states. 77

37 Simulated unloaded quality factor (Q_u) of the SIW cavity for different tuning states. 78

38 Layout of the two-pole SIW RF MEMS tunable filter. 79

39 Simulated: (a) insertion loss and (b) return loss of the two-pole 1.2—1.6 GHz tunable SIW filter. 80

40 Fabricated 1.2—1.6 GHz SIW RF MEMS tunable filter. 81

41 Measured: (a) insertion loss and (b) return loss of the two-pole 1.2—1.6 GHz tunable SIW filter. 83

42 (a) Simulated/measured center frequency and measured insertion loss. (b) Measured fractional bandwidth of the filter (3.7% $\pm$ 0.5%). 84

43 Comparison between the measured and simulated insertion loss for three arbitrary states at 1.2 (State 1), 1.4 (State 8), and 1.6 GHz (State 14). 85

FIGURE Page

44 Layout of the (a) two-pole SIW tunable filter employing LPFs at the input/output for spurious suppression, (b) type-I LPF, and (c) type-II LPF. 86

45 (a) Simulated wideband response of the tunable filter and lowpass responses of Type-I and Type-II filters, and (b) spurious suppression for the lowest tuning state for various combinations of LPFs. . . 88

46 Measured wideband response of the 1.2—1.6 GHz tunable SIW filter with spurious suppression. 89

47 (a) SIW with width W operating in the TE_{10}-mode with an open-circuit along its symmetry plane, (b) higher order microstrip line with width W operating in the EH_1-mode with a short-circuit along its symmetry plane, and (c) HMSIW with width $W/2$ as a consequence of cases (a) and (b). 92

48 (a) Transverse equivalent network representation of the HMSIW resonator. (b) HMSIW resonator with width $w = W/2$ and length L with via-holes of diameter d and spacing b. 92

49 (a) Transverse network representation, and (b) graphical representation of resonance conditions of the HMSIW resonator. 94

50 Complete circuit model of a tunable HMSIW resonator. 94

51 (a) Layout implementation of a tunable HMSIW resonator and layout details for a pair of (b) coarse-tuning and (c) fine-tuning branches. 98

52 Variation of resonance frequency and normalized admittance of the tuning network for 15 different tuning states. 100

53 Implementation of the inter-resonator J-inverter. 102

54 Simulated electric and magnetic resonance peaks when two HMSIW resonators are weakly-coupled at the input/output for different values of (a) w_{12}, and (b) L_{12}, and (c) variation of coupling coefficient k_{12} for different values of w_{12} and L_{12}. 103

FIGURE Page

55 Variation of k_{12} versus tuning frequency of the resonator for different values of L_{12}. In each case, w_{12} is adjusted to maintain $k_{12} = 0.07$ at the lowest tuning frequency. 104

56 Implementation of the input/output J-inverter and the microstrip-to-HMSIW transition. 106

57 (a) Variation of Q_e as a function of w_{io} and L_{io}, and (b) variation of Q_e versus tuning frequency of the resonator. In each case, w_{io} is adjusted to have $Q_e = 16.8$ at the lowest tuning frequency. 107

58 Simulated: (a) insertion loss and (b) return loss of the two-pole 1.2—1.6 GHz tunable HMSIW filter. 109

59 Fabricated 1.2—1.6 GHz HMSIW RF MEMS tunable filter. 110

60 Measured: (a) insertion loss and (b) return loss of the two-pole 1.2—1.6 GHz tunable HMSIW filter. 111

61 (a) Simulated/measured center frequency and insertion loss, and (b) measured absolute 1-dB and 3-dB bandwidth of the filter. 112

62 Comparison between measured and simulated (a) insertion loss and (b) return loss, for three arbitrary states at 1.2 (State 1), 1.4 (State 7), and 1.6 GHz (State 13). 114

63 Measured resonator unloaded quality factor (Q_u). 115

64 Measured wideband response of the tunable HMSIW filter. 116

65 (a) A two-pole tunable bandpass filter, (b) three-bit RF MEMS switched capacitor bank and (c) nonlinear electromechanical model of the RF MEMS switch. 122

66 Simulated S_{21} of the tunable filter for fractional bandwidths of 0.5% and 5% for $Q = 200$. 124

67 Variation of RMS voltage across the switch with frequency for different values of input power in a tunable filter of (a) 0.5% fractional bandwidth and (b) 10% fractional bandwidth. 126

FIGURE Page

68 Variation of RMS voltage across the switch with frequency for different values of input power in a tunable filter of (a) 0.5% fractional bandwidth and (b) 10% fractional bandwidth. 127

69 Phase of S_{21} versus frequency for the two-pole filter shown in Fig. 65(a) for different fractional bandwidths. 128

70 Variation of phase noise with input power and bandwidth, for unloaded quality factor Q=100 and 200. Phase noise values are evaluated at $P_{in} < P_{in,max}$ with all switches in the up-state position and $\omega' = 2\pi \times 13$ kHz ($\omega' < \omega_m$). 129

71 Simulated phase noise for different tuning states of the filter. The tuning state $(S_1, S_2, S_3) = (0, 0, 0)$ shows the highest phase noise evaluated at $P_{in} = 0$ dBm ($P_{in} < P_{in,max}$), $\omega' = 2\pi \times 13$ kHz ($\omega' < \omega_m$) and Q=200. 131

72 Simulated phase noise as a function of mechanical frequency offset for different filter bandwidths. All switches are in the up-state position, $P_{in} = 0$ dBm ($P_{in} < P_{in,max}$) and Q=200. 132

73 Three-pole tunable filter employing input/output capacitive inverters and inter-resonator inductive inverters. 133

74 Inductively-coupled lumped element tunable filter of order N. 133

75 Variation of phase noise with filter order for different fractional bandwidths. All switches are in the up-state position. Phase noise is evaluated at $P_{in} = 0$ dBm ($P_{in} < P_{in,max}$) and $\omega' = 2\pi \times 13$ kHz ($\omega' < \omega_m$). 135

76 (a) Generalized all-pole Butterworth/Chebyshev bandpass filter with ideal admittance inverters and lossless shunt resonators, and (b) equivalent lowpass filter for a particular tuning state. 139

77 Recursive algorithm to find the nonlinear voltage distribution and large signal s-parameters of a tunable filter. 142

78 N-pole lossless tunable filter implemented using GaAs varactors. The RF chokes (RFC) are ideal and have no effect on the filter. . . . 142

FIGURE Page

79 Nonlinear reactance deviations as a function of frequency for Case A in (a) resonator 1, and (b) resonator 2, for different input powers. . 144

80 Nonlinear reactance deviations as a function of frequency for Case B in (a) resonator 1, (b) resonator 2, (c) resonator 3 and (d) resonator 4, for different input powers. 146

81 Voltage distribution for Case A across (a) resonator 1, and (b) resonator 2, for different input powers, for different input powers. . . 147

82 Voltage distribution for Case B across (a) resonator 1, (b) resonator 2, (c) resonator 3, and (d) resonator 4, for different input powers. 147

83 Large signal s-parameters for (a) Case A, and (b) Case B, for different input powers. 148

84 (a) Generalized all-pole bandpass filter of order N with ideal admittance inverters and lossless shunt resonators, and (b) equivalent low-pass ladder network. 151

85 Distribution of poles on the complex s-plane for Butterworth filters with (a) odd order (eg. N=5) and (b) even order (eg. N=4). . . 155

86 Distribution of poles on the complex s-plane for Chebyshev filters with (a) odd order (eg. N=5) and (b) even order (eg. N=4). 156

87 (a) A tunable RF MEMS shunt resonator, and (b) various displacements in an RF MEMS shunt capacitive switch. 161

88 A tunable MEMS resonator implemented with P switched capacitors. 163

89 (a) An N-pole lossless Butterworth/Chebyshev tunable filter with ideal admittance inverters, (b) variable capacitor implementation using 2-bit RF MEMS switched capacitor banks, and (c) simulated S-parameters of a lossless two-pole tunable Butterworth filter with 1% fractional bandwidth. 165

FIGURE Page

90 (a) Nonlinear pole displacements in a two-pole Butterworth and three-pole Chebyshev filter, (b) angular displacements of poles as a function of applied input power for different filter fractional bandwidths, and (c) group delay as a function of input power in two-pole Butterworth and three-pole Chebyshev filters for different filter fractional bandwidths. Theoretical values are compared to large signal S-parameter (LSSP) simulations in ADS. 167

91 Phase noise of lossless two-pole Butterworth and three-pole Chebyshev filters as a function of input power for different fractional bandwidths, evaluated at an offset of $\omega' = 2\pi \times 9$ kHz ($\omega' < \omega_m$) around $f_0 = 18$ GHz. 170

92 Phase noise of lossless two-pole Butterworth and three-pole Chebyshev filters versus tuning state for different fractional bandwidths, evaluated at an offset $\omega' = 2\pi \times 9$ kHz ($\omega' < \omega_m$) from the center frequency of that tuning state with $P_{in} = -20$ dBm. 171

93 Phase noise as a function of mechanical frequency offset around f_0=18 GHz in lossless two-pole Butterworth and three-pole Chebyshev filters for different fractional bandwidths at P_{in}=-20 dBm. . . . 172

94 Phase noise as a function of filter order for different fractional bandwidths of lossless Butterworth and Chebyshev filters, evaluated at an offset $\omega' = 2\pi \times 9$ kHz ($\omega' < \omega_m$) around f_0=18 GHz with P_{in}=-20 dBm. 173

95 (a) Displacement of poles to the left by δ due to losses present in the resonators of the tunable filter, and (b) Phase noise (P_{ph}) versus Q_u for different fractional bandwidths in a two-pole Butterworth and three-pole Chebyshev filter with noise calculation performed at a frequency offset $\omega' = 2\pi \times 9$ kHz ($\omega' < \omega_m$) around $f_0 = 18$ GHz with $P_{in} = -20$ dBm and normalized to the phase noise of the equivalent lossless filter. 175

96 Variation of phase noise versus input power in a two-pole Butterworth and three-pole Chebyshev filter with 1% fractional bandwidths for $Q_u = 100$ and $Q_u = 500$. Phase noise is evaulated at a frequency offset $\omega' = 2\pi \times 9$ kHz ($\omega' < \omega_m$) around $f_0 = 18$ GHz. . . 175

FIGURE Page

97 Equivalent π-models for admittance inverters using (a) inductors, and (b) capacitors. (c) Generalized lossy admittance inverter. 177

98 Comparison of phase noise versus tuning state in lossless Butterworth ($N = 2$) and Chebyshev ($N = 3$) filters with (a) 1% and (b) 8% fractional bandwidths employing ideal, capacitive and inductive inverters. Phase noise is evaluated with $P_{in} = -20$ dBm at a frequency offset $\omega' = 2\pi \times 9$ kHz around the center frequency of that tuning state. 178

99 (a) A lossless two-pole Chebyshev filter tunable from 15-18 GHz with a constant fractional bandwidth of 8±0.1% with two-bit switched-capacitor bank implementations of (b) input/output capacitor C_{io}, (c) resonator capacitance C_r and (d) inter-resonator capacitance C_g. 179

100 Variation of phase noise with tuning state in a two-pole Chebyshev filter with a constant fractional bandwidth of 8±0.1% considering only noisy inverters, only noisy resonators and both noisy inverters and resonators. Phase noise is evaluated with $P_{in} = -20$ dBm at a frequency offset $\omega' = 2\pi \times 9$ kHz around the center frequency of that tuning state. The MEMS switch combinations for each state are also shown in the figure where '0' and '1' represent up- and down-state positions, respectively. 181

101 (a) Antenna and tunable filter in a 50 Ω system, (b) thermal and phase noise when the received signal is weak (Thermal noise region: $P_{ph,abs} << P_{th}$) and (c) thermal and phase noise when the received signal is strong (Phase noise region: $P_{th} << P_{ph,abs}$). 183

102 Total noise power and SNR calculated using harmonic balance in a 1-Hz bandwidth around $f_0 = 18$ GHz for (a) Butterworth (N = 2) and, (b) Chebyshev (N = 3) filters versus received signal power (P_{in}), for different fractional bandwidths and quality factors, when all switches are in the up-state position. The filter insertion loss for each case is also listed. 187

FIGURE Page

103 (a) Generalized all-pole Butterworth/Chebyshev tunable bandpass filter with ideal admittance inverters and shunt resonators, (b) reduction of filter topology with respect to the ith resonator, and (c) simplified bandpass filter with the ith noisy resonator and complex terminating admittances. 190

104 Variation of filter phase noise for different fractional bandwidths versus (a) input power, (b) mechanical frequency offset, (c) tuning state, and (d) filter order. Unless stated otherwise, phase noise is calculated at an offset of $2\pi \times 9$ kHz at filter center frequency for $P_{in} = -20$ dBm. 194

105 Variation of Butterworth filter phase noise with Q_u for different fractional bandwidths. Phase noise is calculated at an offset of $2\pi \times 9$ kHz at filter center frequency for $P_{in} = -20$ dBm. 196

106 Comparison of phase noise in Butterworth filters versus tuning state for different inverter configurations for fractional bandwidths of (a) 1% and (b) 8%. Phase noise is calculated at an offset of $2\pi \times 9$ kHz at filter center frequency for $P_{in} = -20$ dBm. 197

107 Real and imaginary components of complex permittivity for common organic liquids as predicted by the Debye model. 204

108 Simplified schematic of the negative resistance oscillator used for permittivity measurement. 205

109 (a) Simulation setup for the determination of C_s (DC biasing not shown), (b) variation of magnitude of reflection coefficients at gate and drain with C_s, and (c) phase variation of gate reflection coefficient with frequency. 206

110 (a) Three-dimensional view of the sensing element, and (b) dimensions of the split-ring resonator (SRR). 208

111 Magnitude and phase variation of reflection coefficient of the gate network as a function of the electrical length of the gate transmission line. 209

FIGURE Page

112 Simulated: (a) phase of reflection coefficient of the gate network caused by the presence of MUTs, and (b) change in oscillation frequency and effective sensor capacitance versus dielectric constant. 211

113 Simulated: (a) Real part of sensor admittance when lossy, isotropic MUTs with arbitrary ϵ_r'-value and various ϵ_r''-values are placed in the sample well. Oscillation condition in (5.4) as a function of ϵ_r'' for the case of (b) constant oscillation frequency and (c) constant varactor voltage. 214

114 (a) Top-view of the fabricated permittivity-sensing oscillator prototype, (b) side-view of the fabricated VCO, (c) measured oscillation spectrum without MUT, and (d) tuning characteristics of the VCO. 216

115 (a) Measured oscillator frequency shift versus ϵ_r' for 10 μL MUT samples. Error bars are shown only for calibration materials. (b) Error bars in measurement of MUTs for 10 μL sample volumes. In both graphs, plotted symbols depict mean values. 217

116 (a) Measured oscillator frequency shift versus ϵ_r' for 20 μL MUT samples. Error bars are shown only for calibration materials. (b) Error bars in measurement of MUTs for 20 μL sample volumes. In both graphs, plotted symbols depict mean values. 218

117 Block diagram of a frequency synthesizer system digitally interfaced to a microcontroller unit. 221

118 Different phases of chemical detection using the frequency synthesizer system. 222

119 Detailed implementation of the frequency synthesizer system with a digital interface. 224

120 Schematic of the passive lowpass loop filter. 225

121 Schematic of the signal conditioning block. 226

122 Fabricated frequency synthesizer system for detection of organic liquid materials. 228

FIGURE Page

123 Measured frequency shift versus sample volumes for several MUTs. . 231

124 Chemical calibration curves for different sample volumes using air, ethanol and methanol as reference materials. 233

125 Extracted dielectric constant values for 2-butyl alcohol, o-xylene and ethyl acetate for sample volumes between 10 μL and 200 μL. . . 235

126 Block diagram of a dual-band receiver which uses a diplexer to separate the received signal into appropriate frequency bands. 241

127 Frequency synthesizer architecture for organic liquid detection including power detector circuitry for detection of material loss. 242

LIST OF TABLES

TABLE		Page
I	Summary of Filter Performances (λ_g: Guided Wavelength at Filter Center Frequency)	45
II	Final Dimensions of the Dual-Band HMSIW Filter	55
III	Cavity Parameters	67
IV	Positions of Tuning Posts (in mm)	75
V	Coarse and Fine Tuning Configurations	76
VI	ADS Model Element Values ($\epsilon_r = 10.2$, $h = 0.635$ mm, $\tan\delta = 0.0023$ at 10 GHz)	99
VII	Coarse and Fine Tuning Configurations (0:Open Switch, 1:Closed Switch)	100
VIII	Filter Parameters for Different Filter Bandwidths	123
IX	Physical Dimensions and Electromechanical Parameters of the RF MEMS Capacitive Switch	123
X	Resonator Model Element Values Used for ADS Simulations	166
XI	MEMS Switch Model Parameters	166
XII	Tunable Filter Model Element Values	180
XIII	Debye-Model Parameters for Organic Solvents @ 20°C [112].	203
XIV	Comparison of the Extracted ϵ_r' Values with the Debye Model at 4.5 GHz	219
XV	Chemical Calibration Coefficients for the Frequency Synthesizer-Based Measurement System	233

TABLE Page

XVI Comparison between Theoretical and Measured Values of Dielectric Constant for a Sample Volume $S_v = 100\mu$L, at 4.5 GHz 234

CHAPTER I

INTRODUCTION

Filters are among the most important components of communication and radar systems, primarily due to their ability to select specific signal frequencies while rejecting unwanted interference. In the era of modern wireless communications, the frequency spectrum is a valuable resource that has been divided to serve a wide range of applications. Conventionally, wireless systems only operate at a single frequency band allocated for that application. Thus, communication systems that operate at adjacent frequency bands appear as interference to the narrowband system that must be rejected by appropriate filtering mechanisms. By selecting only a narrow range of frequencies around a desired signal frequency, the signal-to-noise ratio (SNR) of a narrowband communication system is greatly improved. Numerous books [1], [2] have been devoted to the design and implementation of single passband filters using a variety of microwave components such as waveguides, microstrip lines, striplines, etc.

For many applications, a single communication system may be required to work over multiple bands corresponding to several communication standards. The requirements on such filters are much more stringent, and correspondingly their synthesis and design are much more involved. A trivial approach to filter design with multiple passband frequencies is to use a switched bank of single-passband filters in parallel combination. However, this approach often dramatically impacts size, cost and efficiency of the overall system and is avoided where possible. An elegant alternative is to design a single filtering structure that is capable of producing multiple passbands

---

´The journal model is *IEEE Transactions on Microwave Theory and Techniques.*

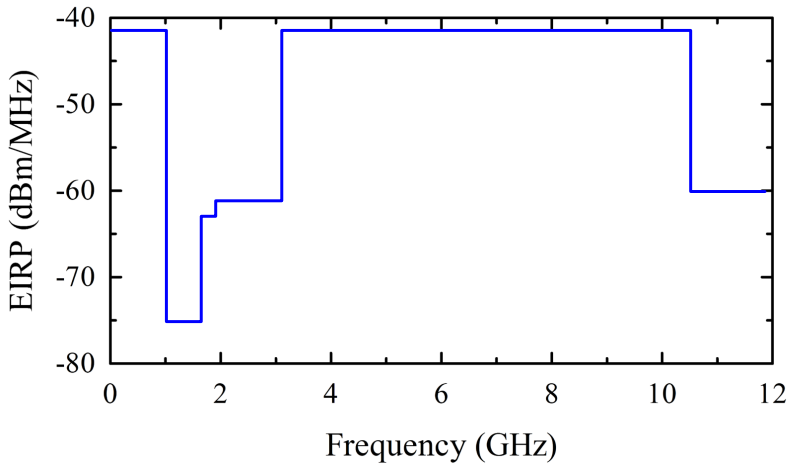

Fig. 1. UWB spectrum mask for indoor hand-held devices.

simultaneously. For this purpose, a variety of techniques have been developed for multiple passband synthesis and have been implemented using waveguide and microstrip technologies [3], [4]. Since majority of the communication systems are inherently narrowband in nature, design techniques for single and multiple passband filters are generally limited to fractional bandwidths lower than 20% around the desired signal frequency.

Recently, the license-free assignment of the 3.1-10.6 GHz frequency range by the United States Federal Communications Commission (FCC) has pioneered the research and development of ultra-wideband (UWB) devices for low cost wireless sytems in military or commercial applications [5]. Fig. 1 shows the UWB spectrum mask for indoor hand-held devices specified by the FCC. UWB communication systems provide high bandwidth, reduced fading from multipath propagation and low power operation. For such applications, the design, implementation and fabrication of UWB filters used in UWB communication modules is a challenging problem when compared to narrow band systems primarily due to the very wide filter bandwidth (110% around center frequency of 6.85 GHz). In addition, the group delay flatness over the filter passband

is an important design parameter to avoid distortion of transmitted/received signals. An intuitive way to generate very wideband filters is to cascade highpass and lowpass filters with a corner frequencies at the lower and upper edges of the desired passband, respectively. A systematic procedure for the design of UWB filters using this approach is reported in [6]. However, a plethora of alternative design techniques have also been proposed which involve the use of multiple mode resonators [7], periodic structures [8], lumped elements on liquid crystal polymer [9], etc. A summary of these design techniques, along with their relative merits and demerits, is published in [10].

In addition to allocating the frequency spectrum according to fixed frequency bands, there is also a necessity to have narrowband filters whose center frequencies can be continuously changed. For example, in electronic support measures (ESM) systems, it may be required to classify the incoming signal according to frequency so that appropriate electronic countermeasures (ECM), such as signal-jamming, may be performed when necessary. To do this, the entire receive band is divided into smaller sub-bands and electronically scanned using a tunable filter with variable center frequency. In modern wireless communication systems, multi-band devices are becoming a major trend due to their ability to cover multiple standards using a single device [11]. Tunable filters are very important for such applications since they replace the use of a switched filter bank with a single component. Tunable filters are also essential components of "cognitive radios" which have the ability to change their network parameters (frequency, bandwidth, modulation) according to the available frequency spectrum for maximum data transfer. Most tunable filters belong to three basic types: mechanically tunable, magnetically tunable and electronically tunable.

Mechanically tunable bandpass filters are typically implemented using either coaxial or waveguide resonators [1], and offer large power handling capability with low insertion loss. However, their large size and slow tuning speeds render them

useless for modern highly integrated systems. Magnetically tuned filters typically employ Yttrium-Iron-Garnet (YIG) spheres in their resonators and are popular for their multi-octave tuning capability, spurious free response, low insertion loss and high quality factor (up to 10,000 in the 0.1 to 6 GHz range) [12]. However, their large size, slow tuning speed and high power consumption make them unacceptable in the context of modern low-power RF transceivers.

Electrically tunable filters use compact tunable capacitors as part of the resonators so that the filter center frequency can be tuned very fast over a wide frequency range, making them ideal candidates for integrated RF front ends. Three major technologies are employed in electrically tuned filters [13].

(a) *Semiconductor varactors:* Varactor tuned filters rely on the change in junction capacitance when reverse bias is applied across the varactor diode. Although they exhibit superior tuning speed and have a compact size, they suffer from poor power-handling, significant non-linearity and poor quality factor at millimeter wave frequencies.

(b) *Ferroelectric thin-film varactors:* The ferroelectric nature of Barium-Strontium-Titanate (BST) thin films has been used to develop a planar varactor technology that can be easily integrated with RF front ends. Much like semiconductor varactors, reverse biasing the BST varactors results in a change in capacitance that is used to tune an RF filter. BST varactors are highly tunable at room temperature while having improved quality factors (60-100) and moderately nonlinear behavior.

(c) *RF microelectromechanical systems (MEMS) switches:* RF MEMS switches are miniature devices which use mechanical movements to achieve an open- or short-circuit in a transmission line, and are actuated using electrostatic, thermal, magnetostatic or piezoelectric mechanisms. Among these, electrostatic and piezoelectric mechanisms are widely used due to its simplicity, compactness and low power con-

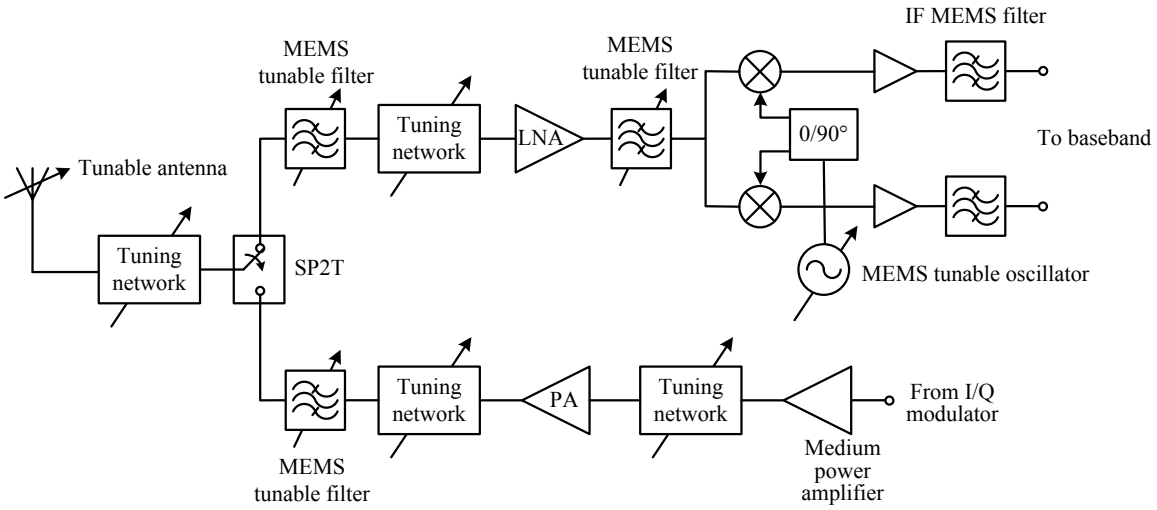

Fig. 2. Block diagram of a multi-band wireless transceiver using RF MEMS technology.

sumption. Although MEMS switches have a moderate switching speed (3-100 μs) and low power handling capability (1-2 W), they provide very low insertion loss (<0.2 dB) even up to 100 GHz, very high linearity ($IIP_3 > 65$ dBm), extremely low power consumption and very high isolation. They can also be integrated in a planar fashion with modern RF front-end electronics. Fig. 2 is an example of a multi-band wireless transceiver where tunability is implemented using RF MEMS technology.

The major themes of this dissertation are discussed in greater detail in the following sections.

A. Filter Miniaturization

For applications where low-loss and high-selectivity are required, single- and dual-band filters have been implemented using waveguide technology in [1] and [14], respectively, since waveguide cavity resonators typically have very high quality factors (> 1000). However, such filters tend to be very bulky and expensive, and are not practical solutions for applications which require compactness. Planar, transmission-

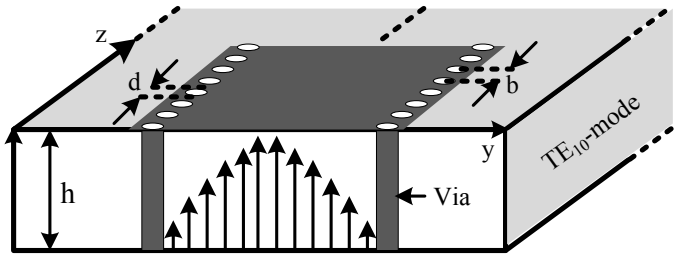

Fig. 3. A substrate integrated waveguide formed by linear arrays of metallic via-holes drilled in a planar substrate to emulate waveguide walls.

line based single- and dual-band filters are an excellent alternative when overall filter size is critical, and has emerged as a popular research topic in recent times. Design techniques for implementation of planar single passband filters using microstrip technology has been discussed in [15]. Several novel approaches have been developed to design dual-band filters which involve the use of stepped-impedance resonators (SIRs) [16], combline filters loaded with lumped series resonators [17] and reduced length parallel coupled lines [18]. While these techniques result in compact filters, the insertion loss performance and selectivity is relatively poor compared to their waveguide counterparts, primarily due to the low quality factor (100-150) of planar resonators.

Over the last decade, the search for middle ground between waveguide and planar structures that provide high quality factor while still maintaining a relatively compact form-factor has given rise to the concept of substrate-integrated-waveguide (SIW) technology which was first introduced by Deslandes and Wu in [19]. Using SIW technology, waveguide components are implemented in planar substrates using an array of closely spaced via holes to emulate the waveguide walls as shown in Fig. 3. As a consequence, relatively high resonator quality factors are achieved (300-400) using a technology that is relatively inexpensive to fabricate. Also, the

quasi-planar nature of SIWs makes it feasible for a lot of applications which require high performance filters but cannot tolerate the large size of conventional waveguide components. The excellent propagation characteristics of SIWs have resulted in rapid development of advanced single-band filtering structures that exhibit low insertion losses and good selectivity [20], [21]. In the context of multi-band filters, inverter-coupled bandpass/bandstop resonators have been utilized to implement dual passband filters using SIW technology in [22]. However, the size of SIW bandpass filters are still larger than their transmission-line based equivalents. Although there is some published work on the miniaturization techniques for SIWs in general [23], very little attention has been paid to miniaturization techniques for SIW filters to make them comparable in size to their planar counterparts while maintaining their excellent low-loss properties [24], [25]. Thus, one of the major purposes of this dissertation is to embark on the challenging issues of miniaturization of SIW filters, in an attempt to replace well-adopted planar filters with their SIW counterparts.

For UWB filters, high quality factor is not critical because the very wide fractional bandwidths involved often result in low insertion losses even for moderate quality factors. However, their miniaturization is still a primary concern. A variety of techniques have been proposed to design UWB filters, and a comprehensive review is provided in [10]. Among these, a configuration that has been increasingly popular is based on the use of multiple-mode resonators (MMRs) to generate the UWB passband. Here, the multiple resonant modes of a microstrip or coplanar waveguide (CPW) resonator are designed to be quasi-equally distributed throughout the filter passband, and then strongly coupled to the input/output feed-lines using broadband coupling structures. In microstrip implementations [7], the coupling structures are implemented using parallel-coupled microstrip lines. However, to produce the necessary amount of coupling, the spacing between the coupled lines must be made

extremely narrow and hence imposes severe fabrication challenges. To overcome the fabrication complexity, composite microstrip-CPW transitions have been proposed in [26] that employ broadside coupling between microstrip and CPW lines to achieve tight coupling, and prove to be a feasible choice for easy implementation of UWB filters.

Within the 3.1-10.6 GHz communication band, there are a number of other communication standards operating at power levels that are much higher than that specified for UWB communication. To avoid interference between the UWB radio system and other narrowband standards present in the UWB frequency range, single- or multiple-notched bands are introduced in the UWB filter response. Several approaches have been proposed to produce frequency notches in the UWB filter response including folded coupling fingers [27] and SIR resonators [28]. However, these structures are difficult to incorporate into composite microstrip-CPW transitions without degrading the extent of coupling. Hence, new mechanisms for notch generation that are compatible with composite microstrip-CPW UWB filters are highly desired.

As specifications on system portability get more stringent, UWB filter miniaturization becomes a challenging problem considering that smaller size should not be accompanied by increased fabrication complexity. Thus, a part of this dissertation is devoted to developing techniques to miniaturize UWB filters, without increasing fabrication complexity, while producing interference rejection notches in the filter response and good out-of-band performance.

Besides the antennas, RF filters are generally the bulkiest parts of most communication and radar systems. While the entire RF front-end electronics can be included in a single chip using modern integrated circuit (IC) technology, RF filters are mostly off-chip components that result in increased size and cost of the transceiver. From a system point of view, greatest miniaturization and cost-saving is achieved if the RF

filter is designed and implemented on-chip. While this approach has numerous advantages, various limitations pose challenging problems that need to be overcome before on-chip filters become a practical reality. First, the substrate losses in conventional IC processes such as complementary metal oxide semiconductor (CMOS) makes it difficult to realize high quality factor elements on chip. As a result, on-chip narrowband filters often exhibit very high insertion losses. Second, the available area on-chip is very limited, and this makes transmission-line based approaches difficult to implement on-chip due to their large size. Several distributed approaches to implementing on-chip passive filters have been reported in [29], [30] based on thin-film microstrip technology. However, these works have very large filter sizes even at frequencies of 60- and 77-GHz. Semi-lumped and distributed approaches have been reported on CMOS technology in [31] and [32] that uses a multi-layer approach to implement compact on-chip filters. In this dissertation, techniques to implement K-band lumped-element filters will be studied in detail, in an effort to make fully-integrated system-on-chips feasible for 24-GHz Industrial-Scientific-Medical (ISM) unlicensed communication applications.

B. RF MEMS Tunable Filters: Hybrid Approach and Noise Analysis

RF MEMS switches or varactors have a thin mechanical membrane suspended over a signal line, and provide a varying capacitance value depending on electrostatic or piezoelectric force applied to it. In varactors, application of an actuating force deforms the membrane, thereby continuously changing the capacitance between the membrane and signal line. However, MEMS varactors provide a narrow range of capacitance ratio (max/min $\approx$ 2), and are known to have poor reliability. On the other hand, MEMS switches provide only two values of capacitance depending on

whether the switch is in the up- or down-state position. When an actuating voltage is applied, the bridge collapses to its down-state thereby allowing the signal to pass through it. RF MEMS switches have better reliability and a much higher range of capacitance variation (max/min $\approx$ 20-100). Based on the type of contact made in the down-state position, MEMS switches are classified as metal-contact or capacitive switches. In both cases, when the switch is in the up-state position, it creates an open-circuit ($C_{up} \approx 6 - 80$ fF). When in the down-state, a short circuit is created using a metal-metal contact in metal-contact switches ($R_s < 2\Omega$) or a metal-dielectric contact in capacitive switches ($C_{down} \approx 1-2$ pF). A detailed account of issues involved in design and fabrication of RF MEMS switches in given in [33].

RF MEMS switches have been used to develop a variety of high performance tunable filters, and a comprehensive summary of the current state-of-the-art is published in [34]. A wide variety of planar RF MEMS tunable filters have been reported with unloaded quality factors between 50-150 [35]-[37]. By inserting monolithic RF MEMS capacitor modules into evanescent-mode waveguide cavities, very high quality factors between 300-400 have been obtained [38]. However, all these filters require extensive microfabrication in a clean-room environment which makes their implementation very expensive and time-consuming. The detailed steps involved in fabrication of these filters are described in [39].

Recently, in an attempt to make RF MEMS switches more appealing to the automated-test equipment (ATE) industry, several efforts have been made to hermetically package these switches. Fig. 4 shows the packaged metal-contact RF MEMS switches developed by Radant MEMS [40], Omron Inc. [41], and MIT Lincoln Laboratories [42]. These switches have all been tested up to at least a 100 million cycles and have very good reliability. However, increased reliability comes at the cost of increased parasitic elements associated with the hermetic package. As a result, the

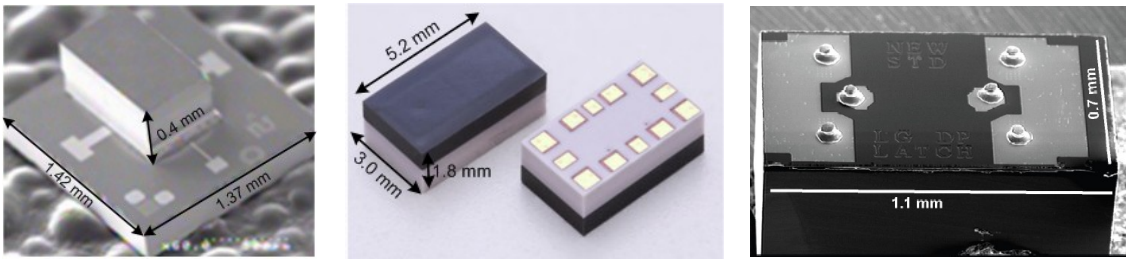

(a) (b) (c)

Fig. 4. Metal-contact RF MEMS switches developed by (a) Radant MEMS [40], (b) Omron Inc. [41], and (c) MIT Lincoln Laboratories [42].

quality factor of the packaged switches are lower than those of the actual switches themselves. This limits the use of packaged RF MEMS switches to the low-GHz frequency ranges, and results in very moderate performance when used with low quality factor elements such as transmission lines.

As discussed earlier, high quality factor resonators are easily obtained using SIW technology, while still being easy to fabricate using conventional printed circuit board technology. The use of packaged RF MEMS switches to develop tunable SIW filters gives rise to a new class of RF MEMS tunable filters with unprecedented performance that are very easy to fabricate and assemble. The concept of SIW "hybrid" RF MEMS tunable filters is relatively unexplored so far, and is one of the major goals of this dissertation.

As devices are scaled to the micro-scale, noise sources that are negligible in the macro-scale become significant and limit the performance of micro-devices. In RF MEMS switches, several noise sources impact switch performance including Brownian noise, acoustic noise, acceleration noise, and power supply noise [43] and are shown to have an impact on MEMS phase shifters and tunable filters [44]. From a system point of view, noise in RF MEMS tunable filters can have important SNR implications since they typically appear before the low-noise amplifier when used as band-select

filters. In current literature, the impact of Brownian noise on RF MEMS tunable filters has not been studied thoroughly although it can significantly impact system performance. In this dissertation, the effect of Brownian motion in RF MEMS tunable filters is presented in detail by developing fully-analytical, iterative and simulation-based methods to predict the level of signal degradation at the filter output.

C. Overview

The main purpose of this dissertation is two-fold. First, to develop state-of-the-art filter solutions for single/multi-band, ultra-wideband and tunable frequency allocations with major emphasis on: (1) filter miniaturization, (2) high quality factor, (3) ease of fabrication and (4) good out-of-band performance. Second, to develop mathematical and simulation-based methods to derive fundamental limitations imposed by nonlinear noise in RF MEMS tunable filters. It also comprises the development of a self-sustained microwave platform for detection of organic liquids.

Chapter II focuses on miniaturization techniques for single-band, dual-band and UWB bandpass filters. First, methods to miniaturize composite microstrip-CPW UWB filters based on slow-wave capacitively-loaded CPW multiple-mode resonators are developed. A frequency notch is introduced using a bridge structure over the CPW resonator, and defected ground structures are used to improve the stopband performance. Second, a lumped-element K-band integrated filter is implemented in 90nm CMOS technology that is very compact compared to other reported on-chip passive filters at this frequency. Third, fractal structures are used to lower the size of half-mode SIW bandpass filters while simultaneously improving its quality factor. Finally, a very compact dual-band filter is implemented using half-mode SIW structures that results in a deep rejection notch between filter passbands, low insertion

loss and excellent upper stopband suppression.

Chapter III presents full-mode and half-mode hybrid SIW filters that are tunable from 1.2-1.6 GHz using discrete surface-mount RF MEMS switches. The SIW cavity resonators are tuned using via-holes to perturb the fields within the cavity. These filters are designed to have either constant fractional or constant absolute bandwidths, and exhibit high quality factors are they are tuned. Techniques to improve the upper stopband performance are also discussed in detail. It is shown that half-mode SIW tunable filters are much smaller than their full-mode counterparts while having comparable performance.

Chapter IV discusses the fundamental noise limits imposed by nonlinear noise in RF MEMS tunable filters, and their implications on SNR. First, a simulation-based approach is presented that employs the nonlinear model of the RF MEMS switch to predict nonlinear noise in RF MEMS tunable filters. Second, a nonlinear nodal analysis method customized to predict nonlinear effects in RF MEMS tunable filters without the use of computer-based techniques, is presented. Third, a mathematical approach to predict nonlinear noise in all-pole RF MEMS tunable filters is developed based on perturbation of the filter poles. The effect of filter nonidealities is discussed in detail. Finally, a unified approach to predict nonlinear noise in all-pole RF MEMS tunable filters is presented that is much simpler to use than the perturbation approach.

Chapter V covers the design and implementation of a self-sustained microwave platform for the detection of lossy organic liquids. A novel technique to detect the dielectric constant of liquids based on microwave oscillators is presented. By using the microwave oscillator in a frequency synthesizer system, the whole measurement system is digitally interfaced to a computer and enables accurate determination of dielectric constant.

Chapter VI is the conclusion and future work. Half-mode SIW technology pro-

vides a compact and high quality factor solution for many advanced filtering structures, and can be used to develop diplexers with high rejection and isolation performance. A compact, low-loss, half-mode SIW tunable filter for 12-18 GHz applications is also proposed using RF MEMS switches which are monolithically fabricated along with the filter structure. Future research efforts must also be focused on experimental verification of the theories of nonlinear noise. The self-sustained detection platform must also be extended to detect the loss factor of materials, which is important for many practical applications.

CHAPTER II

NOVEL TECHNIQUES FOR FILTER MINIATURIZATION*

With the advent of wireless technology and ever increasing demand for high data rate mobile communications, the number of radios on mobile platforms have been steadily growing. Typically, each radio system is designed for a particular communication standard and requires the use of RF filters that select the required band of interest. In such cases, the overall size of each filter in the communication module must be as small as possible to reduce the overall size of the transceiver. Thus, techniques to miniaturize RF filters and reduce the overall circuit size are of vital importance. However, as it turns out, there is no generalized miniaturization technique that is equally applicable to all kinds of filtering structures. In this context, custom design techniques must be developed based on the actual filter topology for a particular application, that result in smaller filter sizes. As a result, as newer filtering structures are developed to better suit the needs of a particular communication system, innovative filter miniaturization techniques are always required to make them smaller.

In this chapter, miniaturization techniques are developed for single-band, dual-band and UWB bandpass filters. First, slow-wave phenomena in capacitively loaded

---

coplanar waveguides are utilized to make the multiple-mode resonator used in UWB filters up to 40% smaller. Second, a very compact lumped element filter at K-band is designed and implemented on 90-nm CMOS technology. Lastly, miniaturization techniques for single-band and dual-band SIW filters are developed based on half-mode SIWs and cross-shaped fractals. For all cases, filter prototypes are fabricated and measured to validate the proposed design techniques.

A. Miniaturized UWB Bandpass Filters With Notch Using Slow Wave CPW Multiple Mode Resonators

1. Introduction

Recently, there is increased interest in the development of ultra-wideband (UWB) systems operating between 3.1 to 10.6 GHz because they are capable of high data rates while consuming very low power. To this end, a variety of UWB filter topologies have been implemented to reject unwanted signal interference [10]. One popular approach is to employ stepped-impedance multiple-mode resonators (MMRs) using composite microstrip-coplanar waveguide (CPW) structures [26]. Since such filters are relatively large, there is a need for novel miniaturization schemes that result in filter sizes comparable to those in [45]-[48]. The UWB filters reported in [26]-[46] do not have broad upper stopbands with good rejection levels but this can be achieved in a compact way using defected ground structures (DGS) [47]. In addition, UWB filters employing composite microstrip-CPW structures such as those reported in [26]-[47] have no provision for generation of a frequency notch to reject WLAN interference.

In this section, a novel UWB filter using CPW MMR is presented with the following advantages: (1) miniaturization using slow-wave CPW lines that result in 40% size reduction without DGS (25% with DGS) compared to the CPW MMR filter in

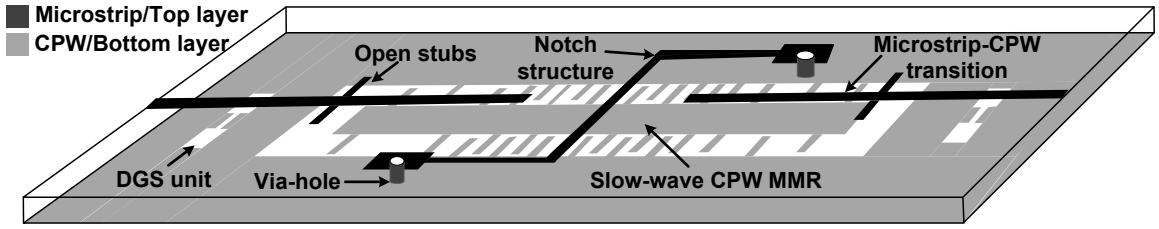

Fig. 5. Three-dimensional view of the proposed UWB BPF with notch using slow-wave CPW multiple-mode resonator (MMR).

[26], and comparable size to the slow-wave UWB microstrip filter in [48], (2) frequency notch generation using a novel bridge structure to reject WLAN interference, and (3) good upper skirt selectivity using stub-loaded microstrip-CPW transition and improved upper stopband rejection of greater than 22 dB from 11 to 16 GHz using DGS.

Fig. 5 shows the layout of the proposed UWB BPF with notch employing a slow-wave CPW MMR etched in the bottom layer which consists of CPW lines loaded with interdigital capacitors to create the slow-wave effect [49]. The slow-wave MMR is excited by a broadband microstrip to CPW transition to which open-ended stubs are attached to improve the upper skirt selectivity by introducing a transmission zero in the upper stopband. DGS units are located in the ground plane of the microstrip feed line to improve the upper stopband rejection. To produce a notch in the transmission response at a desired frequency, a novel bridge structure is etched in the top layer and connected to the bottom layer through via holes.

2. Initial UWB BPF

a. Slow-Wave CPW MMR

Fig. 6 shows the slow-wave CPW MMR consisting of cascaded capacitively-loaded CPW lines indicated by Sections A and B, and the corresponding MMR equivalent

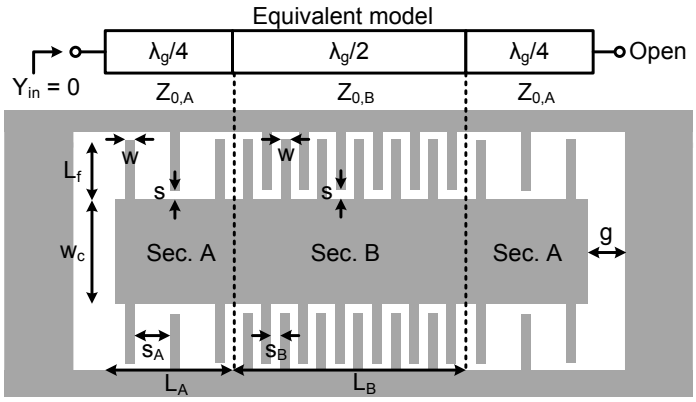

Fig. 6. Slow-wave CPW MMR and its equivalent circuit model.

model. The fringing capacitance between interdigital fingers results in a higher capacitance per unit length of the CPW line, and the electrical length of the resonator which is proportional to $\beta = \omega\sqrt{LC}$, is increased. Conversely, the required physical length of a CPW line for a given electrical length is smaller and hence results in miniaturization. Also, the characteristic impedance of the CPW line decreases because $Z_0 = \sqrt{L/C}$. Thus, the characteristic impedance and electrical length of each Section in the CPW MMR are controlled by appropriately choosing the number of fingers and the spacing between them, for a fixed finger length. The slow-wave CPW MMR design procedure is as follows: First, a standard high impedance CPW line is designed, typically around 70 Ω so that reasonable impedances are achieved after capacitive loading. Next, Section B of the slow-wave MMR is designed by maximally loading the CPW line using an arbitrary finger length L_f for greatest miniaturization and lowest impedance, $Z_{0,B}$. The number of fingers is chosen so that Section B is $\lambda_g/2$-long at mid-band frequency. The minimum achievable size is ultimately limited by fabrication tolerances. The characteristic impedance of Section A, $Z_{0,A}$, is determined using the equivalent model so that the resonant modes satisfying the condition $Y_{in} = 0$ are quasi-equally distributed in the filter passband. Section A is

then designed by adjusting the number and spacing of the fingers so that its electrical length is $\lambda_g/4$ and characteristic impedance is $Z_{0,A}$. The gap g at the open ends of the resonators must be large enough to minimize parasitic capacitance to ground. Finally, the resonator is fine-tuned by adjusting L_f till the required resonance frequencies are obtained. Fig. 7 shows the variation of $Z_{0,A/B}$ normalized to the unloaded impedance of the CPW line (Z_{0U}), and the corresponding change in the first three resonant frequencies of the slow-wave MMR as a function of L_f. By choosing $L_f = 1.2$ mm, the first three resonant frequencies of the CPW MMR are 4.13 GHz, 6.85 GHz and 9.57 GHz, when $Z_{0,A} = 47.3\ \Omega$ and $Z_{0,B} = 24.5\ \Omega$ at 6.85 GHz.

Full-wave simulations show that the slow-wave CPW lines exhibit bandgap behavior around 22 GHz. Hence, $Z_{0,A/B}$ and normalized phase constants (β/k_0) of the CPW lines are almost constant over the filter passband, since it is far away from the bandgap frequency [48]. Any Z_0-variation over the passband range affects both Z_{0A} and Z_{0B} so that their ratio remains constant, and hence the MMR resonant frequencies are unchanged due to frequency dispersion. The final dimensions of the slow-wave CPW MMR design on 0.635 mm thick RT/Duroid 6010 with $\epsilon_r = 10.2$ are: $w_c = 2$ mm, $w = s = s_B = 0.2$ mm, $s_A = 0.7$ mm, $L_f = 1.2$ mm, $g = 0.8$ mm, $L_A = 2.45$ mm and $L_B = 4.4$ mm. The proposed slow-wave MMR is 40% smaller than the CPW MMR in [26].

b. Stub-Loaded Transition with DGS Unit

To design a UWB passband using the resonant modes of the slow-wave MMR, tight broadband-coupling between the feed lines and the slow-wave MMR is achieved with a broadside microstrip-CPW transition as shown in Fig. 8(a). The microstrip line on the top layer is coupled to the center conductor of the CPW on the bottom layer, and the coupling strength is higher if the length (L) and width (W) of the microstrip

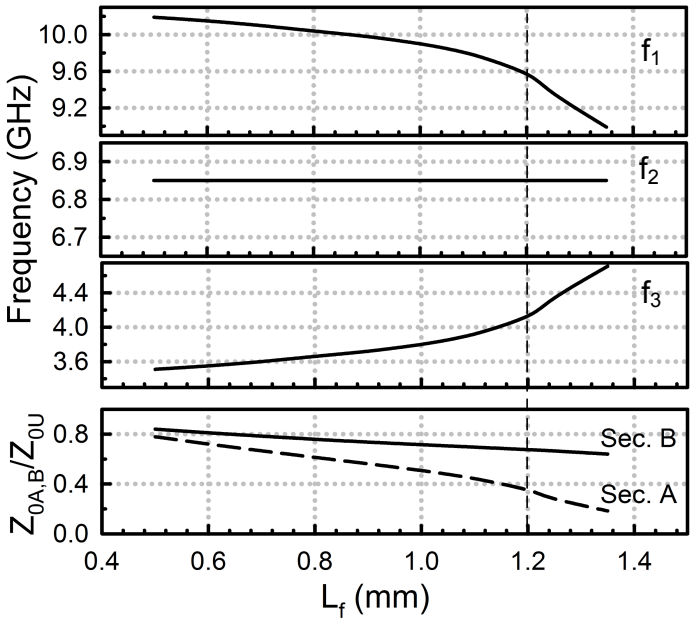

Fig. 7. Variation of loaded-line characteristic impedances, $Z_{0,A/B}$, normalized to the unloaded characteristic impedance Z_{0U}, and the change of resonance frequency of the first three modes of the slow-wave CPW MMR against L_f.

line is increased. To improve the upper rejection skirt of the filter, two open-ended stubs with lengths L_s are attached to the top microstrip line to independently control the upper transmission zero produced by the transition. The broadband transition is initially designed with $L_s = 0$ by increasing L and W till the coupling bandwidth covers the UWB passband. The upper transmission zero is then brought closer to the upper passband edge by increasing the length of the stubs resulting in improved roll-off of the upper rejection skirt. Fig. 8(b) shows the S-parameters of the stub-loaded microstrip-CPW transition for different values of L_s. The final dimensions of the stub-loaded transition are: $L = 3.5$ mm, $W = 0.5$ mm and $L_s = 1.3$ mm.

To improve the upper stopband suppression of the UWB filter, dumb-bell shaped DGS units are etched in the ground plane of the microstrip feed lines as shown in Fig. 8(a), so that each DGS unit resonates at the spurious frequency. As seen later, using

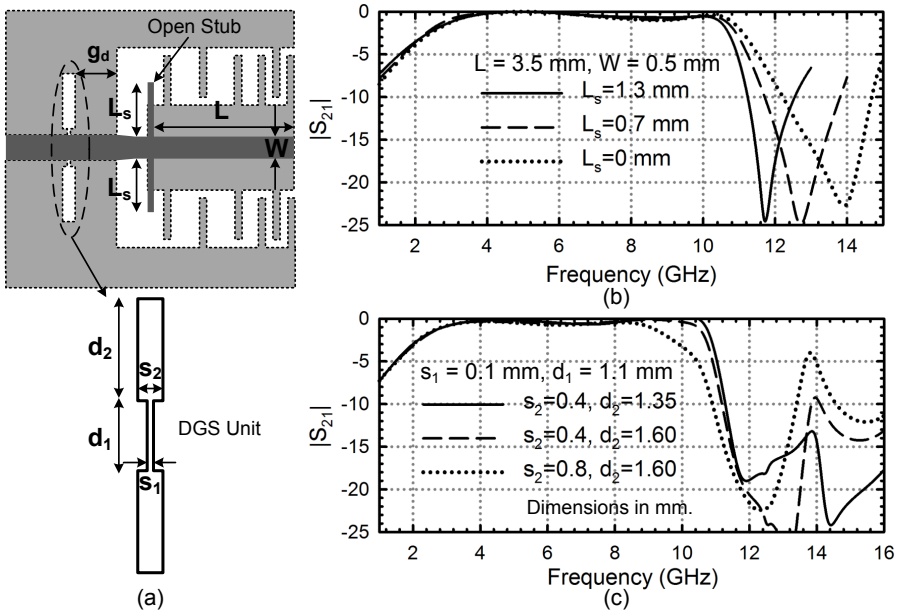

Fig. 8. (a) Stub-loaded transition with DGS unit, (b) improvement of upper rejection skirt as the length of open stubs is increased, and (c) spurious suppression due to one DGS unit placed at the input or output.

a single DGS unit at the input and output of the filter results in a stopband rejection of greater than 20 dB from 11 to 16 GHz. Greater suppression can be achieved by increasing the number of DGS units, at the cost of larger filter area. Fig. 8(c) shows the S-parameters of the stub-loaded transition with DGS unit for different values of s_2 and d_2. The optimized values of the DGS unit are: s_1=0.1 mm, s_2=0.4 mm, d_1=1.1 mm, d_2=1.35 mm and g_d=1.2 mm.

c. Measurements

Fig. 9(a) shows the conventional and proposed UWB BPFs fabricated on 0.635 mm thick RT/Duroid 6010 substrate with $\epsilon_r = 10.2$. The proposed UWB BPF including DGS is 25% smaller in length compared to the conventional filter without DGS in [26]. The proposed UWB BPF was measured using an Anritsu 3680-20 Universal Test

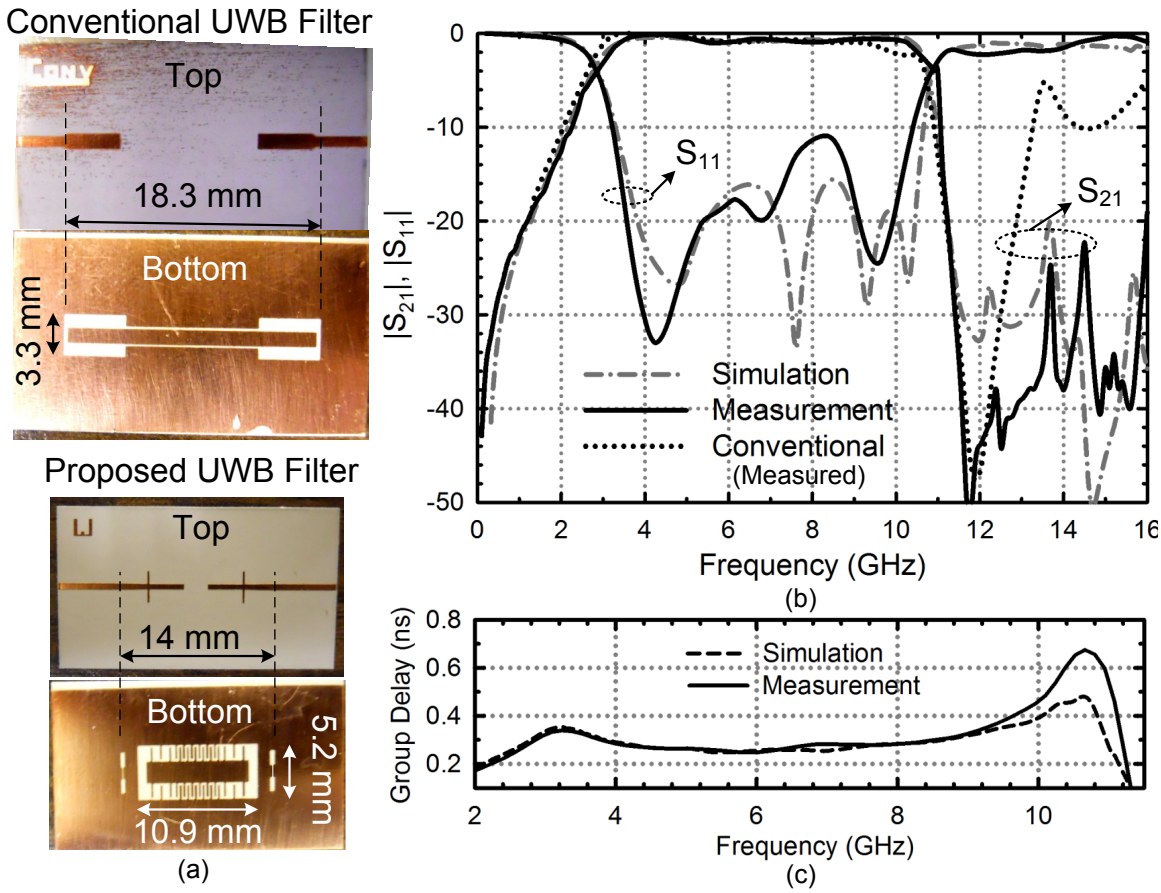

Fig. 9. (a) Fabricated conventional and proposed UWB BPF prototypes, (b) simulated/measured S-parameters of the conventional and proposed UWB BPF, and (c) simulated/measured group delay of the proposed UWB BPF.

Fixture. The simulated/measured filter response and group delay are shown in Fig. 9(b) and (c), respectively. The proposed UWB BPF has a return loss better than 10-dB over the 3.1-10.6 GHz bandwidth with an insertion loss of 0.9 dB. The upper stopband suppression is better than 22 dB from 11 to 16 GHz and the group delay variation is relatively flat over the UWB passband. In comparison, the conventional UWB BPF has very poor stopband performance due to unsuppresed spurious modes.

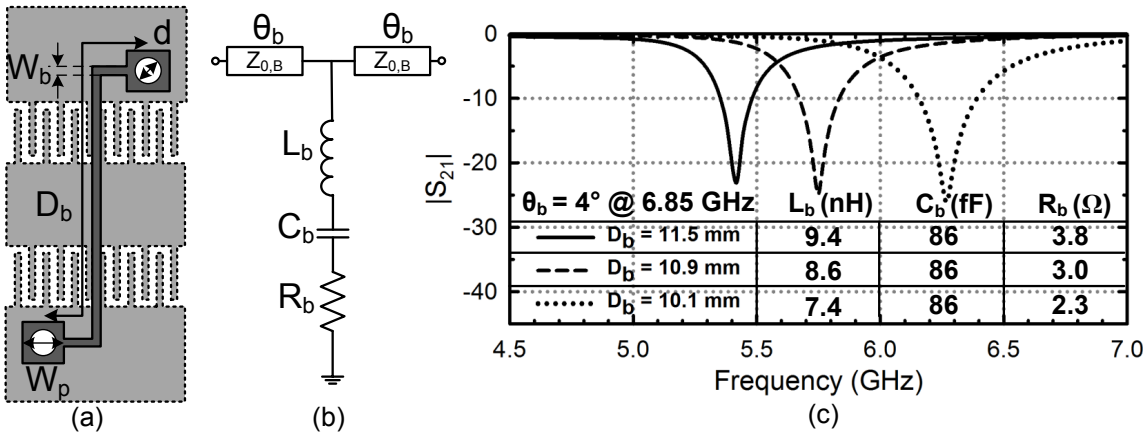

Fig. 10. (a) Proposed bridge structure over the slow-wave CPW MMR for notch generation, (b) equivalent circuit model of the bridge, and (c) simulated response of Section B of CPW MMR with bridge and model parameters for various lengths of the bridge with W_b=0.2 mm, W_p=1 mm and d=0.6 mm.

3. Slow-Wave UWB BPF with Notch

To produce a notch in the frequency response of the UWB BPF at 5.8 GHz, a bridge with width, W_b, and length, D_b, is placed over the center of the slow-wave MMR, as shown in Fig. 10(a). It is connected at each end to the bottom layer using via-holes of diameter d placed at the center of square pads with an edge W_p. The equivalent circuit model is shown in Fig. 10(b), where L_b represents the bridge and via-hole inductance, C_b the capacitance (parallel-plate and fringing) of the bridge over the CPW line, and R_b the resistive loss associated with the bridge and via-holes. The small sections of transmission lines at the input and output correspond to the electrical length of CPW lines, θ_b, under the bridge.

For a fixed value of W_b, the area of the bridge above the CPW line is unchanged and hence C_b remains constant, but L_b increases for longer bridge lengths D_b. The bridge is designed by appropriately choosing W_b and D_b so that its resonance frequency $\omega_b = 1/\sqrt{L_b C_b}$ occurs at the required notch frequency. The resistive losses

in the bridge (R_b) determines the depth of the frequency notch. Fig. 10(c) shows simulated S-parameters of Section B of the MMR with the bridge and as the bridge length D_b is increased, the notch frequency is lowered due to higher values of L_b. The designed dimensions of the bridge, and the corresponding model parameters are: $W_b = 0.2$ mm, $D_b = 10.7$ mm, $d = 0.6$ mm, $W_p = 1$ mm, $L_b = 8.55$ nH, $C_b = 86$ fF, $R_b = 2.9\ \Omega$, θ_b=4° at 6.85 GHz.

The bridge structure for notch generation is included in the UWB BPF filter designed in Section A.2, and the fabricated filter and simulated/measured S-parameters and group delay of the prototype are shown in Fig. 11. The notch at 5.65 GHz exhibits 19.2 dB of rejection with an extremely narrow 10-dB bandwidth of 2% around the notch frequency. The slight shift in the notch frequency is most probably attributed to parasitics due to soldering via-holes. The group delay variation is almost flat from 3.1-10 GHz, except around the notch frequency.

4. Conclusion

A novel slow-wave CPW MMR miniaturized UWB BPF with notch is designed and implemented. The proposed slow-wave CPW MMR is 40% smaller in length compared to an unloaded CPW MMR. Stub-loaded microstrip-CPW transitions are used to improve the upper rejection skirt of the UWB BPF, and the upper stopband rejection greater than 22 dB is obtained by using DGS units. A mechanism for notch generation is demonstrated using a novel bridge structure. At the mid-band frequency, the novel filter with improved rejection and frequency-notch is $0.32\lambda_0$-long compared to similar filters with electrical lengths $0.4\lambda_0$ in [26], $0.77\lambda_0$ in [46], and $0.29\lambda_0$ in [48], and is attractive for UWB system applications.

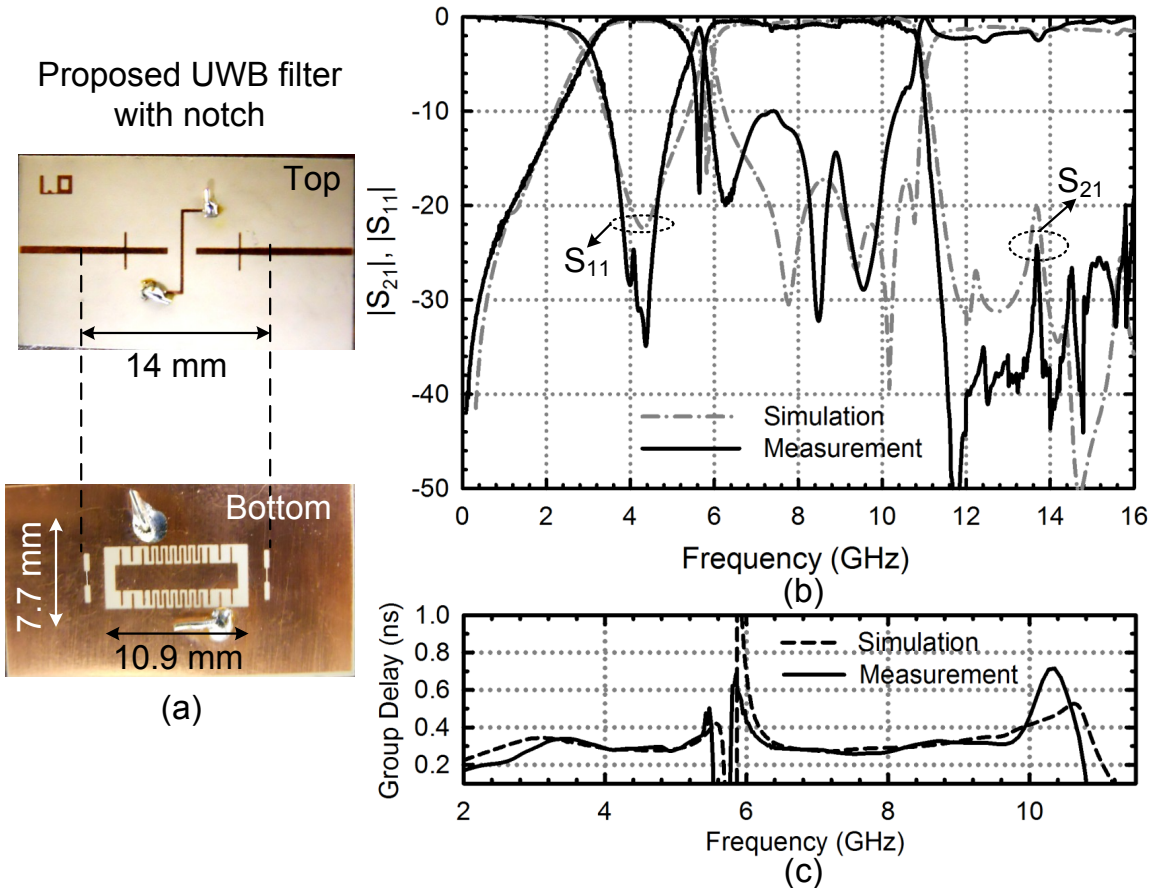

Fig. 11. (a) Fabricated UWB BPF with notch, and simulated/measured performance of the UWB BPF with notch—(b) S-parameters, (c) group delay.

B. A K-Band Integrated Bandpass Filter in 90 nm CMOS Technology

1. Introduction

Miniaturized high performance band-select filters are essential components in front-end of communication or radar systems at microwave/mm-wave frequencies [50]. Typically, such bandpass filters are constructed on low-loss substrates such as glass and alumina at mm-wave frequencies, and are implemented as off-chip components. However, this increases the overall cost of production and size of the receiver.

Low-cost complementary metal oxide semiconductor (CMOS) technology has been recently employed to implement a variety of commercial microwave/mm-wave front-ends [51]. Having the band-pass filter integrated with the rest of the front-end electronics reduces the size and cost of the receiver enormously. However, due to substantial loss of low-resistivity silicon substrate and CMOS metal layers, high-quality passive circuits such as bandpass filters are difficult to implement using standard CMOS technology. Micromachining and high-resistivity silicon techniques [52], [53] improve the substrate loss, but require complex and expensive post-processing steps. Thin-film microstrip (TFM) passive components in CMOS process result in considerable loss reduction. This is due to isolating the lossy silicon substrate from the passive component using the lowest metalization layer as ground plane. Using this technique, bandpass filters have been reported in 0.18-μm standard CMOS technology for 60 and 77 GHz mm-wave applications [29], [30].

Unfortunately, TFM structures are not suitable for CMOS filters at K-band due to their large size compared to the area occupied by integrated front-end electronics. This work presents a 20 GHz miniaturized filter in 90-nm CMOS process implemented with lumped-element passive components to overcome the drawback of TFM-based filters at K-band. Special layout techniques are applied to improve the quality factor

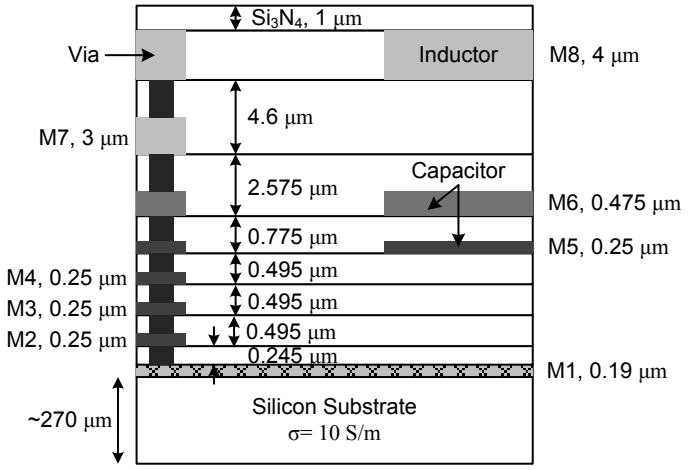

Fig. 12. Layer configuration of the lumped inductors and capacitors in IBM 90-nm CMOS process.

(Q) of lumped inductors in the filter structure and hence the filter insertion loss. The overall area of the filter is 0.315 mm^2 which is at least 10 times smaller than its equivalent TFM-based filter at the same frequency.

2. Filter Design

a. Technology

The profile of a standard 90-nm CMOS technology is illustrated in Fig. 12. The silicon substrate has a thickness of 270 μm and a conductivity of 10 S/m. The top metalization layer (M8) with a thickness of 4 μm is used to implement the inductor. The reduced skin effect due to high thickness of M8 layer makes it suitable for high-Q inductor implementation. The lowest metalization layer (M1) with thickness of 0.19 μm is used as the ground plane of the filter. Metalization layers M6 and M5, and the low-loss SiO_2 layer between them provide high-Q metal-insulator-metal (MIM) lumped capacitors required for filter implementation. The thinner dielectric layer between M5 and M6 provides MIM capacitors with smaller areas compared to capac-

itors implemented using M6 and M7 layers at the expense of slightly lower capacitor Q. The top passivation layer consists of a 1 μm Si_3N_4 layer. Also, a via from M8 layer to M1 ground plane is realized by connecting small pads in each intermediate metal layer using metal vias in CMOS process. A similar approach is used to connect other metal layers to M1 ground plane.

b. Meander-Line Inductor

The standard spiral inductors available in 90-nm CMOS process design kit have very low Q (Q<10) at frequencies greater than 10 GHz. As a result, a new inductor layout with higher Q but compact size needs to be developed. Transmission line-based inductors on CMOS technology have higher Q-factors (Q $\approx$ 30-50) compared to spiral ones, but are large in size for K-band applications. To reduce the inductor size while maintaining high Q, a meander-line grounded inductor is proposed as shown in Fig. 13(a). Since meander-line inductors are not available in the standard design kit provided by the foundry, full-wave simulation is used to evaluate inductance and Q as a function of frequency as shown in Fig. 13(c) using Sonnet. For this purpose, the profile shown in Fig. 12 is employed for full-wave simulation around 20 GHz. To avoid induced eddy currents which lower the Q-factor, the ground plane (M1 layer) is removed underneath the inductor during full-wave simulation. As a result, the inductor Q improves from around 12 to 22 at 20 GHz (Fig. 13(c)). The equivalent circuit model of the inductor extracted from full-wave simulation is shown in Fig. 13(b). A meander-line with a length of 333 μm and a width of 22 μm has an inductance of 194 pH and a resistance of 1.1 Ω. Fig. 14(a) shows the photograph of the fabricated two-port meander-line coupled inductor structure using IBM 90-nm CMOS process for accurate inductor characterization. One side of each inductor is connected to ground plane all the way from M8 to M1 as explained earlier. The S-parameters for

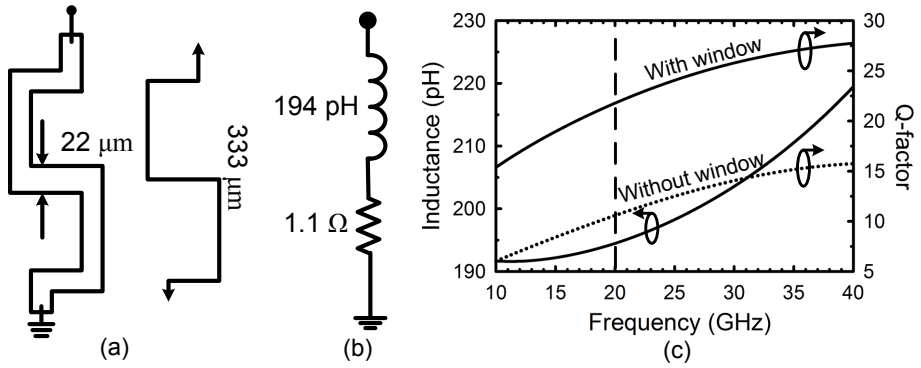

Fig. 13. (a) Meander-line grounded inductor, (b) inductor equivalent circuit model, and (c) simulated inductance and quality factor vs. frequency using Sonnet.

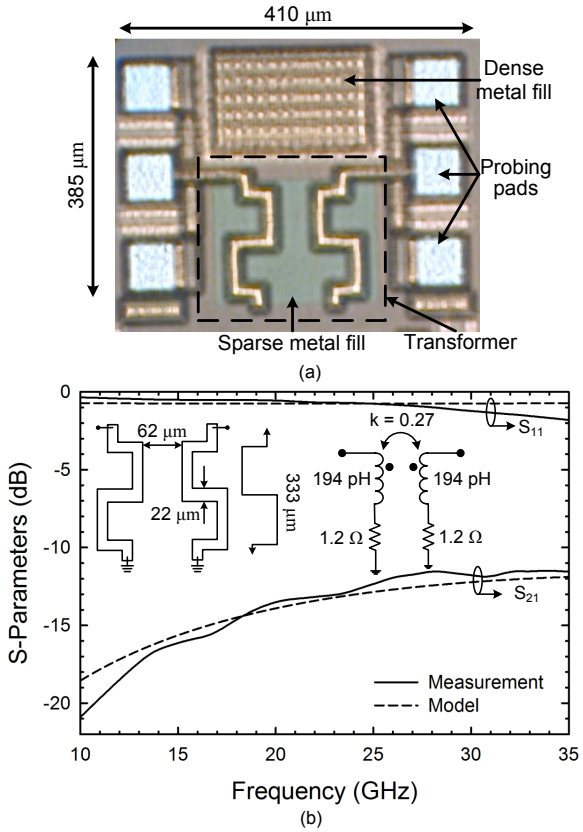

Fig. 14. (a) Photograph of the fabricated two-port meander-line coupled inductor structure in 90-nm CMOS process, and (b) resulting S-parameters from the circuit model and measurements.

the coupled inductors are measured and compared to the simulated S-parameters of the equivalent circuit model shown in Fig. 14(b) over 10-35 GHz (L=194 pH, R= 1.2 Ω and the coupling factor, k=0.27). The results match very well which also proves the accuracy of full-wave simulation. Dense metal filling underneath the coupled inductor in either of eight metalization layers alters the meander-line inductance value and Q significantly. Therefore, it is prohibited during the layout preparation. Although dense metal filling is blocked by the design kit, the CMOS foundry includes sparse metal fill patterns underneath the inductors automatically. Measurement results show that spare metal filling does not have any noticeable effect on the inductor performance.

c. Filter Topology and Implementation

Fig. 15(a) presents a two-pole lumped-element filter with input/output and inter-resonator capacitive coupling. The filter has a ripple of 0.5 dB, fractional bandwidth of 7% and is a practical realization of a standard Chebyshev bandpass filter with parallel LC resonators and J-inverters [54], [55]. A ripple factor of at least 0.5 dB corresponds to a minimum return loss of 10 dB at the filter input/output. Capacitive coupling reduces the required number of inductors in a two-pole implementation, which in turn lowers the overall size of the integrated filter.

Fig. 15(b) shows the top view of the filter layout in 90-nm CMOS process. Two meander-line shunt inductors are implemented using M8 layer. They are located in opposite directions to minimize additional inductive coupling between them. The ground-plane underneath each inductor is removed to improve the quality factor as discussed before. Fig. 15(c) shows the 'AA' cross section of the layout top view. The input/output and inter-resonator coupling MIM capacitors are implemented using the SiO_2 layer sandwiched between M5 and M6 layers. One of the input (output)

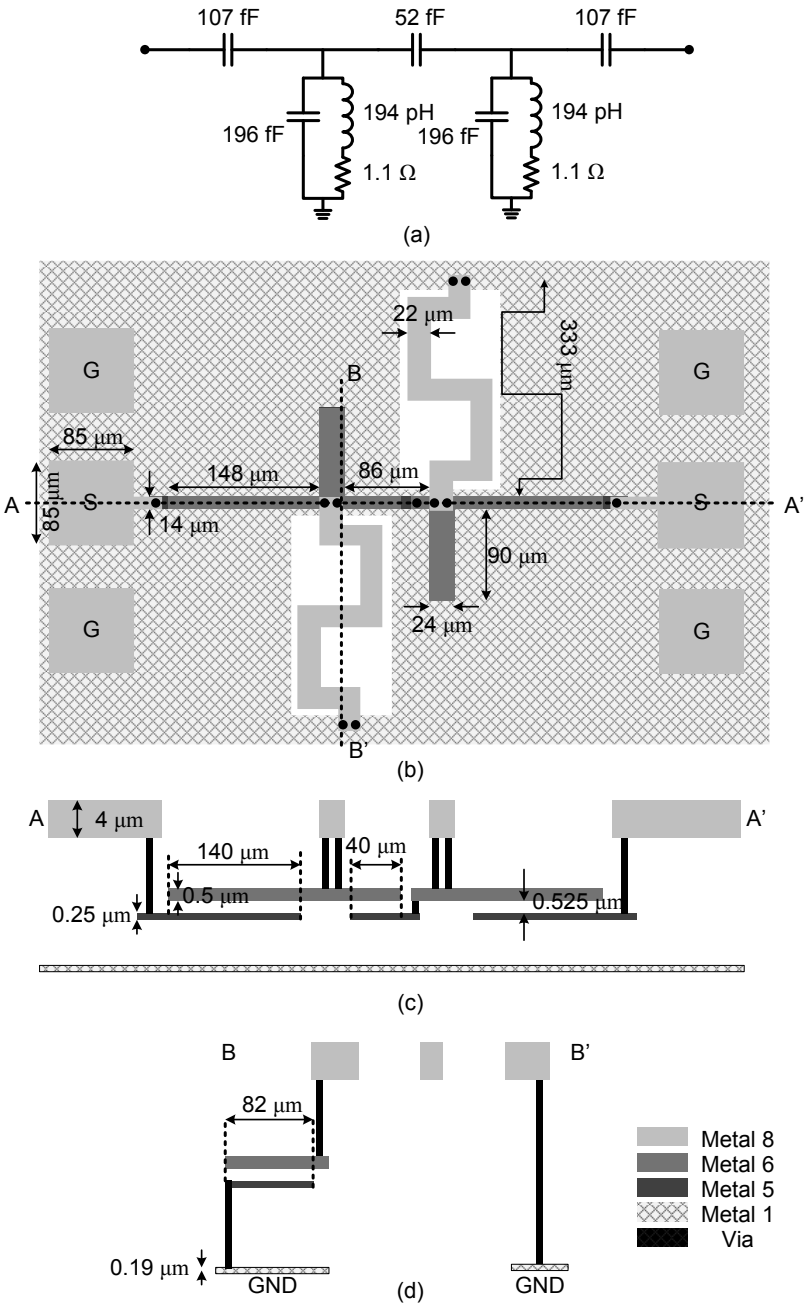

Fig. 15. (a) Schematic of the two-pole Chebyshev bandpass filter, (b) top view of the filter layout, (c) cross section 'AA', of the layout top view, and (d) cross section 'BB' of the layout top view.

capacitor plates is connected to the input (output) signal pad located in M8 layer and the other one is connected to the corresponding meander-line inductor metal layer through via posts. The inter-resonator coupling capacitor plates are connected to adjacent shunt inductors' metal layer. Fig. 15(d) shows the 'BB' cross section of the layout top view. Resonator shunt capacitors are implemented the same way as the coupling capacitors while one of their plates is connected to the inductor metal layer (M8) and the other one is connected to the ground plane through via posts.

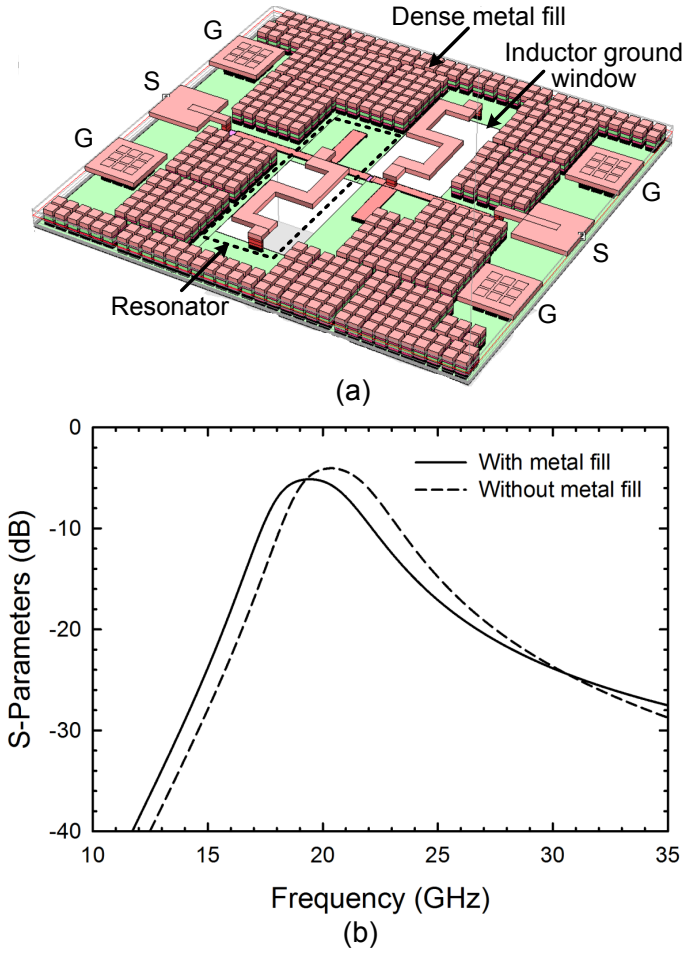

Fig. 16. (a) Bandpass filter layout with dense metal filling around the filter components, and (b) simulated filter response with and without metal filling using Sonnet.

d. Effect of Metal Filling

To be able to predict and minimize the negative effects of IBM 90-nm design kit automatic metal filling on the filter response, protective mask layers are used to prevent dense metal filling underneath the inductors and capacitors for metal layers M1-M6. Metal filling for layers M7 and M8 is under the control of the circuit designer.

To investigate the effect of manual and automatic dense metal filling around filter components, the available empty areas around filter components are filled with metal layers as shown in Fig. 16(a). The effect of metal-filling is then studied by performing full-wave simulation for the filter structure with metal filling. The full-wave simulation results with and without metal filling are shown in Fig. 16(b). As long as the area underneath the inductors are protected, dense metal filling does not degrade filter performance significantly. Unfortunately, the protective mask layer cannot include the entire filter structure to completely avoid dense metal filling. This is due to the design rule limitations for the blocking layer in the IBM 90-nm design kit.

3. Measurement Results

Fig. 17(a) shows the photograph of the fabricated bandpass filter in IBM 90-nm CMOS process. Meander-line inductors, resonator capacitors, input/output and inter-resonator coupling capacitors are all shown in the figure. Also, areas with dense and sparse metal filling are marked. The total filter area including input/output probing pads is 0.315 mm^2. The CMOS bandpass filter chip was tested via on-wafer probing using Ground-Signal-Ground (GSG) coplanar air probes. S-parameter measurements of the circuit were carried out using an Agilent N5230A vector network analyzer. The simulation and measurement results for the fabricated filter are shown

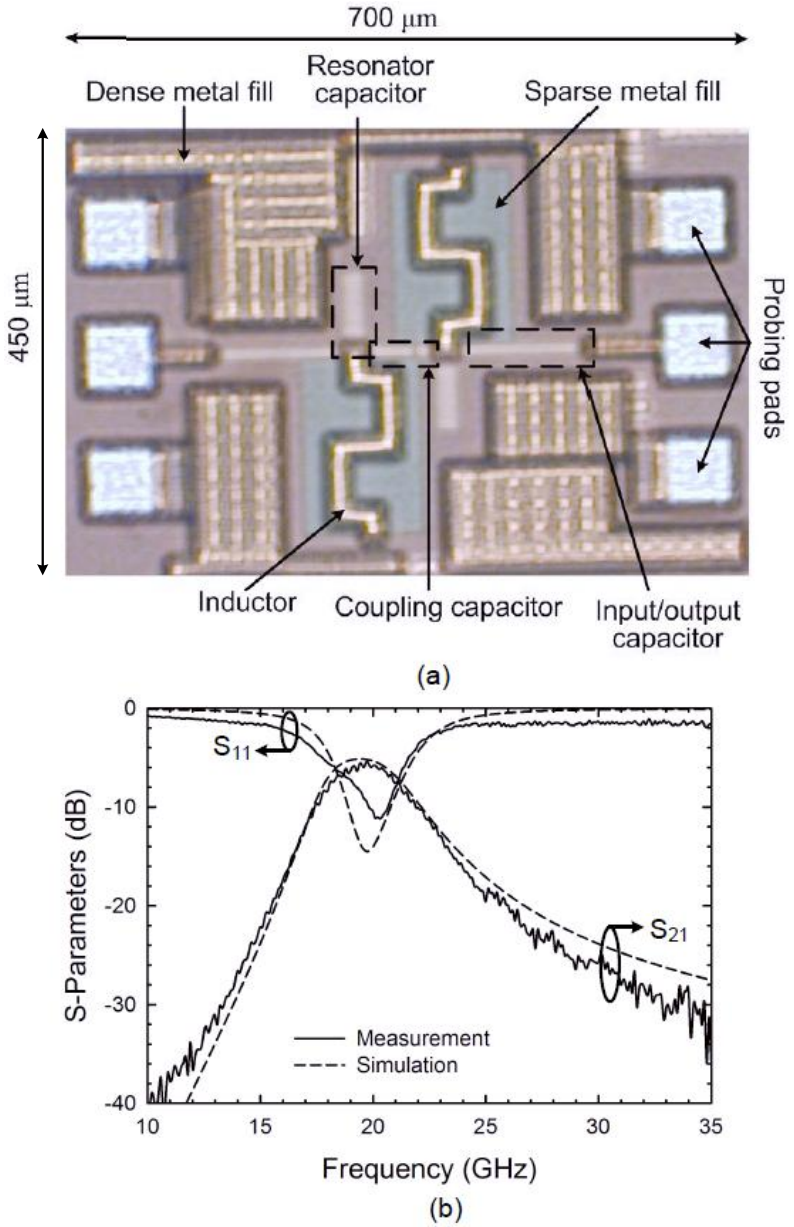

Fig. 17. (a) Photograph of the fabricated bandpass filter in IBM 90-nm CMOS process, and (b) simulated and measured S-parameters of the bandpass filter.

in Fig. 17(b) and are in good agreement. The measured insertion loss at 20 GHz is around 5 dB. The loss mostly is due to the limited quality factor of the meander-line inductors (Q ≈ 22) compared to the MIM capacitors (Q ≈ 250) which results in an overall measured unloaded quality factor of 12.5 for the filter.

4. Conclusion

This study has demonstrated the potential of implementing lumped-element K-band CMOS bandpass filters in standard 90-nm CMOS process without any post-processing steps for the first time. A two-pole bandpass filter with 1-dB bandwidth of 7% is implemented using lumped element meander-line inductors and MIM capacitors in CMOS process. The 1-dB bandwidth is measured instead of the traditional 3-dB bandwidth since it is closer to the designed ripple bandwidth of 0.5 dB. The effect of dense metal filling is also considered in the filter implementation.

Measurement results show an insertion loss of 5 dB, a return loss better than 10 dB and an unloaded quality factor of 12.5 at 20 GHz. The return loss can be further improved by slightly decreasing the input/output capacitor value. The proposed lumped element filter designed using narrowband filter theory can be implemented for fractional bandwidths up to around 20%. The reported filter is at least 10 times smaller compared to its TFM-based equivalent filter at similar frequency. Thus the filter presented in this study has promising applications in the realization of fully-integrated commercial front-ends at K-band.

C. Miniaturized Half-Mode Substrate Integrated Waveguide Bandpass Filters Using Cross-Shaped Fractals

1. Introduction

Low-loss waveguide bandpass filters (BPFs) are widely used in microwave and millimeter wave communication systems to reject unwanted signal interference. However, conventional waveguide BPFs are very bulky and expensive when portability is critical, for example, in airborne platforms. Substrate integrated waveguide (SIW) BPFs have become a very popular alternative to conventional waveguide BPFs due to their low-profile and high-performance [20], [21]. In addition, SIW filters can be easily integrated with other planar circuits which greatly reduces system cost and improves manufacturing repeatability.

Recently, half-mode SIW (HMSIW) BPFs have been proposed which result in a size-reduction by almost half compared to their SIW counterparts [56]. An HMSIW is obtained by placing an open-circuit along the symmetry plane of a SIW thereby reducing its size by half while maintaining the low-loss performance obtained from SIW structures [57]. Additionally, HMSIW BPFs provide wider stopband rejection due to the absence of even-order spurious resonances [58]. However, there is a need for further miniaturization of HMSIW BPFs as specifications on the compactness of portable systems get more stringent. The usefulness of fractal structures in achieving compact HMSIW BPFs is investigated in this work.

Fractals are repetitive geometric modifications applied to a base structure and exhibit two important properties [59]; self-similarity, which implies that an object is exactly similar to part of itself, and space-filling, which means that any number of repetitions (or iterations) of the geometric modification occupies the same area. Fractal structures utilizing the space-filling property have been extensively studied

to reduce the physical size of antennas [60]. Recently, fractals have been employed to miniaturize coupled-line BPFs and simultaneously suppress the second harmonic [61].

In this section, cross-shaped fractal structures are utilized to reduce the physical size of a HMSIW resonator for the first time. Also, to make the overall filter more compact, HMSIW resonators are coupled together using a novel capacitive-coupling mechanism at the open-end of the HMSIW resonator. The 0th, 1st and 2nd fractal iterations of the HMSIW resonator are used to design, fabricate and measure two-pole Chebyshev BPFs with a center frequency of 1.15 GHz on Rogers RT/Duroid 6010LM substrate with a thickness of 0.635 mm. For each successive iteration, the filter size decreases and the quality factor increases so that very-low loss (< 1 dB) filter performance is obtained while having up to 37% reduction in overall filter area.

2. Design

a. Fractal HMSIW Resonators

Fig. 18(a) shows the structure of the HMSIW resonator which is obtained by placing a magnetic-wall (open circuit) along the symmetric center-plane of an SIW with length L and width $2W_0$. At resonant frequency, the width W_0 of the HMSIW resonator is approximately quarter-wavelength long, and resembles a low-impedance, short-circuited quasi-TEM transmission line resonator of length W_0 [58]. This structure is defined as the base structure (or 0th fractal iteration) on which fractal modifications will be made to miniaturize the resonator.

Fig. 18(b) shows a cross-shaped slot etched in the middle of the HMSIW resonator, and constitutes the 1st fractal iteration of the resonator. This geometric modification results in three major effects: (1) the induced surface currents on the

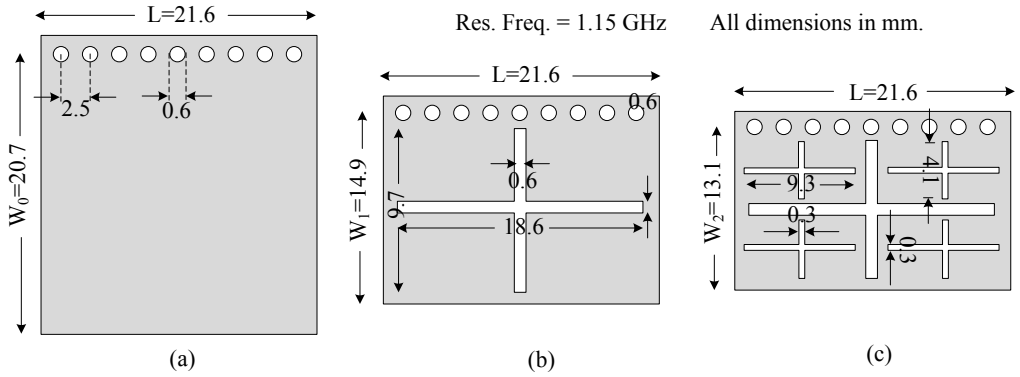

Fig. 18. (a) Conventional HMSIW resonator (0th-iteration), (b) the 1st fractal iteration, and (c) the 2nd fractal iteration.

top metallic layer of the HMSIW resonator traverse longer paths between the short and open ends of the resonator, resulting in longer electrical length for a given width W_1, (2) the capacitance between the top metal layer and ground plane is slightly decreased due to presence of slots, and slightly decreases the resonator electrical length, and (3) the reduced area of the top metal layer results in lower resistive losses, and consequently in a higher resonator unloaded quality-factor (Q_u). Overall, the width of the HMSIW resonator is smaller for a given resonance frequency and results in miniaturization while having lower loss.

The resonator can be made even more compact by introducing cross-shaped slots in each square portion of the 1st-iteration HMSIW resonator, as shown in Fig. 18(c). This geometric modification is the 2nd fractal iteration of the HMSIW resonator, which results in further size-reduction and Q-improvement in the resonator. Although infinite number of fractal iterations are possible on the base resonator structure, the number of fractal iterations is typically limited to two in practice. This is because the miniaturization obtained from higher iterations does not justify the increased fabrication complexity of the resonator [62].

Fig. 19 shows the simulated S_{21}-parameters of the HMSIW resonator and its

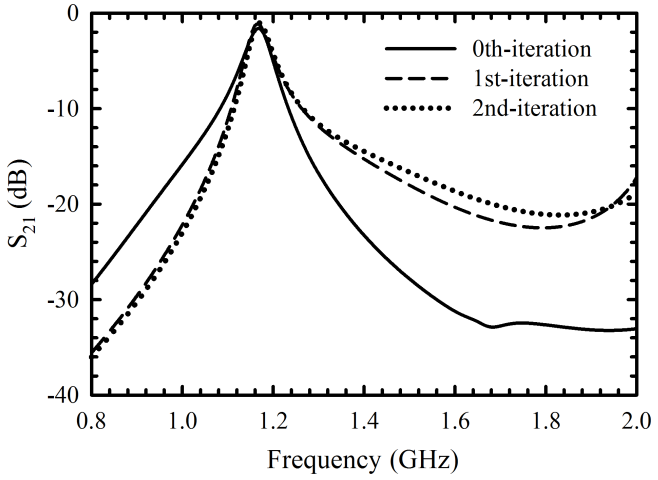

Fig. 19. Simulated S_{21}-parameters for various fractal iterations of the HMSIW resonator.

first two fractal iterations (Fig. 18). The widths W_1 and W_2 of the fractal HMSIW resonators are decreased to maintain a resonance frequency of 1.15 GHz. Changing L only affects the spurious responses of the resonator, and almost has no effect on the fundamental resonance frequency. Compared to the base HMSIW resonator, higher order fractal iterations have a steeper rejection skirt in the lower stopband while having poorer upper stopband performance. As the widths W_1 and W_2 are lowered, the cutoff frequency of the dominant-mode in the fractal HMSIW moves to higher values. As a consequence, at frequencies below the resonant frequency, the fractal HMSIWs operate deeper in evanescent regime resulting in a steeper rejection skirt. At frequencies above the resonant frequency, infinite number of modes are excited by the slot discontinuities in the fractal HMSIW and hence the isolation between the input and output is lower. However, for the same center frequency, the 1st- and 2nd-iteration fractal HMSIW resonators are 28% and 37% smaller in area compared to the 0th-iteration, respectively.

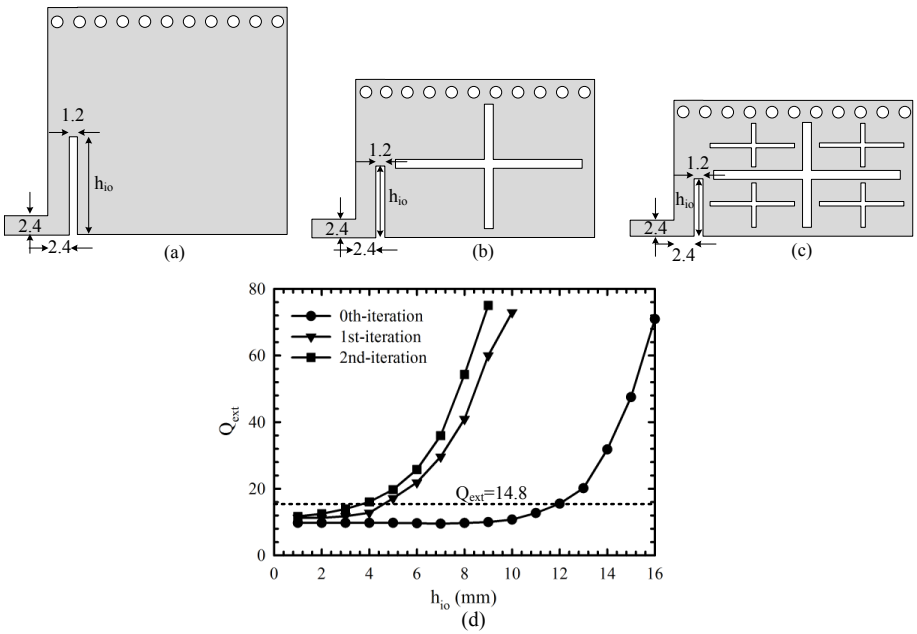

Fig. 20. Inductive input/output J-inverter for the (a) 0th-iteration, (b) 1st-iteration, and (c) 2nd-iteration, and (d) variation of Q_{ext} with h_{io} for various fractal iterations.

b. Coupling

The fractal iterations of the HMSIW resonator are used to design a two-pole Chebyshev filter by properly coupling the two resonators to the input/output ports, and to each other using J-inverter networks. In [58], J-inverters are implemented using inductive sections of evanescent HMSIW between resonators. Using this technique, the resonators can only be coupled in an end-to-end fashion which increases the filter length. To make the filter more compact, the inductive J-inverters in [58] are used to couple the resonators to the feed lines, while a novel capacitive coupling mechanism is introduced to couple the resonators together. Both these coupling mechanisms are discussed in detail as follows.

External Quality Factor (Q_{ext}). Figs. 20(a)-(c) show the fractal iterations of the HMSIW resonator coupled to a microstrip feed line of width 2.4 mm. The slot in

the HMSIW with width 1.2 mm and height h_{io} acts as an inductive J-inverter whose Q_{ext} value is controlled by properly adjusting the value of h_{io} [58]. For a filter with fractional bandwidth Δ, the required value of Q_{ext} is obtained as [15]

$$Q_{ext} = \frac{g_0 g_1}{\Delta} \tag{2.1}$$

where, $g_0, \ldots, g_3$ are the prototype element values of the equivalent 2nd-order Chebyshev lowpass filter. To relate Q_{ext} values to the physical dimensions of the inverter, Q_{ext} values are extracted from full-wave simulations of a singly-loaded resonator as described in [15]. Fig. 20(d) shows the variation of Q_{ext} with h_{io} for various fractal iterations of the HMSIW resonator. A two-pole, 4.5% Chebyshev filter with 0.043 dB ripple requires a Q_{ext} of 14.8, which is obtained by choosing $h_{io} = 12, 4.6$, and 3.6 mm for the 0th, 1st, and 2nd fractal iterations, respectively.

Inter-Resonator Coupling Coefficient (k_{12}). Figs. 21(a)-(c) show two fractal HMSIW resonators (0th, 1st, and 2nd iterations, respectively) capacitively coupled to each other using interdigital coupling fingers with an overlap length of L_c and slot width of 0.3 mm. Since the electric field is highly confined to the substrate in a HMSIW, a large number of closely-spaced inter-digital fingers are required to achieve any significant coupling. For a filter with fractional bandwidth Δ, the required value of k_{12} is given by [15]

$$k_{12} = \frac{\Delta}{\sqrt{g_1 g_2}} \tag{2.2}$$

To relate the value of L_c to the coupling coefficient k_{12}, two resonators are first weakly coupled at the input/output (high Q_{ext}-values), and then the k_{12} values are extracted from the resonant peaks in the S_{21}-response obtained from full-wave simulation [15]. Fig. 21(d) shows the variation of k_{12} with overlap length L_c for different fractal iterations of the HMSIW resonator. For a two-pole, 4.5% Chebyshev filter

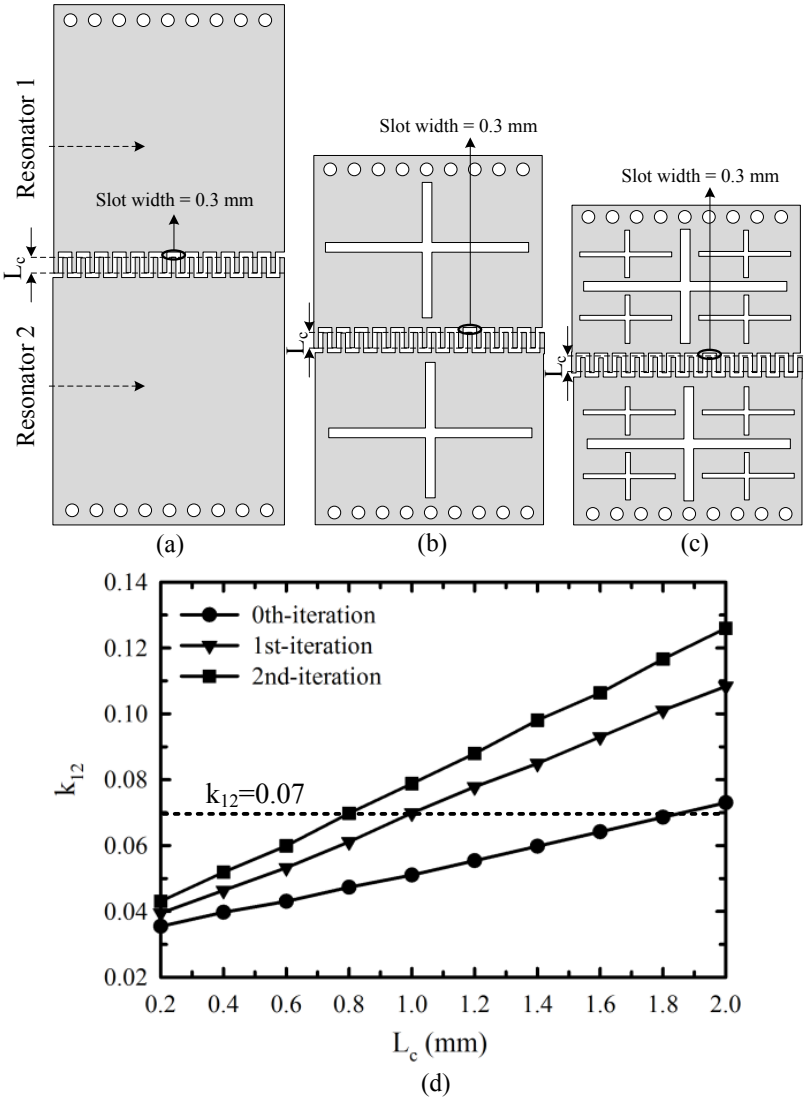

Fig. 21. Capacitive inter-resonator J-inverter for the (a) 0th-iteration, (b) 1st-iteration, and (c) 2nd-iteration, and (d) variation of k_{12} with L_c for various fractal iterations.

with 0.043 dB ripple, choosing $L_c = 1.8, 1.0$, and 0.8 mm gives the required coupling coefficient $k_{12} = 0.07$ for the 0th, 1st, and 2nd fractal iterations of the filter.

3. Fabrication and Measurement

The fractal iterations of the HMSIW filter are fabricated on Rogers RT/Duroid 6010LM substrate ($\epsilon_r = 10.2, \tan\delta = 0.0023$, $h = 0.635$ mm) using conventional PCB etching technology. Holes are drilled through the fabricated filter at appropriate locations and short pieces of wire with 0.6 mm diameter are soldered to the top and bottom metal layers to create the via-holes. The filter response is measured through the Subminiature-A (SMA) connectors soldered at the input/output of the filter using an Agilent N5230A network analyzer by first calibrating it using the Short-Open-Load-Thru (SOLT) technique.

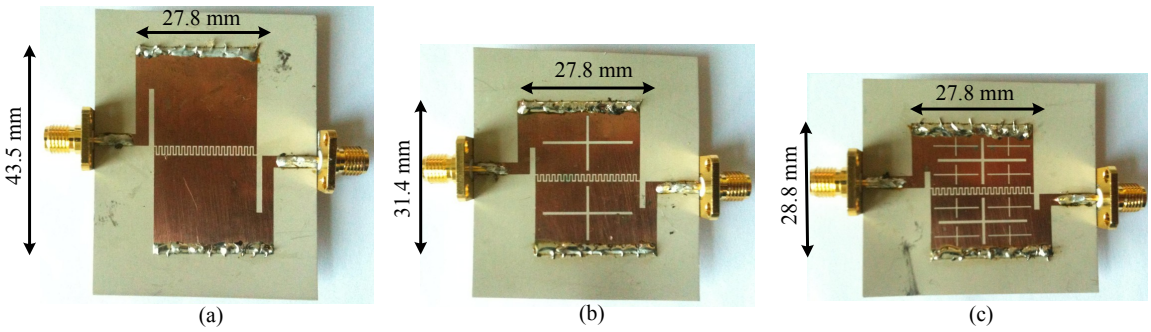

Fig. 22. Photographs of the fabricated filter prototypes.

Fig. 22 shows the fabricated filter prototypes and Fig. 23 shows the simulated and measured filter responses of the 0th, 1st, and 2nd fractal iterations of the HMSIW filter. Table I shows the comparison between simulation and measurement for various fractal iterations of the filter. In each case, the filter exhibits an insertion loss <1dB, and matching better than 11 dB at the filter center frequency. Compared to the 0th-iteration filter, the 1st and 2nd fractal iterations are smaller in area by 28% and

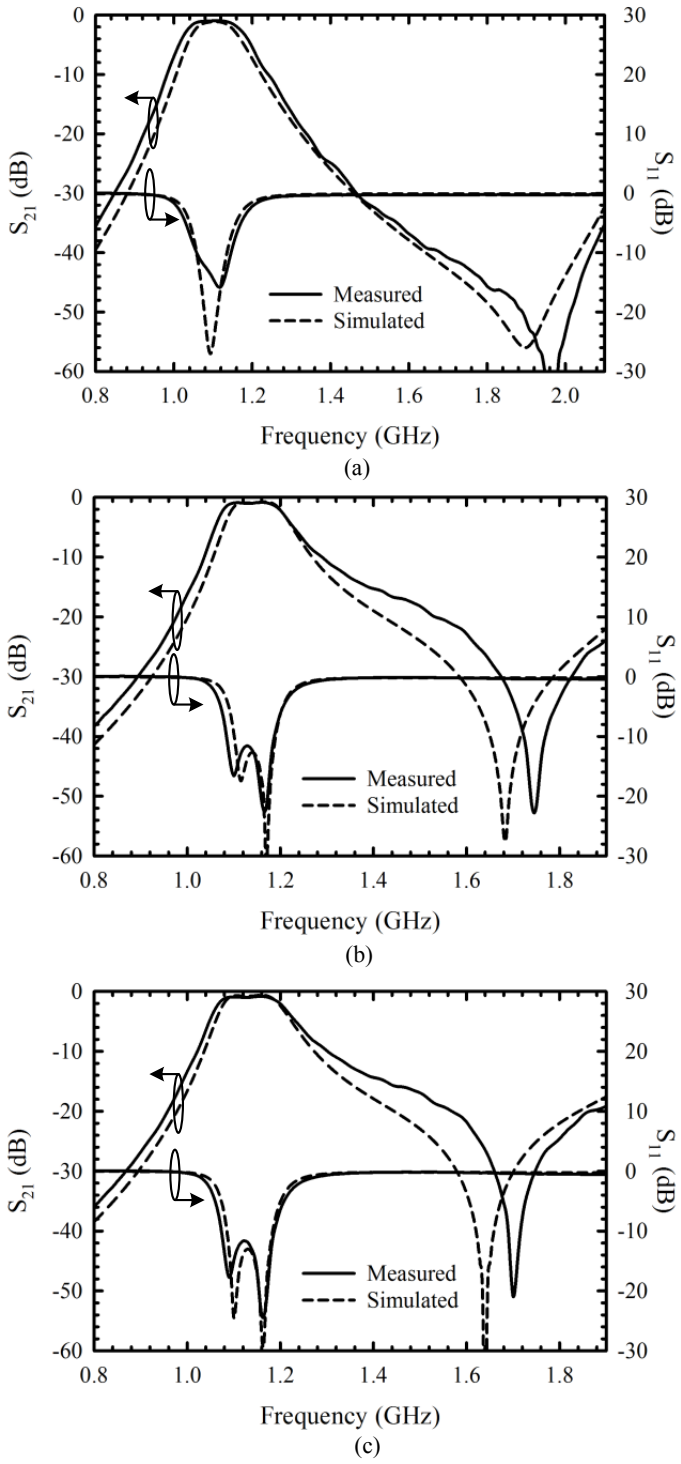

Fig. 23. Comparison between simulated and measured S-parameters for (a) 0-th iteration, (b) 1st-iteration, and (c) 2nd-iteration HMSIW bandpass filters.

Table I. Summary of Filter Performances (λ_g: Guided Wavelength at Filter Center Frequency)

-	**0th-iteration**		**1st-iteration**		**2nd-iteration**	
Param.	**Sim.**	**Meas.**	**Sim.**	**Meas.**	**Sim.**	**Meas.**
f_0 (GHz)	1.11	1.11	1.13	1.14	1.12	1.13
Δ (%)	4.2	4.4	4.2	4.3	4.2	4.3
I.L. (dB)	0.89	0.94	0.75	0.82	0.71	0.80
R.L. (dB)	27	15.5	12.8	11.5	13	11.8
Q_u	244	221	288	258	303	264
Area	$0.43\lambda_g \times 0.3\lambda_g$		$0.31\lambda_g \times 0.3\lambda_g$		$0.28\lambda_g \times 0.3\lambda_g$	
f_T (GHz)	1.90	1.97	1.69	1.75	1.64	1.70

37%, respectively. In addition, the resonator unloaded quality factor increases from 221 to 264 for higher fractal iterations of the filter due to lower losses in the top metal layer.

In all cases, a transmission zero at frequency f_T is formed in the upper passband of the fractal filters due to the resonance between the inductive inverters at the filter input/output, and the capacitive inverter between resonators. As such, the inductive and capacitive inverters provide opposite coupling signs which results in phase cancellation at the filter output, at the transmission zero frequency (f_T).

The presence of the transmission zero results in improved stopband performance

compared to filters designed using inverters of the same sign as reported in [58]. The measured responses show a slight increase in the filter bandwidth, and shift in the transmission zero frequency compared to simulation. This is most likely due to fabrication inaccuracies in the interdigital fingers of the capacitive J-inverter which leads to slightly higher k_{12} values.

4. Conclusion

In this study, the space-filling property of cross-shaped fractals is utilized to miniaturize the size of HMSIW bandpass filters by up to 37%. A novel capacitive coupling mechanism is introduced to make the filter more compact. Using inductive and capacitive inverters results in better upper stopband performance due to the presence of a transmission zero. Although HMSIW filters have similar unloaded quality factors compared to SIW filters, the inclusion of fractal structures improves the quality factor for each fractal iteration. Hence, fractal HMSIW filters have significant advantages over conventional SIW filters both in terms of size and low-loss performance, and are very suitable for applications which require compact, high performance bandpass filters.

D. A Novel Compact Dual-Band Half-Mode Substrate Integrated Waveguide Bandpass Filter

1. Introduction

Recently, multi-band communication systems have been developed at microwave and millimeter wave frequencies that operate over multiple communication standards simultaneously. Dual-band bandpass filters (BPFs) are essential components for such multi-band systems since they allow the use of a single component instead of two independent switched filters. Low-loss dual-band BPFs have been implemented using conventional metallic waveguides [14] but are very bulky and expensive for applications where size, cost and system integration are critical.

Substrate integrated waveguide (SIW) BPFs have become a very popular alternative to conventional waveguide BPFs due to their low profile and high performance [21]. In addition, SIW filters can be easily integrated with other planar circuits which greatly reduces system cost and improves manufacturing repeatability. Recently, SIW technology was used to implement multi-band BPFs with Chebyshev and elliptic responses for the first time [22].

In the past few years, half-mode substrate integrated waveguide (HMSIW) technology has been proposed as an alternative to SIW for filter applications [58]. An HMSIW is obtained by placing a magnetic wall (open circuit) along the symmetry plane of a SIW thereby reducing its size by nearly half. Although the HMSIW is significantly smaller, it still maintains low-loss properties comparable to a conventional SIW provided it is operated at frequencies higher than the dominant-mode cutoff frequency [63]. Under this condition, the radiation losses from the open end are not significant. While the resonance frequency of a conventional SIW resonator depends on the length and width of the SIW cavity, the resonance frequency of a

HMSIW resonator depends only on the width of the resonator [23]. Hence, the length of the resonator can be made arbitrarily small without affecting the filter passband as long as HMSIW operation is not affected. This additional feature of the HMSIW resonator enables the realization of highly compact filters that are several times smaller in area compared to their SIW counterparts, while maintaining low-loss performance. Also, HMSIW BPFs provide exceptional stopband performance due to absence of even-order spurious resonances [58] which is otherwise difficult to achieve using conventional SIW structures.

In this section, a novel compact dual-band HMSIW BPF that is six times smaller than an SIW filter with similar specifications is proposed for the first time. A dual-band HMSIW resonator is created by using a capacitive J-inverter to couple bandpass and bandstop HMSIW resonators together at their open ends. A three-pole, Chebyshev dual-band BPF having passbands centered around 1.05 GHz and 1.3 GHz is designed, fabricated and tested. The filter has low insertion loss (< 2 dB) and exhibits a stopband suppression better than 40 dB around twice the filter passband frequencies due to absence of even-order resonances.

2. Filter Synthesis

a. Dual-Band Resonator

Fig. 24 shows an inverter-coupled dual-band resonator consisting of a bandstop resonator coupled to a bandpass resonator through an admittance inverter in order to achieve a dual-band response [22]. The equivalent shunt admittance of the dual-band resonator is given by

$$B(\omega) = jb_1\left(\frac{\omega}{\omega_{01}} - \frac{\omega_{01}}{\omega}\right) + \frac{J_2^2}{jb_2\left(\frac{\omega}{\omega_{02}} - \frac{\omega_{02}}{\omega}\right)} \tag{2.3}$$

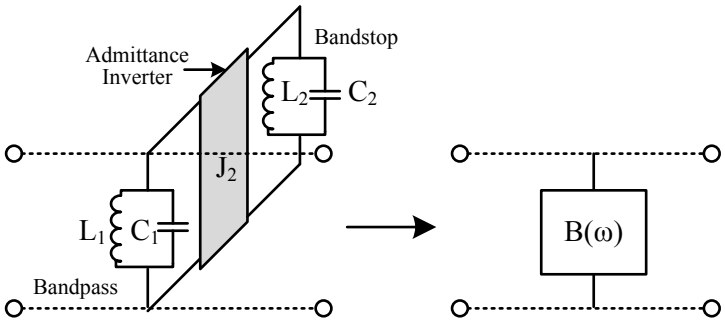

Fig. 24. A dual-band inverter coupled resonator.

where, $b_i = \omega_{0i}C_i$, $\omega_{0i} = 1/\sqrt{L_iC_i}$ for $i = 1, 2$. The two reflection zeros of the resonator found by solving the polynomial equation obtained by setting $B(\omega) = 0$, are used to form the filter passband. A transmission zero is obtained at $\omega_z = \omega_{02}$, which is in between the two reflection zeros, when $B(\omega)$ approaches infinity.

b. Methodology

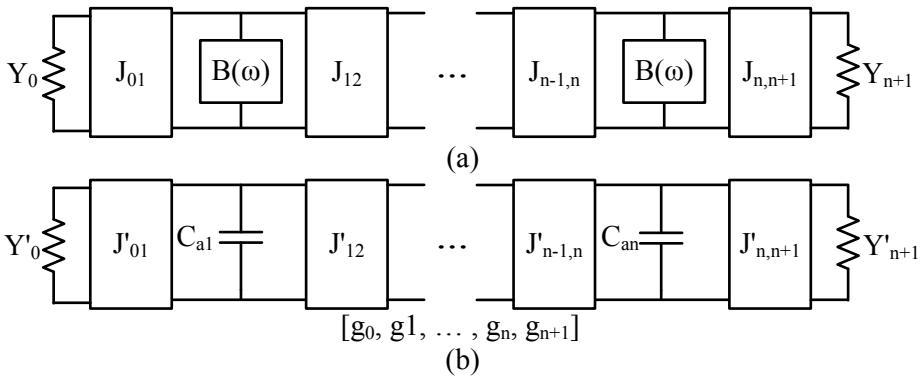

Fig. 25. (a) Generalized nth-order bandpass filter with ideal admittance inverters, and (b) equivalent lowpass prototype network.

Figs. 25(a) and (b) represent a Chebyshev BPF employing inverter-coupled dual-band resonators and its equivalent lowpass prototype network, respectively. The low-pass prototype element values for an nth-order Chebyshev response are represented

by $g_0, \ldots, g_{n+1}$. The J-inverter values of the lowpass prototype filter $(J'_{01}, \ldots, J'_{n,n+1})$ can be calculated using unit capacitances $C_{a1}, \ldots, C_{an}$ and prototype element values $g_0, \ldots, g_{n+1}$ by employing formulas in [15]. For the lowpass prototype circuit and the bandpass filter to be equivalent, the resonator admittance and inverters should be equalized appropriately. Admittance equalization is done by equating the resonator admittance $B(\omega)$ to the admittance of a unit capacitor at a lowpass frequency ω' as [22]

$$B(\omega) = j\omega' \tag{2.4}$$

The inverter parameters of the bandpass filter are assumed to be frequency independent and are given in terms of lowpass prototype element values as [15]

$$\begin{aligned} J_{01} &= \sqrt{\frac{Y_0}{g_0 g_1}} \\ J_{n,n+1} &= \sqrt{\frac{Y_{n+1}}{g_n g_{n+1}}} \\ J_{i,i+1} &= \sqrt{\frac{1}{g_i g_{i+1}}} \end{aligned} \tag{2.5}$$

If the lower and upper passband edges of the two filter passbands are represented by $(\omega_{Li}, \omega_{Hi})$ for $i = 1, 2$, then the following conditions must be satisfied during the lowpass-bandpass transformation: (1) $\omega' = 1$ should correspond to upper passband edge angular frequencies $\omega = \omega_{H1}$ and $\omega = \omega_{H2}$, and (2) $\omega' = -1$ should correspond to lower passband edge angular frequencies $\omega = \omega_{L1}$ and $\omega = \omega_{L2}$. The procedure described in [22] for synthesis of the dual-band filter based on these conditions is summarized below.

1. Choose the desired passband edge frequencies $(\omega_{Li}, \omega_{Hi})$, $i = 1, 2$, and the transmission zero frequency $\omega_z = \omega_{02}$.

2. Calculate the J-inverter values using (2.5) for a given return loss specification.

3. Put $\omega' = \pm 1$ and $\omega = (\omega_{Li}, \omega_{Hi})$, $i = 1, 2$ in (2.4) so that the lowpass-bandpass transformation conditions are satisfied. This results in four equations with four unknowns b_1, b_2, ω_{01} and J_2, which can be solved numerically.

4. Calculate coupling values (k) corresponding to admittance inverter values by employing the following formulas.

$$k_2 = \frac{J_2}{\sqrt{b_1 b_2}}; \qquad k_{i,i+1} = \frac{J_{i,i+1}}{b_1}, i = 1, \ldots, n-1 \tag{2.6}$$

5. Calculate the external coupling coefficients corresponding to input/output J-inverters using

$$Q_{e1} = b_1 g_0 g_1; \qquad Q_{en} = b_1 g_n g_{n+1} \tag{2.7}$$

This synthesis method is suitable for dual-band BPFs whose passband center frequencies are relatively close to each other with a sharp rejection notch in between. This procedure is used to synthesize a three-pole Chebyshev dual-band filter with passbands between 1.030-1.075 GHz and 1.26-1.34 GHz and a transmission zero at 1.14 GHz, for a return loss of 20 dB. The design values obtained for the filter are $f_{01} = 1.20$ GHz, $k_{12} = k_{23} = 0.1103$, $k_2 = 0.198$ and $Q_{e1} = Q_{e3} = 7.96$. Fig. 26 shows the synthesized response of the dual-band filter.

3. Design and Implementation

Fig. 27 shows the geometrical structure of the proposed dual-band HMSIW filter. Linear arrays of closely spaced via-holes emulate an electric wall at one end of the HMSIW resonator. A HMSIW bandstop resonator is coupled to a HMSIW bandpass resonator using interdigital fingers at the open ends of the resonators, which act as

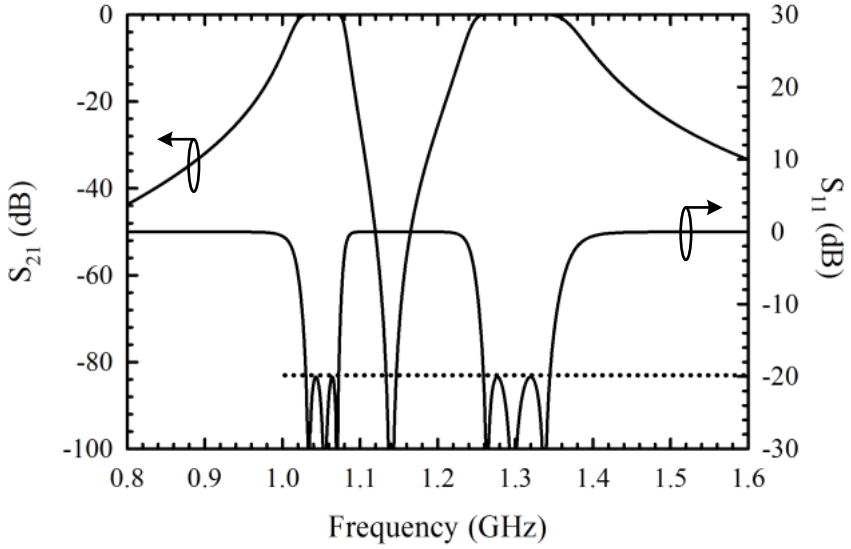

Fig. 26. Synthesized response of the dual-band Chebyshev filter.

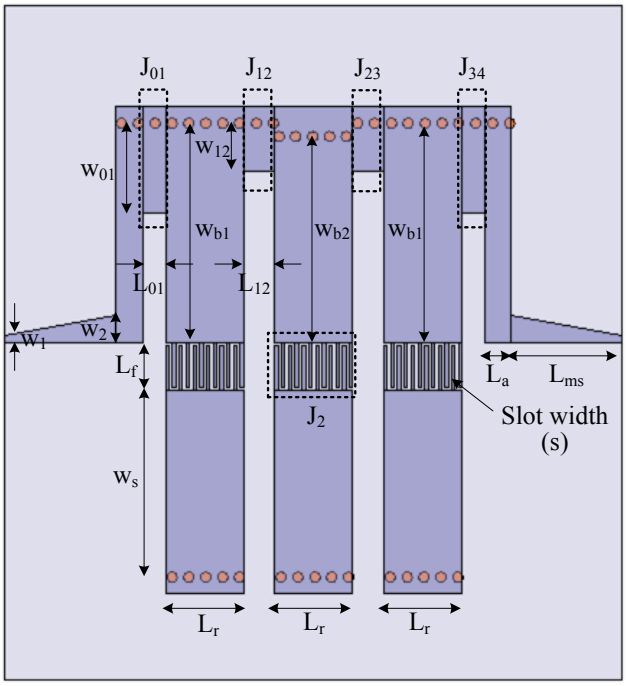

Fig. 27. Geometrical structure of the proposed dual-band Chebyshev HMSIW BPF.

capacitive J-inverters (J_2). The dual-band resonators are coupled to each other, and to the filter input/output using short sections of evanescent mode HMSIW which act as inductive J-inverters ($J_{01}, \ldots, J_{34}$) with predominantly magnetic coupling. A tapered microstrip line is used to create a microstrip-HMSIW transition with minimum reflections.

The filter layout design procedure is summarized as follows. First, the initial sizes of the bandpass and bandstop resonators are determined, so that they have center frequencies of f_{01} and f_{02}, respectively. To do so, the HMSIW resonator is assumed to be a quasi-TEM line with width L_r and length $w_{b1,2}$ (or w_s). The length $w_{b1,2}$ (or w_s) is adjusted so that the quasi-TEM line is a quarter-wavelength long at the desired resonance frequency. The quasi-TEM approximation of a HMSIW is derived by considering the HMSIW to be half of a wide microstrip line excited in its first higher order mode [23]. This approximation is valid as long as L_r is chosen so that the quasi-TEM line has a low characteristic impedance ($< 10\ \Omega$).

To determine the internal coupling coefficients, a full-wave electromagnetic simulator [Ansoft High Frequency Structure Simulator (HFSS)] is used to simulate (1) a pair of coupled bandpass HMSIW resonators, and (2) a pair of coupled bandpass and bandstop HMSIW resonators. In both cases, the resonators are weakly coupled at the input/output. The simulated S_{21}-parameters show two resonant peaks (f_1, f_2) and (f_1', f_2') corresponding to split-mode frequencies for cases 1 and 2, respectively. The coupling coefficient between bandpass resonators (for case 1) is extracted using [15]

$$k_{12} = \frac{f_1^2 - f_2^2}{f_1^2 + f_2^2} = k_{23} \tag{2.8}$$

Increasing w_{12} and decreasing L_{12} results in higher values of coupling coefficient. The value of L_{12} is chosen so that the capacitive J-inverters (J_2) are sufficiently far

away from each other and do not contribute to stray coupling between resonators. The value of w_{12} is then adjusted so that the required coupling coefficient is obtained.

Since the resonant frequencies of the bandpass and bandstop frequencies are different, the coupling coefficient k_2 (for case 2) is extracted using [15]

$$k_2 = \frac{1}{2}\left(\frac{f_{01}}{f_{02}} + \frac{f_{02}}{f_{01}}\right)\sqrt{\left(\frac{f_1'^2 - f_2'^2}{f_1'^2 + f_2'^2}\right)^2 - \left(\frac{f_{01}^2 - f_{02}^2}{f_{01}^2 + f_{02}^2}\right)^2} \tag{2.9}$$

where, f_{01} and f_{02} are the resonant frequencies of the bandpass and bandstop resonators, respectively. For a fixed slot width s, a higher length of the interdigital fingers (L_f) results in a larger coupling coefficient. The slot width s is minimized to obtain the required coupling coefficient in a compact area, and is limited by manufacturing tolerances. The finger length L_f is then adjusted to get the required coupling coefficient k_2.

The external quality factor (Q_e) is determined by simulating a doubly-loaded bandpass HMSIW resonator which is coupled to the tapered microstrip line using inductive J-inverters. The length of the initial HMSIW (L_a) is made equal to the broader width of the tapered microstrip line (w_2) to minimize reflection losses in the transition. The value of Q_e is calculated using [15]

$$Q_e = \frac{2f_0}{\Delta f_{-3dB}} \tag{2.10}$$

where f_0 is the frequency at which S_{21} reaches its maximum value and Δf_{-3dB} is the bandwidth for which S_{21} is 3 dB lower than its maximum value. The inverter dimensions w_{01} and L_{01} are adjusted till the required Q_e value is obtained.

Finally, the entire filter structure is fine tuned using the full-wave electromagnetic simulator. The loading effect of inductive and capacitive inverters on the bandpass and bandstop resonators results in a shift of resonant frequencies that must be con-

Table II. Final Dimensions of the Dual-Band HMSIW Filter

Symbol	**Value (mm)**	**Symbol**	**Value (mm)**
w_1	0.6	w_s	16.7
w_2	2.4	L_r	6.9
w_{01}	7.9	w_{b1}	18.6
L_{01}	2.0	w_{b2}	17.45
w_{12}	4.2	L_f	3.9
L_{12}	2.8	s	0.3
L_a	2.4	L_{ms}	9.9

sidered during the optimization process. As a result, the dimensions w_{b1}, w_{b2} and w_s are different from the initial designed values. Table II shows the final dimensions of the dual-band HMSIW filter. The full-wave simulation response is shown in Fig. 28(b).

4. Fabrication and Measurements

The dual-band HMSIW Chebyshev filter designed is fabricated on Rogers RT/Duroid 6010LM (ϵ_r=10.2, $\tan\delta$=0.0023 @ 10 GHz, h=0.635 mm) using a conventional PCB etching process. The linear array of via-holes with center-to-center pitch of 1.5 mm is created by drilling holes of diameter 0.9 mm through the substrate, and soldering short pieces of wire to the top and bottom of the substrate metallization. Fig. 28(a) shows the photograph of the fabricated filter prototype.

The filter response is measured using an Agilent N5230A vector network analyzer and an Anritsu 3680-20 universal test fixture after short-open-load-thru (SOLT) calibration. Fig. 28(b) shows the measured and simulated S-parameters. The measured insertion losses are 1.7 dB and 1.8 dB at the mid-band frequency of the first and

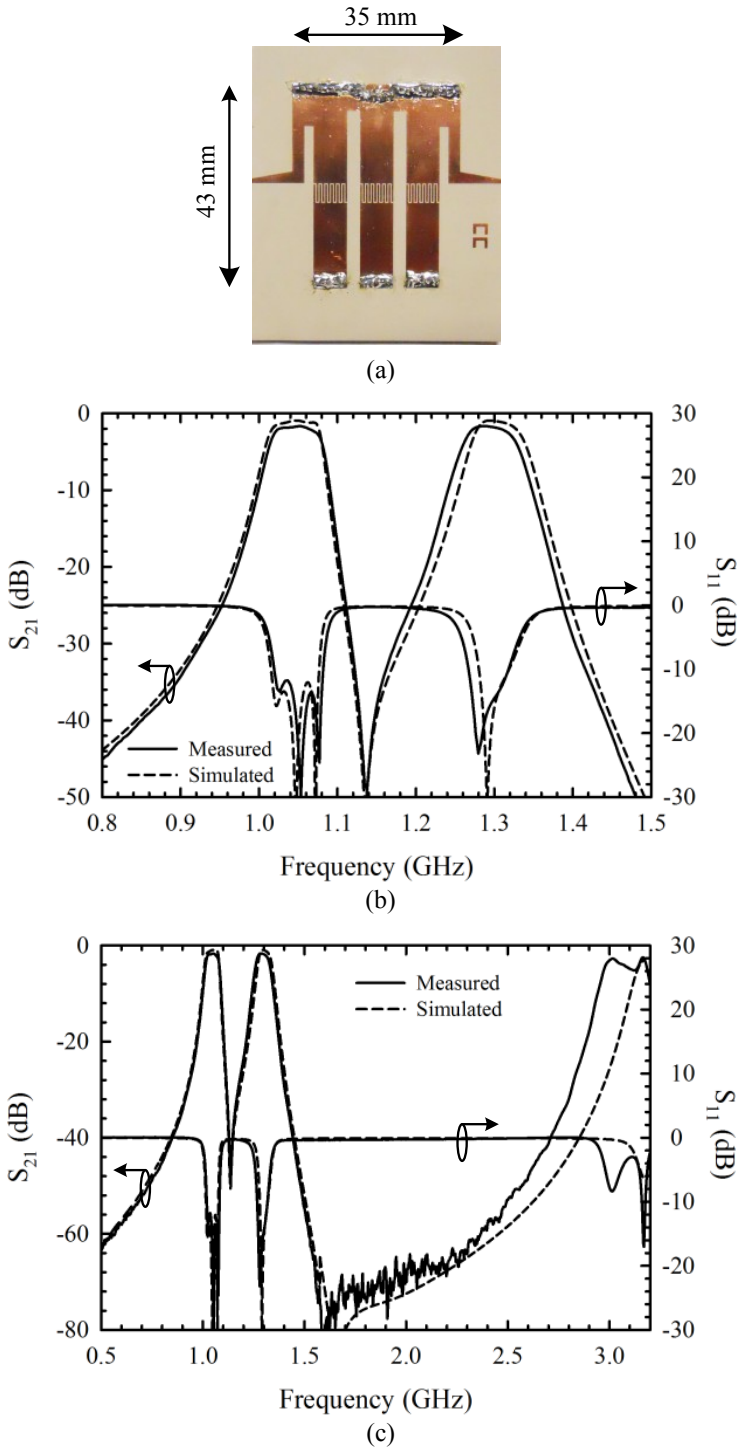

Fig. 28. (a) Photograph of the fabricated filter prototype, (b) measured and simulated filter response, and (c) filter response up to 3.2 GHz.

second passbands, respectively. The filter exhibits a return loss better than 12 dB over both passbands. The transmission zero at 1.138 GHz exhibits a rejection of 50 dB, and provides excellent frequency separation between the filter passbands.

Fig. 28(c) shows the simulated and measured response of the filter up to 3.2 GHz. Due to the absence of even-order resonances in an HMSIW, the first spurious filter passband occurs at 3.1 GHz while providing a rejection level >40 dB between 1.45-2.71 GHz. The transmission zero created at 1.681 GHz due to resonance between inductive and capacitive inverters results in a rejection level of 70 dB in close vicinity of the higher filter passband. In comparison, the size of a single square SIW bandpass cavity resonator at 1.2 GHz is 45 mm $\times$ 45 mm which is larger than the proposed filter with six HMSIW resonators. Hence, the proposed approach results in a size reduction by at least a factor of six compared to the topology reported in [22] for similar specifications.

5. Conclusion

In this study, a dual-band BPF using HMSIW technology has been designed and implemented for the first time. The proposed filter topology has low insertion loss, good frequency separation between passbands, exceptional stopband performance in close vicinity of the upper filter passband, and wide spurious-free range, while being around six times smaller than its SIW counterpart. This work shows that HMSIW technology has immense potential for the development of advanced filtering structures.

CHAPTER III

SUBSTRATE INTEGRATED WAVEGUIDE RF MEMS TUNABLE FILTERS*

A. Introduction

Low-loss tunable filters are essential components in multi-band communication systems and wideband tracking receivers. Recently, tunable filters at frequencies <10 GHz employing RF microelectromechanical systems (RF MEMS) switches have demonstrated high quality factor (Q), wide tuning range and high linearity, while having zero power consumption [34]. Since RF MEMS switches are inherently very low loss, the Q of planar tunable filters, and consequently insertion loss, is mostly limited by the resonator Q.

In recent years, a wide variety of planar techniques resulting in filter Q values between 50—170 have been reported [35]-[37]. These filters require the RF MEMS switches to be constructed monolithically along with the filter structure for good performance. To drastically improve the filter Q, an RF MEMS tunable filter from 4—6 GHz using evanescent-mode waveguide cavities was developed in [38] and resulted in exceptional Q values from 300-500 over the tuning range. Here, the Q-value is only limited by the losses in the RF MEMS switches since waveguide cavity resonators have very high Q (>1000). This filter requires a fabricated monolithic MEMS chip module inserted into the waveguide structure to implement the tunable filter. As a result, the fabrication of filters reported in [35]-[38] is complicated and requires expensive microfabrication technology.

Recently, there has also been a drive towards using commercially available surface

---

mount RF MEMS switches for the development of tunable filters using conventional printed circuit board (PCB) etching technology. A 4-bit lumped element tunable filter from 25—75 MHz was demonstrated in [64], using RF MEMS switches developed by Radant MEMS[1]. An accurate model of the RF MEMS switch including package parasitics was developed for successful filter design. The reported Q value was between 50—70 due to limited Q of the surface mount inductors. Using the same packaged switch, a planar switched filter with Q around 75 was developed in the 1.5-2.3 GHz frequency range [65]. However, Q-factors >100 are difficult to achieve using packaged RF MEMS switches and planar filter topologies due to limited Q of planar and surface-mount components at microwave frequencies.

As an alternative to planar filters, substrate-integrated-waveguide (SIW) filters on planar dielectric substrates have been proposed due to their high quality factor [19], [21]. Such filters provide a low-profile, low-cost alternative to bulky metallic waveguide filters and are fabricated using conventional PCB technology. In [66], a method has been proposed to tune the resonant frequency of a SIW cavity resonator by 5% around 10 GHz, based on vertical tuning posts within the cavity and metal strips that emulate the presence of a closed switch. This technique is extended to a tunable filter with six tuning states from 1.5—2.0 GHz using p-i-n diodes with Q-factor between 100—120 [67]. However, utilizing p-i-n diodes for filter tuning results in intermodulation distortion and power consumption. Recently, RF MEMS switch technology has been employed to develop a tunable SIW filter on low-temperature co-fired ceramic (LTCC) substrate with limited tuning range ($\approx$ 7%) [68].

In Section B of this chapter, an SIW RF MEMS tunable filter with 28% tuning range from 1.2—1.6 GHz and quality factor between 93—132 is presented for the

[1]Radant MEMS Inc., Stow, MA. [Online]. Available: www.radantmems.com

first time. The frequency band is covered by 14 tuning responses (states) with very fine frequency resolution so as to behave as a continuous-type filter. Vertical tuning posts are used for frequency tuning by employing packaged RF MEMS switches from OMRON Corp.[2], because they can be directly soldered on to the filter circuit without utilizing wirebonds. As a result, the package parasitics are reduced considerably enabling the realization of a high performance tunable filter. The tunable filter is constructed using a two-layer structure to isolate the RF MEMS switches and biasing lines from the SIW filter. Using lowpass filters (LPFs) at the filter input/output, the upper stopband performance of the tunable bandpass filter is greatly improved.

Although the tunable filter presented in Section B of this chapter represents the first high performance SIW tunable filter implemented using RF MEMS technology, it requires multi-layer fabrication and occupies a relatively large area. The high filter size is due to asymmetrically-fed dual-mode cavities used to improve the upper stopband rejection of the filter, which is otherwise poor due to the presence of spurious resonances. Also, design of the tuning mechanism by cavity field perturbation is entirely based on full-wave simulations which is very time consuming. As discussed in Chapter II, half-mode substrate-integrated-waveguides (HMSIWs) are an alternative to conventional SIW due to their small size [57], [76], low-loss [63] and improved stopband performance due to the absence of even-order resonant modes [58].

In Section C of this chapter, an HMSIW RF MEMS tunable filter with 13 distinct frequencies between 1.2–1.6 GHz and Q values between 75–140, is presented for the first time. The proposed filter is 2.5 times smaller in area than its conventional SIW counterpart in Section B, and maintains relatively constant absolute bandwidth as it is tuned. Equivalent models for the HMSIW resonator and tuning network are de-

[2]OMRON Corporation, Kyoto, Japan. [Online]. Available: www.omron.com

veloped to systematically design the tunable HMSIW filter. A detailed methodology for inverter design is presented so that constant absolute bandwidth is maintained as the filter is tuned. Due to inherently good stopband performance of HMSIW filters, a spurious suppression greater than 20 dB is achieved over the 1.7–2.2 GHz frequency range without employing any additional techniques.

B. A 1.2—1.6-GHz Substrate Integrated Waveguide RF MEMS Tunable Filter

1. Tunable Resonator Structure

a. SIW Cavity

Figs. 29(a) and (b) show the top and cross-sectional views of the two-layer SIW cavity resonator that is tuned using packaged RF MEMS switches, respectively. The bottom substrate of height h_1 is used to design the SIW cavity with width W and length L, where the top and bottom cavity walls are formed by the middle and bottom metal layers, respectively. The resonator side walls are formed by periodic vias of diameter d with a center-to-center pitch, b, between adjacent via holes. A thick substrate is utilized for the SIW cavity to minimize the conductor losses in the waveguide [69]. To access the cavity and perform S-parameter measurement using Subminiature-A (SMA) connectors, microstrip feed lines need to be on the top metal layer. They are connected to the tapered microstrip lines on the middle metal layer using via holes. The additional insertion loss of the via holes through the thin top substrate layer with height h_2 is negligible (< 0.01 dB) in the 1 to 2 GHz frequency range. The tapered microstrip lines excite the cavity by gradually converting the quasi-TEM waves in the microstrip lines into TE_{10}-mode waves inside the SIW sections of length L_i. The amount of energy coupled into the cavity depends on the width of the inductive irises, W_{io}, at the input/output of the cavity. In addition, using a top substrate layer of

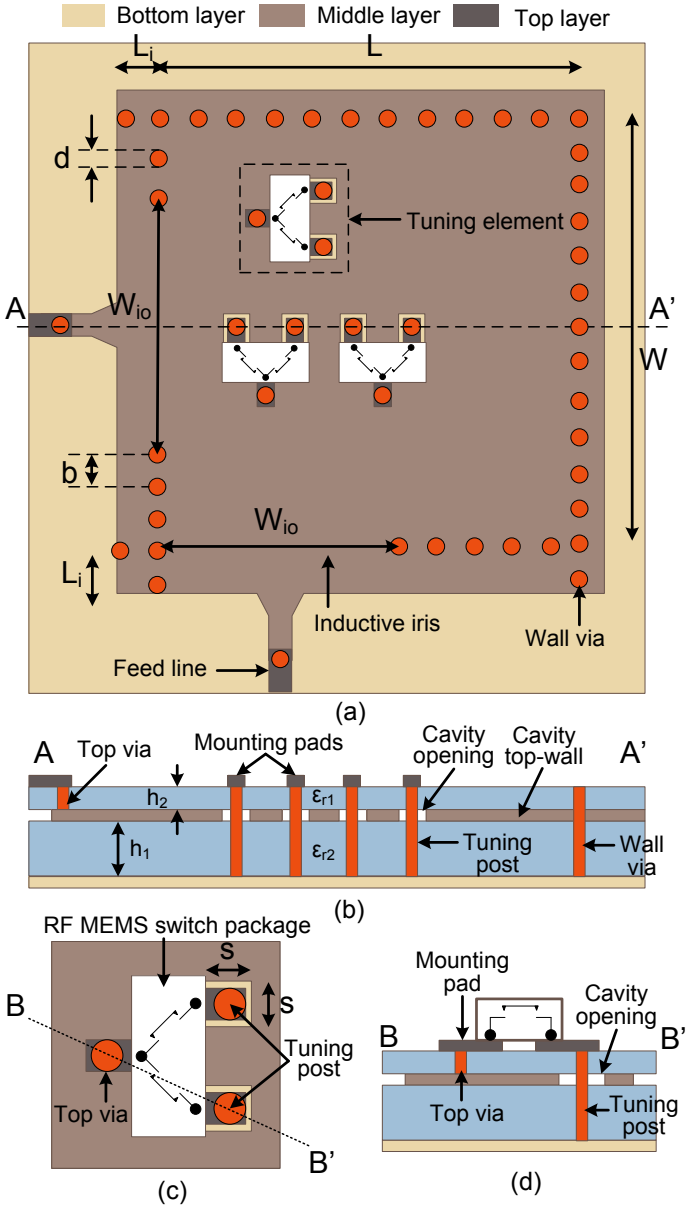

Fig. 29. (a) Top view of the tunable SIW cavity using packaged RF MEMS switches, (b) $A-A'$ cross section of the tuning cavity, (c) top view of the tuning element employing an RF MEMS switch package, two tuning posts and a top via, and (d) $B-B'$ cross section of the tuning element.

height h_2 allows placement of tuning elements and associated bias-line routing (not shown) on the top metal layer without affecting the SIW cavity performance.

To design the filter passband, the dominant TE_{101}-mode resonance at a frequency f_{101} is employed, and is given by

$$f_{101} = \frac{c}{2\sqrt{\mu_r \epsilon_r}} \sqrt{\left(\frac{1}{W_{eff}}\right)^2 + \left(\frac{1}{L_{eff}}\right)^2}; \tag{3.1}$$
$$L_{eff} = L - \frac{d^2}{0.95.b}, \quad W_{eff} = W - \frac{d^2}{0.95.b}$$

where c is the velocity of light in vacuum, and μ_r and ϵ_r are the relative permeability and permittivity of the substrate, respectively [21]. A higher order TE_{201} resonance mode is also excited in a waveguide cavity and leads to poor upper stopband performance when used in filter design. However, by orienting the cavity excitations along adjacent sidewalls, the SIW cavity acts as a dual-mode resonator that provides a transmission zero in the upper passband due to cancellation of signals passing through the TE_{101} and TE_{201} modes, thereby improving stopband rejection performance [21]. The position of the transmission zero depends on the relative coupling of the incident wave to the TE_{101} and TE_{201} modes, and can be controlled by adjusting the relative distance between input and output excitations [70].

b. Tuning Mechanism

To make the resonator tunable, tuning elements consisting of via posts and RF MEMS switches are placed at various locations within the cavity as shown in Fig. 29(a). The top and cross-sectional views of a tuning element are shown in Figs. 29(c) and (d), respectively. Metallic vias between the top and bottom metal layers are used to change the cavity resonance frequency, and are hence called tuning posts. To avoid shorting a tuning post to the cavity top wall (middle metal layer), square openings

with edge 's' in the cavity top wall are placed around each tuning post. Since these openings are small compared to the dimensions of the cavity, the cavity fields remain relatively unaffected.

To change the dominant cavity resonance frequency, tuning posts in the cavity are connected to the cavity top wall (middle metal layer) through top vias located between the top and middle metal layers, by closing RF MEMS switches appropriately. By effectively shorting the tuning posts to the cavity top wall, the resulting cavity field perturbation causes a shift in resonance frequency. However, when all RF MEMS switches are open, each tuning post is isolated from the cavity top wall. Hence, the dominant TE_{101} fields inside the cavity remain relatively unperturbed and the resulting resonance frequency is very close to f_{101}. The tuning range is maximized by reducing the parasitic elements between the tuning post and cavity top wall. This implies that the upper substrate layer must be thin so that the inductance of the top via is small. The parasitics associated with the packaged RF MEMS switches and mounting pads also impose tuning limitations. For maximum tuning, every tuning post and top via must be located as close as possible to the mounting pad of an RF MEMS switch package. Otherwise, the increased inductance from the metal line connecting the tuning post (or top via) to the switch mounting pad decreases the amount of frequency shift, and limits the filter tuning range. Hence, the locations of tuning posts and top via are fixed with respect to a single RF MEMS switch package, and depend on the placement of mounting pads in the layout footprint of the switch package. This practical consideration imposes a design constraint on the allowable locations for a pair of tuning posts. As a result, extra tuning posts may be required to achieve symmetrical tuning states as discussed in Section B.2.c of this chapter. The details of the RF MEMS switch package are provided in the next section.

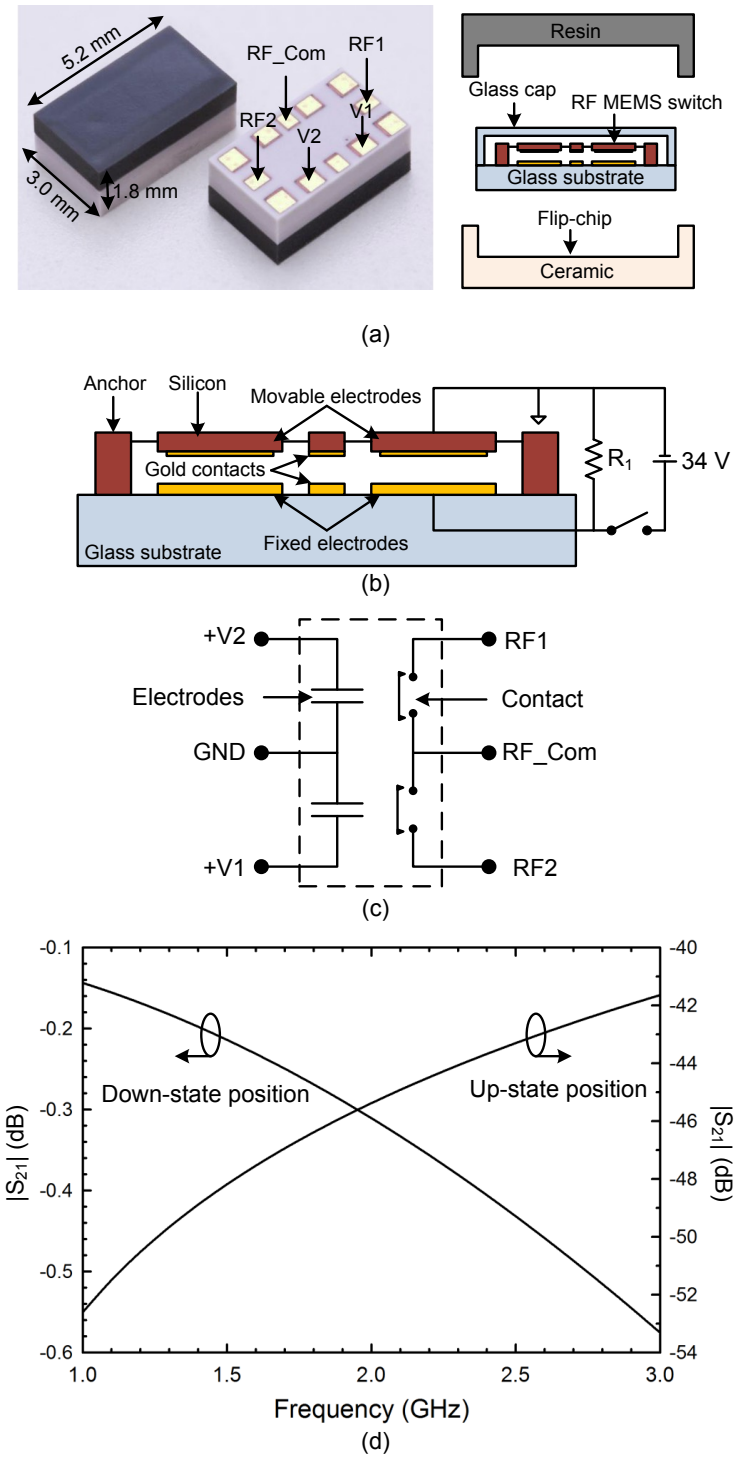

Fig. 30. (a) Photograph and structure of the packaged SPDT RF MEMS switch, (b) side view of the SPST switch, (c) schematic of the SPDT switch, and (d) measured S-parameters of the MEMS switch.

c. Packaged RF MEMS Switch

The RF MEMS switch package (2SMES-01) from OMRON Corp. is shown in Fig. 30(a) and consists of a single-pole dual-throw (SPDT) RF MEMS switch in which each switch can be controlled individually. The SPDT switch has been tested to >100 million cycles for >32 units by OMRON Corp. [41]. The cross-sectional view of one switch is shown in Fig. 30(b). Each RF MEMS switch is a fixed-fixed bridge structure constructed on glass substrate using movable silicon electrodes and gold metal-contacts [71]. When a DC voltage is applied, the switch connects the Cr/Au CPW signal lines present at the RF ports of the RF MEMS switch package and disconnects them when the biasing voltage is removed. Two such RF MEMS switches are flip-chip mounted on a ceramic package and nitrogen-sealed in a hollow glass cap using frit-glass sealing. A resin is then applied on top to protect the packaged RF MEMS switches. Metalized vias through the glass substrate provide access to the RF MEMS switch without wirebonding processes. As a result, the switch can be directly soldered onto the circuit enabling easy assembly and high RF performance.

The schematic of the switch is shown in Fig. 30(c). By applying an actuation voltage of 34V at V1 (or V2), an RF MEMS switch is used to connect the CPW signal lines present between the RF_Com and RF1 (or RF2) ports, respectively. The resistance R_1 is used to discharge any accumulated charge in the RF MEMS switch [Fig. 30(b)]. The switch has a rated maximum switching time of 100 μs[3]. Fig. 30(d) shows the measured S-parameters of each RF MEMS switch in the up- and down-state positions provided by the manufacturer. The S-parameters of the switch were measured using RF probes without employing a mounting board. In the down-state position, each RF MEMS switch has a maximum contact resistance of 1.5 Ω. The

[3]Omron 2SMES-01 RF MEMS relay switch datasheet. Available:www.omron.com.

Table III. Cavity Parameters

W	43.2 mm	W_{io}	23.4 mm
L	43.2 mm	L_i	3.3 mm
b	2.4 mm	d	0.6 mm
h_1	2.54 mm	h_2	0.635 mm
ϵ_{r1}	10.2	ϵ_{r2}	10.2
s	1.2 mm	-	-

switch provides an up-state isolation better than 40 dB, a down-state insertion loss less than 0.6 dB up to 3 GHz, and an excellent choice for tunable filter applications at frequencies below 3 GHz.

2. Tunable Resonator Design

The substrates used to design a tunable SIW cavity are both Rogers RT/Duroid 6010LM ($\epsilon_r = 10.2$, $\tan\delta = 0.0023$ at 10 GHz). The thickness of the upper and lower substrates are 0.635 mm and 2.54 mm, respectively. The dimensions of the SIW cavity are determined using (3.1) so that f_{101} corresponds to the lowest frequency state in the filter tuning range. The width of the inductive irises at input/output are chosen arbitrarily, but they are ultimately determined by the external quality factor and inter-resonator coupling coefficient required for filter design as described in Section B.3 of this chapter. The dimensions for a cavity with resonant frequency of 1.3 GHz are listed in Table III.

a. Resonance Contours

To demonstrate the effect of tuning posts on the resonance frequency and field distribution of an SIW cavity, a tuning post is placed at a position P represented by a

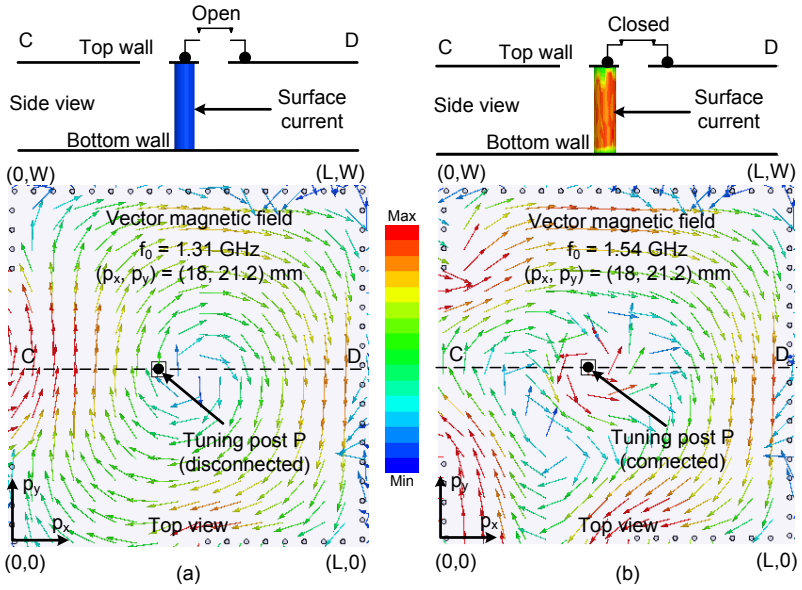

Fig. 31. Surface current distribution on the tuning post and vector magnetic field distribution within the cavity resonator at resonance frequency, when tuning post P is (a) disconnected, (b) connected.

black dot in Fig. 31(a). However, it is disconnected from the cavity top wall by an ideal MEMS switch in the open position. The fields within the cavity and surface currents on the posts are obtained using a commercial FEM simulation tool[4]. When the tuning post is disconnected, Fig. 31(a) shows that no surface current is induced on the tuning post and, as a result, the TE_{101}-mode magnetic field in the cavity is unaffected. The electric field magnitude within the cavity shown in Fig. 32(a) is also unchanged and closely resembles the TE_{101}-mode distribution. Since cavity fields are unchanged, the resonance frequency remains at f_{101}. The simulated magnitude of S_{21} for a disconnected tuning post at position P is shown in Fig. 33(a). A transmission peak occurs at f_{101} and the cancellation of signals through the TE_{101} and TE_{201} modes results in a transmission zero below the TE_{201} mode resonance [21], [70].

[4]Ansoft High Frequency Structure Simulator (HFSS) v11, Ansys Inc., Canonsburg, PA, 2010.

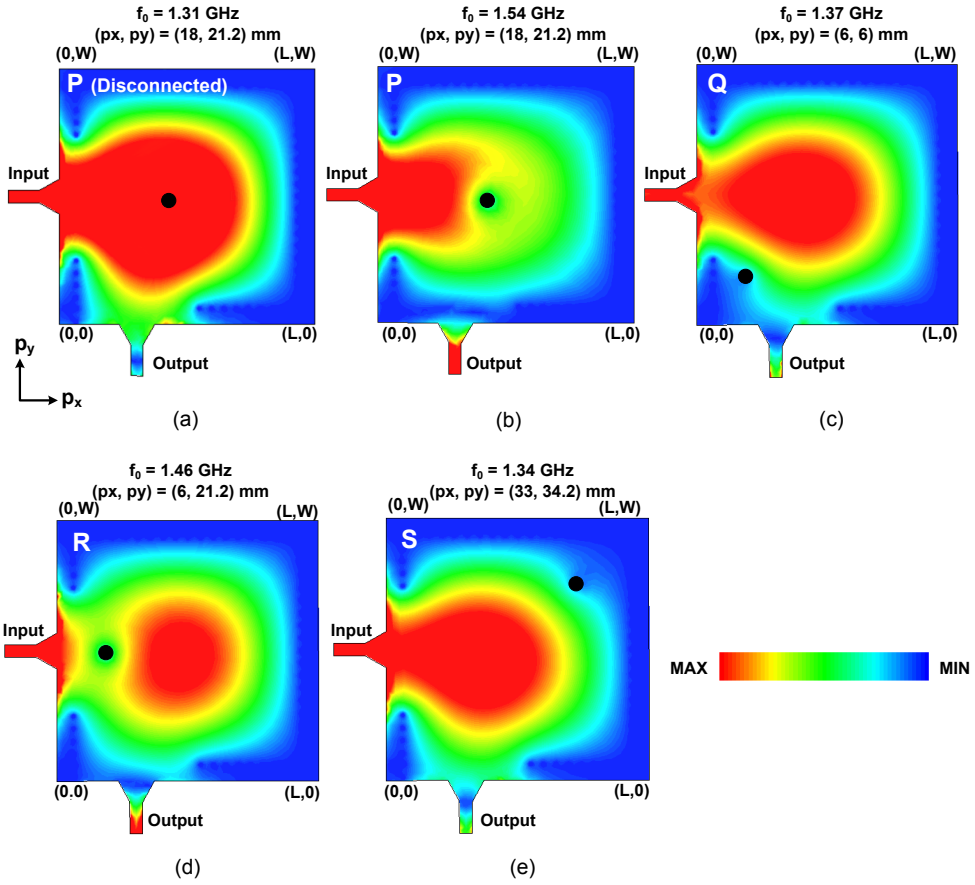

Fig. 32. Magnitude of electric field distribution in the cavity at resonance frequency, for various locations of tuning post; (a) disconnected post P near cavity center, and connected (b) post P near cavity center, (c) post Q near output port, (d) post R near input port, and (e) post S away from ports and cavity center.

When the MEMS switch is closed, surface currents are induced on the tuning post as shown in Fig. 31(b), when the standing waves inside the cavity are incident on it. Also, the magnetic field is concentrated around the tuning post causing perturbation of cavity fields. For the tuning post at position P, Fig. 32(b) shows that the electric field inside the cavity is significantly perturbed and consequently the change in cavity resonance frequency is maximum as shown in Fig. 33(a). When the post is located around the inductive irises (positions Q and R) as shown in Fig. 32(c) and (d), the peak transmission level through the cavity is changed because the presence of posts alters the resonator external quality factor, and hence the coupling to the resonator. However, position R has a greater shift in resonance frequency compared to position Q due to greater field perturbations in the cavity. At position S, the post has very little influence on the field distribution as shown in Fig. 32(e) and hence results in very little frequency shift [Fig. 33(a)]. In all cases, the field perturbation caused by the presence of a tuning post also affects the coupling to the TE_{201} mode of the cavity. As a result, the position of transmission zero and spurious resonances also vary with the tuning post location.

Similarly, the cavity resonance frequency is found from full-wave simulation for every position of the post within the cavity when the MEMS switch is closed, to obtain the resonance contours shown in Fig. 33(b). The maximum frequency shift is obtained when the post is located near the center of the cavity and the frequency shift becomes lower as the post is moved away from the center. Interestingly, the resonance contours closely resemble the electric and magnetic field distributions of the TE_{101} mode within the cavity [Figs. 31(a), 32(a)]. Placing the metallic post at points of maximum electric field or minimum magnetic field magnitudes produces large frequency shift.

To qualitatively understand this effect, the SIW cavity can be assumed to be

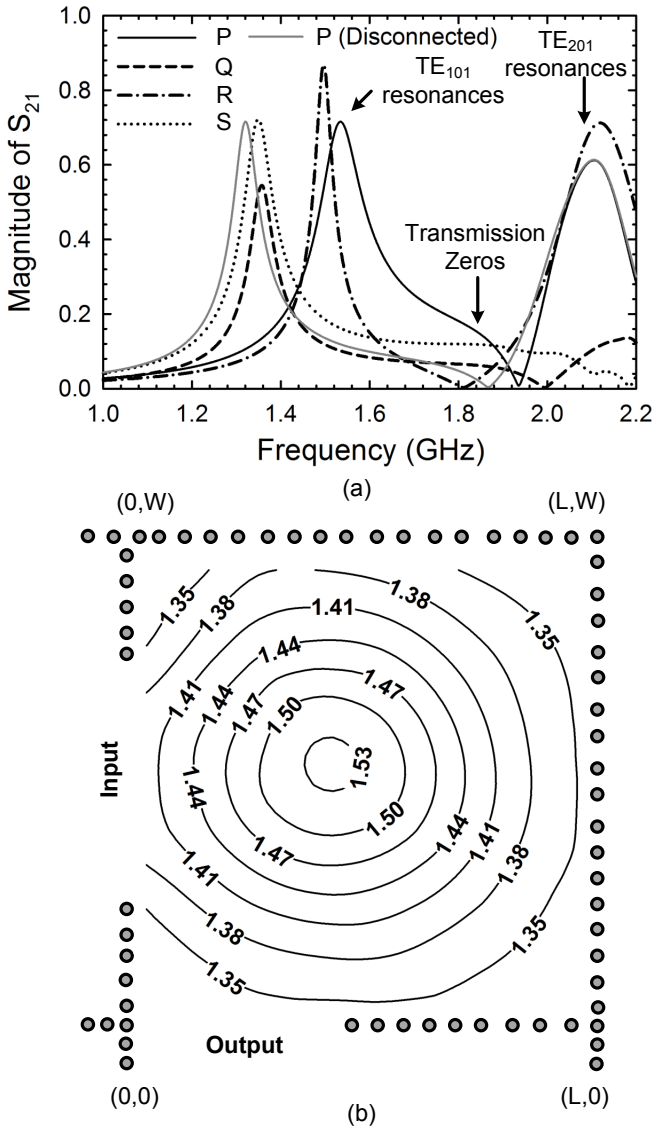

Fig. 33. (a) Simulated magnitude of S_{21} for the tuning post configurations in Fig. 32, and (b) resonance contours for a single tuning post within the cavity.

a parallel L-C resonator with a resonance frequency $f_0 = 1/2\pi\sqrt{LC}$. Since surface currents are induced on the tuning post when it is connected inside a cavity (Fig. 31), the tuning post can equivalently be represented by a shunt inductance (L_p) [72]. The value of the shunt inductance depends on the electric field magnitudes at the position of the post and can be calculated for a TE_{101} cavity using formulas in [72]. Around the center of the cavity, where the electric field magnitudes are highest, the value of L_p is minimum. Thus, for a tuning post around the center of the cavity, the resonance frequency shifts to its highest value which is given by $f_0' = 1/2\pi\sqrt{L_{eq}C}$, where L_{eq} is the parallel combination of L and L_p. By properly controlling the position of the tuning post, the resonant frequency of the cavity can be adjusted to a desired value. The dependence of frequency shift on the field magnitudes within the cavity forms the basis for design of the tunable SIW resonator.

b. External Quality Factor

While the contours in Fig. 33(b) imply that there are multiple post positions for a given resonant frequency, some of these positions affect the coupling to the cavity. In a tunable filter, deviation of coupling coefficients from the designed value results in bandwidth variation and matching degradation. To find these positions, external quality factor (Q_e) at the input and output ports is evaluated using full-wave simulations for a singly-loaded resonator, as the position of the post is varied. The width of the inductive irises, W_{io}, is assumed unchanged. The variation of Q_e is normalized to the external quality factor of the cavity with no post present, to obtain a normalized value, Q_n.

The variation of Q_n with post position at input and output ports is shown in Fig. 34(a) and (b). At both input and output ports, the external quality factor drastically increases if the post is located close to the input/output inductive irises because the

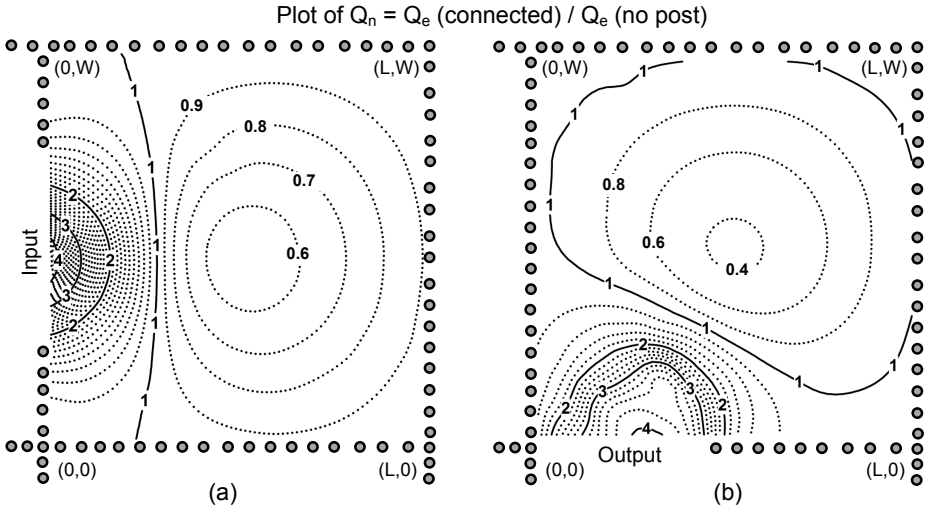

Fig. 34. Normalized variation of external quality factor for various locations of the tuning post with respect to (a) input port, and (b) output port.

post affects coupling to the cavity. Thus, tuning posts must be placed sufficiently far away from the inductive irises to avoid matching and bandwidth degradation as the filter is tuned. If large frequency shifts are desired, tuning posts must be located around the middle of the cavity where Q_n shows relatively less variation. Placing tuning posts away from the center, and towards the top or right walls of the cavity provides smaller frequency shifts while maintaining relatively constant Q_n.

c. Tunable Cavity Implementation

To implement a tunable cavity resonator with maximum tuning range and 16 symmetric tuning states, six tuning posts $(A, \ldots, F)$ controlled by three RF MEMS switch packages (S_1, S_2, S_3) are used as shown in Fig. 35(a). Four tuning posts (A, B, C, D) located around the middle of the cavity are used for coarse tuning control of the resonator because they produce high frequency shifts. Two tuning posts (E, F) located away from the middle and towards the top of the cavity provide small frequency shifts and are used for fine tuning control. Although the fine tuning posts may also

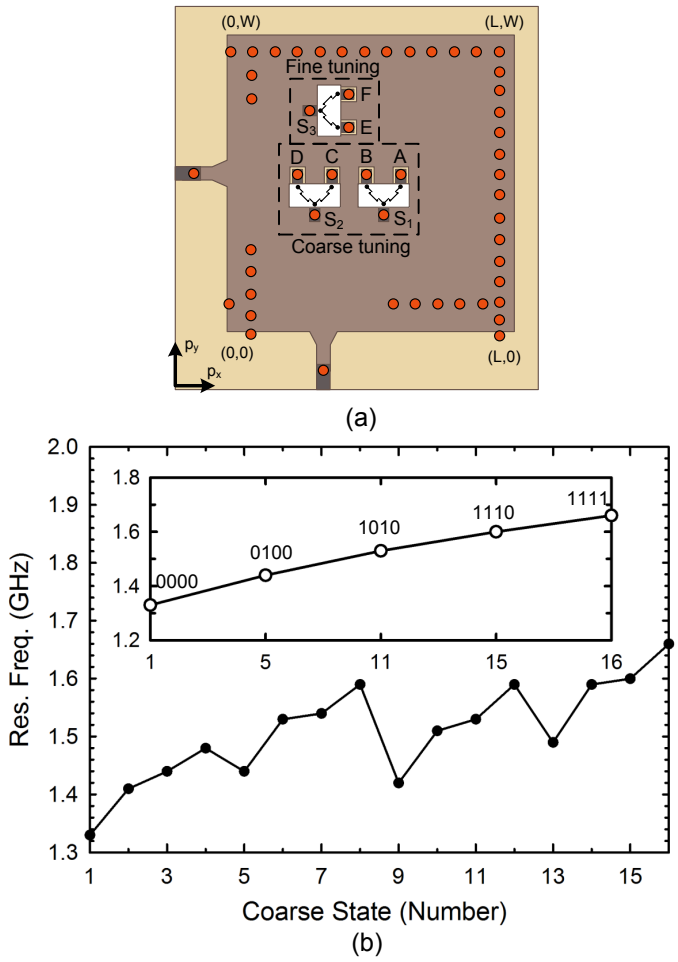

Fig. 35. (a) A tunable SIW resonator employing six tuning posts controlled by three SPDT RF MEMS switch packages, and (b) coarse tuning states obtained using only tuning posts ABCD.

be placed near the right wall of the cavity, the proposed locations allow easy routing of bias lines to the switch package. The positions of tuning posts are always such that the coupling mechanism to the cavity is relatively unaffected. Accordingly, the regions in Fig. 34 corresponding to high values of Q_n are avoided. Also, the tuning posts and top via corresponding to a MEMS switch package are placed as close as possible to the mounting pads of the package to minimize parasitic elements and extend the tuning range.

Table IV. Positions of Tuning Posts (in mm)

Coarse Tuning						Fine Tuning		
Switch 1			Switch 2			Switch 3		
Post	p_x	p_y	Post	p_x	p_y	Post	p_x	p_y
A	26.4	22.8	C	14.4	22.8	E	17.4	31.2
B	20.4	22.8	D	8.4	22.8	F	17.4	37.2

The positions of the coarse tuning posts are optimized by full-wave simulation in Sonnet[5] using S-parameters of the RF MEMS switch in Fig. 30(d) so that maximum frequency shift is obtained when all switches are in the closed position. Although it seems that four tuning posts are sufficient to give $2^4 = 16$ distinct tuning frequencies, it is difficult to obtain maximum tuning range with symmetric tuning frequencies simultaneously. The optimized positions of the coarse tuning posts shown in Table IV for the cavity with dimensions given in Table III provide around 30% tuning range. The 16 possible coarse tuning states are shown in Fig. 35(b) where state 1 corresponds to $ABCD = 0000$ (all switches in the open position), and state 16 corresponds to $ABCD = 1111$ (all switches in the closed position). The tuning frequencies obtained with only coarse tuning posts are non-monotonic and have unequal spacings between each other, and some of the states are unacceptable for a tunable filter with symmetrically-located tuning states. However, coarse tuning states that are equally spaced and monotonically increasing, as shown in the inset of Fig. 35(b), can be used to obtain symmetric tuning capability with the help of fine tuning posts.

The fine tuning posts (E, F) are designed to obtain linearly increasing fine tuning states between two coarse tuning states. The fine tuning post locations obtained from

[5]Sonnet 12.52, Sonnet Software Inc., Syracuse, NY, 2009.

Table V. Coarse and Fine Tuning Configurations

Coarse Tuning		Fine Tuning	
Config.	ABCD	Config.	EF
P	0000	1	00
Q	0100	2	01
R	1010	3	10
S	1110	-	-
T	1111	-	-

full-wave simulations are given in Table IV. For each coarse tuning configuration $ABCD$, three fine tuning states may be obtained using posts E and F. The allowable post configurations for coarse and fine tuning are shown in Table V. The fine tuning state $EF = 11$ is not utilized because the frequency increment produced is almost the same as that of $EF = 10$. This is because the electric field magnitude at the location of post F is low due to the field perturbation caused by the connected post E. As a result, the frequency increments for fine tuning states $EF = 10$ and $EF = 11$ have similar values due to negligible field perturbation caused by post F, when post E is connected to the top cavity wall.

The proposed coarse and fine tuning mechanism results in 15 frequency states as shown in Fig. 36. The coarse and fine tuning configurations corresponding to each state are represented by a tuning code XY where $X = P, \ldots, T$ is the coarse tuning configuration and $Y = 1, 2, 3$ is the fine tuning configuration. However, states 9 and 10 with configurations $R3$ and $S1$ have the same resonance frequency. Thus, only state 9 is used resulting in 14 distinct cavity tuning states.

Fig. 37 shows the simulated resonator unloaded quality factor (Q_u) for 14 different tuning states. This is done using full-wave simulation of a single resonator weakly

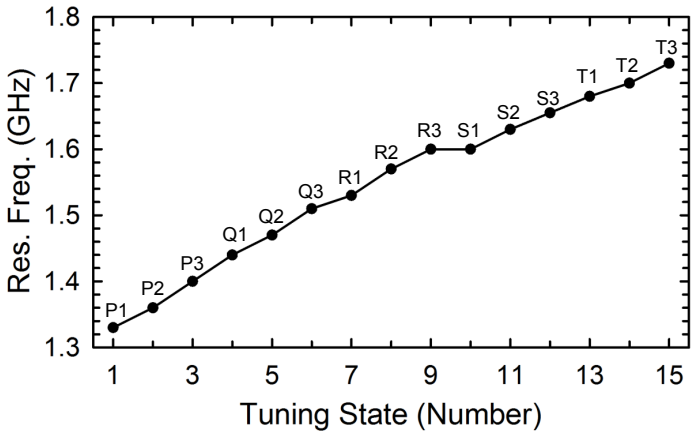

Fig. 36. Simulated resonant frequency of the SIW cavity for different tuning states.

coupled at the input and output ports by employing the switch S-parameters in Fig. 30(d). The resonator has highest Q_u when all switches are in the up-state position (state 1) but decreases when a single MEMS switch is closed due to the down-state resistance of the RF MEMS switch. For states 2-4, it is also seen that Q_u decreases as a single tuning post approaches regions with higher electric field magnitude near the center of the cavity. For states 5-6, two tuning posts are connected and Q_u further decreases due to extra losses in fine tuning posts. For tuning states 7-14, two or more connected tuning posts result in high cavity field perturbation. As a result, Q_u values no longer follow a simple trend, and vary between 93—108. The lowest Q_u corresponds to state 14 due to down-state resistances of five RF MEMS switches in configuration $T3$.

3. Filter Design

Since the upper transmission zero generated due to cancellation of the TE_{101} and TE_{201} modes is sufficiently far away from the filter passband, a pure Chebyshev response in the filter passband can be achieved. Fig. 38 shows the layout of the two-pole 3.5% tunable SIW filter. The inter-resonator coupling coefficient, k_{12}, and

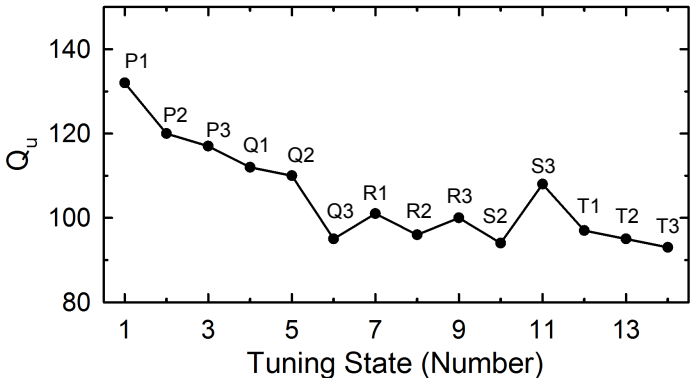

Fig. 37. Simulated unloaded quality factor (Q_u) of the SIW cavity for different tuning states.

the external quality factor, Q_e, are calculated using low-pass Chebyshev prototype values, $g_0, \ldots, g_3$, as [15]

$$k_{12} = \frac{FBW}{\sqrt{g_1 g_2}}; \quad Q_e = \frac{g_0 g_1}{FBW} \tag{3.2}$$

where FBW denotes the filter fractional bandwidth. For 0.01 dB passband ripple, these formulas result in $k_{12} = 0.082$ and $Q_e = 12.8$, respectively.

To determine the coupling coefficient k_{12}, the input/output ports are weakly coupled to the cavities with all MEMS switches in the open position, using narrow inductive irises at the input/output. The width of the inductive iris between resonators, W_c, is then adjusted to obtain the required coupling value, which is given by (2.8). Next, the width of the input/output inductive iris, W_{io}, is adjusted to obtain the required value of Q_e. This can be extracted from full-wave simulation of a singly-loaded cavity resonator with all MEMS switches in the open position, by employing the expression [15]

$$Q_e = \frac{f_0}{\Delta f_{\pm 90}} \tag{3.3}$$

where f_0 is the resonant frequency of the cavity and $\Delta f_{\pm 90^\circ}$ are the frequencies corresponding to a phase shift of $\pm 90^\circ$ in the simulated S_{11} of the cavity, respectively. The

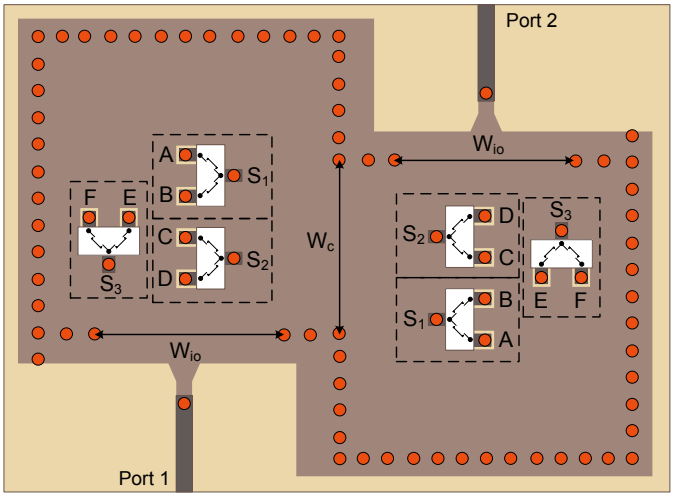

Fig. 38. Layout of the two-pole SIW RF MEMS tunable filter.

final widths of inductive irises used for filter design are $W_{io} = 24$ mm and $W_c = 21$ mm, respectively.

The entire tunable filter is simulated using Sonnet to take into account all parasitics associated with mounting pads on the top layer and bias line routing to the RF MEMS switches. The S-parameters of each RF MEMS switch are included in the complete filter simulation and the whole filter is fine tuned to achieve symmetric tuning states with maximum return loss. The simulated insertion loss and return loss for the tunable SIW filter are shown in Figs. 39(a) and (b).

4. Fabrication and Measurement

a. Fabrication, Implementation and Biasing

The photograph of the 1.2—1.6 GHz SIW RF MEMS tunable filter fabricated on a two-layer RT/Duroid 6010LM substrate is shown in Fig. 40. First, the mounting pads and bias lines for the RF MEMS switches, and 50-Ω feed lines to the filter are etched on the top-side metalization of the upper substrate. Then, the middle layer,

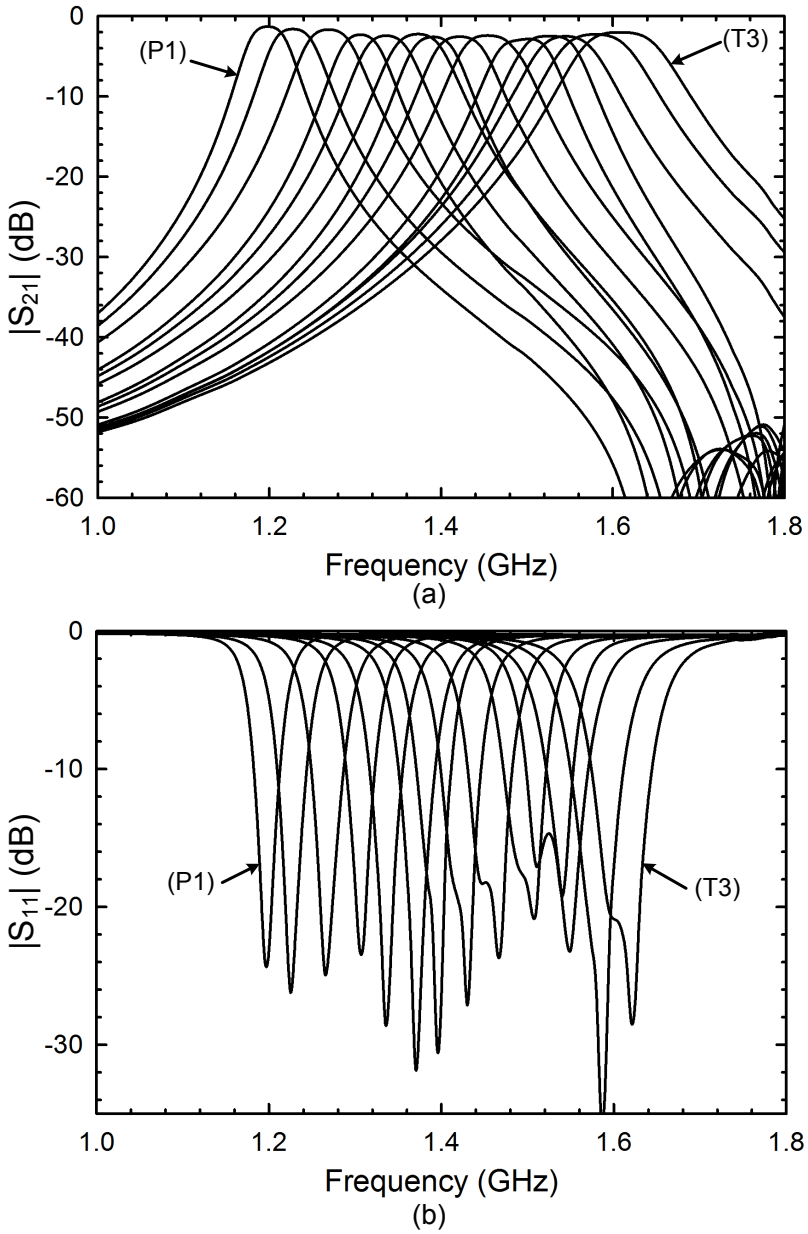

Fig. 39. Simulated: (a) insertion loss and (b) return loss of the two-pole 1.2—1.6 GHz tunable SIW filter.

which has tapered microstrip transitions and the cavity top wall with openings for tuning posts (Fig. 29), is etched on the back-side of the 0.635 mm thick substrate. The top vias connecting the top metal layer to the cavity top wall on the middle layer are fabricated on the upper substrate using metalized plated via-holes with 0.6 mm diameter.

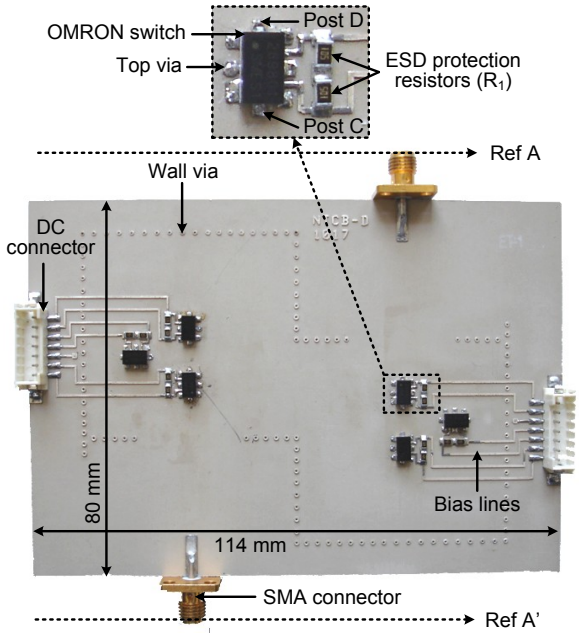

Fig. 40. Fabricated 1.2—1.6 GHz SIW RF MEMS tunable filter.

Next, the top-side metalization of the 2.54 mm thick substrate is completely removed while the back-side metalization is preserved to form the cavity bottom wall. The back-side of the upper substrate is bonded to the top-side of the lower substrate using standard glass fiber (GF) pre-preg material ($\epsilon_r = 3.17$) with a thickness of 0.09 mm. Full-wave simulation of the filter shows that the GF pre-preg bonding material does not affect the performance of the cavity filter. Then, plated via-holes with 0.6 mm diameter are drilled through both substrates at appropriate locations to form the tuning posts and side-walls of the SIW filter. Packaged RF MEMS switches (2SMES-

01) from OMRON Corp. are soldered onto the mounting pads on the top layer. A 1 MΩ resistor (R_1) is connected between each bias line and DC ground, to provide a discharge path for accumulated charge in each MEMS switch. DC ground is easily accessed through a via connecting the top-layer to the cavity top wall located in the middle layer. Since this DC ground via lies above the SIW cavity, it does not interfere with the RF performance of the cavity.

b. Measurements

The fabricated filter is measured using an Agilent N5230A vector network analyzer after calibration with the short-open-load-thru (SOLT) technique. The calibration is performed to the Subminiature-A (SMA) connectors at the input/output of the filter, as indicated by the reference planes A, A' in Fig. 40. The measured insertion and return losses of the tunable SIW filter for 14 different states are shown in Figs. 41(a) and (b), respectively. The measured insertion loss response includes the losses of the SMA connectors at the filter input/output which is negligible (<0.1 dB) at around 1-2 GHz. The measured return loss is better than 15 dB for all tuning states.

Fig. 42(a) shows the simulated/measured center frequency and measured insertion loss for each filter response. The simulated and measured center frequencies from 1.2—1.6 GHz are in very good agreement. The center frequency variation of 1.2—1.6 GHz is equivalent to 28% tuning range with respect to 1.4 GHz. The measured frequency response shows a Q_u ranging from 93—132 with associated insertion losses between 2.2—4.1 dB for all tuning states. The filter has lowest insertion loss when all switches are in the up-state position, and the loss increases as more switches are in the down-state position. However, the maximum measured insertion loss corresponds to state 6 (config: $Q3$) although state 14 (config: $T3$) has the lowest Q_u value (Fig. 37), and is attributed to higher filter fractional bandwidth at state 14 compared to

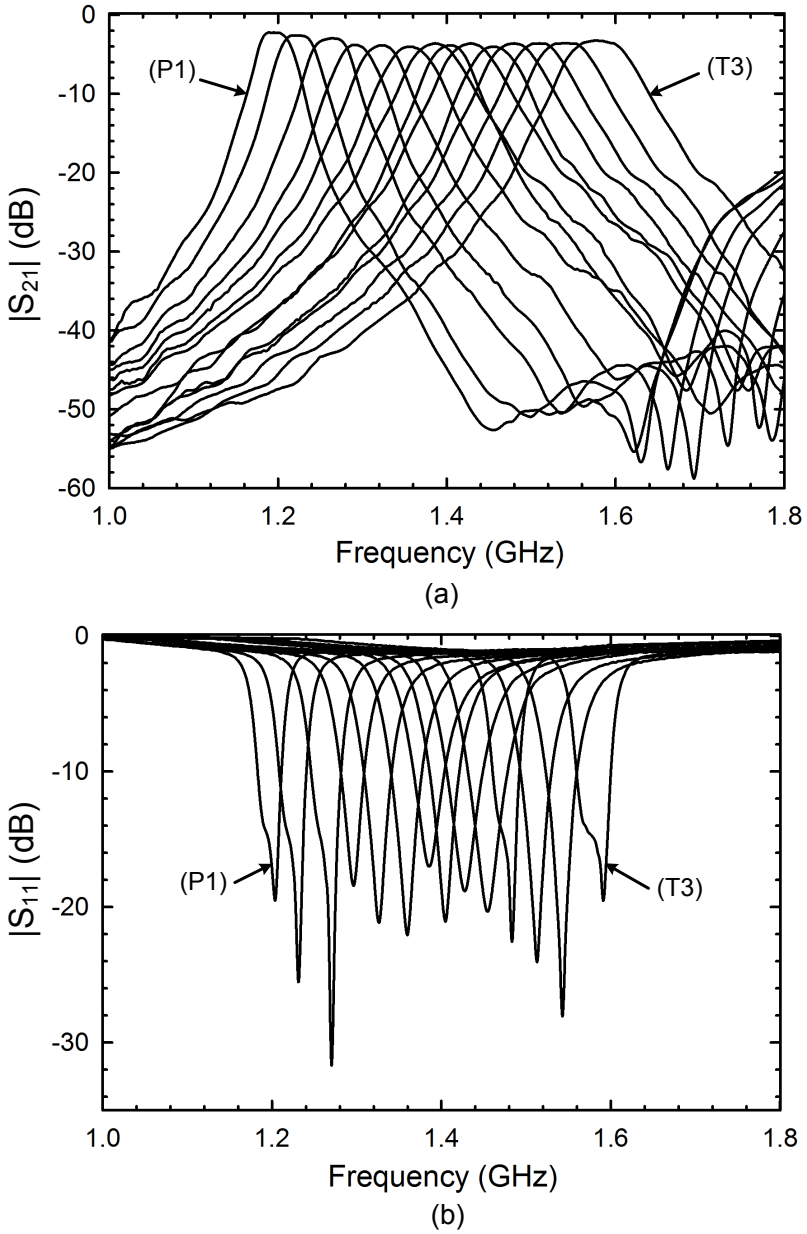

Fig. 41. Measured: (a) insertion loss and (b) return loss of the two-pole 1.2—1.6 GHz tunable SIW filter.

state 6.

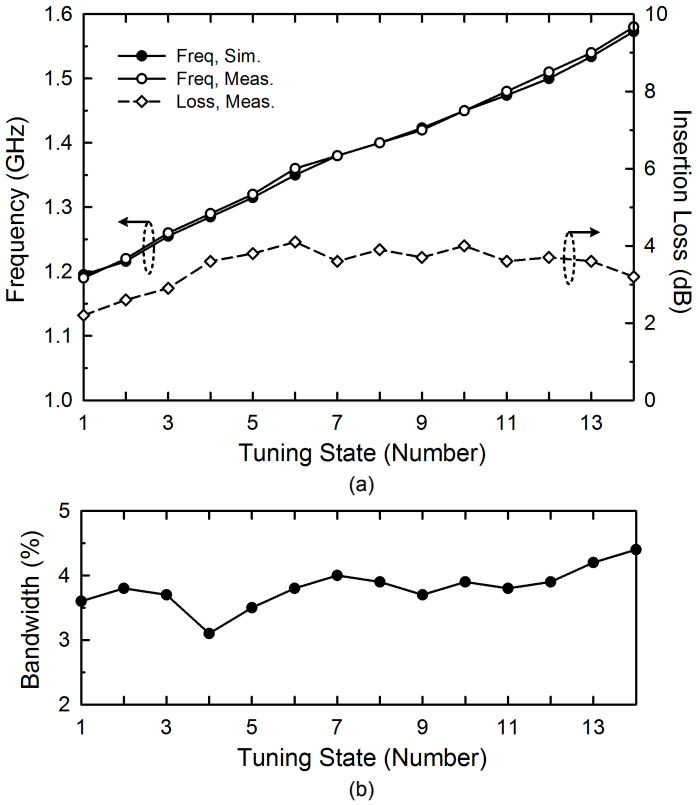

Fig. 42. (a) Simulated/measured center frequency and measured insertion loss. (b) Measured fractional bandwidth of the filter (3.7% ± 0.5%).

Fig. 42(b) shows the measured fractional bandwidth, which varies between 3.7% ± 0.5% for all responses. The relatively constant fractional bandwidth is obtained by placing tuning posts in regions within the cavity where the external quality factor shows relatively less variation, as explained in Section B.2.b of this chapter. Fig. 43 compares the measured and simulated insertion loss for three arbitrary states at 1.2 (State 1), 1.4 (State 8) and 1.6 GHz (State 14), and the simulated and measured responses agree very well.

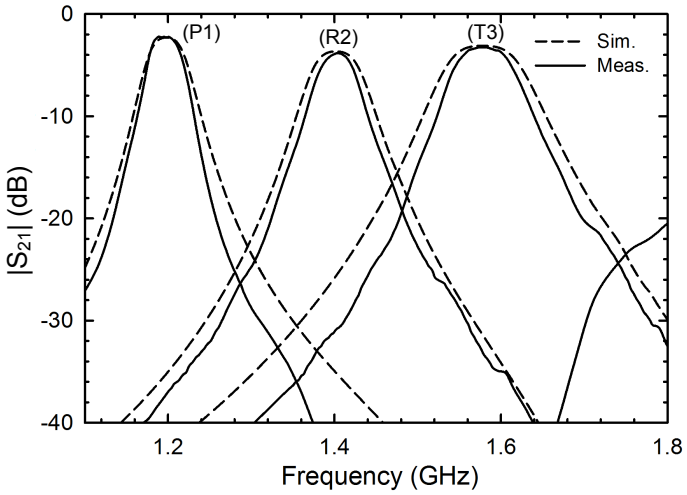

Fig. 43. Comparison between the measured and simulated insertion loss for three arbitrary states at 1.2 (State 1), 1.4 (State 8), and 1.6 GHz (State 14).

5. Spurious Suppression

In the proposed tunable filter, higher order resonant modes present in the cavity degrade the upper stopband performance. The stopband rejection may be improved by employing LPFs at the filter input/output to suppress spurious resonant modes present beyond the upper transmission zero of the filter [73]. In addition, two dissimilar elliptic LPFs at the input/output of the filter are proposed for maximum spurious suppression over a wide frequency range, without increasing the filter area. Fig. 44(a) shows the LPFs included in the middle metal layer at the input/output of the SIW cavity filter.

Fig. 44(b) shows the layout of a five-pole elliptic LPF (Type-I) designed using formulas in [15]. A cutoff frequency of 1.7 GHz is chosen so that it is just beyond the highest tuning frequency of the bandpass filter. Fig. 44(c) shows the layout of two similar five-pole elliptic LPFs connected in parallel (Type-II). The Type-II filter is designed to have a cutoff frequency of 1.7 GHz while having different transmission zeros compared to the Type-I filter. Connecting the filters in parallel results in a

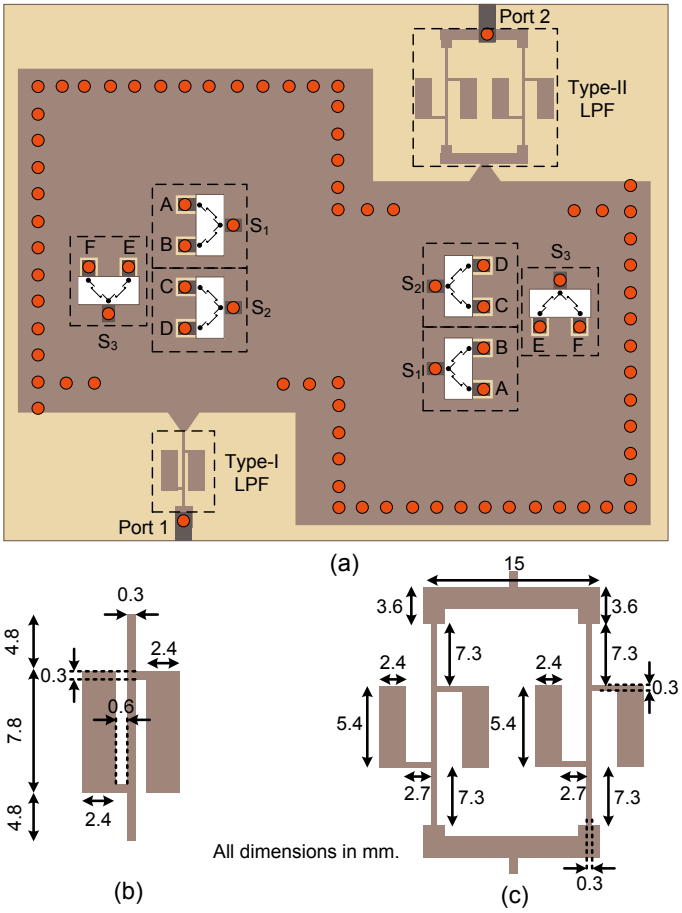

Fig. 44. Layout of the (a) two-pole SIW tunable filter employing LPFs at the input/output for spurious suppression, (b) type-I LPF, and (c) type-II LPF.

steeper upper rejection skirt while maintaining compactness of the LPF.

Fig. 45(a) shows the simulated broadband filter response for the first and last tuning states upto 4 GHz, and the S_{21} of each LPF topology. The Type-II LPF has a steeper upper rejection skirt, and different transmission zero locations compared to the Type-I LPF. To clarify the purpose of using two dissimilar LPFs for stopband suppression, the simulated filter response for the first state using only Type-I, only Type-II, and Type-I and Type-II at the filter input/output is shown in Fig. 45(b). Maximum spurious suppression is achieved when the LPFs are dissimilar because greater number of stopband transmission zeros (four, in this case) are obtained.

The tunable SIW filter is fabricated with the LPFs included at the input/output of the filter, using the procedure described in Section B.4.a of this chapter. The measured insertion loss of the tunable SIW filter with spurious suppression is shown in Fig. 46. Spurious suppression better than -28 dB is observed up to 4.0 GHz for all tuning states. The passband insertion loss comparison for the first and last state for tunable SIW filters with and without LPFs is shown in the inset of Fig. 46. The inclusion of LPFs increases the filter insertion loss by around 0.7—1.0 dB so that the filter insertion loss varies between 3.2—4.8 dB over all tuning states. Although, dissimilar LPFs at the bandpass filter terminals result in different values of S_{11} and S_{22}, the measured return loss values at each port was better than 15 dB. This shows that the filter can still be used as a symmetric 2-port network without affecting system performance.

6. Nonlinear Characterization

The third-order intermodulation components of the tunable filters with and without LPFs were measured using a setup similar to the one shown in [74]. For a particular tuning state, a two-tone signal was applied to each tunable filter within the filter

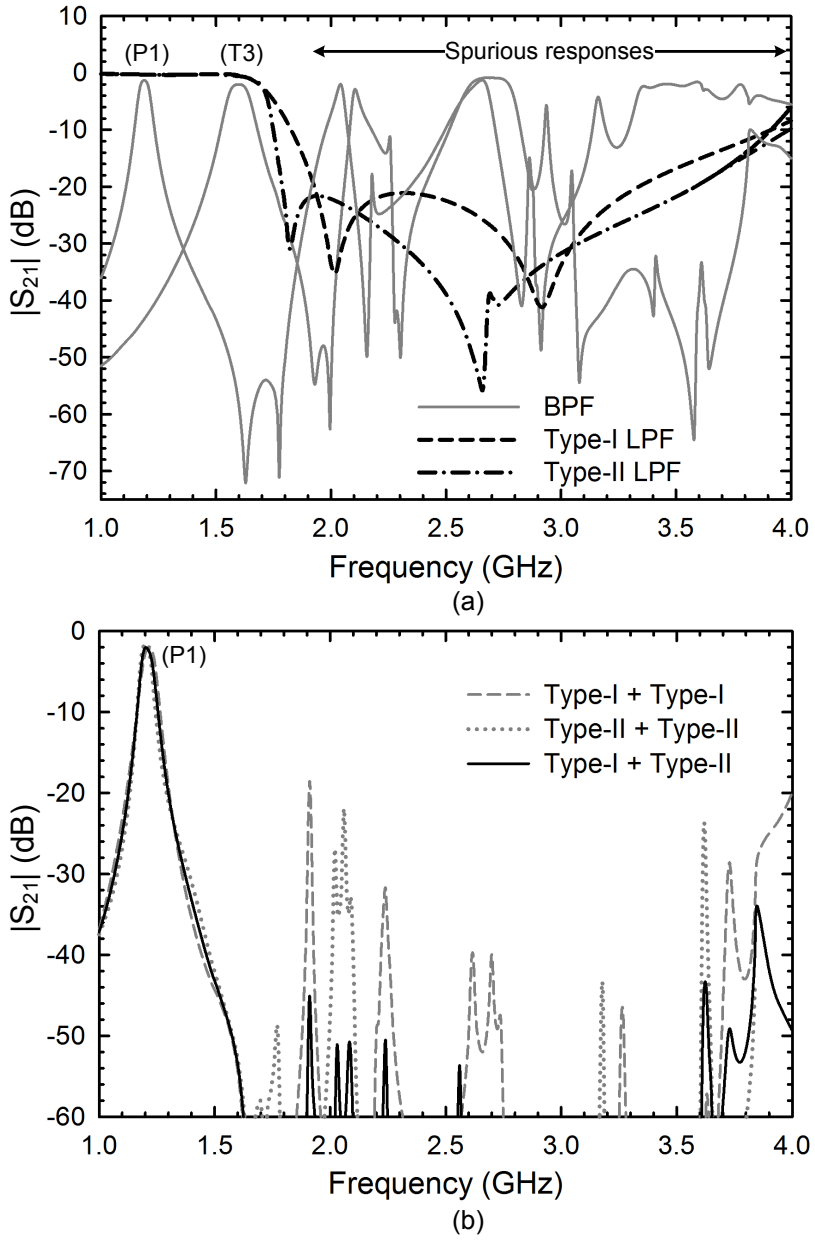

Fig. 45. (a) Simulated wideband response of the tunable filter and lowpass responses of Type-I and Type-II filters, and (b) spurious suppression for the lowest tuning state for various combinations of LPFs.

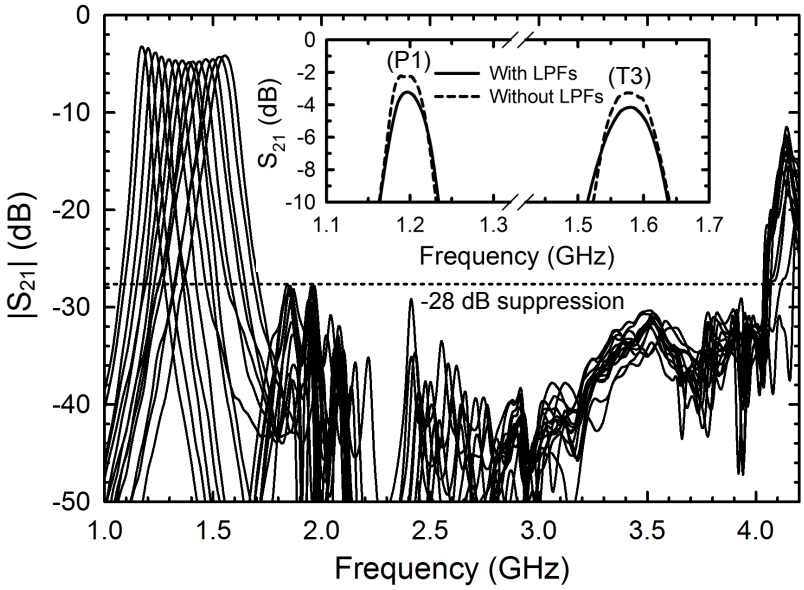

Fig. 46. Measured wideband response of the 1.2—1.6 GHz tunable SIW filter with spurious suppression.

passband with a separation frequency of 10 kHz (or 1 MHz), and the third order intermodulation products were measured using a spectrum analyzer. Due to the extremely linear behavior of the RF MEMS switches, the third-order intermodulation level was always below the noise level of the Agilent E4446A spectrum analyzer as long as the RF mixer of the spectrum analyzer was not saturated by the input signal (a maximum power of 15 dBm was used). As a result, it was impossible to measure the IIP_3 of the tunable filters for any tuning state. Thus, it can be concluded that the IIP_3 of the RF MEMS tunable filters is >65 dBm, which is an incredible number compared to other tuning technologies such as p-i-n diodes.

For comparison, intermodulation components of the tunable SIW filter employing p-i-n diodes developed in [67], was measured. For a two-tone signal with 10 kHz beat frequency, the worst-case measured IIP_3 for this filter was 25 dBm when all p-i-n diodes were reverse-biased. The worst-case IIP_3 was also measured for various beat

frequencies (upto 1 MHz), and remained approximately constant.

Although resistance variations in metal-contact MEMS switches result in intermodulation distortion, the IIP_3 of such MEMS switches due to this mechanism is calculated to be around +80 dBm [75]. As a result, the intermodulation products in circuits employing metal-contact RF MEMS switches are very hard to measure.

7. Conclusion

This section has demonstrated an SIW RF MEMS tunable filter with a tuning range of 1.2—1.6 GHz employing packaged RF MEMS switches. The measured filter Q of 93-132 is the highest reported Q in filters using off-the-shelf RF MEMS switches on conventional PCB substrates. Out-of-band interference is greatly reduced by including lowpass filters at the bandpass filter terminals for improved upper stopband rejection. Since fabrication of this filter only requires conventional PCB processes, the manufacturing cost is significantly lower. Successful implementation of this filter proves that commercialization of RF MEMS switch technology as off-the-shelf components will be highly useful in developing low-cost tunable filters with low-loss, wide-tuning and very high linearity.

C. Half-Mode Substrate Integrated Waveguide RF MEMS Tunable Filters

1. Resonator Design

a. HMSIW Model

Fig. 47(a) shows a conventional SIW with width W chosen so that the dominant TE_{10}-mode propagates in the waveguide. Linear arrays of via-holes with diameter d and center-to-center spacing of b between adjacent via-holes emulate a metallic waveguide wall where the electric field is zero. The electric field distribution in the substrate is a half-sinusoid corresponding to the TE_{10}-mode. Since the substrate height h is typically small compared to a wavelength, the magnetic-field variations in the x-direction along the symmetric plane are negligible and the plane of symmetry resembles an ideal magnetic wall (open circuit) [23]. By placing an open circuit along the symmetrical xz-plane, an HMSIW is created as shown in Fig. 47(c). In practice, the width of the HMSIW is slightly less than half the width of the SIW to account for the fringing fields at the open circuit [63].

Alternatively, an HMSIW can also be regarded as half of a microstrip line excited by its first higher order mode (EH_1), as shown in Fig. 47(b) [23]. A null in the electric field distribution of the EH_1-mode in a wide microstrip line indicates that the symmetric plane can be replaced by an electric wall (short circuit). The resulting structure is exactly the same as an SIW with an open circuit along its symmetry plane. The equivalence between a half-microstrip line and HMSIW is used to develop a circuit representation of the HMSIW resonator.

The transverse equivalent network for a microstrip line operated in the EH_1-mode is shown in Fig. 48(a) [77]. Along any xy-plane, an EH_1-mode microstrip line of width W has the same electric field distribution on either side of the symmetric

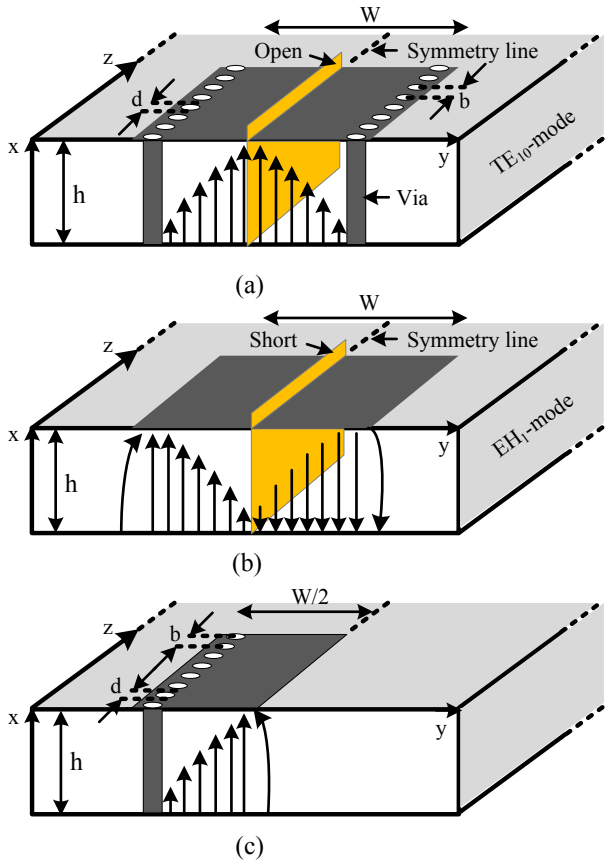

Fig. 47. (a) SIW with width W operating in the TE_{10}-mode with an open-circuit along its symmetry plane, (b) higher order microstrip line with width W operating in the EH_1-mode with a short-circuit along its symmetry plane, and (c) HMSIW with width $W/2$ as a consequence of cases (a) and (b).

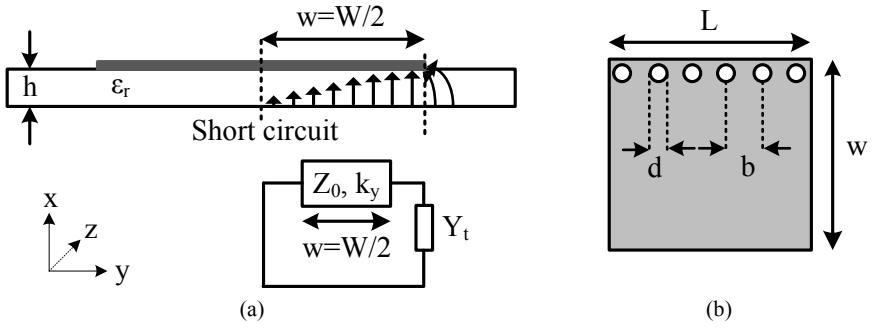

Fig. 48. (a) Transverse equivalent network representation of the HMSIW resonator. (b) HMSIW resonator with width $w = W/2$ and length L with via-holes of diameter d and spacing b.

plane, as a quasi-TEM (EH_0-mode) microstrip line of length $W/2$ terminated by a short circuit at one end and an open circuit at the other. Y_t is the admittance associated with the fringing fields at the open end of the transmission line. Z_0 is the characteristic impedance of the quasi-TEM transmission line with width L. The propagation constant k_y depends on the width and length of the HMSIW and the properties of the substrate material, and can be calculated using the method in [78]. Fig. 48(a) represents an HMSIW resonator if the width $w = W/2$ is chosen so that the quasi-TEM transmission line is 90°-long at resonance frequency. The resulting short-circuited quarter-wavelength resonator has spurious passbands corresponding to only odd-harmonics of the fundamental resonance frequency, and thus provides good upper stopband rejection when used for filter design. The width w must be slightly adjusted to absorb the admittance Y_t, so that the desired resonance frequency is obtained.

b. Tuning Mechanism

To make the HMSIW resonator tunable, a tuning network with a variable admittance Y_n is introduced in parallel with Y_t, as shown in Fig. 49(a). For resonance, the overall shunt admittance Y_{eq} must be zero, implying $jY_{in} + jY_t + jY_n = 0$. This condition may also be expressed as

$$\cot\left(\frac{2\pi w\sqrt{\epsilon_{r,eff}}}{c}f\right) = \frac{Y_t + Y_n}{Y_0} \tag{3.4}$$

where, $\epsilon_{r,eff}$ is the effective dielectric constant of the substrate under the HMSIW, f is the frequency and c is the speed of light. Here, $\epsilon_{r,eff} \approx \epsilon_r$ due to highly confined electric fields under the parallel-plate quasi-TEM line. Consequently, the amount of fringing fields is also neglibible and the quantity Y_t can be neglected for simplicity of analysis.

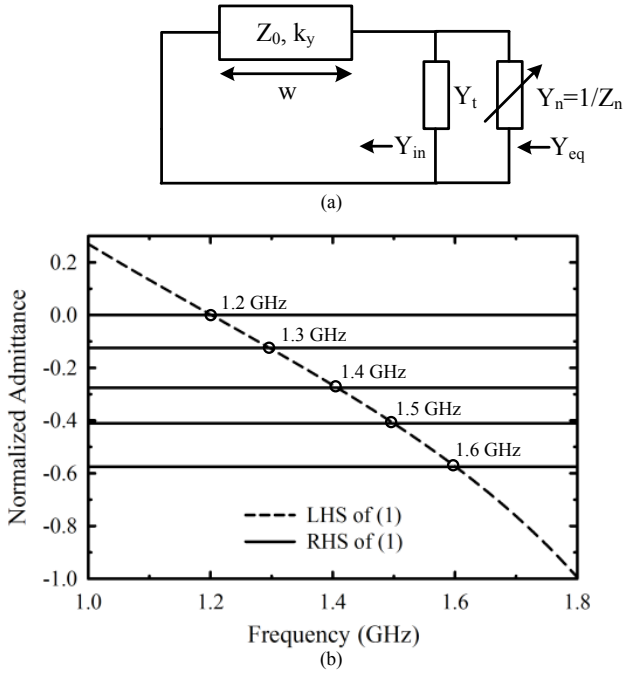

Fig. 49. (a) Transverse network representation, and (b) graphical representation of resonance conditions of the HMSIW resonator.

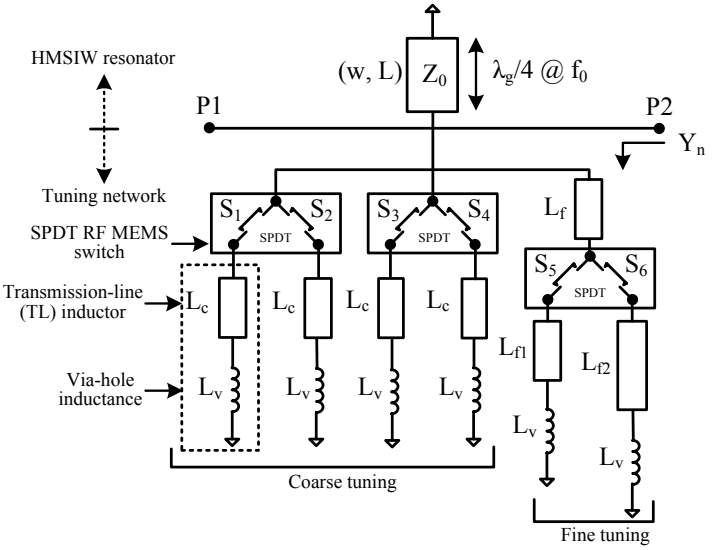

Fig. 50. Complete circuit model of a tunable HMSIW resonator.

Fig. 49(b) shows the left- and right-hand sides of (3.4) plotted as a function of frequency for $w = 20.2$ mm and $\epsilon_{r,eff} = 9.55$, for different values of Y_n/Y_0 ($Y_t = 0$). For simplicity, Y_n is assumed to be independent of frequency for now. The points of intersection of the solid and dashed lines indicate the resonant frequencies of the tunable HMSIW resonator. Thus, as the values of Y_n become more negative, the resonance frequency increases to higher values.

c. Tuning Network

One possible implementation of a tuning network that provides increasingly negative values of Y_n is a switchable array of shunt inductors. The proposed implementation of the switchable tuning network attached to the open end of the HMSIW resonator, is shown in Fig. 50. Each shunt branch of the tuning network consists of an inductor implemented with a short section of transmission line (TL-inductor) in series with a via-hole to the ground layer. To design a tunable resonator with around 15 distinct resonant frequencies, four coarse-tuning and two fine-tuning shunt branches are used. Each shunt branch may be connected to, or disconnected from the HMSIW resonator using surface-mount single-pole dual-throw (SPDT) RF MEMS switches ($S_1, \ldots, S_6$) [33].

If the overall inductance of the tuning network is L_{eq} for a given combination of switches, the admittance of the tuning network at an angular frequency ω is expressed as

$$jY_n = -j/(\omega L_{eq}). \tag{3.5}$$

By adjusting L_{eq} at a tuning frequency ω, the required Y_n values may be obtained to tune the resonator. Since the values of Y_n are more negative as L_{eq} decreases, the highest tuning frequency is obtained when all branches are connected in parallel to

the HMSIW resonator. However, to maximize the tuning range, the total inductance of each coarse-tuning branch must be minimum. The lowest possible inductance for coarse-tuning branches is limited by the inductance of the mounting pads for the SPDT switches (L_c) and the inductance of the via-hole to ground (L_v). As a result, each coarse-tuning branch is exactly the same and only five distinct resonance frequencies are obtained from the coarse-tuning branches. The corresponding admittances of the tuning network when k coarse-tuning branches are connected to the HMSIW resonator are

$$jY_n^k = \begin{cases} 0 & \text{for } k = 0 \\ -\dfrac{j}{\omega}\left[\dfrac{k}{L_c + L_v}\right] & \text{for } k = 1, \ldots, 4 \end{cases} \tag{3.6}$$

To produce fine tuning frequency states between each coarse tuning state, the TL-inductors in the fine-tuning branches are longer to achieve a higher inductance value. The fine-tuning branches provide TL-inductances of $(L_f + L_{f1})$ and $(L_f + L_{f2})$, respectively. Thus, incremental admittance changes are obtained between each coarse value Y_n^k using various combinations of S_5 and S_6 in open/closed positions, resulting in fine control of the resonance frequency. The overall admittance of the tuning network when k $(k = 0, \ldots, 4)$ coarse-tuning branches are connected is given by

$$jY_n = jY_n^k - S_5 \frac{j}{\omega(L_f + L_{f1})} - S_6 \frac{j}{\omega(L_f + L_{f2})} \tag{3.7}$$

where, $\{S_5, S_6\} \in \{0, 1\}$ are the fine-tuning switches in open ('0') and closed ('1') positions, respectively. From (3.7), the intersection of Y_n/Y_0 with the LHS of (3.4) gives the resonance frequencies of the HMSIW resonator.

d. Implementation

The resonator design methodology is as follows.

1. First, the dimensions of the HMSIW resonator are determined. The length L of the HMSIW resonator is chosen so that it is long enough to accommodate the SPDT switches, inductors and biasing circuitry of the tuning network. Z_0 of the quasi-TEM microstrip line with width L is calculated using Agilent Technologies' Advanced Design System (ADS)[6] LineCalc. The width w of the resonator determines the unloaded resonant frequency of the HMSIW resonator and is designed to be $\lambda_g/4$-long at the unloaded center frequency. The spacing between adjacent vias, b, of the HMSIW must be small enough so that the linear array of vias emulate a short circuit.

2. The via-hole inductance L_v is then estimated using full-wave simulation in Sonnet[7] for a given via diameter and length. To maximize the tuning range, the value of L_v must be minimized by avoiding very small via-diameters and utilizing thin dielectric substrates.

3. Using the layout footprint of the RF MEMS switch [Omron Corp. (2SMES-01)], the minimum possible inductance value of L_c, corresponding to the mounting pads of the switch, is simulated in Sonnet.

4. The fine-tuning TL-inductor values (L_f, L_{f1}, L_{f2}) are optimized using ADS so that equally-spaced resonant frequencies are obtained using various combinations of switches $S_1, \ldots, S_6$. The S-parameters of the RF MEMS SPDT switch

[6]ADS, 2006, Agilent Technologies, Palo Alto, CA.

[7]Sonnet 12.52, Sonnet Software Inc., Syracuse, NY, 2009.

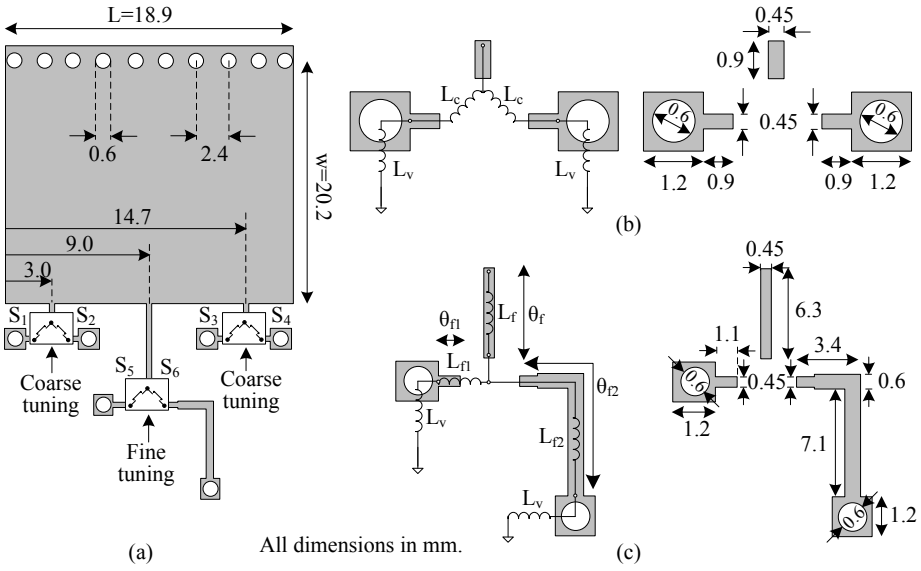

Fig. 51. (a) Layout implementation of a tunable HMSIW resonator and layout details for a pair of (b) coarse-tuning and (c) fine-tuning branches.

in the up- and down-state positions are also included in ADS during design and optimization [Fig. 30(c)].

5. TL-inductors are optimized using Sonnet to achieve the desired values. The HMSIW resonator, TL-inductors, via-holes, mounting pads, and biasing circuitry for the RF MEMS switches are all simulated in Sonnet, and the resonator layout is optimized to meet tuning specifications.

Table VI shows the optimized model element values of the tunable HMSIW resonator designed on Rogers RT/Duroid 6010LM substrate ($\epsilon_r = 10.2$, $h = 0.635$ mm, $\tan\delta = 0.0023$ at 10 GHz). The value of L_v is extracted from full-wave simulation for a via-diameter of 0.6 mm located on a square via-pad with edge-length of 1.2 mm. The total mounting-pad inductance (L_c) at the RF ports of the SPDT MEMS switch is calculated for pad dimensions of 0.9×0.45 mm^2. Fig. 51(a) shows the optimized layout of the tunable resonator. Figs. 51(b) and (c) show the layout of the coarse-

Table VI. ADS Model Element Values ($\epsilon_r = 10.2$, $h = 0.635$ mm, $\tan\delta = 0.0023$ at 10 GHz)

HMSIW Resonator		Tuning Network	
w	20.2 mm	L_c	0.87 nH
L	18.9 mm	L_v	0.24 nH
Z_0	3.7 Ω	L_f	2.95 nH
-	-	L_{f1}	1.20 nH
-	-	L_{f2}	7.25 nH

and fine-tuning branches, respectively. The inductances L_f and L_{f1} are implemented with 55 Ω microstrip lines with electrical lengths $\theta_f = 23°$ and $\theta_{f1} = 4°$, respectively. The inductance L_{f2} is implemented with a 50 Ω microstrip line with electrical length $\theta_{f2} = 40°$.

The allowable coarse- and fine-tuning switch configurations are given in Table VII. Each coarse-tuning state $n, (n = 1, \ldots, 5)$, has $n - 1$ coarse-tuning branches connected to the resonator. For coarse-tuning states $2, \ldots, 4$, the connected coarse-tuning branches are chosen arbitrarily since they are all similar, and hence result in the same resonant frequencies. For each coarse-tuning state, the three combinations of fine-tuning states are possible, and result in 15 different tuning states. The fine-tuning configuration $S_5S_6 = 11$ does not provide a distinct frequency state compared to $S_5S_6 = 10$, and is not utilized.

Fig. 52 shows the resonance frequency variation of the HMSIW resonator versus tuning state. The corresponding coarse- and fine-tuning configurations are indicated by a tuning code 'PQ' where $P \in \{1, \ldots, 5\}$ and $Q \in \{A, B, C\}$. The increasingly negative values of Y_n/Y_0 provided by the switchable inductive-tuning network result in resonator tuning. The tuning frequencies obtained from full-wave simulation and

Table VII. Coarse and Fine Tuning Configurations (0:Open Switch, 1:Closed Switch)

Coarse-Tuning		Fine-Tuning	
Config.	$S_1S_2S_3S_4$	Config.	S_5S_6
1	0000	A	00
2	0100	B	01
3	0101	C	10
4	0111	-	-
5	1111	-	-

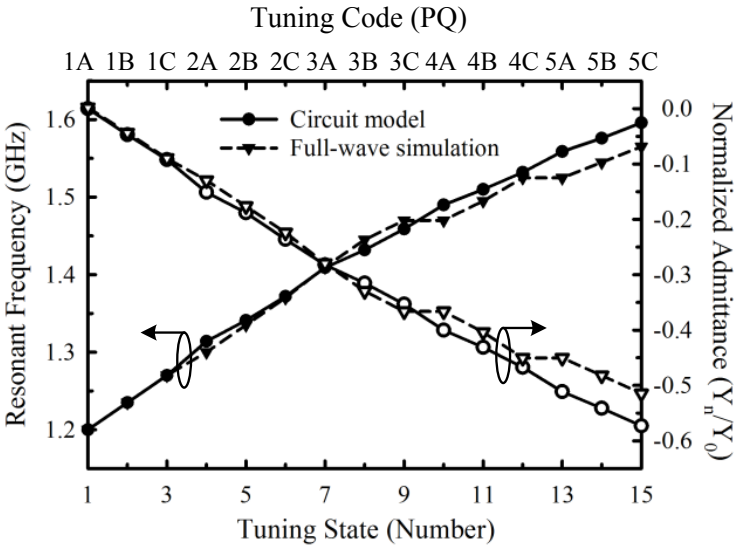

Fig. 52. Variation of resonance frequency and normalized admittance of the tuning network for 15 different tuning states.

the circuit model have slight discrepancies due to parasitic capacitances associated with the tuning network, which was not considered in the circuit model. Since states 9(3C) and 10(4A), and states 12(4C) and 13(5A) have similar resonant frequencies, only 13 distinct tuning frequencies are obtained from the resonator.

2. Filter Design

To implement a tunable two-pole bandpass filter, tunable HMSIW resonators must be coupled appropriately using inverter networks. In this section, the coupling mechanisms and design of input/output and inter-resonator J-inverters are discussed with an emphasis on obtaining constant absolute bandwidth as the filter is tuned.

a. Inter-Resonator Coupling

Fig. 53 shows two tunable HMSIW resonators coupled by a narrow HMSIW section which acts as a J-inverter [56]. The width (w_{12}) and length (L_{12}) of the inverter section determine the mixed coupling coefficient (k_{12}) which is given by [15]

$$k_{12} = \left(\frac{\Delta f}{f_0}\right) \frac{1}{\sqrt{g_1 g_2}} \tag{3.8}$$

where, Δf is the filter bandwidth, f_0 is the filter center frequency, and $g_0, \ldots, g_3$ are Chebyshev low-pass prototype element values.

The narrow HMSIW inverter only supports evanescent waveguide modes because the cutoff frequency of the dominant-mode is much higher than the filter center frequency [63]. As a result, the evanescent-mode HMSIW is equivalent to an inductance, which is directly proportional to the waveguide length (L_{12}), and inversely proportional to the waveguide width (w_{12}), and contributes to the magnetic coupling between resonators [79]. Conversely, the slot with width, $w - w_{12}$, and gap, L_{12}, has stored energy in the capacitance of the fringing electric field and contributes to

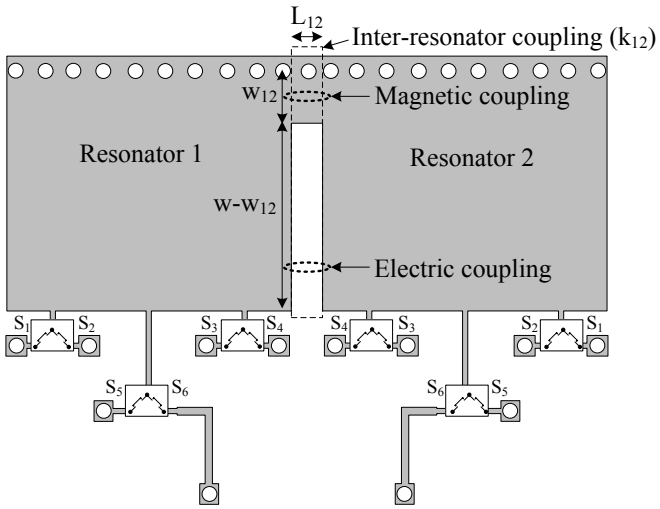

Fig. 53. Implementation of the inter-resonator J-inverter.

electric coupling between resonators. Hence, the amount of magnetic and electric couplings between resonators can be determined by appropriately choosing the dimensions of the inverter. To relate k_{12} to the physical dimensions of the inverter, the resonators are first weakly coupled at the input/output. The simulated frequency responses obtained for different values of w_{12} and L_{12} are shown in Fig. 54(a) and (b), respectively.

For a constant inverter length L_{12}, decreasing the width w_{12} results in lower values of magnetic coupling due to increased inductance between resonators. As a result, the magnetic resonant peak (f_m) moves to lower frequencies as shown in Fig. 54(a). However, the total electric coupling is relatively unaffected, and consequently, the electric resonant peak (f_e) is unchanged. To decrease the amount of electric coupling, L_{12} is increased for a fixed inverter width w_{12}. A larger gap (L_{12}) between resonators implies that lesser energy is stored in the capacitance of the fringing field between the two resonators, and as a result, the resonant peak f_e moves to higher frequencies as shown in Fig. 54(b). However, the increased length of the evanescent

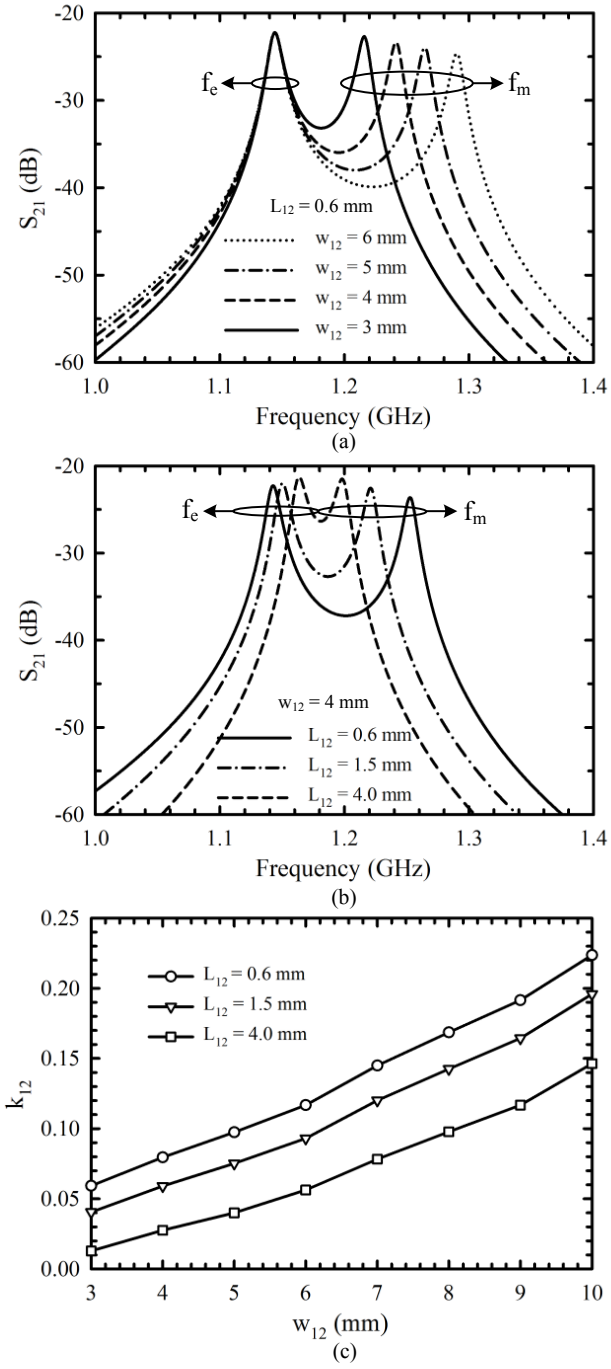

Fig. 54. Simulated electric and magnetic resonance peaks when two HMSIW resonators are weakly-coupled at the input/output for different values of (a) w_{12}, and (b) L_{12}, and (c) variation of coupling coefficient k_{12} for different values of w_{12} and L_{12}.

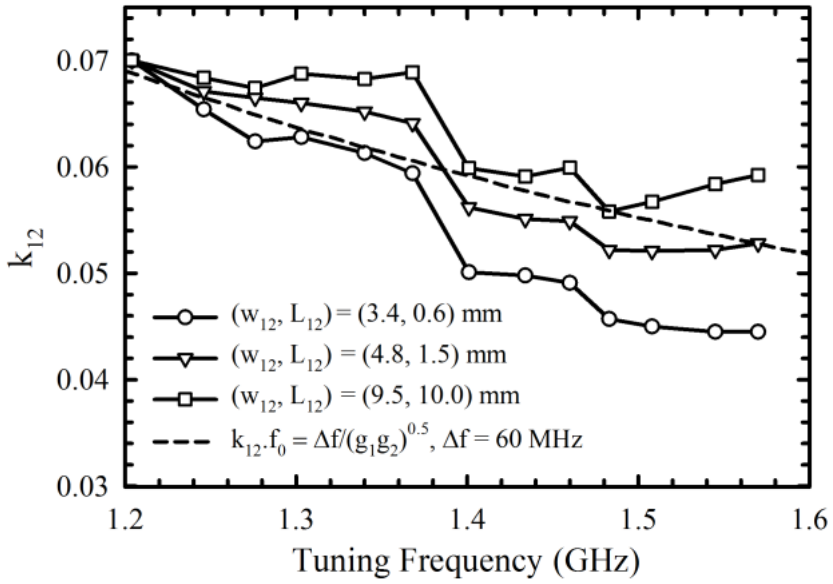

Fig. 55. Variation of k_{12} versus tuning frequency of the resonator for different values of L_{12}. In each case, w_{12} is adjusted to maintain $k_{12} = 0.07$ at the lowest tuning frequency.

HMSIW section results in higher inductance between resonators, and the decreased magnetic coupling causes f_m to move to lower frequencies.

Fig. 54(c) shows the variation of k_{12} with width w_{12} for various inverter lengths L_{12} when the resonator is at its lowest frequency tuning state. k_{12} is calculated directly by finding the resonant peaks (f_e, f_m) in the frequency response as described in [15]. For a given filter bandwidth, various combinations of w_{12} and L_{12} provide the desired value of inter-resonator coupling. However, each combination results in a unique bandwidth-variation characteristic as the filter is tuned.

Fig. 55 shows the variation of k_{12} as the resonators are tuned, for different values of L_{12}. In each case, the width w_{12} is adjusted to provide a coupling coefficient $k_{12} = 0.07$ for state 1, which corresponds to a filter bandwidth of 60 MHz around 1.2 GHz for a passband ripple of 0.1 dB. As the resonator is tuned to higher frequencies,

k_{12} decreases at a faster rate for higher electric coupling and lower magnetic coupling (i.e., L_{12} is lower) in the inverter. Thus, each (w_{12}, L_{12}) combination provides a unique bandwidth-variation characteristic that depends on the value of L_{12}. For example, constant-bandwidth tuning can be obtained if the value of k_{12} varies according to $k_{12}f_0 = \Delta f/\sqrt{g_1 g_2}$ [see (3.8)]. Choosing $w_{12} = 4.8$ mm and $L_{12} = 1.5$ mm approximately provides a constant bandwidth of 60 MHz. Also, the rate of decrease of k_{12} is a relatively weak function of L_{12} when 1.5 mm $< L_{12} <$ 10 mm. The slope of k_{12} strongly depends on L_{12} for $L_{12} <$ 1.5 mm and is critical if the filter is required to have decreasing fractional bandwidth as it is tuned. It is difficult to obtain constant fractional bandwidth tuning with this coupling mechanism which requires k_{12} to be invariant with respect to filter center frequency. This is because the rate of increase in electric coupling versus frequency is always higher than the rate of increase of magnetic coupling. In all cases, the variations in k_{12} around the desired values are due to changes in resonator field distribution induced by the tuning network, and result in slight bandwidth variations as the filter is tuned.

b. External Coupling

Fig. 56 shows the coupling structure at the input/output of the tunable filter, and consists of a microstrip-to-HMSIW transition and an input/output J-inverter. A tapered microstrip line is not used in the transition because the extra length of the tapered section contributes to additional in-band insertion loss and increases the filter size [21]. The discontinuity at the microstrip-HMSIW interface excites higher-order modes that slightly degrade the stopband suppression of the filter. However, as demonstrated later, the stopband suppression is still excellent compared to conventional SIW filters due to the absence of even-order spurious modes. To minimize reflections at the input/output ports, the length L_s is chosen so that the characteristic

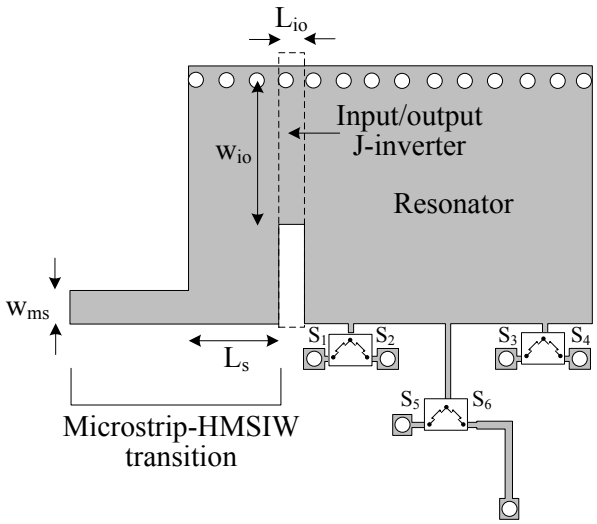

Fig. 56. Implementation of the input/output J-inverter and the microstrip-to-HMSIW transition.

impedance (Z_0) of the HMSIW section is matched to the Z_0 of the microstrip line. The dimensions L_{io} and w_{io} determine the external quality factor (Q_e) of the filter, which is calculated for a given fractional bandwidth ($\Delta f/f_0$) using [15]

$$Q_e = \frac{g_0 g_1}{\Delta f/f_0}. \tag{3.9}$$

The coupling mechanism of the input/output inverter also involves electric and magnetic couplings, as discussed in Section C.2.a of this chapter, and can be controlled by choosing the inverter dimensions appropriately.

To relate Q_e to the physical dimensions of the input/output J-inverter, Q_e is extracted from simulations of a singly-loaded resonator as described in [15]. Fig. 57(a) shows the variation of Q_e as a function of w_{io} and L_{io} when $L_s = w_{ms} =$ 2.4 mm. As w_{io} increases, the external quality factor decreases implying that more energy is coupled into the resonator from the input/output. The increased coupling is a consequence of higher magnetic coupling due to lower inductance of the wide evanescent HMSIW inverter. For larger values of L_{io}, the energy coupled into the

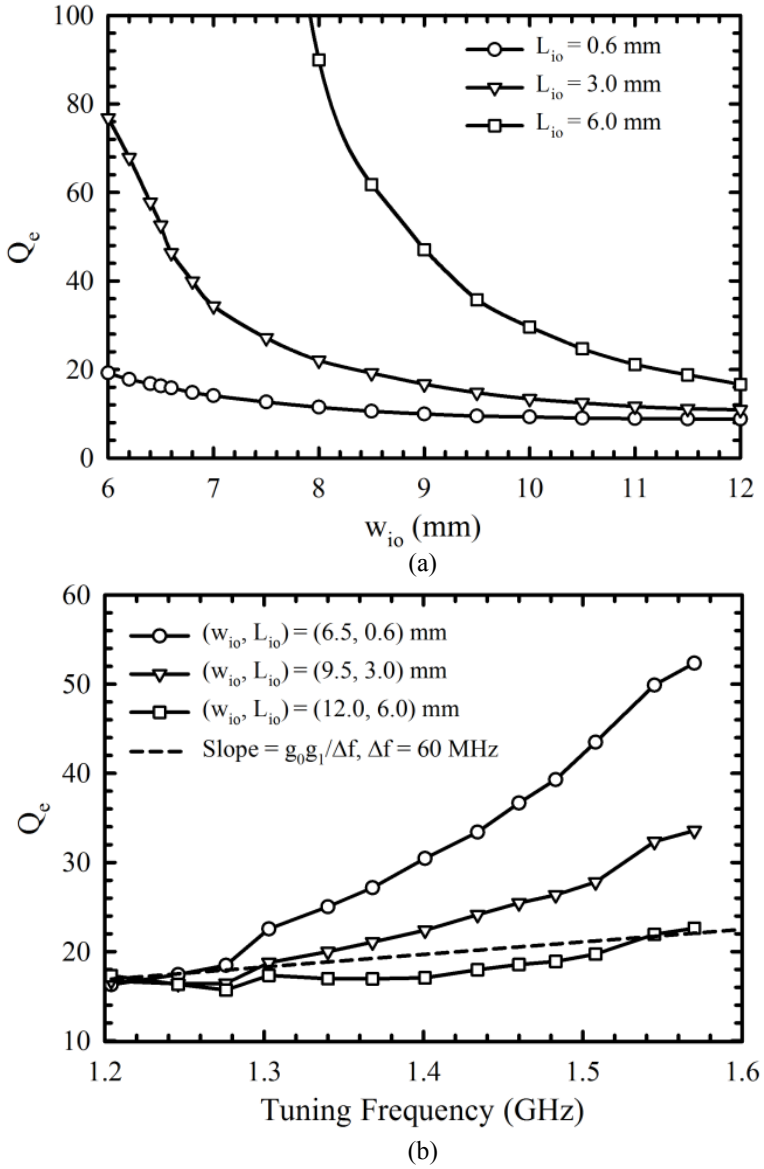

Fig. 57. (a) Variation of Q_e as a function of w_{io} and L_{io}, and (b) variation of Q_e versus tuning frequency of the resonator. In each case, w_{io} is adjusted to have $Q_e = 16.8$ at the lowest tuning frequency.

resonator decreases due to lower electric and magnetic coupling. As a result, the Q_e values are higher.

Although several combinations of w_{io} and L_{io} give a particular value of Q_e, the right choice of parameters for constant absolute bandwidth tuning is that which causes Q_e to be directly proportional to f_0, with a proportionality constant $g_0 g_1/\Delta f$ [see (3.9)]. Fig. 57(b) shows the variation of Q_e with tuning state for different L_{io} values. The value of w_{io} for each case is adjusted to have $Q_e = 16.8$ at 1.2 GHz, which corresponds to $\Delta f = 60$ MHz for a passband ripple of 0.1 dB. Choosing $(w_{io}, L_{io}) = (12, 6)$ mm provides the required slope for the variation of Q_e versus f_0. Since the variation of Q_e versus frequency strongly depends on L_{io}, it is critical to choose L_{io} correctly to obtain the required bandwidth characteristics and maintain good return loss over the tuning range. As the filter is tuned, slight bandwidth variations arise as a result of deviations of Q_e from the ideal values due to the influence of the tuning network on the resonator.

c. Complete Filter Simulation

The entire tunable filter is simulated using Sonnet by employing the up- and down-state parameters of the SPDT RF MEMS switches. The routing of bias lines to the RF MEMS switches is also included in full-wave simulation and is optimized so that the overall filter area is minimized. The filter is then fine tuned to achieve symmetric tuning states with maximum return loss over the entire tuning range. The simulated insertion loss and return loss for the tunable HMSIW filter are shown in Figs. 58(a) and (b).

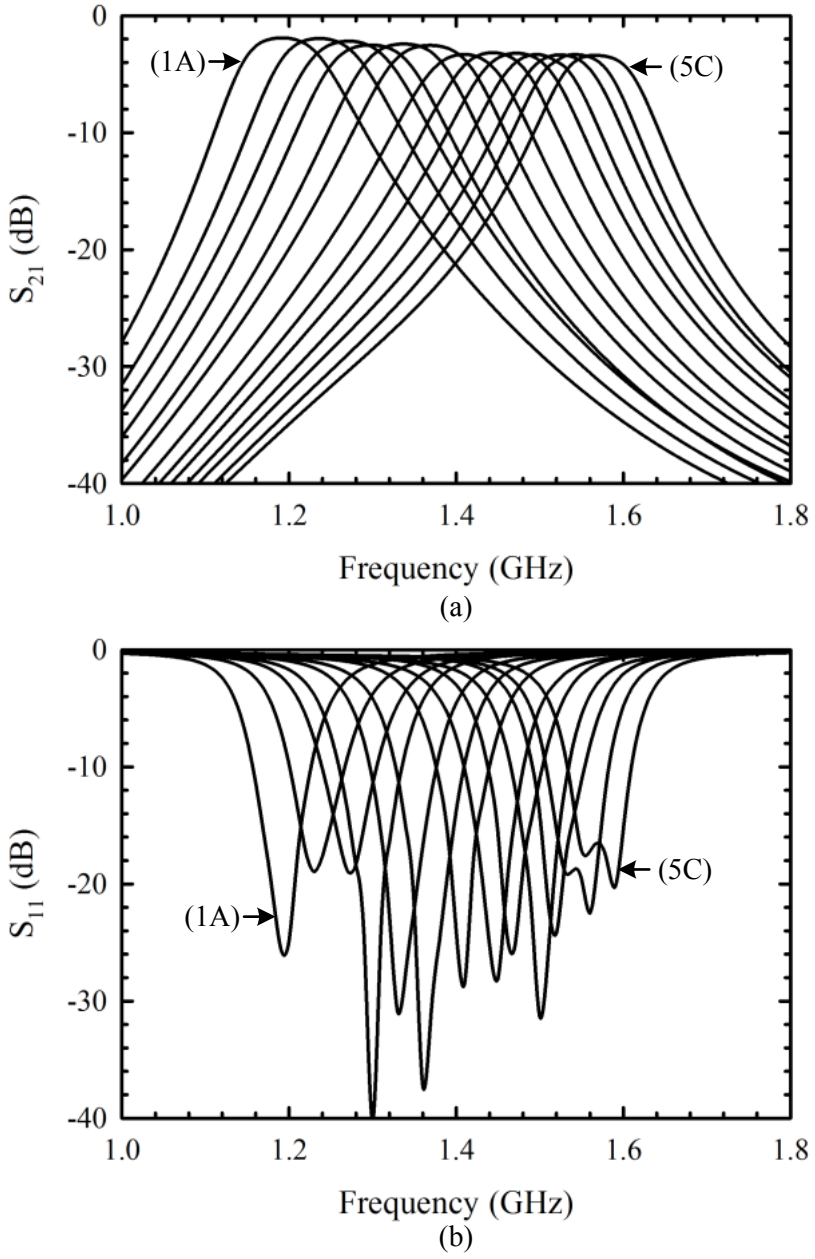

Fig. 58. Simulated: (a) insertion loss and (b) return loss of the two-pole 1.2—1.6 GHz tunable HMSIW filter.

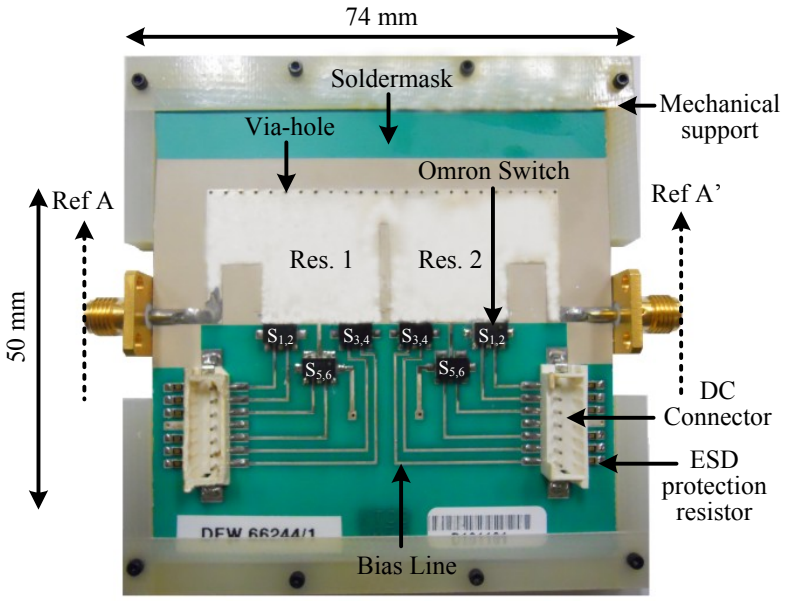

Fig. 59. Fabricated 1.2—1.6 GHz HMSIW RF MEMS tunable filter.

3. Fabrication and Measurement

The photograph of the fabricated HMSIW RF MEMS tunable filter is shown in Fig. 59. The filter is fabricated using a 0.635 mm thick Rogers RT/Duroid 6010LM substrate ($\epsilon_r = 10.2$ and $\tan\delta = 0.0023$). Metal patterns are etched onto the substrate using standard printed circuit board technology. Plated via-holes with 0.6 mm diameter are drilled through the substrate at appropriate locations in the HMSIW filter and tuning networks. Packaged RF MEMS switches (2SMES-01) from Omron Corp. are soldered onto the mounting pads using automated pick-and-place reflow soldering. The board is mounted on a 187 mil thick FR4-G10 Garolite sheet[8] for mechanical support, to prevent board deformation during pick-and-place assembly. The support structure does not affect filter performance because the Garolite sheet is located below the ground plane of the tunable filter. A 1 MΩ resistor is connected between each

[8]Available online: http://www.jjorly.com

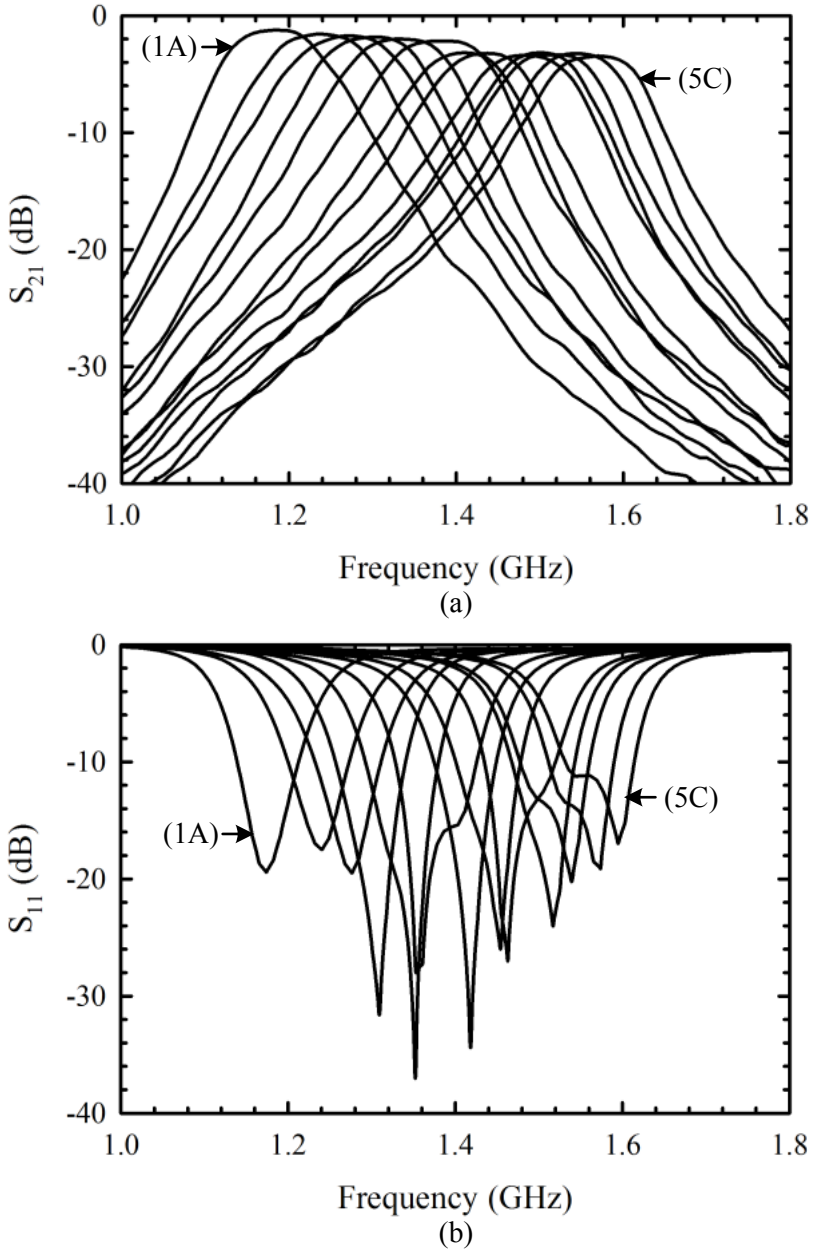

Fig. 60. Measured: (a) insertion loss and (b) return loss of the two-pole 1.2—1.6 GHz tunable HMSIW filter.

bias line and DC ground, to provide a discharge path for accumulated charge in each MEMS switch [80].

The fabricated filter is measured using an Agilent N5230A vector network analyzer after calibration with the short-open-load-thru (SOLT) technique till the reference planes indicated by A, A'. The measured insertion and return losses of the tunable HMSIW filter for 13 different states are shown in Figs. 60(a) and (b), respectively. Insertion loss measurement includes the losses of the SMA connectors at the filter input/output which is negligible (<0.1 dB) at around 1-2 GHz. The measured return loss is better than 11 dB at both ports, for all tuning states.

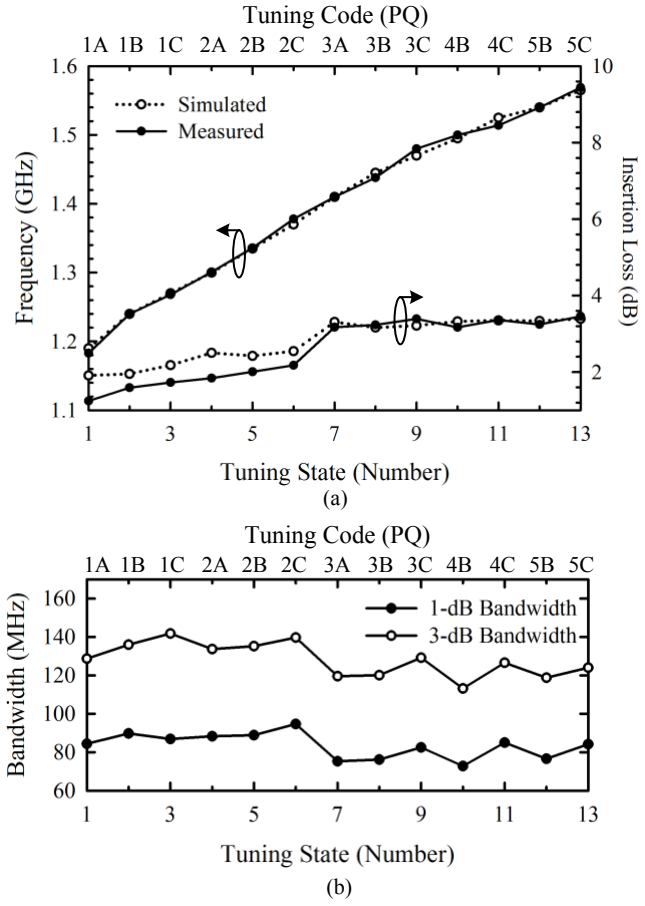

Fig. 61. (a) Simulated/measured center frequency and insertion loss, and (b) measured absolute 1-dB and 3-dB bandwidth of the filter.

Fig. 61(a) shows the simulated/measured center frequency and insertion loss for each filter response, and are in good agreement. The center frequency variation of 1.2–1.6 GHz is equivalent to 28% tuning range with respect to 1.4 GHz. The measured insertion loss varies between 1.2–3.4 dB with lowest and highest loss when all switches are in the up- and down-state positions, respectively. The resistance of the RF MEMS switches in the down-state position decreases resonator unloaded quality factor (Q_u), while the fractional bandwidth decreases for higher tuning states (constant absolute bandwidth), and hence results in higher insertion losses.

Fig. 61(b) shows the simulated and measured absolute 1-dB and 3-dB bandwidths which vary between 85±10 MHz and 127±14 MHz, respectively. The bandwidth variations are due to changes in k_{12} and Q_e as the filter is tuned. Fig. 62 compares the measured and simulated insertion and return losses for three arbitrary states at 1.2 (State 1), 1.4 (State 7) and 1.6 GHz (State 13), and are in good agreement.

Fig. 63 shows that the measured resonator Q_u varies between 75–140 for 13 different tuning states. Q_u is highest when all switches are in the up-state position and is comparable to the Q_u values of the tunable SIW resonator presented in Section B of this chapter, proving that HMSIW resonators have the same low-loss properties associated with conventional SIW resonators. As the filter is tuned to higher frequencies, the down-state resistance of the RF MEMS switches decreases the resonator Q_u. For states 10–13, the fields within the HMSIW resonator are highly perturbed due to most switches being in the down-state position, and hence the variation of Q_u no longer follows a simple decreasing trend. The value of Q_u at the highest tuning state for the HMSIW resonator is lower than the Q_u value at the highest tuning state of the SIW resonator in Section B of this chapter because the tuning network in the HMSIW resonator is located in the region of highest electric field where resistive losses have

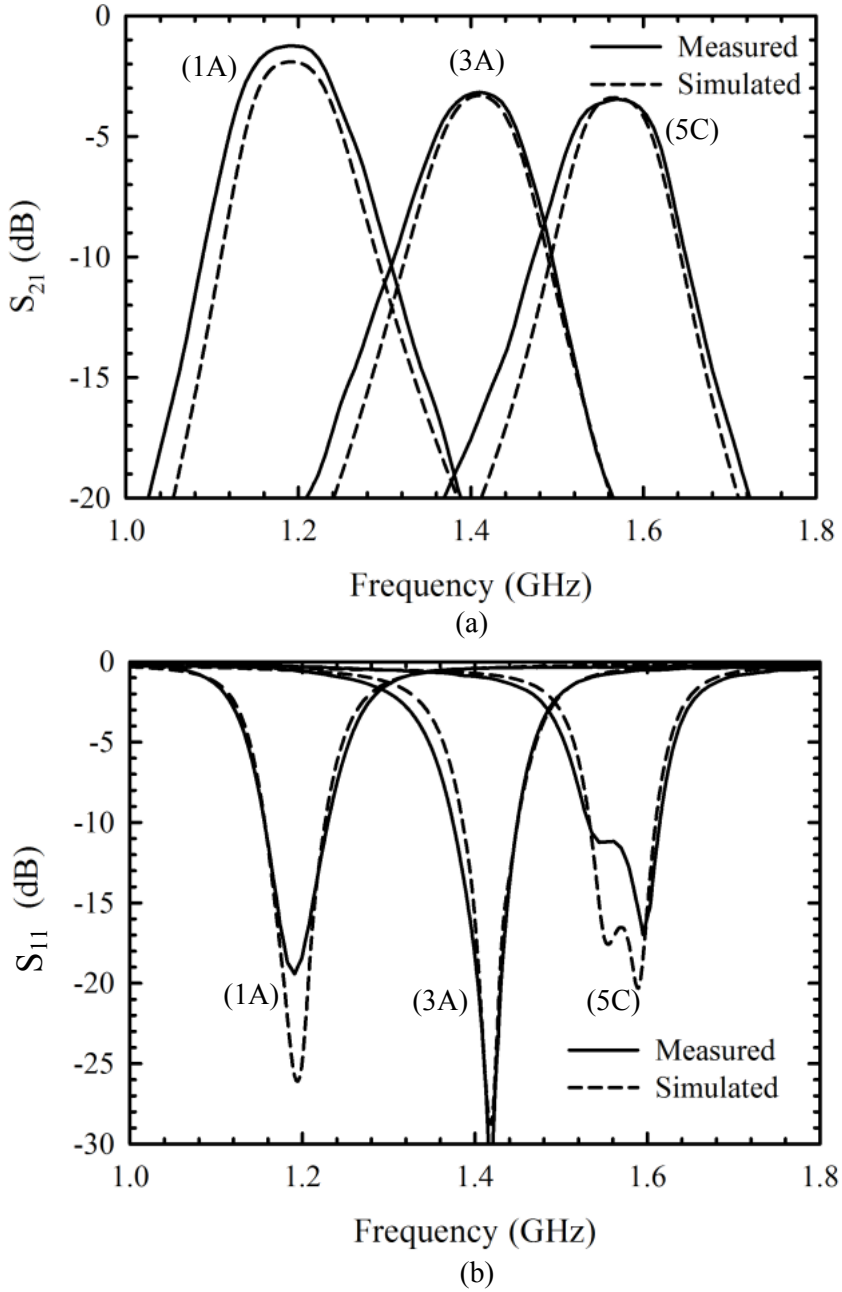

Fig. 62. Comparison between measured and simulated (a) insertion loss and (b) return loss, for three arbitrary states at 1.2 (State 1), 1.4 (State 7), and 1.6 GHz (State 13).

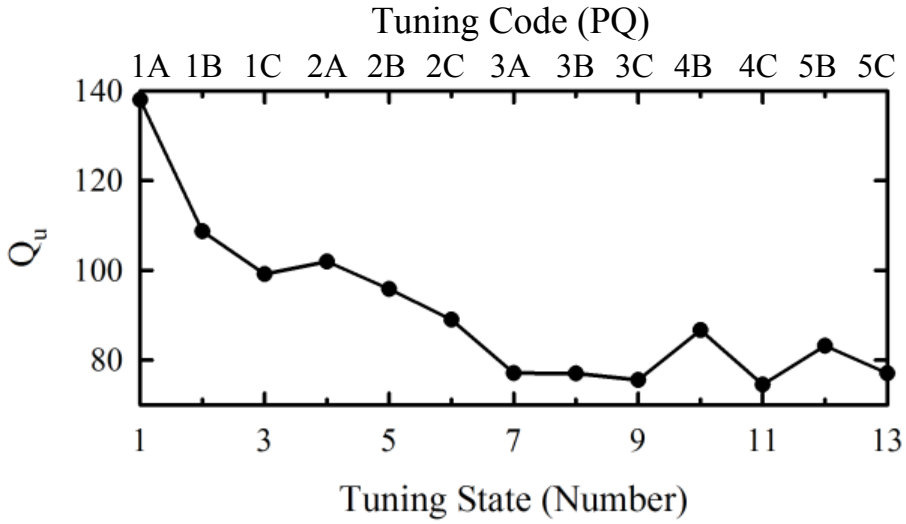

Fig. 63. Measured resonator unloaded quality factor (Q_u).

the greatest impact on Q_u degradation.

Fig. 64 shows the measured wideband response of the tunable filter for all tuning states, and shows that a stopband rejection of greater than 20 dB is obtained from 1.7–2.2 GHz due to the absence of even-order resonant modes in the HMSIW resonator. In comparison, SIW filters with iris coupling between resonators exhibit poor stopband performance due to spurious resonances in close proximity to the filter passband [81]. To obtain better stopband rejection in SIW filters, dual-mode SIW cavities are utilized to introduce transmission zeros in the upper passband. This was achieved using asymmetric cavity feeds in Section B of this chapter and using over-sized cavities in [21]. On the contrary, HMSIW tunable filters inherently exhibit excellent stopband performance without employing any additional techniques. The stopband frequency range can be easily extended by using dissimilar elliptic low-pass filters at the filter input/output as demonstrated in Section B of this chapter.

The third-order intermodulation components (IM_3) of the HMSIW tunable filter was measured using a setup similar to the one shown in [74] at separation frequencies

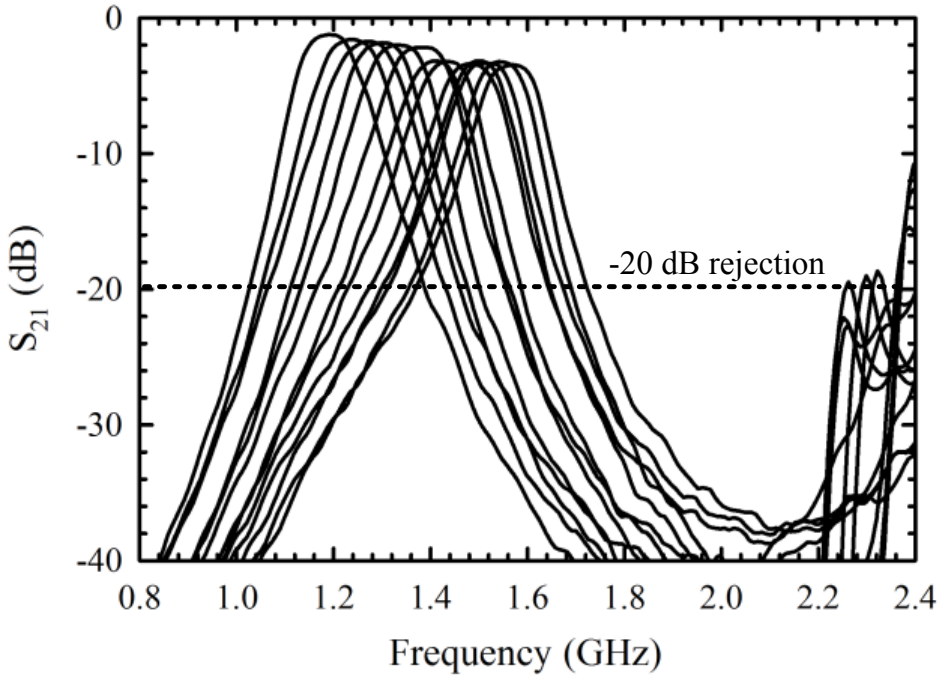

Fig. 64. Measured wideband response of the tunable HMSIW filter.

of 10 kHz, 100 kHz and 1 MHz, for all tuning states. Due to the extremely linear behavior of the RF MEMS switches, the IM_3 level was always below the noise level of the Agilent E4446A spectrum analyzer as long as the RF mixer of the spectrum analyzer was not saturated by the input signal (a maximum power of 15 dBm was used). As a result, it was impossible to measure the IIP_3 of the tunable filters for any tuning state and is concluded that the IIP_3 of the RF MEMS tunable filters is >65 dBm. These results are in agreement with those reported in Sec. B since IIP_3 of metal-contact MEMS switches due to nonlinear resistance variations is calculated to be around +80 dBm [75].

4. Conclusion

This study has demonstrated a compact HMSIW RF MEMS tunable filter with a tuning range of 1.2—1.6 GHz employing packaged RF MEMS switches. The design and

implementation of the proposed filter is simple because of the existence of equivalent circuit models and single-layer board fabrication. The filter area is reduced by 2.5 times compared to the conventional tunable SIW filter while still having a measured resonator Q_u of 75–140. Absence of even-order resonant modes greatly improves the stopband performance of the filter. Successful implementation of this filter proves that off-the-shelf RF MEMS switches are a viable alternative for tunable filters with low-loss, wide-tuning and very high linearity.

CHAPTER IV

NONLINEARITY AND NOISE ANALYSIS OF ALL-POLE RF MEMS TUNABLE FILTERS*

A. Introduction

Microwave bandpass filters are essential components in modern wireless communication systems as band-select filters. Typically, band-select filters appear between the antenna and the low-noise amplifier (LNA) in a receiver system. Intrinsic noise mechanisms in bandpass filters can severely degrade the receiver signal-to-noise ratio (SNR) since there is no signal amplification before the LNA.

In recent years, microelectromechanical systems (MEMS) have been used to develop a variety of devices such as accelerometers, detectors, switches and tunable lasers. However, as the dimensions of the mechanical structures become increasingly small, noise sources that are negligible in the macroscopic scale become significant and potentially limit the resolution of micro-devices. With the advent of multi-band, multi-standard wireless communication systems [11], RF MEMS tunable microwave filters are becoming increasingly important in RF front-end systems. RF MEMS switches have low loss, outstanding linearity ($IIP_3 >$ 40-50 dBm) and do not require

---

any DC current, and hence offer a very low power solution for tuning applications [33]. However, RF MEMS switches are prone to thermal-mechanical noise due to Brownian motion which results in noise at the output of the switch [43]. Since RF MEMS switches exhibit nonlinear behavior at high input power, switch noise is a nonlinear function of input power which is not considered in the small-signal analysis presented in [43].

In this chapter, simulation-based methods and theoretical approaches to calculate nonlinear noise in RF MEMS tunable filters due to Brownian motion in the RF MEMS switches are presented. First, computer-aided design (CAD) techniques to calculate nonlinear noise are introduced. The effect of filter nonlinearity is included during noise simulation using the harmonic balance method. To analytically find the effect of filter nonlinearity, a generalized iterative approach is presented to find the peak internal voltages in nonlinear microwave filters. Two independent theoretical approaches based on pole perturbation and admittance variation, respectively, are presented. The noise values estimated using the CAD-based and analytical methods are compared with each other as a function of filter input power, tuning state, fractional bandwidth, filter order and frequency offset. The effects of nonidealities arising from practical realizations of filter components on filter phase noise are also considered. Finally, it is shown that filter phase noise is most significant in MEMS tunable filters with low bandwidth, high order and high quality factor.

B. Nonlinear Noise Analysis of RF MEMS Tunable Filters Using Harmonic Balance Simulation*

1. Brownian Motion Noise

Random fluctuations in temperature and molecular agitation (Brownian motion) in microstructures result in a thermal-mechanical noise that limits the performance of micro-systems. A mechanical structure with a spring constant k, a damping factor b, and a mechanical self-resonant frequency ω_m has a thermally induced mechanical force acting on the bridge whose power spectral density (PSD) is $f_n = \sqrt{4k_bTb}$, where k_b is the Boltzmann constant and T is the temperature in Kelvin. Thus, the PSD of Brownian motion is expressed as [82],

$$x_n = \frac{f_n/k}{1 + \left(\frac{j\omega'}{Q_m\omega_m}\right) - \left(\frac{\omega'}{\omega_m}\right)^2} \tag{4.1}$$

where ω' is the mechanical offset frequency and $Q_m = k/\omega_m b$ is the mechanical quality factor. In the absence of an RF signal, a sinusoidal component of Brownian noise in a 1-Hz bandwidth around $\omega'/2\pi$ is expressed as [43]

$$x_n(t) = \sqrt{2\overline{x_n^2}(\omega')}\sin(\omega' t) \tag{4.2}$$

where $\overline{x_n^2}(\omega') = 4k_BTb/k^2$ at low mechanical offset frequencies ($\omega' < \omega_m$). The random displacements in bridge height results in a change in the up-state capacitance of the MEMS switch given by [43],

$$C_{up}(t) = C_{MEMS,up}\left(1 - \frac{1}{1+\gamma}\frac{x_n(t)}{g_0}\right) \tag{4.3}$$

where g_0 is the initial bridge height, $C_{MEMS,up}$ is the up-state capacitance when Brownian noise not present and γ is the fringing factor. When this randomly varying

capacitance forms a part of the filter structure, the amplitude and phase of the signal at the filter output also show random variation and result in amplitude and phase noise, respectively.

2. RF MEMS Tunable Filter

Fig. 65(a) shows the equivalent circuit model of a two-pole Chebyshev filter with a tunable center frequency from 1.8-2.22 GHz [13]. The resonator inductance is chosen as $L_r = 2.48$ nH. The input/output J-inverters are realized with capacitors C_M, and the resonators are inductively coupled with a coupling coefficient k_r. The filter is tuned by changing the value of the resonator capacitance C_R while keeping the inverter values fixed. C_R is implemented as a three-bit RF MEMS switched capacitor where each RF MEMS switched capacitor is a series combination of a fixed capacitor and an RF MEMS switch as shown in Fig. 65(b). The nonlinear electromechanical model of the RF MEMS switch is shown in Fig. 65(c) [44]. This model is composed of: (A) an electrostatic force generation due to the RF voltage across the switch, (B) a white noise source describing Brownian motion in the membrane, (C) a low-pass filtering effect of the mechanical bridge and (D) a variable parallel-plate capacitor.

A series of filters are designed for different bandwidths by recalculating C_M and k_r using the design formulas in [54]. The resonator capacitance, C_F, is also adjusted for each bandwidth to maintain similar filter center frequencies as the filter is tuned. Table VIII shows the calculated element values for filters with different bandwidths. Fig. 66 shows the simulated S-parameters for fractional bandwidths of 0.5% and 5% obtained by using the values of C_M, k_r and C_F from Table VIII for 0.5% and 5% bandwidths, respectively. The center frequency of the filter is tuned by controlling the switches S_1, S_2 and S_3 in the switched capacitor bank in Fig. 65(b). The center frequencies obtained for different combinations of switches ($S_1S_2S_3$)

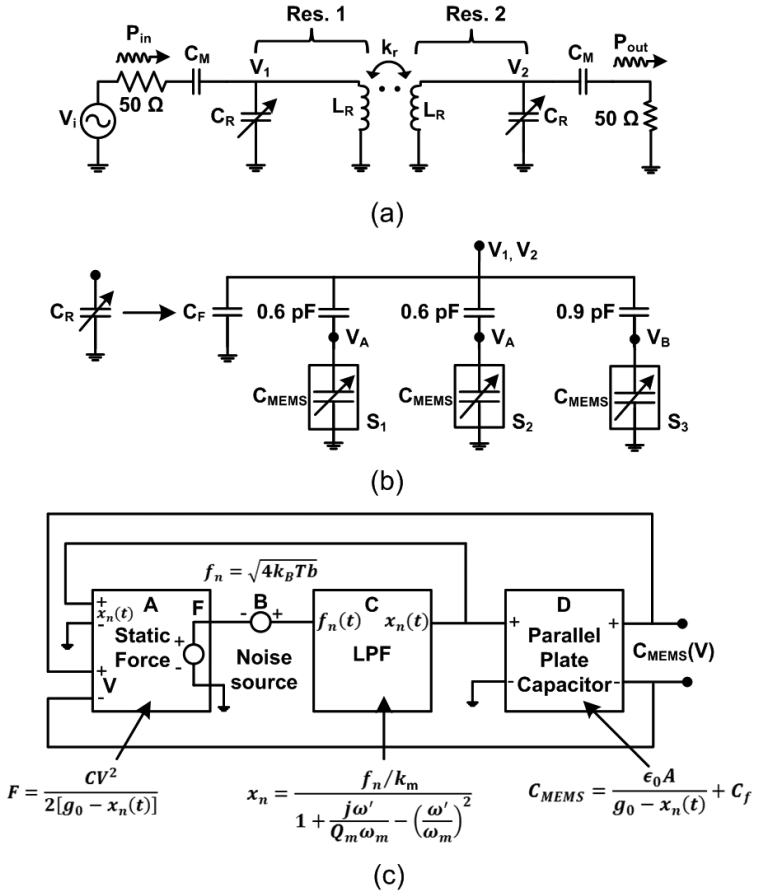

Fig. 65. (a) A two-pole tunable bandpass filter, (b) three-bit RF MEMS switched capacitor bank and (c) nonlinear electromechanical model of the RF MEMS switch.

Table VIII. Filter Parameters for Different Filter Bandwidths

BW (%)	0.5	0.8	1	3	5	8	10
C_M (pF)	0.16	0.20	0.23	0.42	0.54	0.70	0.80
k_r	0.007	0.011	0.013	0.040	0.070	0.110	0.138
C_F (pF)	1.62	1.58	1.56	1.40	1.30	1.19	1.13

Table IX. Physical Dimensions and Electromechanical Parameters of the RF MEMS Capacitive Switch

Parameter	**Value**	**Parameter**	**Value**
Bridge length, L (μm)	280	Pull-down voltage, V_p (V)	26
Bridge width, w (μm)	130	Switch inductance, L_s (pH)	10
Air gap, g_0 (μm)	2	Switch resistance, R_s (Ω)	0.6
Bridge thickness, t (μm)	0.8	$C_{MEMS,up}$ (pF)	0.11
Spring constant, k (N/m)	52	$C_{MEMS,down}$ (pF)	3.5
Electrode width, W (μm)	160	Mech. Res. Freq. f_m (kHz)	76
Dielectric thickness, t_d (μm)	0.2	Mech. Q factor Q_m	1
-	-	Fringing factor γ	0.2

are: $f_0 = 1.8(011, 101), 1.88(110), 1.95(001), 2.02(010, 100), 2.22(000)$ GHz, where '0' represents a switch in the up-state position and '1' represents a switch in the down-state position. The simulated return loss for all filters is better than 12 dB. Assuming that the inductor has a quality factor $Q = 200$ ($R = 0.15\ \Omega$) at $f_0 = 1.95$ GHz, the insertion loss increases for low fractional bandwidths and varies as 0.5 dB, 1.6 dB and 8.7 dB for 10%, 3% and 0.5% bandwidths, respectively. The electrical and physical parameters of the MEMS switch developed by the University of Michigan are shown in Table IX [33], [13], [83].

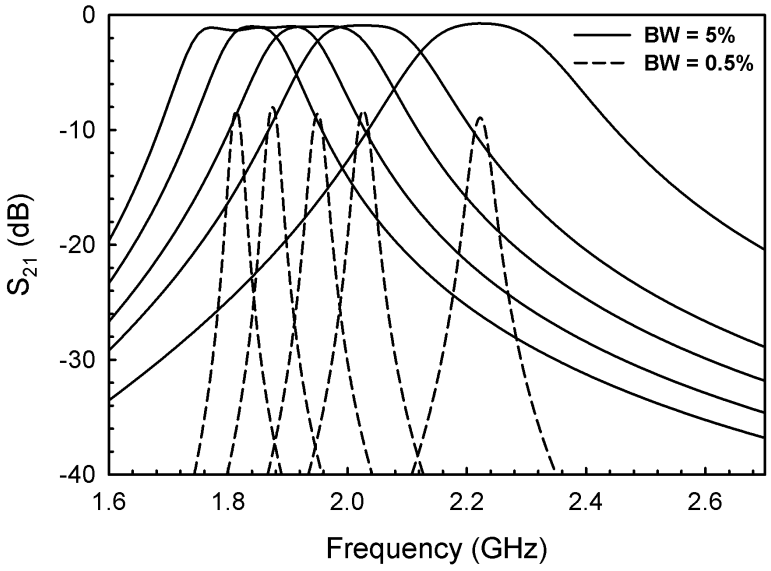

Fig. 66. Simulated S_{21} of the tunable filter for fractional bandwidths of 0.5% and 5% for $Q = 200$.

3. Power Handling versus Bandwidth

Since the electrostatic force on the MEMS bridge has a square-law dependence on the voltage across the switch, the power-handling capability of the tunable filter shown in Fig. 65(a) is determined by the voltage across each switch S_1, S_2 and S_3 (V_A, V_B) in Fig. 65(b). For any given resonator node voltage (V_1, V_2), $V_B > V_A$ due to the capacitive divider. The power-handling capability of the filter is defined as the value of input power for which $V_{B,rms} < V_P$, where V_P is the pull-down voltage of the MEMS switch. For $V_{B,rms} \geq V_P$, at least one switch in the filter structure is in the down-state, resulting in a change in center frequency [33], [13].

To examine the effect of input power on the voltage across each switch in the tunable filter, the nonlinear switch model in Fig. 65(c) is constructed in ADS and the tunable filter shown in Fig. 65(a) is simulated using harmonic balance analysis in ADS. Figs. 67(a) and (b) show the variation of rms-voltage at V_B for different input

powers (P_{in}) for the filter with 0.5% and 10% bandwidths, respectively. The rms-voltage across the switch S_3 in resonator 2 is reduced compared to the switch S_3 in resonator 1 due to the inter-resonator inductive inverter. Increasing the input power beyond 22 dBm (0.16 W) for the 0.5% filter, and beyond 33 dBm (2 W) for the 10% filter causes the rms-voltage across the switch S_3 to exceed pull-down voltage and hence determines the power handling capability of the tunable filter. The variation of voltage with frequency is asymmetric with respect to the filter center frequency for the filter with 0.5% bandwidth because an increase in input power causes a reduction in bridge height and a corresponding increase in resonator capacitance. Since the rms-voltage across the switch is different in each resonator (due to the inverter), each resonator tunes to a different frequency resulting in distortion of the filter response. For a 10% filter, the shift in resonator center frequency is negligible compared to the filter bandwidth and hence this effect becomes insignificant. Fig. 68 shows the power-handling capability of the filter for different fractional bandwidths. Since the ratio of the voltage at any resonator node to the input voltage (V_1/V_i,V_2/V_i) is inversely proportional to the square root of the fractional bandwidth of the filter for a given center frequency [84], there is a linear relationship between the maximum allowable input power to the filter and its fractional bandwidth. To evaluate the dependency of the phase noise of the tunable filter to the input power, the input power must be chosen such that the filter does not enter breakdown region for a given fractional bandwidth.

4. Phase Noise

A thermally-induced displacement noise in a 1-Hz bandwidth around a mechanical frequency ω' ($\omega' < \omega_m$) results in a MEMS switch capacitance variation given by $C_{up}(t)$ in (4.3). For the filter shown in Fig. 65(a), this corresponds to an overall

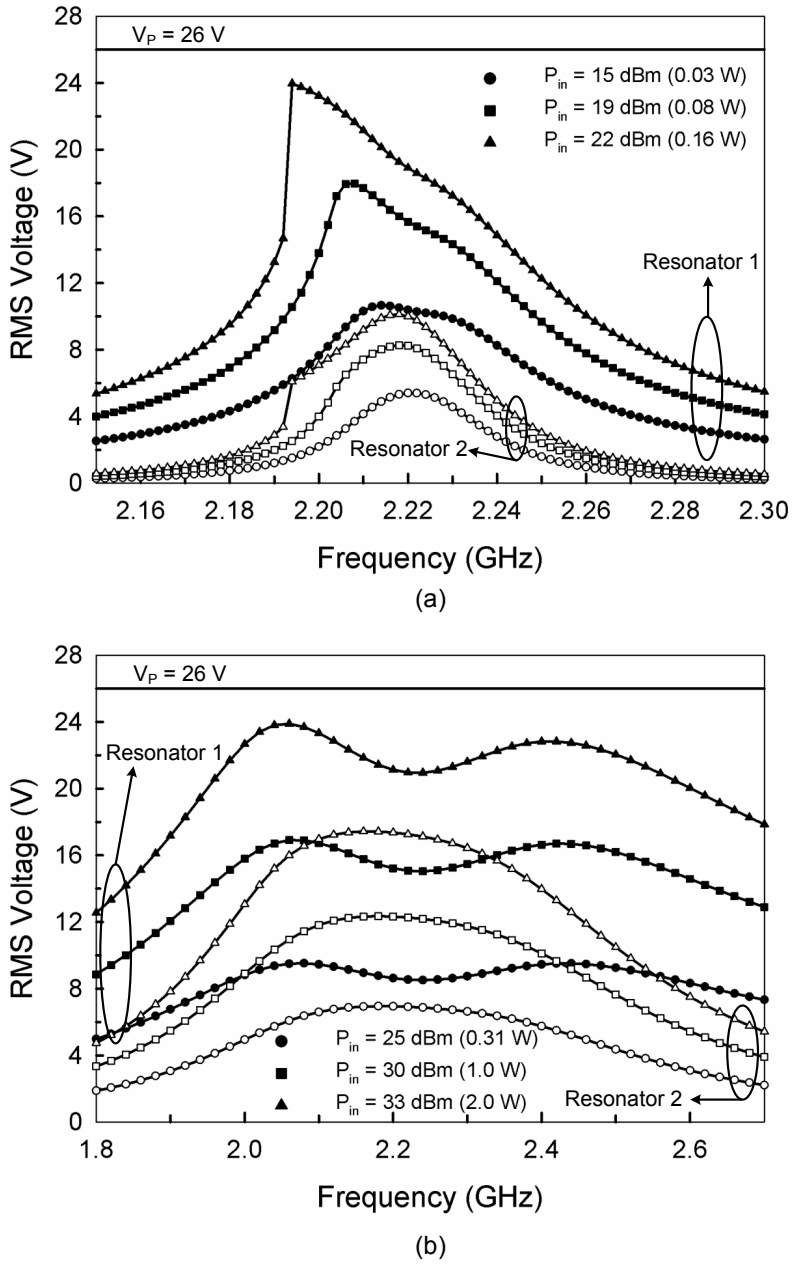

Fig. 67. Variation of RMS voltage across the switch with frequency for different values of input power in a tunable filter of (a) 0.5% fractional bandwidth and (b) 10% fractional bandwidth.

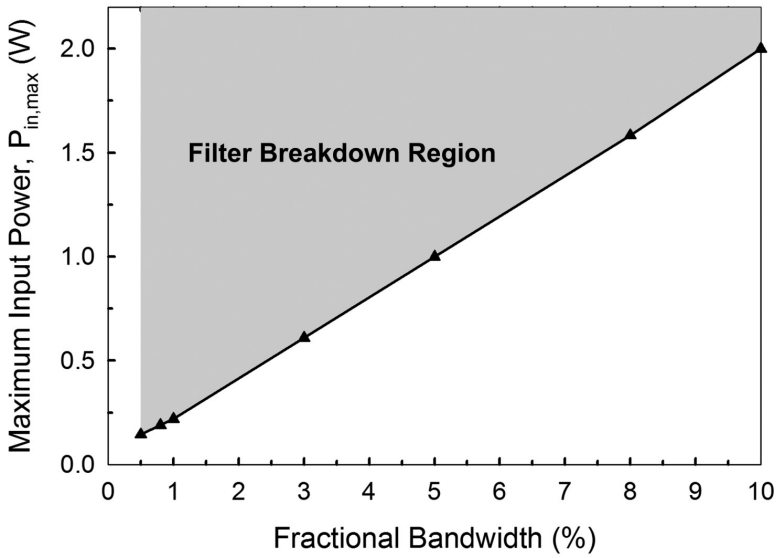

Fig. 68. Variation of RMS voltage across the switch with frequency for different values of input power in a tunable filter of (a) 0.5% fractional bandwidth and (b) 10% fractional bandwidth.

variation in the resonator capacitance $C_R(t)$ which causes a variation in the resonator center frequency given by $\omega_{res}(t) = 1/\sqrt{L_R C_R(t)}$. The resonator susceptance slope associated with a parallel LC resonator also varies as $b_{res} = \omega_{res} C_R(t) = \sqrt{C_R(t)/L_R}$. Equivalently, there is a variation in the amplitude, $|S_{21}(j\omega, t)|$, and phase, $\angle S_{21}(j\omega, t)$ of a filter with a transfer function of $S_{21}(j\omega)$. If the filter is excited by the RF carrier signal, $A_0 \cos(\omega_0 t)$, where ω_0 is the filter center frequency, the resulting output signal is,

$$V_0(t) = A_0 |S_{21}(j\omega, t)| \cos(\omega_0 t + \angle S_{21}(j\omega, t)) \tag{4.4}$$

The filter output signal contains two sidebands $\omega_0 \pm \omega'$ in the frequency domain which is the result of a low frequency sinusoidal signal of frequency ω' modulating a high frequency carrier signal of frequency ω_0. Since $\omega' << \omega_0$, any shift in center frequency by $\omega_0 \pm \omega'$ will still be in the passband of the signal. The bandwidth of a 0.5% filter centered on 2.223 GHz is 11.1 MHz which is still much greater than

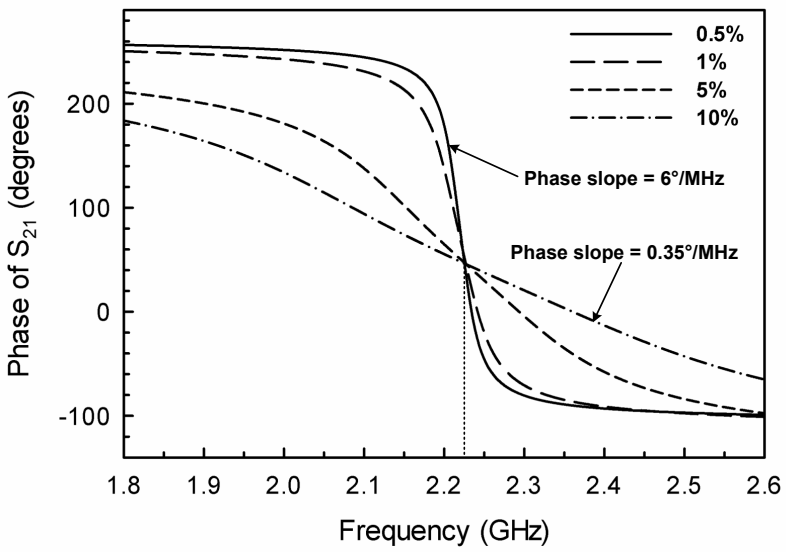

Fig. 69. Phase of S_{21} versus frequency for the two-pole filter shown in Fig. 65(a) for different fractional bandwidths.

mechanical frequency, f_m, in the kHz range. Thus, the change in the amplitude of the transfer function, $|S_{21}(j\omega, t)|$ is negligible and can be assumed constant in noise analysis. The single side-band power relative to the carrier power is the additional phase noise at the output of the filter due to variations in the MEMS bridge.

Phase noise generation in a tunable filter is the result of the change in susceptance slope of the resonator, or equivalently, the slope of phase response around the filter center frequency, for a given fractional bandwidth. The phase responses for the two-pole filter shown in Fig. 65(a) for different fractional bandwidths are shown in Fig. 69. The slope of phase around $f_0 = 2.223$ GHz for filters with 10% and 0.5% bandwidths varies from 0.35°/MHz to 6°/MHz. Since filters with smaller fractional bandwidths have greater phase slope versus frequency [15], any small frequency shift around the center frequency ($\omega_0 \pm \omega'$) results in a large deviation of phase. Thus, filters with smaller bandwidths exhibit higher phase noise.

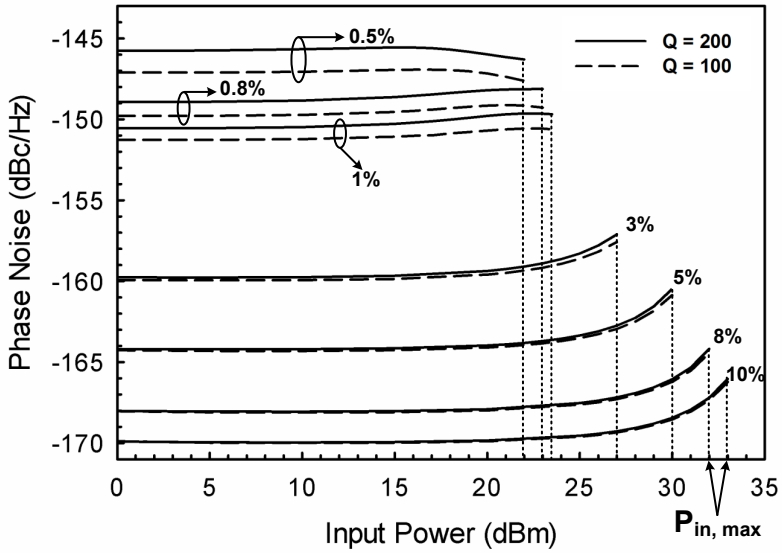

Fig. 70. Variation of phase noise with input power and bandwidth, for unloaded quality factor Q=100 and 200. Phase noise values are evaluated at $P_{in} < P_{in,max}$ with all switches in the up-state position and $\omega' = 2\pi \times 13$ kHz ($\omega' < \omega_m$).

Phase noise at the output of the filter shown in Fig. 65(a) due to noisy capacitors is evaluated using harmonic balance noise analysis in ADS. Fig. 70 shows the variation of phase noise with input power for different bandwidths at $\omega' = 2\pi \times 13$ kHz ($\omega' < \omega_m$), with all switches in the up-state position. The mechanical offset frequency ω' is arbitrarily chosen such that it is below the mechanical self-resonant frequency ω_m. Any mechanical offset frequency can be chosen and results are independent of ω' as long as $\omega' < \omega_m$. The maximum input power ($P_{in,max}$) for a given fractional bandwidth is determined by Fig. 68. Filters with lower unloaded quality factor (Q) show lower phase noise at the output. The increased loss associated with lower Q results in attenuation of phase noise power at the filter output relative to the input carrier power. This effect is significant in filters with smaller fractional bandwidths.

For filters with higher fractional bandwidth (say 10%), increasing the input power

above 20 dBm causes an increase in phase noise. As the input power increases, the rms-voltage across each switch in the tunable filter also increases causing a static displacement in the bridge resulting in a continuous increase in $C_{MEMS,up}$. According to (4.3), this results in a higher variation in $C_{up}(t)$, thereby resulting in greater phase noise at the output of the filter.

Also, for filters with smaller fractional bandwidths (say 0.5%), phase noise increases when the input power is 10-15 dBm, but decreases when the input power is greater than 15 dBm. This phenomenon can be explained as follows: Increasing the power between 10-15 dBm increases phase noise due to higher variation in $C_{up}(t)$ similar to a 10% filter. When the filter's input power is increased beyond 15 dBm, the change in $C_{MEMS,up}$ causes a shift in the filter center frequency which is greater than the filter bandwidth. Outside the filter passband, the slope of phase response is decreased as shown in Fig. 69 and therefore a lower phase noise is observed at the output of the filter. This phenomenon is not observed for filters with higher bandwidths because the frequency shift caused by change in $C_{MEMS,up}$ is not large enough to exceed the filter bandwidth, and thus does not result in reduction of phase noise.

Fig. 71 shows the variation of phase noise at the filter output for different filter tuning states and bandwidths at $\omega' = 2\pi \times 13$ kHz ($\omega' < \omega_m$), $P_{in} = 0$ dBm ($P_{in} < P_{in,max}$) and Q=200. For a given filter bandwidth, phase noise increases with the number of switches in the up-state position due to increase in the number of noisy capacitors. Phase noise in the '110' state is higher than '011' and '101' states due to the higher value of capacitance in series with switch S_3. The capacitance variation in switch S_3 forms a larger fraction of the overall capacitance variation compared to switches S_1 and S_2 in Fig. 65(b). Similarly, the phase noise of the states '100' and '010' is greater than state '001'. Also, there is no phase noise generated when all the switches are in the down-state position [43].

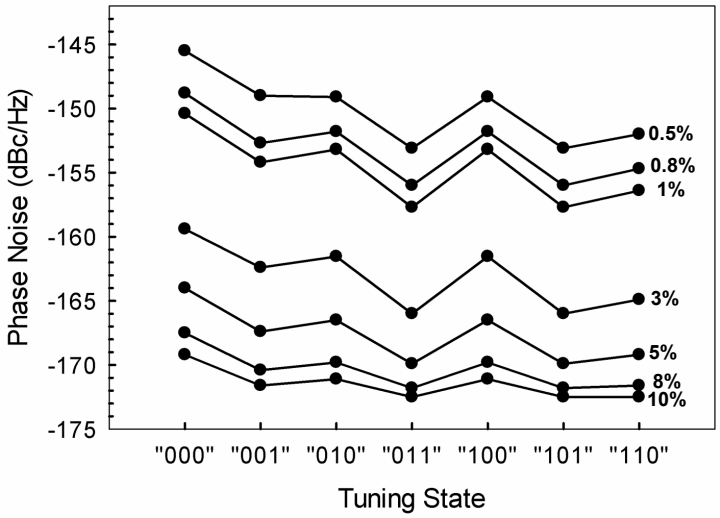

Fig. 71. Simulated phase noise for different tuning states of the filter. The tuning state $(S_1, S_2, S_3) = (0, 0, 0)$ shows the highest phase noise evaluated at $P_{in} = 0$ dBm ($P_{in} < P_{in,max}$), $\omega' = 2\pi \times 13$ kHz ($\omega' < \omega_m$) and Q=200.

Fig. 72 shows phase noise variation in a tunable filter versus mechanical frequency offset, with all the switches in the up-state position, $P_{in} = 0$ dBm ($P_{in} < P_{in,max}$) and Q=200. For $\omega' < \omega_m$, the phase noise remains almost constant and changing the filter fractional bandwidth results in a constant increase in phase noise at the filter output, for all mechanical frequencies. For offset frequencies larger than mechanical resonance, the phase noise decreases at a rate of -40 dB/dec and is eventually limited by the 3-db loss in the filter [44].

5. Higher Order Filters

The filter discussed so far is a good example of a practical RF MEMS tunable filter because the input/output capacitive J-inverters can be easily implemented at microwave frequencies [2]. Also, they are easily tunable to achieve good matching if wider tuning range is expected. A wide-band two-pole RF MEMS tunable filter with

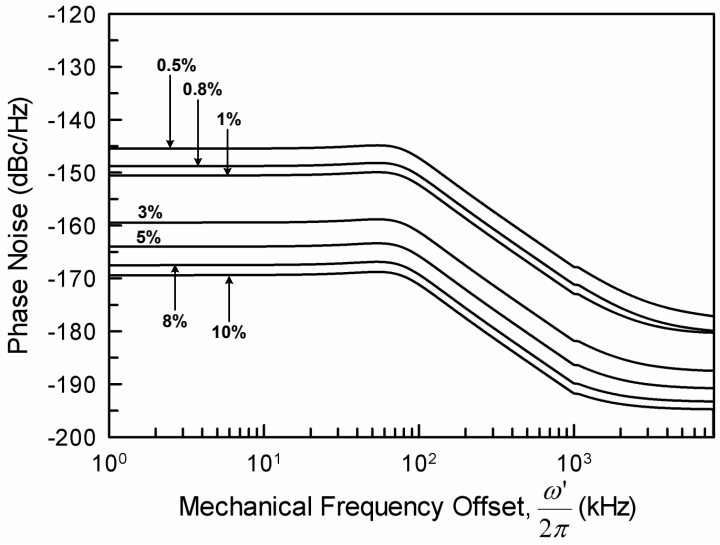

Fig. 72. Simulated phase noise as a function of mechanical frequency offset for different filter bandwidths. All switches are in the up-state position, P_{in} = 0 dBm ($P_{in} < P_{in,max}$) and Q=200.

44% tuning range and matching better than 16 dB has been demonstrated using this topology [83]. To extend this topology to higher order filters, capacitive source/load-resonator coupling and inductive inter-resonator coupling can be employed in the filter structure. However, the capacitances associated with the first and last resonators need to be adjusted to account for the capacitive J-inverters at the input and output while the capacitances associated with the internal resonators remain unchanged. For filters with orders greater than two, this results in unequal resonator capacitances and different susceptance slopes for each resonator. Hence the proposed method for order extension does not provide a fair comparison between the phase noise of a second order filter and higher order filters. Fig. 73 shows a three-pole filter using this topology and the unequal capacitances in the filter structure are indicated. The extension of a two pole filter to higher orders can also be achieved by employing only capacitive J-inverters but it is known that filters with capacitive-coupling and

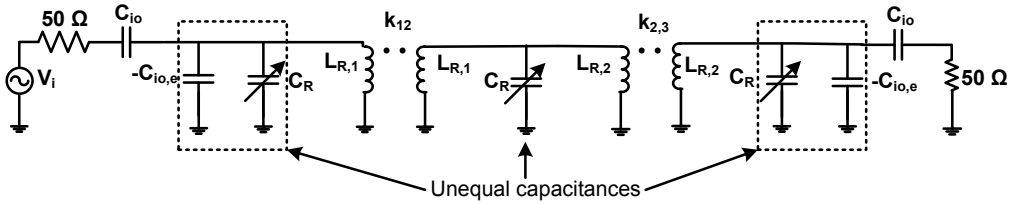

Fig. 73. Three-pole tunable filter employing input/output capacitive inverters and inter-resonator inductive inverters.

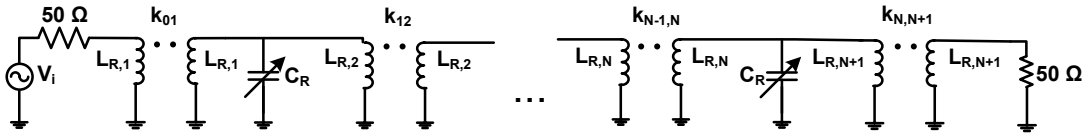

Fig. 74. Inductively-coupled lumped element tunable filter of order N.

capacitive-tuning have a large bandwidth variation over the tuning range. However, filters with inductive-coupling and capacitive-tuning show a relatively constant bandwidth over the tuning range [85]. Fig. 74 shows a tunable filter with only inductive J-inverters. Since all the resonator capacitances are equal in this topology, it is reasonable to compare the phase noise of a second order filter with the phase noise of higher order filters.

The filter element values for the filter topology in Fig. 74 can be found from design formulas in [54] and [83]. The center frequencies and fractional bandwidths used for filter design are the same as in Table VIII. The variable resonator capacitance, C_R, is realized using the switched capacitor configuration shown in Fig. 65(b). It is assumed that the loss in the capacitive MEMS switch bank (C_R) is low compared to the loss due to finite inductor Q-factor in the resonator of the filter in Fig. 74. Hence, the unloaded Q-factor of the resonator is dominated by the inductor Q-factor alone. The inductors are assumed to have either $Q = 200$ or $Q = 300$ at $f_0 = 1.95$ GHz to study the effect of resonator quality factor on the phase noise of the filter. These

values of Q-factor are reasonable since evanescent-mode high-Q MEMS tunable filters have been developed by S-. J. Park et al. [86] that exhibit unloaded resonator quality factors around 200-300 with similar lumped equivalent circuit model as shown in Fig. 65(a).

Fig. 75 shows simulated values of phase noise for 2-5 pole filters versus fractional bandwidth with all switches in the up-state position. The phase noise is evaluated at kHz $\omega' = 2\pi \times 13$ kHz ($\omega' < \omega_m$) and $P_{in} = 0$ dBm. The power-handling analysis method described earlier is used to ensure that $P_{in} < P_{in,max}$ for the filter topology shown in Fig. 74, for all fractional bandwidths. For a two-pole filter, the phase noise of a filter with mixed capacitive/inductive inverters in Fig. 65(a) is lower than the phase noise of a filter with purely inductive inverters because the capacitive inverters located at the input/output of the filter lower the susceptance slope of each resonator, which results in a smaller phase slope around the filter center frequency. For a two-pole, 0.5% filter, the phase slope around the filter center frequency is 15°/MHz with purely inductive inverters compared to 6°/MHz for the filter with mixed capacitive/inductive inverters (see inset in Fig. 75). Consequently, the filter with purely inductive inverters exhibits higher phase noise. The effect of resonator quality factor ($Q = 200, 300$) on the phase noise is insignificant for filters with fractional bandwidths greater than 3%. For filters with small fractional bandwidth, higher resonator quality factor results in less attenuation of the phase noise at the filter output. However, a change in resonator quality factor from 200 to 300 causes an increase in phase noise that is insignificant even for narrow fractional bandwidths.

In the complex s-plane, the poles of a Chebyshev filter lie on an ellipse where the ith pole is at an angle of $(2i-1)\pi/2N$ radians from the imaginary axis (N is the filter order) [15]. Noise in the filter structure causes a change in the angle of each pole and correspondingly affects $\angle S_{21}(j\omega, t)$ of the filter. The noise contribution from each

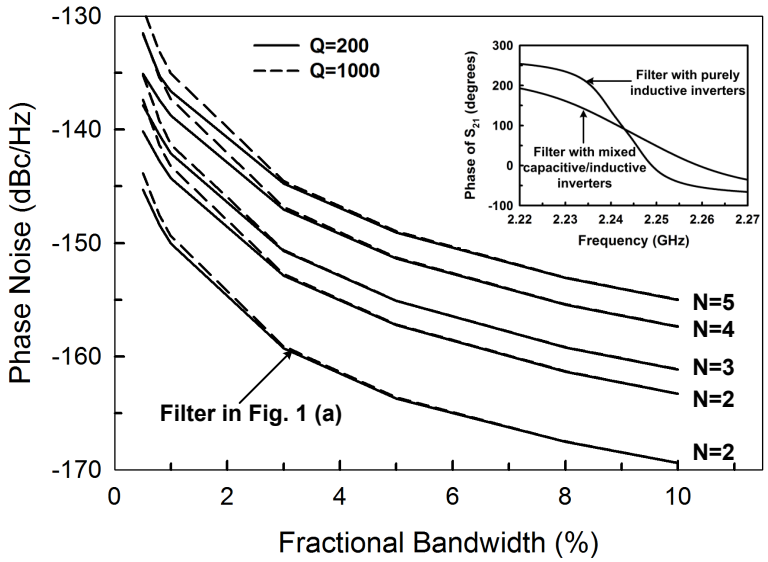

Fig. 75. Variation of phase noise with filter order for different fractional bandwidths. All switches are in the up-state position. Phase noise is evaluated at $P_{in} = 0$ dBm ($P_{in} < P_{in,max}$) and $\omega' = 2\pi \times 13$ kHz ($\omega' < \omega_m$).

pole depends on its location on the complex plane. The overall phase noise of the filter is the sum of the noise contribution of each pole. Increasing the filter order by two corresponds to the addition of a pair of complex conjugate poles to the existing poles. By increasing the filter order from two to four (or three to five), there is a 6 dB increase in phase noise, or equivalently, an increase of 3 dB per pole as a result of simulations shown in Fig. 75. Increasing the filter order from two to three (or four to five) corresponds to the addition of a purely real pole on the complex plane and subsequent rearrangement of existing poles such that they still lie on the ellipse. In this case, there is only a 2.2 dB increase in phase noise as shown in Fig. 75. Hence, simulation results show that the addition of a pair of complex conjugate poles adds more phase noise per pole compared to the addition of a real axis pole to the filter shown in Fig. 75.

6. Conclusion

This study demonstrates the phase noise of RF MEMS tunable filters as a function of the filter order, fractional bandwidth, resonator quality factor, tuning state and input power. Due to the nature of the voltage distribution inside the filter, the power-handling capability of the tunable filter is directly proportional to the filter bandwidth and hence defines the acceptable input power range where phase noise calculation is valid. Phase noise in a tunable filter with a given fractional bandwidth remains constant for low input power and low mechanical offset frequencies. At higher input powers, narrow- and wide-bandwidth filters exhibit different trends in phase noise. Phase noise is greater for filters with higher order due to the increase in the number of noisy elements in the filter structure. For all the tunable filters presented in this section, employing capacitive RF MEMS switches with parameters shown in Table IX, the phase noise is so low that it is hard to measure using even the state-of-the-art measurement equipment. It has been shown that the phase noise penalty of tunable filters with capacitive shunt switches in reconfigurable front ends is not considerable and thus makes the reported RF MEMS tunable filters suitable for high performance applications.

C. Nonlinear Nodal Analysis of Tunable Microwave Filters

1. Introduction

Microwave tunable filters using semiconductor-based or ferroelectric varactors, or RF microelectromechanical systems (MEMS) switches have been developed for application in multi-band communication systems [11]. Nonlinear behavior of tunable filters results in spectral regrowth due to generation of higher-order intermodulation products [13].

Tuning elements have a nonlinear relationship between the capacitance and bias-voltage (C-V) and are used in the resonators of tunable filters to change the filter center frequency by adjusting the bias voltage. At high input power, the internal voltages affect the bias voltage of each tuning element, thereby changing the filter response. Internal voltages in a coupled-filter have been studied in [84] for cavity filters, when the center frequency of each resonator is not a function of the voltage across it. In a tunable filter, the nonlinear C-V dependence of center frequency results in filter distortion at high input power.

In this section, a simple analytical technique is presented to study effects of high input power on tunable filters. Nonlinear nodal analysis is performed in the lowpass domain by calculating the nonlinear reactance deviation at each node using an iterative approach. The nonlinear admittance matrix obtained is used to find the filter response by simple matrix inversion. Internal voltages and s-parameters obtained from theory are compared to harmonic balance simulations for verification. This method eliminates the need for commercial nonlinear circuit simulators to study nonlinear phenomena in tunable filters. Although the theory presented in this section is applied to nonlinear varactor diodes, it is equally applicable to nonlinear RF MEMS switches. Hence, the proposed nodal analysis technique forms the basis for theoretical

nonlinear noise analysis of RF MEMS tunable filters, which is discussed throughout the rest of this chapter.

2. Theory

Fig. 76(a) shows a generalized all-pole tunable Butterworth or Chebyshev bandpass filter of order N and fractional bandwidth $\overline{\omega}$, with lossless admittance inverters, lossless shunt resonators and termination admittances Y_0. The variable capacitance is typically implemented with a varactor bank. V_i $(i = 0, \ldots, N+1)$ and V_s are the voltages across node i and the input voltage in the bandpass filter, respectively.

The equivalent lowpass filter representation of all-pole bandpass filters for a particular tuning state is shown in Fig. 76(b), where N unit capacitors are coupled through ideal admittance inverters, M_{ij}. The source and load terminating admittances are y_0=1. v_i $(i = 0, \ldots, N+1)$ and v_s are the voltages across node i and the input voltage in lowpass filter, respectively. The bandpass voltages $V_1, \ldots, V_N$ are greater than the lowpass voltages $v_1, \ldots, v_N$ by a factor of $1/\sqrt{T}$, where T is a constant that equalizes the susceptance slopes of the lowpass and bandpass filters [84]. However, the terminal voltages remain unchanged, implying $v_0 = V_0$, $v_{N+1} = V_{N+1}$ and $v_s = V_s$.

$M_{ii}(\omega, V_i)$ is the nonlinear reactance deviation in a synchronously-tuned filter that represents the detuning of resonator i due to nonlinearity of the tuning element at a bandpass frequency ω. For synchronously-tuned tunable filters at low input powers, the capacitance of the tuning element is weakly dependent to the voltage, and hence $M_{ii} \rightarrow 0$ as $V_i \rightarrow 0$. However, at high input power, the nonlinear C-V relationship of the tuning element causes detuning of each resonator to lower frequencies. The lowpass internal node voltages v_i are found by solving the nonlinear system of nodal

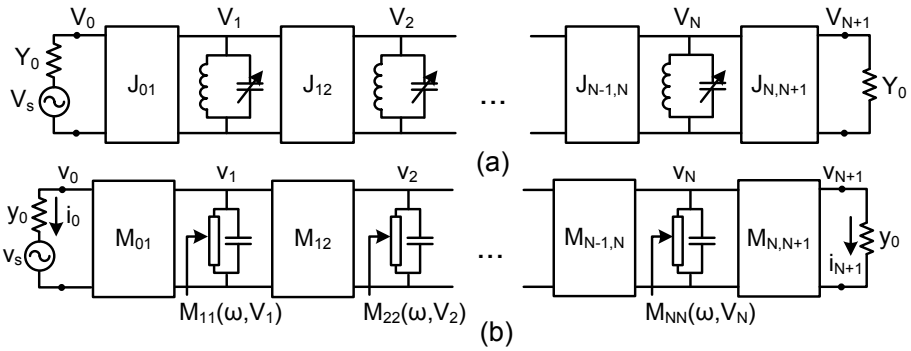

Fig. 76. (a) Generalized all-pole Butterworth/Chebyshev bandpass filter with ideal admittance inverters and lossless shunt resonators, and (b) equivalent lowpass filter for a particular tuning state.

equations of the equivalent lowpass filter, expressed as [84]

$$\mathbf{Y}(\omega, \mathbf{v})\mathbf{v} = \mathbf{i} \tag{4.5}$$

where,

$$\begin{aligned}
Y_{ii} &= \begin{cases} s + jM_{ii}(\omega, V_i) & \text{for } i = 1, \ldots, N \\ 0 & \text{for } i = 0, N+1 \end{cases} \\
Y_{im} = Y_{mi} &= \begin{cases} jM_{im} & \text{for } m = i+1,\ i = 0, \ldots, N \\ 0 & \text{for } m \neq i, i+1 \end{cases} \\
\mathbf{v} &= [v_0\ v_1\ \ldots\ v_N\ v_{N+1}]^T \\
\mathbf{i} &= [i_0\ 0\ \ldots\ 0\ i_{N+1}]^T
\end{aligned} \tag{4.6}$$

$\mathbf{Y}(\omega, \mathbf{v})$ represents the admittance matrix that is a nonlinear function of the node voltages $\mathbf{v}$ of the equivalent lowpass filter. The values of $\mathbf{i}$ represent the node currents in the equivalent lowpass filter and s is the lowpass frequency variable found by transforming the bandpass frequency ω around ω_0 as $\frac{j}{\bar{\omega}}\left(\frac{\omega}{\omega_0} - \frac{\omega_0}{\omega}\right) \rightarrow s$. The vectors $\mathbf{v}$ and $\mathbf{i}$ are also functions of ω.

To solve (4.5), an independent expression for $M_{ii}(\omega, V_i)$ must be known. The nonlinear angular frequency of the ith-resonator, $\omega_{0i}(V_i)$, may be expressed in terms

of lowpass frequency variables as

$$s_i'(V_i) = s + jM_{ii}(\omega, V_i) \tag{4.7}$$

s and $s_i'(V_i)$ are lowpass frequencies corresponding to center frequencies ω_0 and $\omega_{0i}(V_i)$, respectively. An explicit expression for $M_{ii}(\omega, V_i)$ is obtained by rearranging (4.7) as

$$M_{ii}(\omega, V_i) = \frac{\omega_0 - \omega_{0i}(V_i)}{\overline{\omega}\omega_0}\left[\frac{\omega}{\omega_{0i}(V_i)} + \frac{\omega_0}{\omega}\right] \tag{4.8}$$

When $\mathbf{Y}(\omega, \mathbf{v})$ is known completely, $\mathbf{Z}(\omega, \mathbf{v}) = \mathbf{Y}(\omega, \mathbf{v})^{-1}$ is found and the voltage at node i for a current $i_0(\omega)$ driving the equivalent low-pass filter is given by

$$v_i(\omega) = \left(Z_{i,0}(\omega, \mathbf{v}) - \frac{Z_{i,N+1}(\omega, \mathbf{v})Z_{N+1,0}(\omega, \mathbf{v})}{z_0 + Z_{N+1,N+1}(\omega, \mathbf{v})}\right) i_0(\omega) \tag{4.9}$$

where $i = 0, \ldots, N$ and z_0=1/y_0=1. However, since $M_{ii}(\omega, V_i)$ depends on the voltage across the ith-resonator in the bandpass filter, the bandpass voltage at frequency ω for an applied voltage V_s, is expressed as

$$V_i(\omega) = \frac{1 + S_{11}(\omega, \mathbf{v})}{\sqrt{T}} \frac{v_i(\omega)}{v_0(\omega)} V_s \tag{4.10}$$

for $i = 1, \ldots, N$, where $S_{11}(\omega, \mathbf{v})$ is the reflection parameter found from $\mathbf{Y}(\omega, \mathbf{v})$ [15]. The system of nonlinear algebraic equations in (4.5)-(4.10) does not have a purely analytical solution and hence is solved by iterative methods to obtain node voltages $V_i(\omega)$ across each resonator, as described in the next section.

3. Iterative Solution of Nonlinear Equations

An iterative method is presented to solve the nonlinear system of equations in (4.5)-(4.10) and calculate the values of $V_i(\omega)$ and $M_{ii}(\omega, V_i)$ for a given input power. The initial voltage across each resonator i is assumed to be zero at iteration step k=0 ($V_{i,k=0}$=0), implying $M_{ii}(\omega, 0)$=0. This ensures that the filter is not already detuned

when an input voltage is applied to it and hence the resonator frequency detuning $\delta\omega_{i,k=0} = 0$. Input power is applied to the filter at iteration k=1. The voltage across each resonator at iteration k is calculated using the M_{ii} values at iteration $k-1$. Fig. 77 shows the iterative method and involves the following steps:

Step 1) At the k^{th} iteration ($k = 1, \ldots, \infty$), voltage $V_{i,k}(\omega)$ appears across each resonator and is found from Eqs. (4.5)-(4.10) using $M_{ii}(\omega, V_{i,k-1})$. The center frequency of resonator i during the $(k-1)^{th}$ time step, $\omega_{0i}(V_{i,k-1}) = \omega_0 - \delta\omega_{i,k-1}$, is found using the nonlinear C-V relationship of the tuning element.

Step 2) The residual change in the voltage across resonator i is evaluated as

$$\eta_{ik}(\omega) = \left| \frac{V_{i,k}(\omega) - V_{i,k-1}(\omega)}{V_{i,k}(\omega)} \right| \tag{4.11}$$

If $\eta_{ik}(\omega)$ has not converged to an arbitrarily small value, ζ, for all frequencies, then continue to step 3. Otherwise, proceed to step 5.

Step 3) The node voltage $V_{i,k}(\omega_0 - \delta\omega_{i,k-1})$ causes detuning of the center frequency of resonator i to a lower frequency represented by $\omega_0 - \delta\omega_{ik}$, due to a nonlinear change in resonator capacitance. The frequency shift at an arbitrary frequency ω is the same as the center frequency shift, $\delta\omega_{ik}$, because there is a linear shift in the resonance curve towards lower frequencies due to the capacitance change.

Step 4) Once $\delta\omega_{ik}$ is known, $M_{ii}(\omega, V_{i,k})$ in the lowpass filter is calculated using (4.8) when $\omega_{0i}(V_{i,k}) = \omega_0 - \delta\omega_{ik}$. The iteration number is incremented and step 1 is repeated.

Step 5) When convergence is achieved, $M_{ii}(\omega)$ and $V_i(\omega)$ are fully determined. Consequently, $\mathbf{Y}(\omega, \mathbf{v})$ is also known, and the large signal S-parameters of the tunable filter are calculated from the impedance matrix of the equivalent lowpass filter [15].

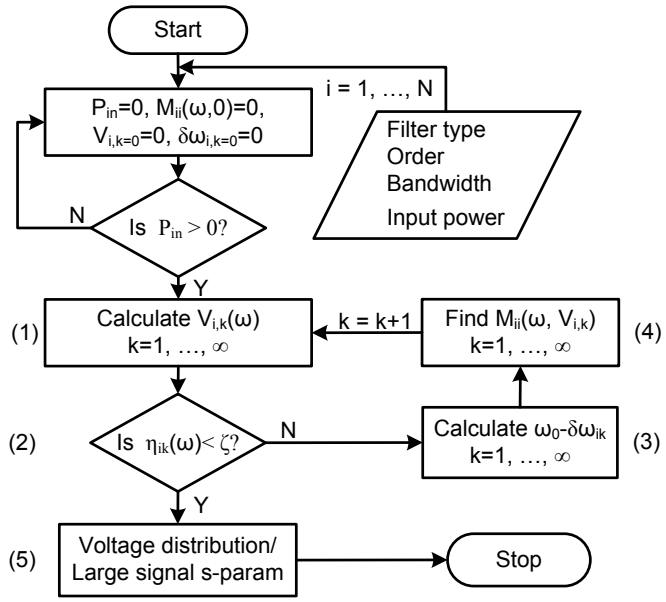

Fig. 77. Recursive algorithm to find the nonlinear voltage distribution and large signal s-parameters of a tunable filter.

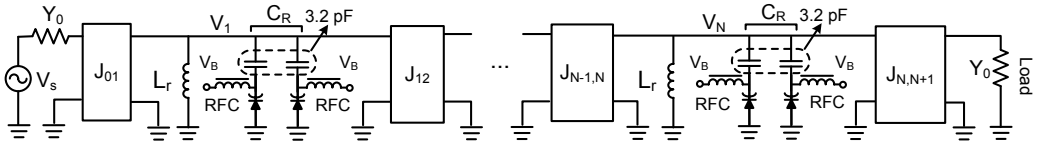

Fig. 78. N-pole lossless tunable filter implemented using GaAs varactors. The RF chokes (RFC) are ideal and have no effect on the filter.

4. Nonlinear Varactor Model

Gallium Arsenide (GaAs) varactor diodes are a popular choice for tunable microwave filter implementation due to their high switching speed, low cost and reliability [87]. However, GaAs varactor-tuned filters exhibit poor linearity ($IIP_3 \approx$ 15-20 dBm) [13], as a consequence of nonlinear C-V relationship of a GaAs varactor which can be expressed as

$$C(V) = C_{j0}/\left(1 + V/V_j\right)^m \tag{4.12}$$

C_{j0} is the zero-bias junction capacitance, V_j is the junction potential and m is the grading coefficient. Typical values for a linearly graded varactor junction are $C_{j0} =$ 4 pF, $V_j = 5$ V and $m = 0.5$ [88]. If the varactor diode is biased at a voltage V_B, then an applied RF signal $V_p \sin(\omega t)$ results in $V = V_B + V_p \sin(\omega t)$ across the varactor. A single-tone voltage excitation applied to the GaAs varactor results in harmonics of the varactor diode current (i_c) due to the nonlinear C-V dependence. Since tunable filters are narrowband and frequency selective, the nonlinearity is well-described by considering only the first harmonic of i_c, and is found by expanding (4.12) using binomial series and evaluating $i_c = C(V)dV/dt$. The approximate equivalent capacitance due to the first harmonic component of i_c is expressed as

$$C(V) \approx C(V_B)\left(1 + \frac{3}{16}p^2 + \frac{35}{512}p^4\right) \tag{4.13}$$

where $p = V_p/(V_B + V_j)$. The nonlinear capacitance variation described by (4.13) for a given input signal power is used in the calculation of nonlinear reactance deviations of each resonator. Nonlinear harmonic balance simulation is performed in Agilent ADS. using the varactor model in (4.12) to verify the nonlinear analysis presented.

5. Case Study

Fig. 78 shows an N-pole, lossless Butterworth or Chebyshev filter tunable from $1.7 - 2.2$ GHz using varactor diodes [13]. The values of ideal admittance inverters are calculated using formulas in [15]. The resonator inductance $L_r = 2.48$ nH and the GaAs varactor is biased at $V_B = 10$ V so that the varactor capacitance is 2.3 pF. The overall resonator capacitance (C_R) is 2.7 pF (2*(3.2 pF || 2.3 pF)) and results in a filter center frequency of 1.95 GHz for $V_B = 10$ V. Two filter examples will be used to present the nonlinear analysis and simulation: *Case A* - Two-pole 3% Butterworth filter and *Case B* - Four pole 5% Chebyshev filter. The iterative algorithm shown in Fig. 77 is applied to both cases to find the nonlinear reactance deviations, internal voltages and large signal s-parameters in the tunable filters, for a given input power.

a. Nonlinear Reactance Deviations

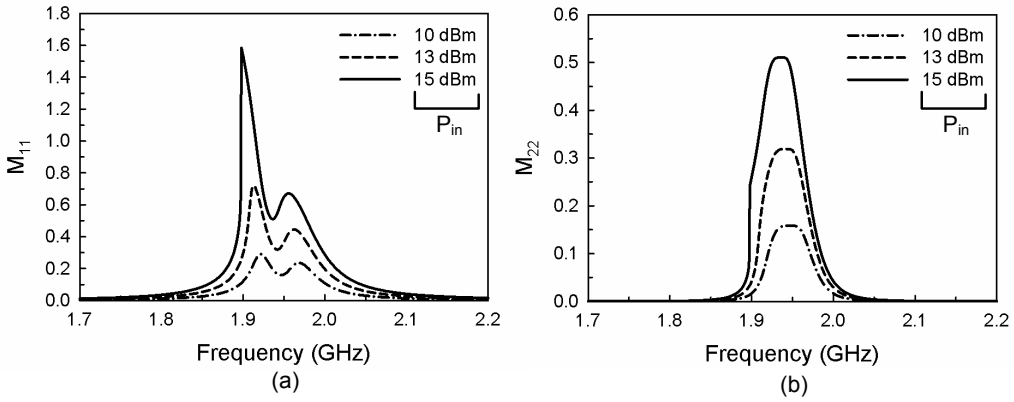

Fig. 79. Nonlinear reactance deviations as a function of frequency for Case A in (a) resonator 1, and (b) resonator 2, for different input powers.

Figs. 79 and 80 show the reactance deviations as a function of frequency obtained from the recursive algorithm, for different input powers. Non-zero reactance deviations around the filter passband imply that nonlinearity is significant at these

frequencies. As the input power increases, the peak in M_{11} at the lower passband edge for case A implies highly nonlinear behavior in resonator 1, at this frequency. Similarly, M_{11}, M_{22} and M_{33} show peaks at the lower passband edge at high input power for case B. In both cases, the resonator closest to the load exhibits only shifts in center frequency and minimal distortion at high input powers. If the input power is increased beyond 15 dBm for case A and 17 dBm for case B, high nonlinearity causes multi-valued reactance deviation values at lower passband edge and results in a large *jump* in its value [89]. As a result, the recurring algorithm fails to converge.

b. Peak Internal Voltage Distribution

Figs. 81 and 82 show the internal voltages obtained from the iterative algorithm for cases A and B, and show good agreement between theory and harmonic balance simulations. A small *jump* in the voltage is observed around 1.90 GHz for case A (P_{in} = 15 dBm) and 1.86 GHz for case B (P_{in} = 17 dBm) as predicted by the theory and are also observed from harmonic balance simulations at 15.5 dBm and 17.5 dBm for cases A and B, respectively. The slight discrepancies observed are a result of the varactor model approximation in (4.13). For a particular filter type, higher bandwidths imply lower peak voltages due to a lower value of the scaling factor, $1/\sqrt{T}$ [90]. Thus, narrow bandwidth filters have greater internal voltage distortion at high input power.

c. Large Signal S-Parameters

The reactance deviations for cases A and B at different input powers are used in the lowpass admittance matrix $\mathbf{Y}(\omega, \mathbf{v})$, and the S_{21}-parameter is calculated from $\mathbf{Z}(\omega, \mathbf{v}) = \mathbf{Y}(\omega, \mathbf{v})^{-1}$. The resulting large signal S_{21} for both cases are shown in Fig. 83 and shows good agreement between theory and harmonic balance simulation. The

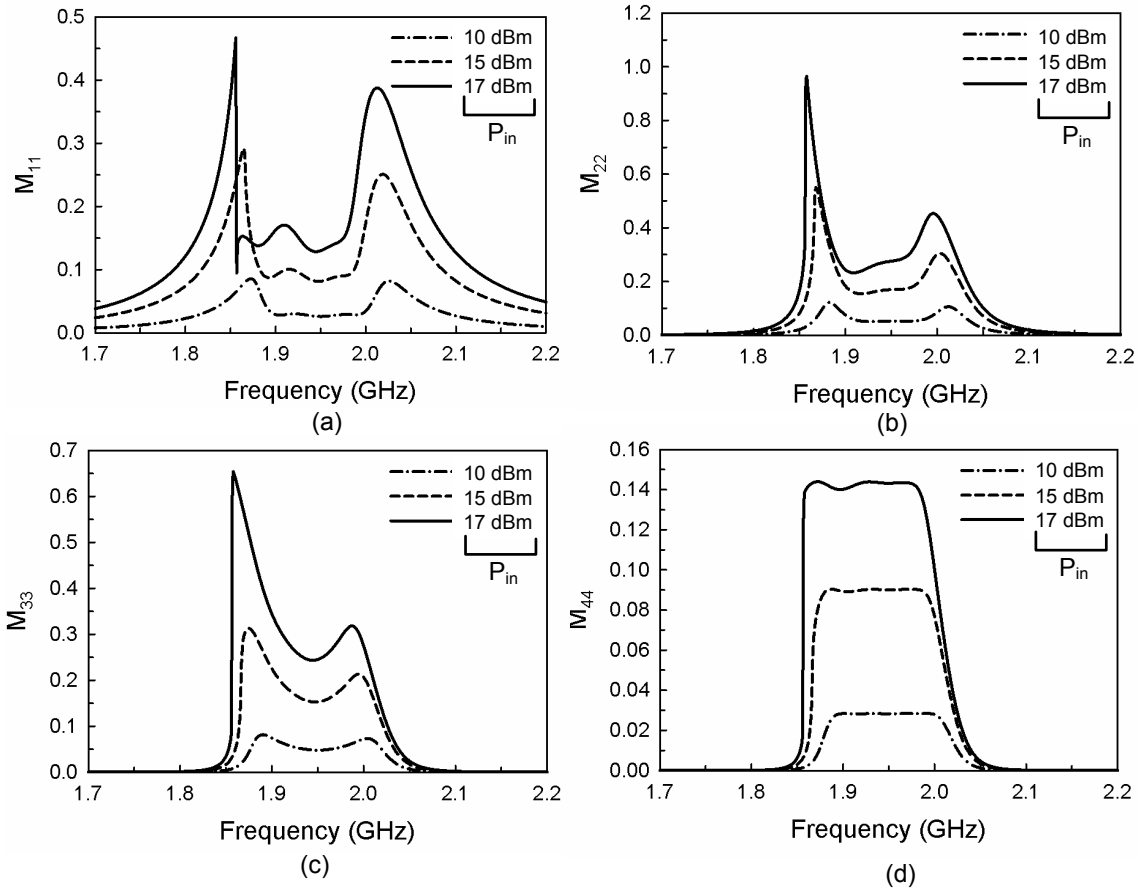

Fig. 80. Nonlinear reactance deviations as a function of frequency for Case B in (a) resonator 1, (b) resonator 2, (c) resonator 3 and (d) resonator 4, for different input powers.

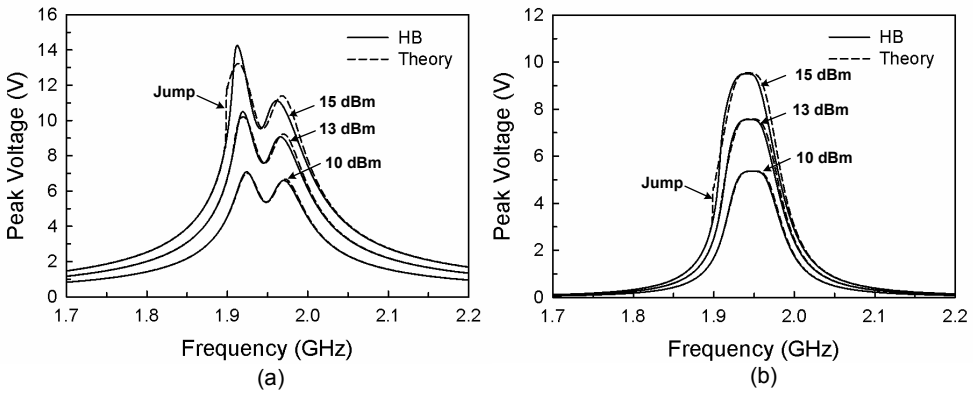

Fig. 81. Voltage distribution for Case A across (a) resonator 1, and (b) resonator 2, for different input powers, for different input powers.

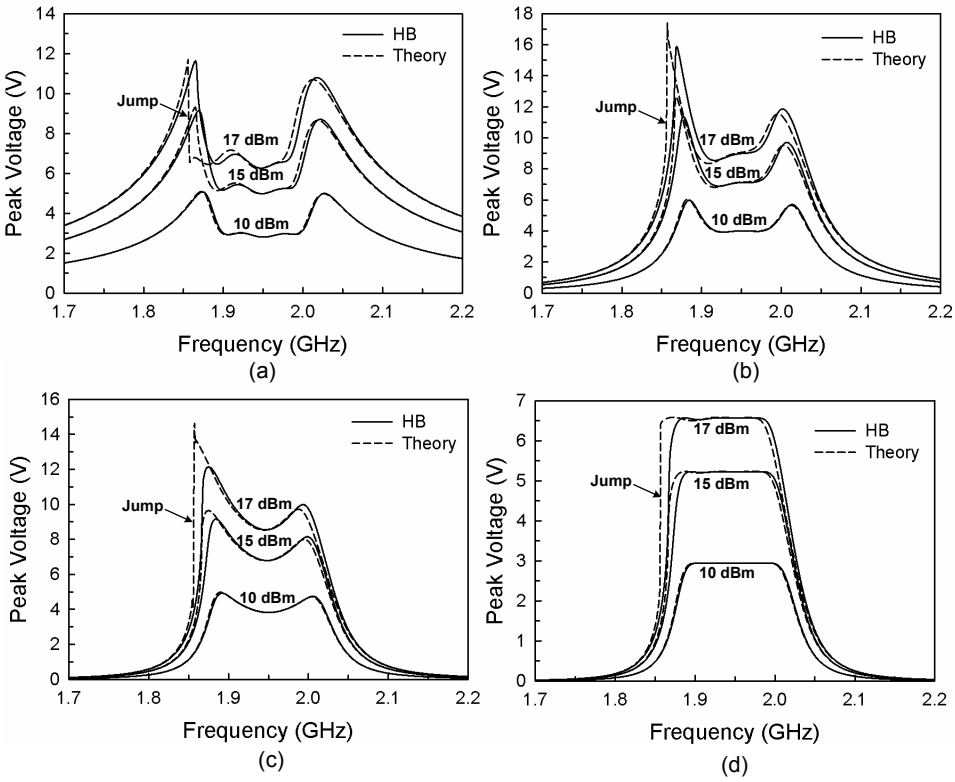

Fig. 82. Voltage distribution for Case B across (a) resonator 1, (b) resonator 2, (c) resonator 3, and (d) resonator 4, for different input powers.

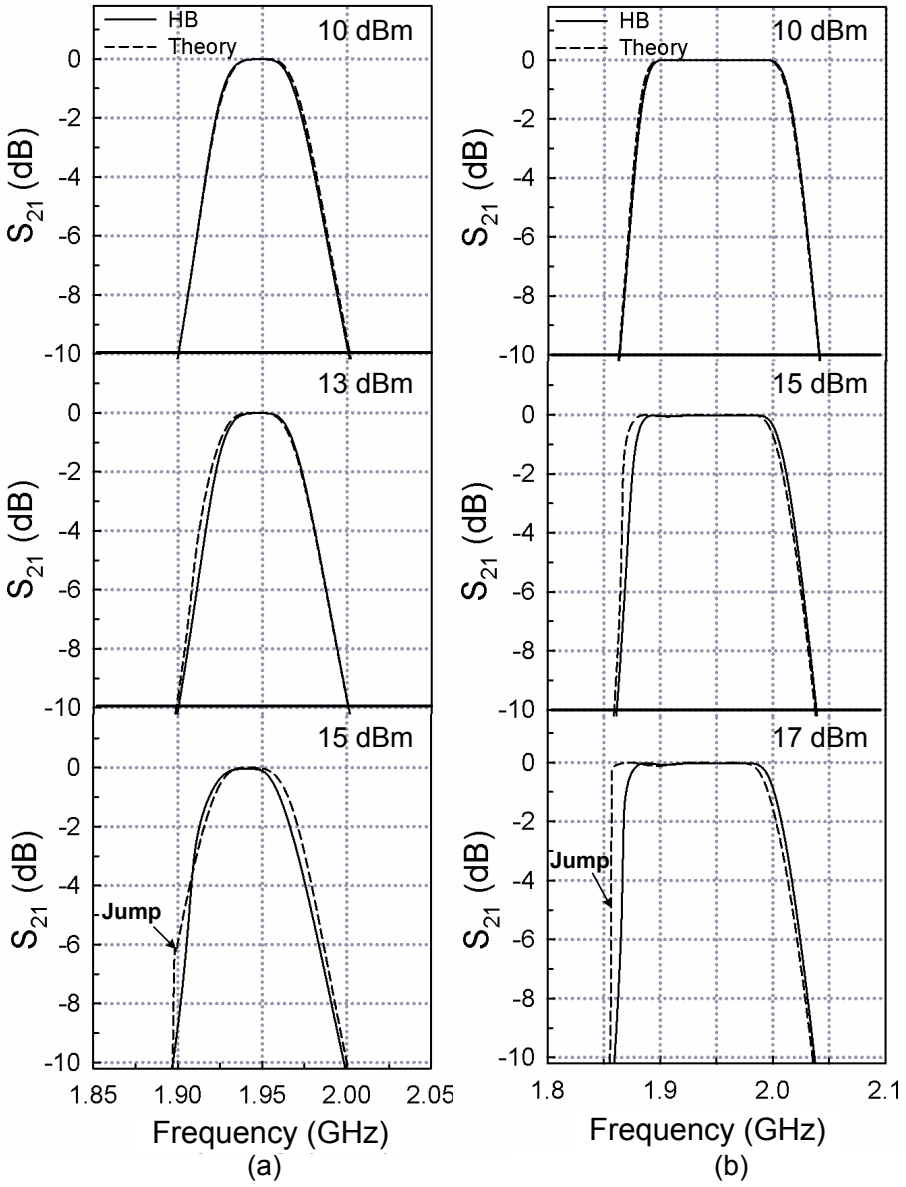

Fig. 83. Large signal s-parameters for (a) Case A, and (b) Case B, for different input powers.

discrepancies observed are a result of the finite binomial series expansion in (4.13) used to find the reactance deviation values. The voltage *jump* at the lower passband edge at high input power manifests as a *jump* in the S_{21}-parameter at the same frequency resulting in distortion of the filter response. Similar jumps are observed in harmonic balance simulations if power is increased to 15.5 dBm and 17.5 dBm for cases A and B, respectively.

6. Conclusion

In this study, a nonlinear nodal analysis method has been developed to effectively predict the nonlinear response of varactor-tuned filters. It is shown that nonlinearity is attributed to the detuning of each resonator in the tunable filter at high input power. This nonlinear detuning phenomenon must be accounted for while calculating phase noise of RF MEMS tunable filters due to Brownian motion. In the CAD-based method presented in Section B of this chapter, the nonlinear behavior of the RF MEMS switch was included in the switch model in Fig. 65(c). Hence, phase noise values calculated in Section B of this chapter take the filter nonlinearity into account. Throughout the rest of this chapter, theoretical methods to calculate nonlinear noise in RF MEMS tunable filters will be discussed in detail.

D. Pole Perturbation Theory for Nonlinear Noise Analysis of RF MEMS Tunable Filters

1. Introduction

So far, the effect of nonlinear noise in RF MEMS tunable filters has been studied only using CAD-based simulation techniques in Section B of this chapter. The goal of this section is to develop a theory to predict the effect of nonlinear noise in all-pole RF MEMS tunable filters. This is achieved by calculating variations in the filter transfer function due to presence of nonlinear noise by perturbing poles of the filter transfer function in the complex plane. The pole-perturbation approach has been previously used to study the effect of coefficient accuracy in the implementation of digital filters [91]. Also, pole-perturbations have been used for passivity enforcement of non-passive rational models [92].

In this work, a pole-perturbation approach is introduced to calculate nonlinear noise due to Brownian motion in RF MEMS tunable filters for the first time. To find the effect of nonlinearity, the generalized iterative approach presented in Section C is used to find the peak internal voltages in nonlinear microwave filters. The variation in filter response due to nonlinear noise is used to theoretically predict filter phase noise as a function of input power, tuning state, fractional bandwidth, filter order and frequency offset, and is compared to results of the CAD-based method in Section B of this chapter. The effects of nonidealities arising from practical realizations of filter components on filter phase noise are also considered. Finally, it is shown that filter phase noise is most significant in MEMS tunable filters with low bandwidth, high order and high quality factor.

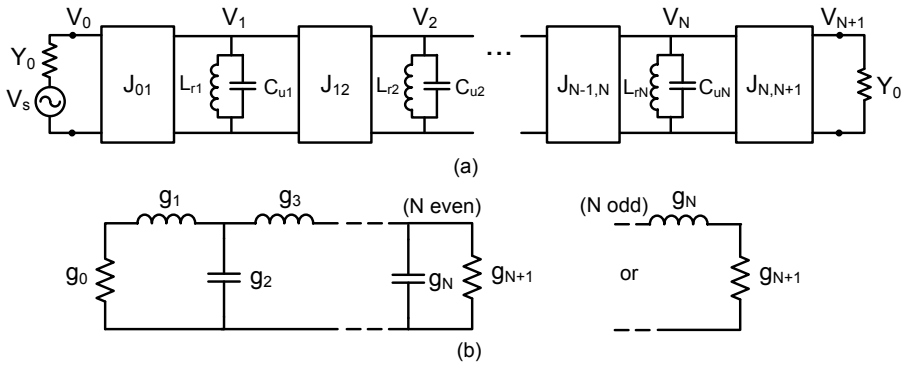

Fig. 84. (a) Generalized all-pole bandpass filter of order N with ideal admittance inverters and lossless shunt resonators, and (b) equivalent low-pass ladder network.

2. Perturbation Theory

Fig. 84(a) shows a generalized Butterworth or Chebyshev bandpass filter of order N with ideal admittance inverters ($J_{i,i+1}, i = 0, \ldots, N$), lossless shunt resonators and termination admittances Y_0, for which all formulations are presented in this paper. Similar results can be derived for the filter with impedance inverters and series resonators. The discussion is limited to synchronous filters in which all resonators are tuned to $\omega_{0i} = 1/\sqrt{L_{ri}C_{ui}} = \omega_0$ for $i = 1, \ldots, N$. $V_1, \ldots, V_N$ are the node voltages across each resonator due to the applied input excitation V_s. Fig. 84(b) shows the equivalent low-pass ladder network starting with a series element where $g_0, \ldots, g_{N+1}$ are the prototype element values for all-pole filters. Each resonator in the bandpass filter or reactive low-pass prototype value in the ladder network represents a pole on the left-half of the complex plane which is located at an angle $\theta_i = (2i-1)\pi/2N$, $i = 1, \ldots, N$, from the imaginary axis for Butterworth and Chebyshev filters.

a. Methodology

The pole-perturbation approach in microwave filters presented here involves mapping any change in the component values of the bandpass filter into the perturbation of the reactive low-pass prototype element values, $g_1, \ldots, g_N$, of the equivalent ladder network. Perturbations may arise due to nonlinear device behavior inside the filter at high input power or internal noise sources. Thus, the position of the ith-pole in the complex plane at a given angular frequency, input power and time instant may be represented by the complex quantity $p_i(\omega, V_i, t)$, $i = 1, \ldots, N$. If the perturbations in the microwave filter are due to changes in the reactive elements only, then it will be shown later that the perturbation of low-pass prototype values may be completely represented in terms of an angular displacement, $\theta_i(\omega, V_i, t)$. Since the driving point impedance of the prototype filter must always be a positive real function [93], the pole-perturbations are restricted as follows:

1. The complex conjugate property of complex poles is maintained during perturbation.

2. Perturbed poles always have negative or zero real parts.

In general, the pole-perturbation may be decomposed into perturbations along the real (σ-axis) and imaginary (Ω-axis) directions represented by $g_{\sigma,i}(\omega, V_i, t)$ and $g_{\Omega,i}(\omega, V_i, t)$, respectively, so that the overall pole-perturbation is given by

$$p_i(\omega, V_i, t) = -g_{\sigma,i}(\omega, V_i, t) \pm j g_{\Omega,i}(\omega, V_i, t) \tag{4.14}$$

The impact of perturbations $p_i(\omega, V_i, t)$ on the filter transfer function can be obtained from rational polynomial approximations for Butterworth and Chebyshev filters which

is expressed as [15]

$$S_{21}(\omega, V_i, t) = \frac{K_A}{\prod_{i=1}^{N} \left(j\Omega_i(\omega, V_i, t) - p_i(\omega, V_i, t)\right)} \tag{4.15}$$

where,

$$\Omega_i(\omega, V_i, t) = \frac{1}{\overline{\omega}} \left(\frac{\omega}{\omega_{0i}(V_i, t)} - \frac{\omega_{0i}(V_i, t)}{\omega} \right) \tag{4.16}$$

is the lowpass angular frequency corresponding to the angular frequency ω of a bandpass filter with a fractional bandwidth of $\overline{\omega}$. The value of $\omega_{0i}(V_i, t)$ is perturbation of the center frequency of resonator i. The constant K_A is given by

$$K_A = \begin{cases} 1 & \text{for Butterworth filters,} \\ \prod_{i=1}^{N} \left[\eta^2 + \sin^2\left(i\pi/N\right)\right]^{1/2} & \text{for Chebyshev filters.} \end{cases}$$

and for a Chebyshev filter with a ripple of L_{Ar} dB,

$$\eta = \sinh[(1/N)\sinh^{-1}(1/\epsilon)]; \quad \epsilon = \sqrt{10^{L_{Ar}/10} - 1} \tag{4.17}$$

Substituting (4.14) in (4.15) results in

$$S_{21}(\omega, V_i, t) = \frac{K_A}{\prod_{i=1}^{N} \{g_{\sigma,i} + j\Omega_i \pm j g_{\Omega,i}\}} \tag{4.18}$$

Thus, the transmission response of the filter is easily determined from (4.18) once the perturbations in the reactive low-pass prototype values, $g_1(\omega, V_i, t), \ldots, g_N(\omega, V_i, t)$, are known and decomposed into real and imaginary pole-perturbation components.

b. Prototype Perturbation

In this section, explicit formulas are derived for the equivalent perturbations of reactive low-pass prototype values due to component variations in the bandpass filter.

The values of J-inverters in Fig. 84 for a filter with fractional bandwidth $\overline{\omega}$ are given by [15]

$$J_{0,1} = \sqrt{\frac{Y_0 \overline{\omega} b_1}{g_0 g_1}}; \qquad J_{N,N+1} = \sqrt{\frac{Y_0 \overline{\omega} b_N}{g_N g_{N+1}}}$$
$$J_{i,i+1} = \overline{\omega} \sqrt{\frac{b_i b_{i+1}}{g_i g_{i+1}}} \qquad (i = 1, \ldots, N-1) \tag{4.19}$$

where the susceptance slope of each resonator is represented by $b_i = \omega_{0i} C_{ui} = \sqrt{C_{ui}/L_{ri}}$, $(i = 1, \ldots, N)$. Reactive variations in resonators and admittance inverters result in changing susceptance slopes, $b_i(\omega, V_i, t)$, and inverter values $J_{i,i+1}(\omega, V_i, t)$, respectively. The perturbations of the prototype values are obtained by rearranging (4.19) as (see Appendix A)

$$\overline{g}_i(\omega, V_i, t) = g_i(\omega, V_i, t)/2 = \frac{\overline{\omega} b_i(\omega, V_i, t) \gamma_{0,i}(\omega, V_i, t)}{2} \tag{4.20}$$

where,

$$\gamma_{0,i}(\omega, V_i, t) = \left(\frac{Y_0}{g_0} \left(\frac{\prod_{k=1}^{[i/2]} J^2_{2k-1,2k}(\omega, V_i, t)}{\prod_{k=0}^{[(i-1)/2]} J^2_{2k,2k+1}(\omega, V_i, t)} \right) \right)^{(-1)^{i+1}} \tag{4.21}$$

where [.] refers to the floor function. $\gamma_{0,i}(\omega, V_i, t)$ is the impedance normalization factor for the ith lowpass prototype.

c. Pole Perturbation

The prototype perturbations due to reactive variations in the bandpass filter are used to find the real and imaginary pole-perturbation components for Butterworth and Chebyshev filters as follows:

Butterworth Filters: Fig. 85 shows the poles of a Butterworth filter arranged in a circle of unit radius in the complex s-plane. For Butterworth filters, the general

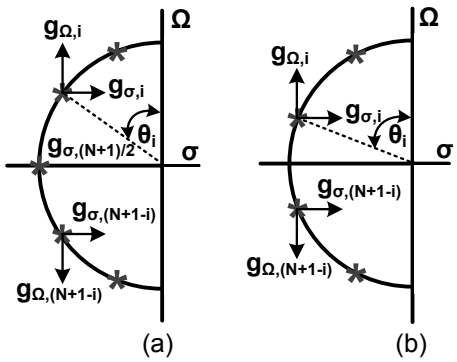

Fig. 85. Distribution of poles on the complex s-plane for Butterworth filters with (a) odd order (eg. N=5) and (b) even order (eg. N=4).

formula for a pole in terms of its angular location is given as [15]

$$\begin{aligned} p_i(\omega, V_i, t) &= j e^{\theta_i(\omega, V_i, t)} \\ &= -\sin\theta_i(\omega, V_i, t) + j\cos\theta_i(\omega, V_i, t) \end{aligned} \tag{4.22}$$

Thus, the pole-perturbations are limited to points on the unit circle and may be completely defined in terms of angular displacements $\theta_i(\omega, V_i, t)$. In odd-order filters, the $g_{\Omega,i}$ component of pole-perturbation causes the purely real pole to deviate from the real-axis. In this case, the driving point impedance of the prototype filter is no longer a positive real function implying that the filter output may be complex when the input is purely real. Clearly, this is untrue when the filter is composed of only RLC elements. Also, any perturbations by the $g_{\sigma,i}$ component leads to deviation from the unit circle and violates (4.22). Hence, the real axis poles remain *unperturbed* in odd-order filter realizations.

To obtain a direct relation between pole-perturbation p_i and reactive prototype values of the ladder network filter, $g_1, \ldots, g_N$, (4.22) is rewritten in terms of low-pass

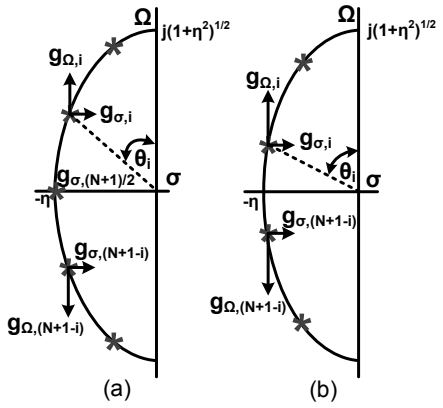

Fig. 86. Distribution of poles on the complex s-plane for Chebyshev filters with (a) odd order (eg. N=5) and (b) even order (eg. N=4).

prototype values using [15]

$$\sin\theta_i(\omega, V_i, t) = \overline{g}_i(\omega, V_i, t) \tag{4.23}$$

so that, the real and imaginary components of the pole-perturbation $p_i(\omega, V_i, t)$ for $i = 1, \ldots, N$ are expressed as

$$\begin{aligned} g_{\sigma,i}(\omega, V_i, t) &= \overline{g}_i(\omega, V_i, t); \\ g_{\Omega,i}(\omega, V_i, t) &= \pm\sqrt{1 - \overline{g}_i(\omega, V_i, t)^2} \end{aligned} \tag{4.24}$$

Chebyshev Filters: Fig. 86 shows the distribution of poles of a Chebyshev filter in the complex s-plane. The poles lie on an ellipse with major axis $\sqrt{1+\eta^2}$ and minor axis η. For Chebyshev filters, the general formula for a pole in terms of its angular location is given as [15]

$$p_i(\omega, V_i, t) = -j\cos\left[\sin^{-1} j\eta + \theta_i(\omega, V_i, t)\right] \tag{4.25}$$

By trigonometric manipulation, (4.25) can also be written as

$$p_i(\omega, V_i, t) = -\eta \sin\theta_i(\omega, V_i, t) - j\sqrt{1+\eta^2}\cos\theta_i(\omega, V_i, t) \tag{4.26}$$

Here, perturbations result in pole displacements along the ellipse and are completely defined in terms of angular displacements $\theta_i(\omega, V_i, t)$. However, real axis poles in odd-order filters remain *unperturbed* as in the case of Butterworth filters.

To determine pole-perturbations in a Chebyshev filter, a relationship between the angular pole locations $\theta_i(\omega, V_i, t)$ and the normalized low-pass prototype values $\overline{g}_i(\omega, V_i, t)$ is derived in Appendix B. The resulting expression is given by

$$\sin\theta_i(\omega, V_i, t) = \overline{g}_i(\omega, V_i, t) G_i \tag{4.27}$$

where,

$$G_i = \begin{cases} \gamma & i = 1 \\ \dfrac{1}{\gamma}\displaystyle\prod_{k=1}^{i/2} A(2k-1) \Big/ \prod_{k=2}^{i/2} A(2k-2) & i = 2, 4, 6, \ldots \\ \gamma \displaystyle\prod_{k=1}^{(i-1)/2} A(2k) \Big/ \prod_{k=1}^{(i-1)/2} A(2k-1) & i = 3, 5, 7, \ldots \end{cases} \tag{4.28}$$

with,

$$\begin{aligned} A(k) &= \gamma^2 + \sin^2(k\pi/N) \\ \gamma = \sinh(\beta/2N); &\qquad \beta = \ln(\coth(L_{Ar}/17.37)) \end{aligned} \tag{4.29}$$

Using (4.27) in (4.26), the real and imaginary components of pole-perturbation are given by

$$\begin{aligned} g_{\sigma,i}(\omega, V_i, t) &= \eta \overline{g}_i(\omega, V_i, t) G_i \\ g_{\Omega,i}(\omega, V_i, t) &= \pm\sqrt{(1+\eta^2)(1 - (\overline{g}_i(\omega, V_i, t) G_i)^2)} \end{aligned} \tag{4.30}$$

Since the pole-perturbation components are known explicitly for variations in the bandpass filter, the perturbed response of Butterworth or Chebyshev filters is calculated from (4.18). This methodology can be used to find the filter response due to any reactive perturbation in all-pole microwave bandpass filters.

d. Discussion

The analysis presented so far shows that the perturbation of poles is along the unit circle or ellipse in Butterworth or Chebyshev filters, respectively, only when the changes in the filter components are purely reactive in nature. This assumption is valid for the analysis of RF MEMS tunable filters because the dominant source of perturbations arise in the capacitance of the MEMS switches. If the quality factor of the resonator varies due to resistive perturbations, then the poles are laterally displaced as explained in Sec. a. Since the resonator quality factor is time invariant for a particular filter tuning state, more emphasis is given to purely reactive perturbations in tunable filters.

In odd order filters, the presence of an unperturbed real-axis pole seems to imply that its contribution to filter nonlinearity and noise is zero. However, this is not true because the perturbations of the filter transfer function arise from variations in the low-pass frequency variable $j\Omega_i$ associated with the real-axis pole, and hence contributes to the filter nonlinearity and noise.

3. Nonlinear Noise Perturbation in RF MEMS Tunable Filters

The exact nature of pole-perturbation components depends on the nonlinear noise mechanisms in the filter implementation. In RF MEMS tunable filters, Brownian, acceleration, acoustic and power-supply noise in MEMS switches [43] cause pole-perturbations. The perturbations also depend on the nonlinear behavior of the MEMS

switch. In this section, the nonlinear noise perturbations in RF MEMS tunable filters are discussed.

a. Nonlinear Analysis

The perturbation of an arbitrary pole on the complex plane is a function of the RF drive level in nonlinear microwave filters. Tunable filters employing RF MEMS switches exhibit nonlinear behavior due to nonlinear reactance change of the tuning element at high input power [13]. As a result, the resonance frequency of each resonator shifts and causes distortions in the amplitude and phase response of the tunable filter [94]. The degree of nonlinearity typically depends on the peak voltage appearing across the nonlinear element in the tunable filter. It is customary to use a power series expansion of the nonlinear capacitance variation in tuning elements expressed as [88]

$$C_u(V) = \sum_{m=0}^{\infty} c_m V^m \tag{4.31}$$

where c_m are constant coefficients obtained by curve fitting a polynomial to the characteristic function of the nonlinear tuning element. Fig. 76(a) shows a generalized all-pole tunable Butterworth or Chebyshev filter employing nonlinear tuning elements. The perturbation of each resonator depends on the node voltages $V_1, \ldots, V_N$ and consequently, the perturbation in the angular resonance frequency of each resonator due to capacitive nonlinearity is expressed as

$$\omega_{0i}(V_i) = \frac{1}{\sqrt{L_{ri} C_{ui}(V_i)}} \tag{4.32}$$

Also, since b_i is proportional to $\sqrt{C_{ui}(V_i)}$, the prototype perturbation $\overline{g}_i$ [(4.20)] and consequently pole-perturbation components $g_{\sigma,i}$ and $g_{\Omega,i}$ [(4.24), (4.30)] are functions of input power. Hence, to find the nonlinear perturbation of the filter response using

(4.18), the node voltages $V_1, \ldots, V_N$ for the bandpass filter must be known.

A method to calculate internal node voltages of a nonlinear microwave filter was described in Section C of this chapter. The lowpass internal node voltages v_i, and consequently the bandpass voltages V_i, are found by solving the nonlinear system of nodal equations of the equivalent lowpass filter [Fig. 76(b)] expressed by (4.5)-(4.10) using the iterative method in Fig. 77. At high input power, the voltages V_i may be high enough to cause pull-down in MEMS switches [33]. In this case, the system of nonlinear equations will not have convergent solutions due to drastic change in the nonlinear capacitance-voltage relationship of the tuning element. Once V_i is known, the capacitance and angular frequency variations in (4.31) and (4.32), respectively, are used to find the nonlinear perturbations in the real and imaginary directions using (4.20), (4.24) and (4.30).

b. Noise Analysis

The time-varying nature of pole-perturbations is due to noise sources that cause random capacitance variations in an LC resonator employing shunt capacitive MEMS switches [33]. It is important to derive expressions for random capacitance variations in a MEMS resonator in the presence of nonlinearity. Here, the approach is presented for Brownian noise and similar equations corresponding to other noise sources in MEMS switches can be derived accordingly.

Fig. 87(a) shows an RF signal with peak voltage V_s and angular frequency ω_0 applied across the resonator. The MEMS switch has an up-state capacitance of C_u, bridge inductance L_s, and switch resistance R_s. The resonator inductance is assumed lossless and has a value of L_r. Fig. 87(b) shows various displacements in a MEMS switch, under the influence of an applied RF signal. In the absence of a biasing voltage and RF signal, the bridge height is g_0. When the RF signal is applied, the

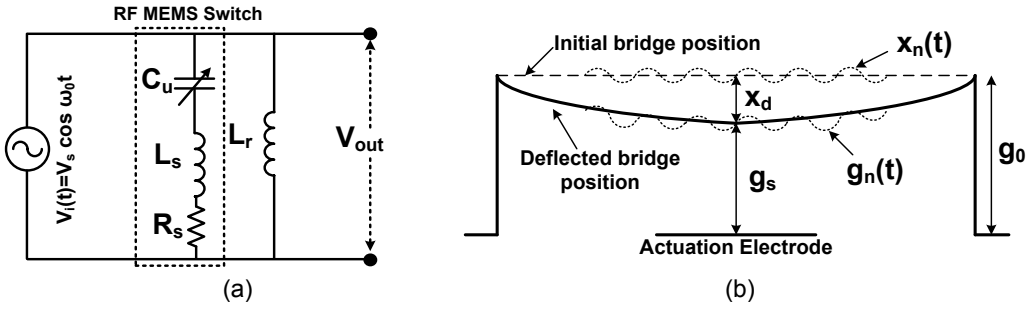

Fig. 87. (a) A tunable RF MEMS shunt resonator, and (b) various displacements in an RF MEMS shunt capacitive switch.

self-biasing effect [33] causes beam deflection of x_d resulting in a static bridge height of g_s. Brownian motion results in random displacements of $x_n(t)$ when an RF signal is absent, and $g_n(t)$ when an RF signal is present $[x_n(t) \neq g_n(t)]$, so that the overall bridge displacement is $g = g_s + g_n(t)$.

As mentioned in Section B of this chapter, a MEMS switch with an effective area A, spring constant k, damping factor b and mechanical self-resonant frequency ω_m has a thermally induced, root-mean-square mechanical force acting on the bridge given by $f_n = \sqrt{4k_BTb}$, where k_B is the Boltzmann constant and T is the temperature in Kelvin. The power spectral density of Brownian motion displacement noise is given by (4.1). In the absence of an RF signal, a sinusoidal component of Brownian noise in a 1-Hz bandwidth around $\omega'/2\pi$ is given by (4.2).

If the MEMS switch capacitance has a parallel-plate capacitance, $C_{pp} = \epsilon_0 A/g$, and a fringing capacitance, $C_f = \gamma C_{pp}$, where γ is the fringing factor ($\gamma < 1$), then $C_u = C_{pp} + C_f$ and $E_c = (1/2)C_u V_r^2$ is the stored energy when the rms-voltage across the MEMS switch is V_r. However, in an LC resonator, E_c is a time-varying function due to energy transfer between the capacitor and inductor. The instantaneous electrostatic force on the MEMS switch is obtained by differentiating E_c with respect to g. The bridge displacements in the presence of an RF signal are then obtained by

equating the electrostatic and spring restoring force to the total applied noise force and is expressed as

$$\left|\frac{\partial E_c}{\partial g}\right| - k(g_0 - g) = f_n(t) \tag{4.33}$$

where $f_n(t) = kx_n(t)$ is the applied noise force that causes noisy displacements.

In the absence of Brownian noise ($f_n(t) = 0$), (4.33) is solved to find the static bridge height g_s. Random displacements in the presence of Brownian noise are obtained by dividing (4.33) by spring constant k and using binomial approximations ($g_n << g_s$) to find $g_n(t)$ as

$$g_n(t) \cong \frac{x_n(t)}{1 - (2x_d/g_s)} \tag{4.34}$$

where $x_d = g_0 - g_s$. The overall capacitance variation in the MEMS resonator is given by

$$C_u(t) \cong (1 + \gamma)\frac{\epsilon_0 A}{g_s + g_n(t)} \tag{4.35}$$

In the absence of an RF signal, $x_d = 0$ in (4.34), and $g_n(t)$ reduces to $x_n(t)$. The noisy displacements in (4.34) are accurate at low input power levels. When the rms-voltage across the switch approaches pull-down voltage at high input power, $x_d \rightarrow g_0/3$ and $g_s \rightarrow 2g_0/3$ so that the denominator of (4.34) approaches zero. Clearly, this is unrealistic and hence higher order binomial terms must be considered in (4.33) for calculating $g_n(t)$ when the switch is close to self-actuation at high input power.

In practice, tunable MEMS resonators are realized with a parallel combination of 'P' switched capacitors as shown in Fig. 88. Each switched capacitor is a series combination of a MEMS switch and a fixed metal-air-metal capacitor [74]. The noisy capacitance variation of each MEMS switch is calculated using (4.34) and (4.35) but the voltage V'_{rp}, ($p = 1, \ldots, P$) must be used for calculation of static bridge displace-

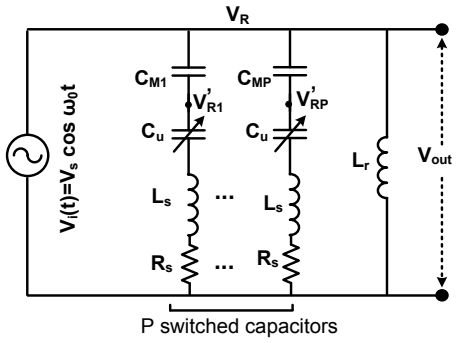

Fig. 88. A tunable MEMS resonator implemented with P switched capacitors.

ment due to capacitive voltage division. Thus, the overall capacitance variation of a capacitor bank is the superposition of the noisy contribution of each MEMS switch. Since the Brownian noise sources are independent of each other, the resulting capacitance variations in each switch are also uncorrelated to each other [43]. Thus, noise sources in the resonator result in a time-varying capacitance that can be mapped to prototype perturbations using (4.20), and the corresponding time-varying pole-perturbations. The time-varying low-pass frequencies are calcuated using $\omega_{0i}(V_i, t)$ in (4.16) and the perturbed filter response is found using (4.18).

c. Phase Noise Calculations

If the pole-perturbations due to nonlinearity and noise in the tunable filter are known, then the response of the filter to these variations can be calculated. The uncorrelated nature of independent Brownian noise sources implies that the noise power contribution due to each noise source must be calculated independently. For example, in a tunable filter with ideal inverters which employs MEMS resonators with 'P' MEMS switches per resonator (Fig. 88), the perturbation of the ith-resonator only due to noise in the pth switch ($p = 1, \ldots, P$) is calculated, while assuming all other switches are noiseless. Since the amplitude noise of RF MEMS switches is at least 20 dB lower

than its phase noise [43], the effect of phase variations at the filter output will be considered. Using (4.18), the phase variations of S_{21} when the ith-pole is perturbed due to noise in the pth-switch is expressed as

$$\angle S_{21}^{i,p}(\omega, V_i, t) = -\sum_{i=1}^{N} \tan^{-1}\left(\frac{\Omega_i(\omega, V_i, t) + s(\psi) g_{\Omega,i}(\omega, V_i, t)}{g_{\sigma,i}(\omega, V_i, t)}\right) \tag{4.36}$$

where $\psi = \mathrm{Im}(p_i(\omega, V_i, t))$ is the imaginary component of pole variation described in (4.14) and $s(\psi)$ is the signum function defined as

$$s(\psi) = \begin{cases} -1 & \text{if } \psi < 0, \\ 0 & \text{if } \psi = 0, \\ +1 & \text{if } \psi > 0; \end{cases}$$

In odd order filters, the real-axis pole is unperturbed and thus $g_{\Omega,(N+1)/2} = 0$ and $g_{\sigma,(N+1)/2}$ has a constant value independent of input power and noise. The signal at the filter output is expressed as

$$V_o^{i,p}(\omega_0, V_i, t) = V_s \cos(\omega_0 t + \angle S_{21}^{i,p}(\omega_0, V_i, t)) \tag{4.37}$$

The phase noise power ($P_{ph}^{i,p}$) due to pth-switch in resonator i, normalized to the output carrier power, is obtained by taking the Fourier transform of $V_o^{i,p}(\omega_0, V_i, t)$. The overall filter phase noise is obtained by summing the phase noise contributions of each switch in every resonator in the filter topology, and is given by

$$P_{ph} = \sum_{i=1}^{N} \sum_{p=1}^{P} P_{ph}^{i,p} \tag{4.38}$$

Fig. 65(c) shows the non-linear electromechanical CAD model of the RF MEMS switch [44], which is implemented using equation-based blocks in Agilent ADS. The power-dependent, noisy behavior of a MEMS switch is described by this non-linear

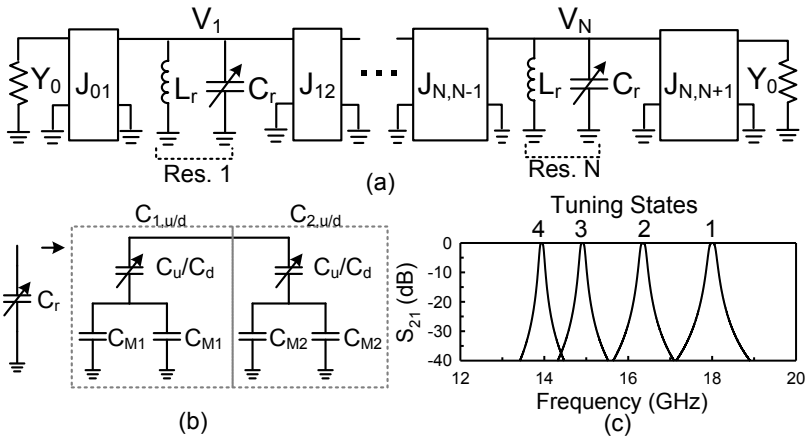

Fig. 89. (a) An N-pole lossless Butterworth/Chebyshev tunable filter with ideal admittance inverters, (b) variable capacitor implementation using 2-bit RF MEMS switched capacitor banks, and (c) simulated S-parameters of a lossless two-pole tunable Butterworth filter with 1% fractional bandwidth.

CAD model and is used in a resonator or inverter to find the tunable filter phase noise by performing harmonic balance noise simulation in ADS, and provides an independent means to verify the theory presented in this paper.

4. RF MEMS Tunable Filter Example

In this section, the theory of pole-perturbations developed so far will be applied to an RF MEMS tunable filter. The effect of nonlinearity on the pole distributions will be discussed and verified by group delay calculations. Phase noise due to Brownian noise will be evaluated for different filter parameters and verified by harmonic balance noise simulations.

a. Design

A lossless N-pole Butterworth/Chebyshev filter with a tunable center frequency from 14-18 GHz is shown in Fig. 89(a). In Fig. 89(b), the resonator capacitance is

Table X. Resonator Model Element Values Used for ADS Simulations

-	L_r		0.46 nH
-	C_{Mp} (fF)	$C_{p,u}$ (fF)	$C_{p,d}$ (fF)
$p = 1$	55	71	107
$p = 2$	90	95	171

Table XI. MEMS Switch Model Parameters

Bridge length, L (μm)	285	Initial bridge height, g_0 (μm)	1
Bridge width, w (μm)	130	Spring constant, k (N/m)	45
Electrode width, W (μm)	160	Mech. Q-factor, Q_m	1
Bridge thickness, t (μm)	1.5	Mech. res. freq, f_m (kHz)	65
Dielectric thickness, t_d (μm)	0.2	Switch inductance, L_s (pH)	10
Up-state cap., C_u (fF)	202	Switch resistance, R_s (Ohm)	0.6
Down-state cap., C_d (pF)	3.5	Pull-down voltage, V_p (V)	8.5
Fringing factor, γ	0.1	-	-

implemented as a 2-bit RF MEMS capacitor bank. The values of ideal, lossless J-inverters are calculated for a given fractional bandwidth using formulas in [15]. Table X shows the resonator inductance (L_r), fixed metal-air-metal capacitors (C_{Mp}), and up/down-state capacitances ($C_{p,u}$, $C_{p,d}$) for each switched capacitor using the MEMS switch parameters in Table XI. This switch could be the standard capacitive switch with a center pull-down electrode developed in [95] or a capacitive switch developed by the University of Michigan [74]. Fig. 89(c) shows the ADS simulation of S_{21}-parameters for a two-pole lossless 1% Butterworth filter. States 1 and 4 represent the situation where all the switches are in the up- and down-state, respectively.

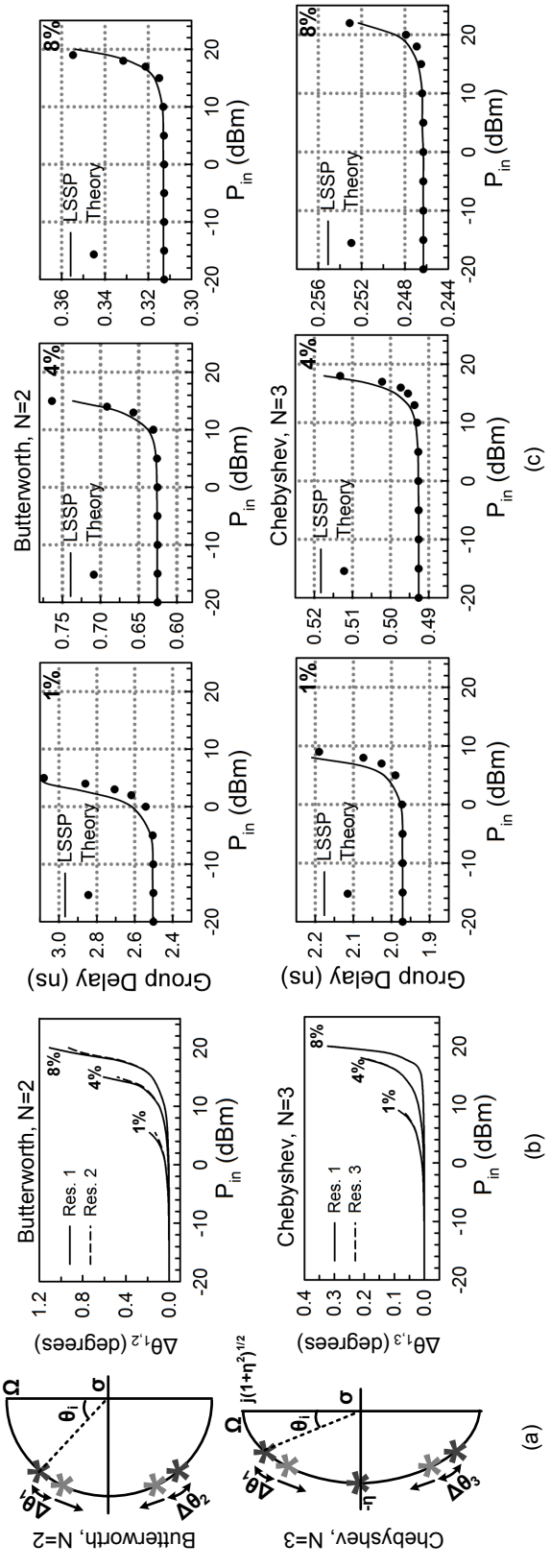

Fig. 90. (a) Nonlinear pole displacements in a two-pole Butterworth and three-pole Chebyshev filter, (b) angular displacements of poles as a function of applied input power for different filter fractional bandwidths, and (c) group delay as a function of input power in two-pole Butterworth and three-pole Chebyshev filters for different filter fractional bandwidths. Theoretical values are compared to large signal S-parameter (LSSP) simulations in ADS.

b. Nonlinearity

Using the switch parameters in Table XI, the capacitance-voltage variation in the up-state position is obtained by solving (4.33) in the absence of noise and curve-fitting to a power-series approximation as

$$C_u(V) = 202.52 + 0.175V^3 \qquad \text{(in fF)} \tag{4.39}$$

where V is the rms-voltage across the MEMS switch. The nonlinear expression in (4.39) is valid as long as V is less than the pull-down voltage V_p of the MEMS switch. The resonator voltages V_i, $i = 1, \ldots, N$, in Fig. 89 are calculated using (4.39) in the nonlinear system of nodal equations as described in Section D.3.a of this chapter. The resulting prototype perturbations due to nonlinearity are evaluated using (4.20) corresponding to resonator perturbations $C_u(V_i)$.

Fig. 90(a) shows nonlinear pole displacements in the absence of noise, in a two-pole Butterworth and three-pole Chebyshev filter. As input power increases, higher resonator capacitance and susceptance slope implies that complex conjugate poles are angularly displaced by $\Delta\theta_i$ towards the real axis along the circle or ellipse. However, the real axis pole of the three-pole Chebyshev filter is unperturbed. The angular displacements calculated using (4.23) and (4.27) are shown in Fig. 90(b) as a function of input power for different fractional bandwidths. Filters with smaller fractional bandwidth exhibit greater nonlinearity due to larger resonator voltages, V_i, and consequently have higher angular displacements for the same input power.

The small angular pole-perturbations caused by filter nonlinearity do not noticeably affect the amplitude response of the filter. However, changes in the phase response affect the group delay of the bandpass filter. Nonlinear pole displacements are used to derive an analytical expression for power-dependent group delay at filter

center frequency in the absence of noise by differentiating (4.36) with respect to ω which is given by

$$\tau(\omega_0, V) \cong \tau_{\text{real}} + \frac{2}{\overline{\omega}\omega_0} \times \sum_{\substack{\text{complex} \\ \text{poles}}} \frac{g_{\sigma,i}(\omega_0, V)}{(\Omega_i(\omega_0, V) + s(\psi) g_{\Omega,i}(\omega_0, V))^2 + g_{\sigma,i}^2(\omega_0, V)} \tag{4.40}$$

where the summation includes the group delay contribution of each complex-conjugate pole and τ_{real} is the power-independent group delay contribution of the real axis pole in odd-order filters which is given by

$$\tau_{\text{real}} = \frac{2}{\overline{\omega}\omega_0} \begin{cases} 1 & \text{for Butterworth} \\ 1/\eta & \text{for Chebyshev} \end{cases} \tag{4.41}$$

For even order filters, $\tau_{\text{real}} = 0$ due to the absence of a real axis pole. To verify (4.40)-(4.41), group delay values are calculated using large signal S-parameter simulations in Agilent ADS for lossless Butterworth (N=2) and Chebyshev (N=3) filters in Fig. 89 and the results show good agreement between theory and simulation [Fig. 90(c)]. Small discrepancies between theory and simulation are due to the nonlinear approximation in (4.39). Since group delay is inversely proportional to filter bandwidth ($\overline{\omega}\omega_0$), filters with small fractional bandwidth have higher and rapidly changing group delay values as input power is increased. Also, filters with larger group delay have greater sensitivity to noise as was seen in Sec. B of this chapter. Hence, similar trends are expected in tunable filter phase noise as a function of input power. This is discussed in the next section.

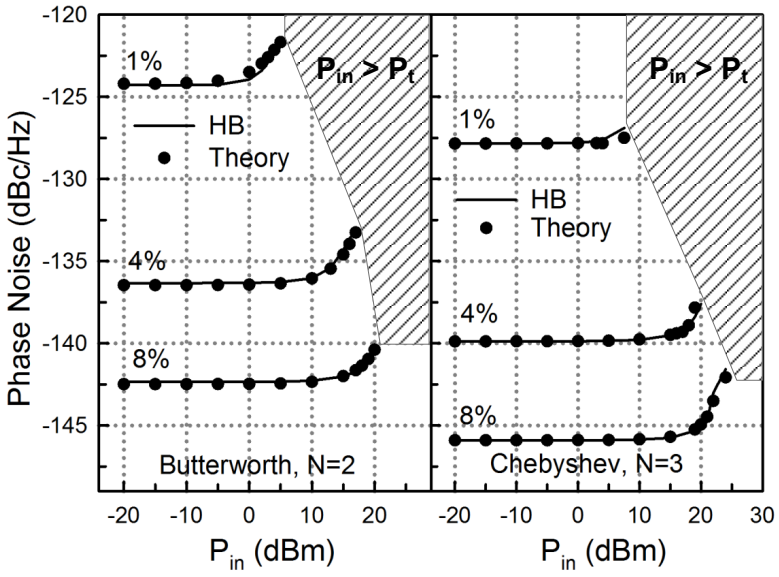

Fig. 91. Phase noise of lossless two-pole Butterworth and three-pole Chebyshev filters as a function of input power for different fractional bandwidths, evaluated at an offset of $\omega' = 2\pi \times 9$ kHz ($\omega' < \omega_m$) around $f_0 = 18$ GHz.

c. Phase Noise

The nonlinear noise perturbations in RF MEMS tunable filters are used to calculate phase noise as described in Section D.3.c of this chapter. Phase noise is evaluated at a mechanical offset frequency of $\omega' = 2\pi \times 9$ kHz from the filter center frequency of a particular tuning state with $P_{in} = -20$ dBm, unless otherwise specified. The frequency offset is an arbitrary choice and gives the same phase noise values for other frequency offsets as long as $\omega' < \omega_m$. In the graphs that follow, all results obtained from harmonic balance simulations are denoted by 'HB'.

The phase noise of Butterworth (N=2) and Chebyshev (N=3) filters versus input power for different fractional bandwidths are shown in Fig. 91. In both cases, only two poles are fluctuating since real axis poles are unperturbed. Also, smaller bandwidth filters exhibit higher phase noise and increasing the input power results

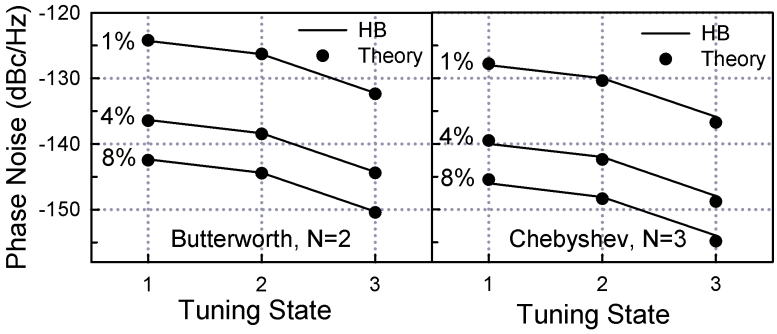

Fig. 92. Phase noise of lossless two-pole Butterworth and three-pole Chebyshev filters versus tuning state for different fractional bandwidths, evaluated at an offset $\omega' = 2\pi \times 9$ kHz ($\omega' < \omega_m$) from the center frequency of that tuning state with $P_{in} = -20$ dBm.

in higher phase noise. This is because smaller bandwidth filters have higher group delay and increasing input power results in higher values of group delay as explained in the previous section. When the input power exceeds a threshold value ($P_{in} > P_t$), the resonator voltages V_i results in the pull-down of MEMS switches in the tunable filter (shaded region in Fig. 91). Phase noise values calculated around filter center frequency in this region are invalid due to change in the filter tuning state.

Fig. 92 shows the variation of phase noise with filter tuning state in lossless Butterworth and Chebyshev filters for different fractional bandwidths. MEMS switches in the down-state position are not affected by Brownian noise because the bridge is fixed [43], and hence state 4 does not exhibit phase noise. For states 2 and 3, phase noise decreases because the fluctuation of each pole is reduced due to the presence of only one Brownian noise source in the resonator. However, compared to state 2, state 3 exhibits lower phase noise because the resonator capacitance variation is smaller due to a higher fixed capacitance ($2C_{M2}$) in series with the MEMS switch [Fig. 89(b)].

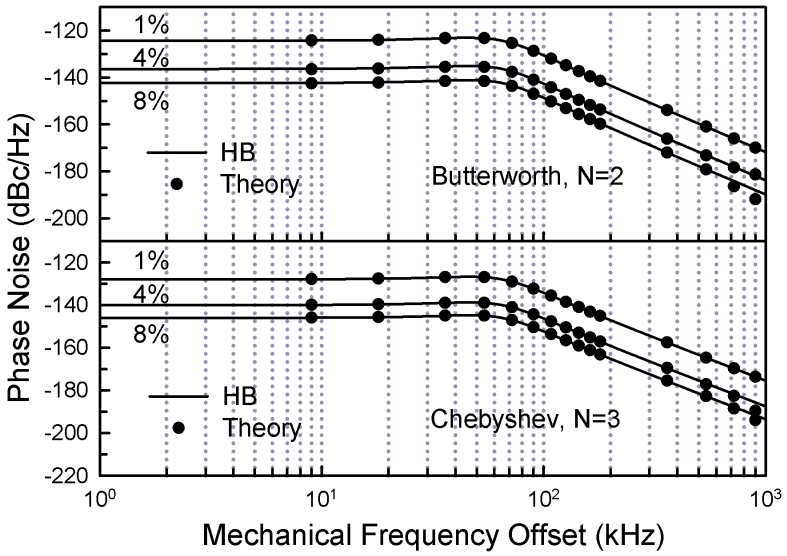

Fig. 93. Phase noise as a function of mechanical frequency offset around f_0=18 GHz in lossless two-pole Butterworth and three-pole Chebyshev filters for different fractional bandwidths at P_{in}=-20 dBm.

Fig. 93 shows the variation of phase noise with mechanical frequency offset ($\omega'/2\pi$) for different fractional bandwidths. As the mechanical frequency offset is increased, the magnitude of pole fluctuations follow the low-pass displacement noise spectrum described in (4.1). Consequently, phase noise remains approximately constant for $\omega' < \omega_m$ and decreases at a rate of -40 dB/decade for $\omega' > \omega_m$.

For higher filter orders, the group delay given by (4.40)-(4.41) increases due to greater number of positive summation terms, resulting in higher filter phase noise as shown in Fig. 94 for the lossless case. Phase noise increases with filter order more rapidly in Chebyshev filters compared to Butterworth filters due to rapid increase of group delay with filter order in Chebyshev filters which can be found using (4.40)-(4.41).

In practice, filter resonators and inverters always dissipate energy due to loss

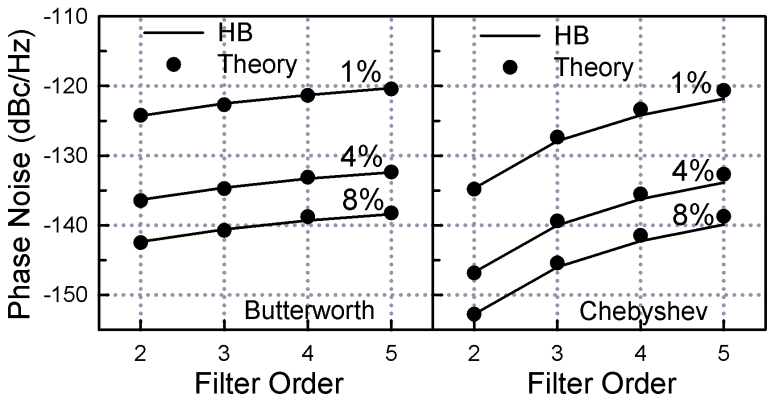

Fig. 94. Phase noise as a function of filter order for different fractional bandwidths of lossless Butterworth and Chebyshev filters, evaluated at an offset $\omega' = 2\pi \times 9$ kHz ($\omega' < \omega_m$) around f_0=18 GHz with P_{in}=-20 dBm.

mechanisms. Also, inverters exhibit frequency-dependent behavior as the filter center frequency is tuned. These bandpass filter nonidealities affect the pole-perturbations of the equivalent prototype filter and need to be considered in greater detail.

5. Filter Nonidealities

a. Resonator Q-factor

In the practical realization of tunable filters, energy dissipation due to resistive losses in the resonator results in a finite unloaded resonator Q-factor (Q_u). If losses in the filter transfer function are taken into account, each pole on the left-half of the complex plane is moved to the left by a constant value δ as shown in Fig. 95(a). For a lossy bandpass filter with fractional bandwidth $\overline{\omega}$, the dissipation factor δ, is calculated as [96]

$$\delta = \frac{1}{\overline{\omega} Q_u} \tag{4.42}$$

Thus, the real-axis component of pole p_i is obtained by the transformation $g_{\sigma,i}(\omega_0, V_i, t)$ $\rightarrow g_{\sigma,i}(\omega_0, V_i, t) + \delta$. The filter group delay obtained by including time-variance in (4.40) decreases because $\tau(\omega_0, V, t)$ is approximately proportional to $1/g_{\sigma,i}(\omega_0, V_i, t)$. The reduction in group delay is more drastic in filters with small fractional bandwidth. Hence, as the filter insertion loss increases due to lower Q_u, reduced filter group delay at center frequency causes phase noise to decrease as shown in Fig. 95(b). The phase noise values obtained from theory are in good agreement with harmonic simulations of the tunable filter shown in Fig. 89 with a resistance $R_r = \omega_0 L_r Q_u$ in parallel with each resonator. All phase noise calculations are performed at a frequency offset $\omega' = 2\pi \times 9$ kHz around $f_0 = 18$ GHz with $P_{in} = -20$ dBm and normalized to the phase noise of an equivalent lossless filter. However, reducing filter phase noise by lowering resonator Q-factors is impractical because the resulting filters have poor insertion loss especially for filters with small fractional bandwidth. For example, a three-pole 1% Chebyshev filter with $Q_u = 50$ has an insertion loss of around 17 dB which is not a realistic value for practical applications.

When resistive losses are present, there is a thermal noise voltage associated with the equivalent resistance in each resonator. Thermal noise does not alter the level of filter phase noise because it does not result in any changes in the reactance of filter components. However, it results in an overall increase in the amplitude noise level at the filter output and is estimated using harmonic balance simulation. For all the cases considered here, the presence of thermal noise increases the amplitude noise level by a maximum value of 5 dB for high fractional bandwidth filters. However, the resulting amplitude noise is still insignificant compared to the phase noise at the filter output.

As input power is increased, the internal node voltages must be calculated as described in Section D.3.a of this chapter, by shunting each node in the low-pass

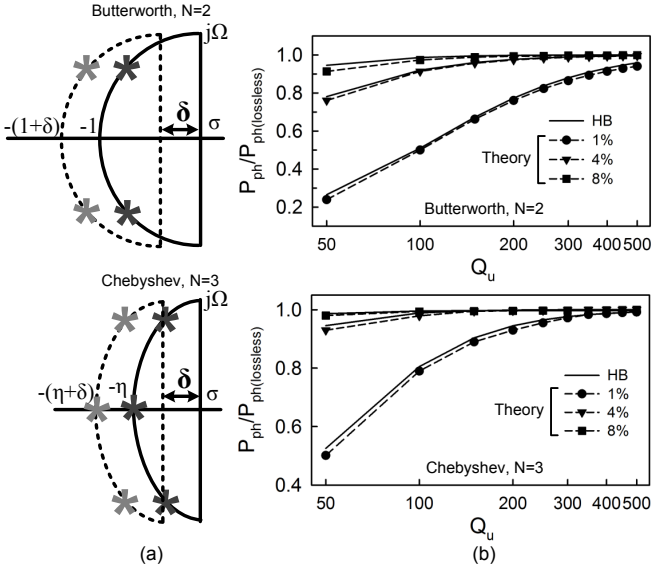

Fig. 95. (a) Displacement of poles to the left by δ due to losses present in the resonators of the tunable filter, and (b) Phase noise (P_{ph}) versus Q_u for different fractional bandwidths in a two-pole Butterworth and three-pole Chebyshev filter with noise calculation performed at a frequency offset $\omega' = 2\pi \times 9$ kHz ($\omega' < \omega_m$) around $f_0 = 18$ GHz with $P_{in} = -20$ dBm and normalized to the phase noise of the equivalent lossless filter.

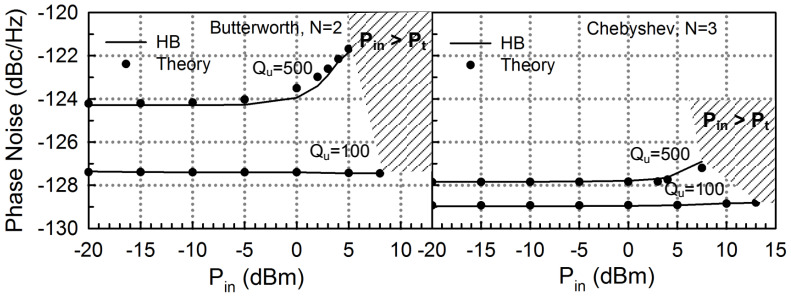

Fig. 96. Variation of phase noise versus input power in a two-pole Butterworth and three-pole Chebyshev filter with 1% fractional bandwidths for $Q_u = 100$ and $Q_u = 500$. Phase noise is evaulated at a frequency offset $\omega' = 2\pi \times 9$ kHz ($\omega' < \omega_m$) around $f_0 = 18$ GHz.

filter [Fig. 76(b)] by a conductance δ. Nonlinear pole displacements due to internal voltages in lossy filters must be considered in phase noise computation. Fig. 96 shows the variation of phase noise versus input power for different values of Q_u, for 1% Butterworth ($N = 2$) and Chebyshev ($N = 3$) filters. Phase noise is relatively insensitive to input power at low Q_u in 1% filters because the pole displacement by δ due to loss makes the group delay function $\tau(\omega_0, V, t)$ relatively insensitive to nonlinear pole displacements. In filters with 8% fractional bandwidth, phase noise increases with input power as shown in Fig. 91 even for $Q_u = 100$ because phase noise is relatively insensitive to Q_u for high bandwidth filters.

b. Nonideal Inverters

Equivalent π-models for inductive and capacitive implementations of admittance inverters are shown in Figs. 97(a), (b). Practical inverter networks exhibit frequency-dependence and dissipate energy due to resistive losses. A generalized frequency-dependent admittance inverter including loss mechanisms is shown in Fig. 97(c) [97]. Tunable inverter networks have also been implemented to achieve constant fractional bandwidth or good input matching over the filter tuning range [64]. In this section, the effect of inverter implementation on RF MEMS filter phase noise is investigated using pole-perturbation method.

Frequency dependence: In practical filters, inverters are designed at the filter center frequency and are considered to be frequency-independent within the filter passband in narrow-band (<10%) filters. However, as the filter is tuned to frequencies away from the design frequency, the change in J-inverter values result in bandwidth variation as the filter is tuned. As a result, the filter phase noise also exhibits frequency-dependent behavior based on the inverter implementation.

The inductive inverter in Fig. 97(a) is commonly implemented as a transformer

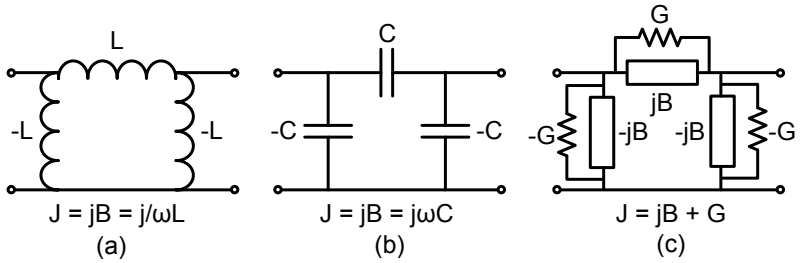

Fig. 97. Equivalent π-models for admittance inverters using (a) inductors, and (b) capacitors. (c) Generalized lossy admittance inverter.

with coupling coefficient k [83], while the capacitive inverter in Fig. 97(b) is implemented as a series capacitor [64]. In both cases, the negative shunt elements are absorbed into adjacent resonators. For an N-pole tunable filter, the expressions for half-admittance input/output J-inverters J_{io}) and inter-resonator J-inverters ($J_{i,i+1}, i = 1, \ldots, N-1$) are expressed as [1]

$$J_{io}(\omega) = \frac{B_{io}(\omega)Y_0}{\sqrt{Y_0^2 + B_{io}^2(\omega)}}; \qquad J_{i,i+1}(\omega) = B_{i,i+1}(\omega) \tag{4.43}$$

where,

$$\begin{aligned} B_{io}(\omega) &= \frac{k_{io}}{\omega(2L_r)(1-k_{io}^2)} \\ B_{i,i+1}(\omega) &= \frac{k_{i,i+1}}{\omega(2L_r)(1-k_{i,i+1}^2)} \quad \text{for inductive inverters} \end{aligned} \tag{4.44}$$

and

$$\begin{aligned} B_{io}(\omega) &= \omega C_{io} \\ B_{i,i+1}(\omega) &= \omega C_{i,i+1} \quad \text{for capacitive inverters} \end{aligned} \tag{4.45}$$

for $i = 1, \ldots, N-1$. For inductive inverters, k_{io} and $k_{i,i+1}$ are the coupling coefficients for the input/output and inter-resonator transformers, respectively, and $2L_r$ is the self-inductance of each transformer winding. Similarly, C_{io} and $C_{i,i+1}$ are series capacitors in capacitive inverters.

The expressions for frequency dependent inverters are used to calculate the

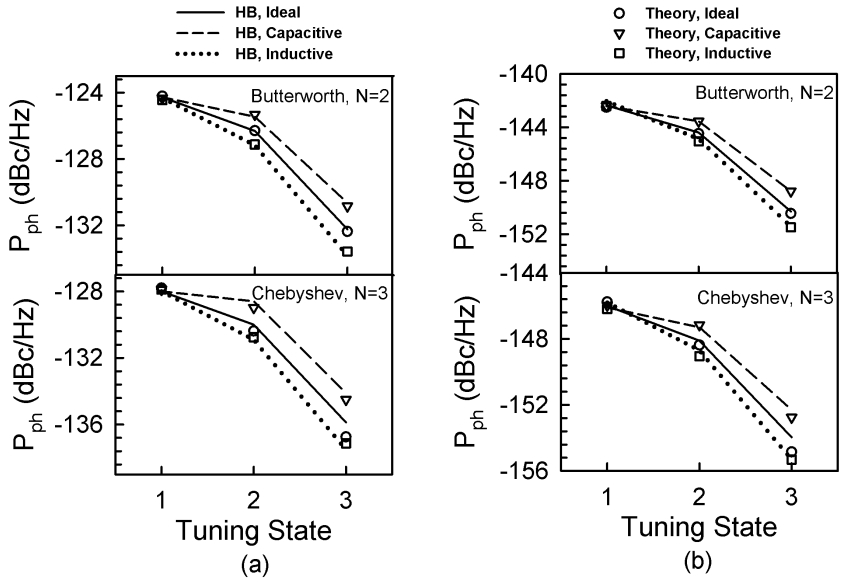

Fig. 98. Comparison of phase noise versus tuning state in lossless Butterworth ($N = 2$) and Chebyshev ($N = 3$) filters with (a) 1% and (b) 8% fractional bandwidths employing ideal, capacitive and inductive inverters. Phase noise is evaluated with $P_{in} = -20$ dBm at a frequency offset $\omega' = 2\pi \times 9$ kHz around the center frequency of that tuning state.

impedance normalization factor $\gamma_{0,i}(\omega)$ as a function of frequency using (4.21). The resulting frequency dependent pole displacements are calculated from (4.20) and used to compute phase noise due to Brownian motion in the resonators.

Fig. 98 shows the phase noise variation in lossless Butterworth ($N = 2$) and Chebyshev ($N = 3$) filters [Fig. 89] with 1% and 8% fractional bandwidths versus tuning state for different inverter implementations. Phase noise is evaluated with $P_{in} = -20$ dBm at a frequency offset $\omega' = 2\pi \times 9$ kHz ($\omega' < \omega_m$) around the center frequency of that tuning state.

For inductive inverters, the J-inverter values are monotonically decreasing functions of frequency so that fractional bandwidth increases as the filter is tuned to lower frequencies. Consequently, lower filter group delay causes a rapid decrease of

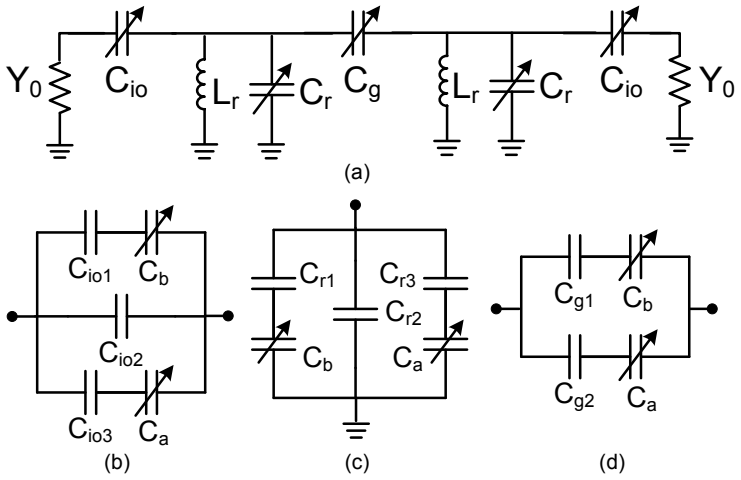

Fig. 99. (a) A lossless two-pole Chebyshev filter tunable from 15-18 GHz with a constant fractional bandwidth of 8±0.1% with two-bit switched-capacitor bank implementations of (b) input/output capacitor C_{io}, (c) resonator capacitance C_r and (d) inter-resonator capacitance C_g.

phase noise as the filter is tuned compared to the ideal case. For capacitive inverters, fractional bandwidth decreases as the filter is tuned to lower frequencies resulting in slower decrease of phase noise compared to the ideal case. In all cases, increasing the input power increases phase noise for all tuning states which depends on the nonlinear behavior of resonators of that tuning state as discussed earlier.

Tunability: Filters with inductively coupled resonators and capacitive tuning mechanisms exhibit relatively constant fractional bandwidth as the filter is tuned but exhibit degradation of input matching in wideband tunable filters [74]. Instead, tunable MEMS capacitive inverters may be employed to adjust the J-inverter values to maintain constant fractional bandwidth and good input matching simultaneously [64]. Fig. 99 shows a lossless two-pole Chebyshev filter tunable from 15-18 GHz implemented with two-bit switched capacitor banks in the resonators and inverters, and has fractional bandwidths of 8±0.1% over all tuning states. The parameters of

the MEMS switch (C_a/C_b) are the same as the one in Table XI and the values of inductors and fixed capacitors are given in Table XII. The resonator implementation is different compared to Fig. 89(b) and hence a corresponding change in phase noise is expected for the same filter bandwidth.

MEMS tunable inverters are additional sources of noise in a tunable filter that increase the level of phase noise at the filter output. The noisy inverter capacitors $C_{io}(t)$ and $C_{i,i+1}(t)$ result in noisy inverter values, $J_{io}(\omega, V_{io}, t)$ and $J_{i,i+1}(\omega, V_{i,i+1}, t)$ [(4.43), (4.45)], where V_{io} and $V_{i,i+1}$ are the voltages across the respective inverters. Thus, the impedance normalization factor $\gamma_{0,i}(\omega, V, t)$ and the resulting pole displacements obtained are used to calculate phase noise.

Table XII. Tunable Filter Model Element Values

-	L_r		0.15 nH
-	$C_{r,p}$ (fF)	$C_{io,p}$ (fF)	$C_{g,p}$ (fF)
$p = 1$	160	130	60
$p = 2$	230	50	120
$p = 3$	325	250	-

Fig. 100 shows the phase noise values obtained from theory and harmonic balance simulation. Phase noise is evaluated with $P_{in} = -20$ dBm at a frequency offset $\omega' = 2\pi \times 9$ kHz around the center frequency of that tuning state. In case 1, the resonators are assumed to be noiseless and phase noise only due to noisy inverters is calculated and results in around 4-6 dB lower phase noise than the filter with noiseless inverters and noisy resonators (case 2), for all tuning states. When the input power is changed from -20 dBm to +20 dBm for case 1, the phase noise increases by less than 0.1 dB, implying that MEMS tunable inverter nonlinearity is not a significant factor in phase noise calculation. Noise from tunable inverters increases the overall phase

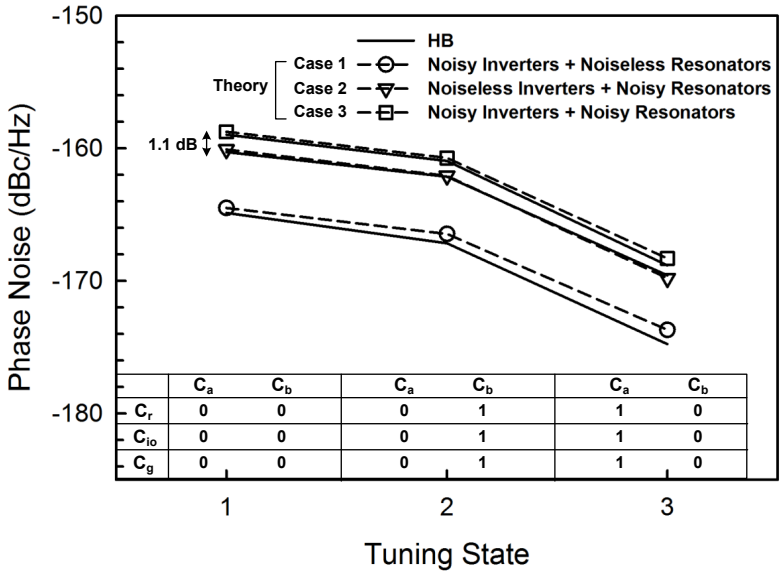

Fig. 100. Variation of phase noise with tuning state in a two-pole Chebyshev filter with a constant fractional bandwidth of 8±0.1% considering only noisy inverters, only noisy resonators and both noisy inverters and resonators. Phase noise is evaluated with $P_{in} = -20$ dBm at a frequency offset $\omega' = 2\pi \times 9$ kHz around the center frequency of that tuning state. The MEMS switch combinations for each state are also shown in the figure where '0' and '1' represent up- and down-state positions, respectively.

noise of the tunable filter (case 3) by just around 1.1 dB for $P_{in} = -20$ dBm. This analysis shows that the dominant source of nonlinear noise in tunable filters is the fluctuations in the resonators and the effect of nonlinear noise in inverters is relatively insignificant.

Loss: Inverter losses result in a resistive signal path between two resonators besides a reactive path and is represented by a complex admittance inverter with susceptance B and conductance G as $J = jB + G$ as shown in Fig. 97(c). If the series element of the inverter has a quality factor of Q_c, then $G = B/Q_c$. The negative loss associated with the shunt elements is absorbed by an adjacent lossy microwave resonator [97]. Assuming resonators have a finite Q-factor, and that all inverters have the same quality factor Q_c, phase noise calculations for Butterworth and Chebyshev tunable filters with different fractional bandwidths using complex values of admittance inverters indicate that filter phase noise variation due to inverter loss is insignificant for $Q_c > 10$. Since typical realizations of fixed/tunable inverters in MEMS filters (interdigital capacitors, coupled-inductors, tunable capacitor banks, etc.) have quality factors much greater than 10, phase noise variation due to inverter losses is negligible.

6. Signal-to-Noise Ratio Analysis

In this section, the implications of phase noise on SNR at the output of the MEMS tunable filter are discussed. Fig. 101(a) shows an antenna connected to the input of a MEMS tunable bandpass filter, in a 50 Ω system. The equivalent noise resistance of the antenna is assumed to be 50 Ω. All power values are expressed in watts unless otherwise specified.

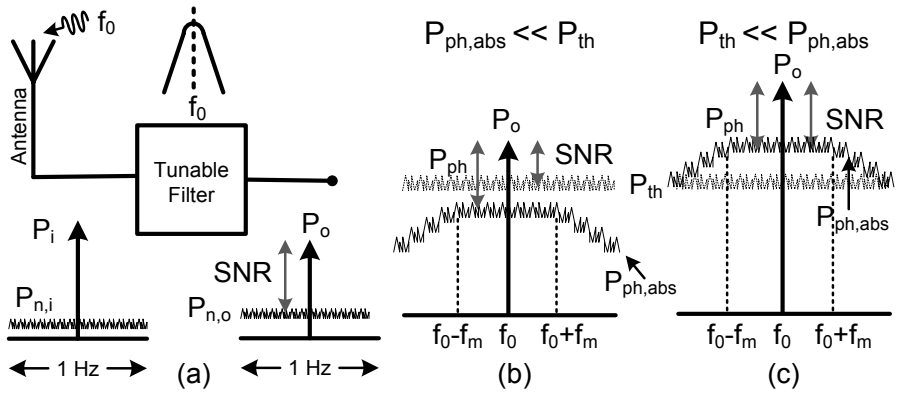

Fig. 101. (a) Antenna and tunable filter in a 50 Ω system, (b) thermal and phase noise when the received signal is weak (Thermal noise region: $P_{ph,abs} << P_{th}$) and (c) thermal and phase noise when the received signal is strong (Phase noise region: $P_{th} << P_{ph,abs}$).

a. Basics

The antenna receives a sinusoidal signal at the center frequency (f_0) of the tunable filter, so that the signal strength at the input of the tunable filter is P_i and thermal noise in a 1-Hz bandwidth around f_0 is $P_{n,i}$. The filter output power is $P_o = T'P_i$, where T' is the fraction of power transmitted from input to output of the filter, and is related to the filter quality factor Q_u and order. The tunable filter is assumed to have both thermal and phase noise so that the total noise at the filter output is

$$P_{n,o} = P_{th} + P_{ph,abs} \tag{4.46}$$

where P_{th} is the total thermal noise power and $P_{ph,abs}$ is the absolute level of phase noise power at the filter output in a 1-Hz bandwidth around f_0 given by

$$P_{ph,abs} = P_o/\rho, \quad \rho = 10^{-P_{ph}/10}, \quad P_{ph}(\text{dBc/Hz}) < 0 \tag{4.47}$$

where P_{ph} is the phase noise power in dBc/Hz calculated as discussed in Section D.3.c of this chapter. The output SNR of the filter is the ratio of P_o and $P_{n,o}$.

If the received signal P_i is weak, then the filter phase noise lies below the thermal noise floor of the system so that $P_{ph,abs} << P_{th}$, and $P_{n,o} \approx P_{th}$ as shown in Fig. 101(b). The range of P_i for which this happens is termed the *thermal-noise region* and the resulting SNR in a 1-Hz noise bandwidth is

$$SNR \approx P_o/P_{th} \tag{4.48}$$

However, if the received signal is strong, the filter phase noise dominates so that $P_{th} << P_{ph,abs}$ and $P_{n,o} \approx P_{ph,abs}$, as shown in 101(c). The corresponding range of P_i is termed the *phase-noise region* and the resulting SNR in a 1-Hz noise bandwidth is

$$SNR \approx P_o/P_{ph,abs} \approx \rho \tag{4.49}$$

Since the quantity ρ is inversely related to the relative phase noise of the filter, P_{ph}, the SNR remains relatively constant at low power but decreases slightly when MEMS switches are close to pull-down due to increase in filter phase noise. Also, SNR given by (4.49) is valid only for offset frequencies ($f_0 \pm \delta f$) lower than the mechanical resonant frequency (f_m) of the MEMS bridge ($\delta f < f_m$). For $\delta f > f_m$, the phase noise decreases at a rate of -40 dB/dec and is eventually limited by the thermal noise floor, and SNR is given by (4.48) for $\delta f >> f_m$.

The received signal strength for which $P_{th} = P_{ph,abs}$ is termed *critical input power* (P_c), and determines the input power for which the transition occurs from the thermal-noise to phase-noise region. Equating (4.47) to P_{th} and using $P_o = T'P_i$ at $P_i = P_c$, the critical input power is given by

$$P_c = P_{th}\left(\frac{\rho}{T'}\right) \tag{4.50}$$

Here, $P_{n,o} = P_{th} + P_{ph,abs} = 2P_{th}$ and the resulting SNR value lies in between the weak and strong signal cases.

b. Results

Fig. 102 shows the noise power and SNR calculated using harmonic balance method in a 1-Hz bandwidth around $f_0 = 18$ GHz. The analysis is performed for Butterworth (N = 2) and Chebyshev (N = 3) filters introduced in Section D.4 of this chapter, as a function of received signal power (P_i), for different fractional bandwidths and quality factors, when all switches are in the up-state position. The filter insertion loss is also specified for each case. The results in each region are discussed as follows:

- In the thermal-noise region ($P_i < P_c$), the output noise floor is a constant value, P_{th}, and SNR increases with $P_i = P_o/T'$ according to (4.48). For filters with high quality factor ($T' \approx 1$), the output SNR is insensitive to filter type, order, bandwidth and mechanical properties of the MEMS switch, as long as $P_i < P_c$. Lowering the filter quality factor decreases the output SNR due to two reasons; (1) the output signal is attenuated due to filter losses and (2) the resistive losses in the filter raises the thermal noise floor as shown in Fig. 102. For example, in a 1% Butterworth filter ($N = 2$), the SNR degradation in the thermal noise region when Q_u is changed from 500 to 100 is 17.5 dB.

- At $P_i = P_c$, the noise power begins to increase due to filter phase noise. From (4.50), P_c has lower values for smaller ρ and larger T' factors. Filters with lower bandwidth and higher order have higher value of P_{ph} which corresponds to smaller ρ factor. On the other hand, higher quality factor filters have large T' factor. Therefore, such filters result in low values of critical input power. For example, $P_c \approx -45$ dBm and -32 dBm for 1% and 4% Butterworth (N = 2) filters, respectively, with $Q_u = 500$ ($T' = 0.6$), and $P_c \approx -25$ dBm for 1% Butterworth (N = 2) filters with $Q_u = 100$ ($T' = 0.1$).

- In the phase noise region ($P_i > P_c$), the SNR reaches a maximum value defined by (4.49) because the phase noise level, $P_{ph,abs}$, increases at the same rate as the signal power P_o. The SNR saturation level is lower for lower bandwidth filters because P_{ph} is higher (Fig. 91). However, lowering the filter quality factor increases the output SNR because P_{ph} is lower for filters with lower quality factor (Fig. 95). For example, in a 1% Butterworth filter ($N = 2$), the SNR improvement is around 3 dB when Q_u is changed from 500 to 100.

As Q_u is lowered, the SNR degradation in the thermal-noise region is drastic compared to the improvement in the phase-noise region. SNR degradation is critical in the thermal-noise region because the received signal is already weak. Thus, a MEMS tunable filter must have a high Q_u value to achieve the best SNR in the thermal-region, at the cost of slightly lower SNR in the phase-noise region.

c. Discussion

The existence of phase noise in MEMS tunable filters imposes an upper bound on the maximum achievable SNR at the filter output, for a given filter topology. However, the relative importance of this phenomena in a MEMS tunable filter application is evaluated by calculating the critical input power P_c. Lower values of P_c imply that the maximum achievable SNR is lower and that the phase-noise region occurs at lower values of received signal power. Both these effects are critical if the received signal is already weak, and are dominant in filters with higher phase noise. Therefore, filters with low fractional bandwidth, high order and high quality factor are most prone to SNR degradation at low values of received input power. The effect of filter phase noise can be safely ignored in MEMS tunable filters with wider bandwidth and moderate quality factor since the phase-noise region occurs at higher input power where SNR

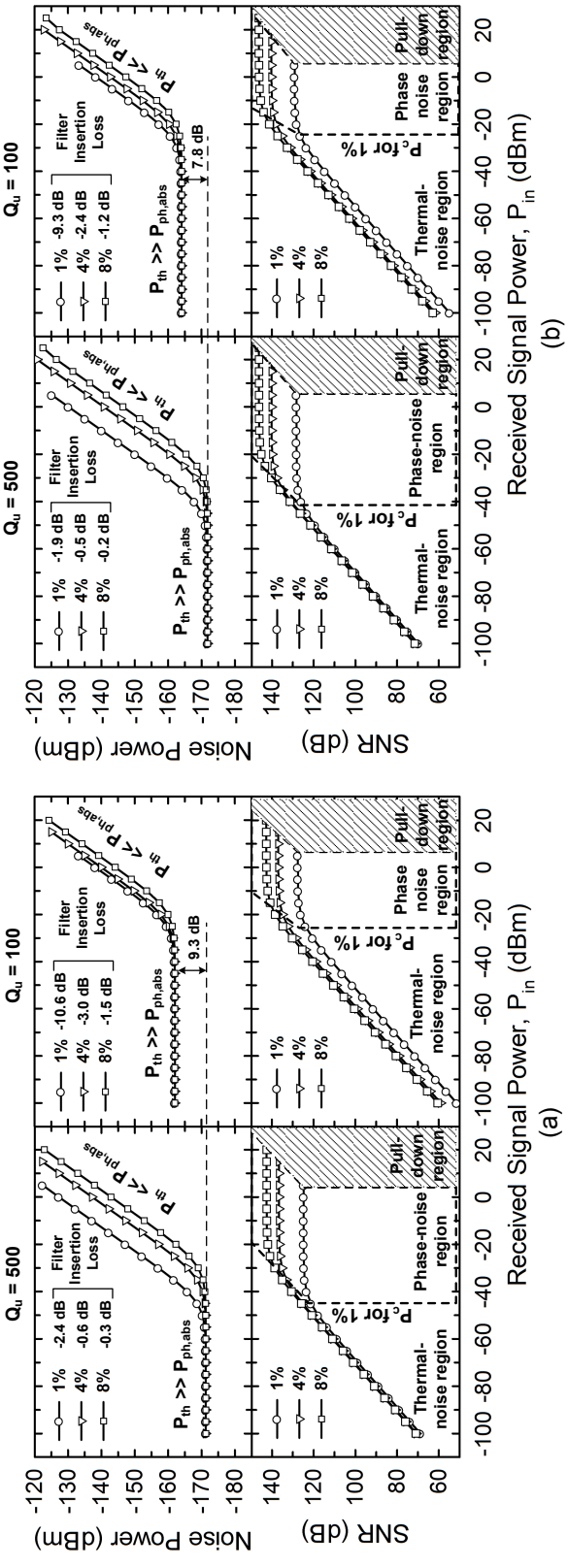

Fig. 102. Total noise power and SNR calculated using harmonic balance in a 1-Hz bandwidth around $f_0 = 18$ GHz for (a) Butterworth (N = 2) and, (b) Chebyshev (N = 3) filters versus received signal power (P_{in}), for different fractional bandwidths and quality factors, when all switches are in the up-state position. The filter insertion loss for each case is also listed.

degradation is not critical to the receiver performance.

7. Conclusion

This study has presented a new methodology to predict the effect of nonlinear noise in all-pole RF MEMS tunable filters. The variations in the filter output signal due to noise were entirely described in terms of pole-perturbations of the filter transfer function. Closed-form equations were derived to find the perturbations of poles in Butterworth and Chebyshev filters due to nonlinearity and noise. The pole-perturbation theory was applied to calculate nonlinear noise in RF MEMS tunable filters due to Brownian motion as a function of filter input power, tuning state, fractional bandwidth, filter order and frequency offset. Higher order filters with small fractional bandwidth exhibited maximum phase noise which increased with input power. Lowering the filter quality factor resulted in decreasing phase noise while increasing the insertion loss. Also, the frequency-dependence of non-ideal fixed and tunable inverters had an insignificant effect on filter phase noise. The maximum output SNR degradation occurs at low input powers in filters with low fractional bandwidth, high order and high quality factor.

E. Unified Method of Nonlinear Noise Analysis Using the Method of Admittances

1. Introduction

Nonlinear noise mechanisms in all-pole RF MEMS tunable filters have been studied theoretically in the previous section using the pole-perturbation approach, and result in degradation of the signal-to-noise ratio (SNR) at the output of the tunable filter. The pole-perturbation approach involves calculating phase noise of the tunable bandpass filter by calculating perturbation of each pole of the equivalent lowpass filter, and estimating the phase variations in the filter transfer function. However, the rigorous mathematical approach in the previous section presents separate analyses for Butterworth and Chebyshev filters which are mathematically intensive for easy estimation of phase noise in MEMS tunable filters.

This section presents a simple, unified approach to calculate nonlinear noise in both Butterworth and Chebyshev RF MEMS tunable filters by performing admittance-based calculations directly in the bandpass domain. Nonidealities such as filter nonlinearity, finite quality factor (Q-factor) and frequency dependence of inverters are all represented in terms of admittance variations, and used to calculate filter phase noise.

2. Theory

Fig. 103(a) shows a generalized all-pole tunable Butterworth or Chebyshev bandpass filter of order N and fractional bandwidth $\overline{\omega}$, with lossless admittance inverters, shunt resonators and termination admittances Y_0. Thus, the overall shunt admittance of

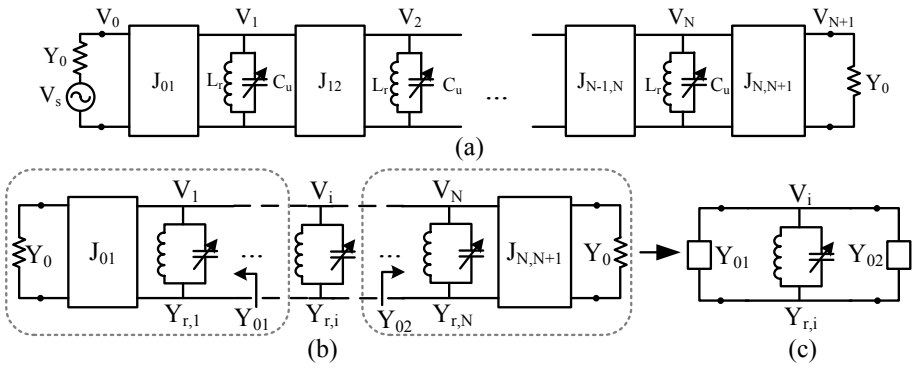

Fig. 103. (a) Generalized all-pole Butterworth/Chebyshev tunable bandpass filter with ideal admittance inverters and shunt resonators, (b) reduction of filter topology with respect to the ith resonator, and (c) simplified bandpass filter with the ith noisy resonator and complex terminating admittances.

each resonator (see Fig. 87 is given by

$$Y_r(\omega, V_r, t) = \frac{1}{R_r} + \left[j\left(\omega L_s - \frac{1}{\omega C_u(V_r, t)}\right) + R_s \right]^{-1} - \frac{j}{\omega L_r} \tag{4.51}$$

Here, R_r is the resistance in parallel with the LC resonator and represents resistive losses in the tunable resonator. If the resonator is implemented with an array of RF MEMS switches, the equivalent admittance variation is found in a similar fashion.

The admittance inverter values $J_{i,i+1} (i = 0, \ldots, N)$ are found using formulas in [15]. The variable capacitance C_u is typically implemented with a MEMS capacitor bank. V_i $(i = 0, \ldots, N+1)$ and V_s are the voltages across node i and the input voltage in the bandpass filter, respectively. The internal node voltages V_i in a tunable filter can be calculated using the iterative approach in Section C of this chapter.

Assuming ideal, noiseless inverters, each resonator in the tunable filter acts as a source of Brownian noise which depends on the voltage V_i across it. The equivalent admittance variation of the ith resonator is expressed as $Y_{r,i}(\omega, V_i, t)$. Due to the

uncorrelated nature of Brownian noise, the noise due to each resonator in the filter is also uncorrelated. The procedure to calculate filter phase noise is as follows.

Step 1) Reduce the filter topology in Fig. 103(a) to a two-port reciprocal network with resonator i as a shunt element, as shown in Fig. 103(b). To ensure uncorrelatedness of independent noise sources, only resonator i is assumed to be affected by Brownian motion while all others are considered noiseless. As a result, at filter center frequency (ω_0), the time-varying admittance of the ith resonator is calculated for a given input power, while all other power-dependent resonator admittances are assumed to be time-invariant. The input admittances looking towards the source and load terminations on either side of resonator i are represented as *power- and frequency-dependent, complex* termination admittances $Y_{01}(\omega, V^-)$ and $Y_{02}(\omega, V^+)$, respectively, whose finite continued fraction expressions are

$$\begin{aligned} Y_{01}(\omega, V^-) &= Y_{01}(\omega, V_1, \ldots, V_{i-1}) \\ &= \cfrac{J_{i,i-1}^2}{Y_{r,i-1}(\omega, V_{i-1}) + \cfrac{J_{i-1,i-2}^2}{Y_{r,i-2}(\omega, V_{i-2}) + \ddots}} \end{aligned} \tag{4.52}$$

$$\begin{aligned} Y_{02}(\omega, V^+) &= Y_{02}(\omega, V_{i+1}, \ldots, V_N) \\ &= \cfrac{J_{i,i+1}^2}{Y_{r,i+1}(\omega, V_{i+1}) + \cfrac{J_{i+1,i+2}^2}{Y_{r,i+2}(\omega, V_{i+2}) + \ddots}}. \end{aligned} \tag{4.53}$$

$Y_{01} = J_{0,1}^2/Y_0$ and $Y_{02} = J_{N,N+1}^2/Y_0$ are purely real and *independent* of power only for $i = 1$ and N, respectively.

Step 2) Find $S_{21}^i(\omega_0)$ of the two-port reciprocal network shown in Fig. 103(c) assuming complex termination admittances. If the tunable resonator is realized using a capacitor bank with 'P' RF MEMS switches in series and/or parallel combination with fixed capacitors (see Fig. 88), then $S_{21}^{i,p}$ ($p = 1, \ldots, P$) must be calculated

assuming that the pth RF MEMS switch is noisy while the other switches are noiseless, and is expressed as

$$S_{21}^{i,p}(\omega, V, t) = \frac{2\sqrt{Re(Y_{01}(\omega, V^-)Y_{02}(\omega, V^+))}}{Y_{01}(\omega, V^-) + Y_{r,i,p}(\omega, V_i, t) + Y_{02}(\omega, V^+)} \tag{4.54}$$

where $Y_{r,i,p}(V_i, t)$ represents the admittance variation of resonator i with a voltage V_i across it assuming RF MEMS switch 'p' is noisy.

Step 3) Since filter amplitude noise due to Brownian motion is negligible, the phase variations in the output signal are given by (4.37). The phase noise power $P_{ph}^{i,p}$ due to switched capacitor p in resonator i, normalized to the output carrier power, is obtained by taking the FFT of the output signal.

Step 4) Repeat steps 1-3 for each switch and resonator in the filter and find the overall filter phase noise by summing the phase noise contributions of all noise sources according to (4.38).

3. Filter Example

To illustrate the method of phase noise calculation using admittances, the filter example in Sec. 4 is considered. The filter implementation and simulated S-parameters are shown in Fig. 89. The filter parameters and the parameters of the RF MEMS switch are given in Tables X and XI, respectively.

The internal node voltage across each RF MEMS switch is iteratively calculated as described in Section C of this chapter, and the static bridge displacement x_d and height g_s are found. Using (4.34), the noisy bridge displacements in the presence of an RF signal can be determined. The overall capacitance variation is then calculated from (4.35) using g_s and $g_n(t)$, and the corresponding admittance variation of each resonator in the filter is calculated from (4.51). The admittance method described earlier is used to calculate the nonlinear phase noise for lossless Butterworth (N=2)

and Chebyshev (N=3) filters.

Fig. 104 shows the filter phase noise for lossless, Butterworth (N=2) and Chebyshev (N=3) filters ($R_s = R_r = 0$) with different fractional bandwidths, as a function of input power, mechanical frequency offset, tuning state, and filter order. In all cases, the results are compared to the perturbation method presented in Section D of this chapter, and shows excellent agreement between the two approaches. As the input power increases, noisy displacements $g_n(t)$ have a larger amplitude for higher static displacements x_d and results in higher phase noise [Fig. 104(a)]. The phase noise variation versus mechanical frequency offset ($\omega'/2\pi$) follows the lowpass response given by (4.1), and has a 40 dB/dec roll-off for $\omega' > \omega_m$ [Fig. 104(b)]. Phase noise is highest when all switches are in the up-state position and decreases as switches are closed. This is because switches in the down-state position do not contribute to phase noise. Consequently, tuning state 4 does not exhibit phase noise [Fig. 104(c)]. Also, higher order filters exhibit larger phase noise due to greater number of noisy resonators [Fig. 104(d)]. In all cases, filters with lower fractional bandwidth exhibit higher phase noise because admittance variations in such filters have a large impact on the phase response of the filter.

4. Nonidealities

In this section, the effect of filter nonidealities is taken into account and phase noise is calculated using the proposed unified method for Butterworth (N=2) filters. Phase noise values for nonideal Chebyshev filters can be calculated in a similar fashion.

a. Resonator Q-Factor

Practical realizations of tunable filters always exhibit a finite Q-factor due to resistive losses in the resonators and switches. Resonator losses are modeled by including a

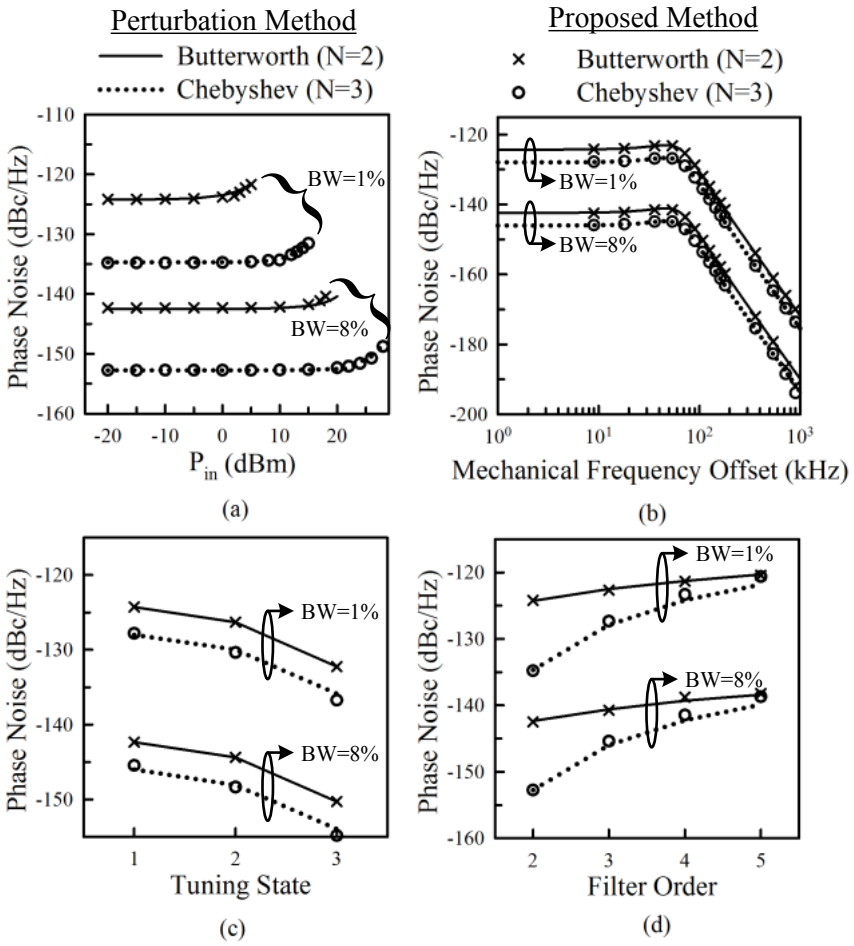

Fig. 104. Variation of filter phase noise for different fractional bandwidths versus (a) input power, (b) mechanical frequency offset, (c) tuning state, and (d) filter order. Unless stated otherwise, phase noise is calculated at an offset of $2\pi \times 9$ kHz at filter center frequency for $P_{in} = -20$ dBm.

resistance R_r in parallel with the LC resonator shown in Fig. 87(b). If the unloaded Q-factor of the resonator is Q_u, then the loss resistance may be expressed as

$$R_r = \omega_0 L_r Q_u. \tag{4.55}$$

To be precise, the switch resistance R_s must also be included in the calculation of Q_u. However, the Q-factor of RF MEMS switches is typically much larger (300—500) than the typical Q-factors of inductors [33], and can be ignored for analytical simplicity. For a given Q_u value, the admittance variation, and consequently phase noise is calculated by including the quantity $1/R_r$ in (4.51).

The variation of phase noise with Q_u is shown in Fig. 105 where the phase noise with finite Q_u is normalized with respect to the lossless case. Good agreement is obtained with the results in Section D of this chapter, where phase noise was calculated by laterally displacing the poles of the filter. Since the constant $1/R_r$ is inversely proportional to Q_u, the relative change in resonator admittance Y_r in the presence of Brownian noise sources is smaller for lower Q_u values. As a result, the phase noise is lower as the losses in the filter increase. Also, phase noise variation with Q_u is more drastic in narrow bandwidth filters.

b. Frequency-Dependence of J-Inverters

So far, lossless J-inverters are assumed to have a fixed value that are frequency-invariant. In reality, J-inverters have a finite loss and show frequency-dependent behavior. Since filter phase noise is relatively independent of inverter loss if the inverter Q-factor > 10 (see Section D of this chapter), phase noise calculations are accurate if the inverters are assumed lossless. However, the frequency-dependence of inverter values depends on their actual implementation. Figs. 97(a) and (b) show inductive and capacitive inverter implementations, respectively. Typically, inductive

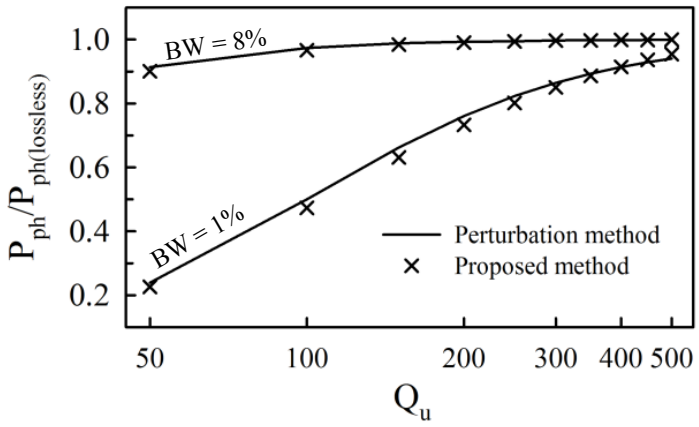

Fig. 105. Variation of Butterworth filter phase noise with Q_u for different fractional bandwidths. Phase noise is calculated at an offset of $2\pi \times 9$ kHz at filter center frequency for $P_{in} = -20$ dBm.

inverters are implemented using transformers with coupling coefficient k_{io} and $k_{i,i+1}$, and capacitive inverters are implemented using series capacitors C_{io} and $C_{i,i+1}$ at the filter input/output and between resonators, respectively. For an N-pole tunable filter, the expressions for half-admittance input/output J-inverters (J_{io}) and inter-resonator J-inverters ($J_{i,i+1}, i = 1, \ldots, N-1$) for inductive and capacitive implementations are given by (4.43), (4.44) and (4.45).

Thus, as the filter is tuned to lower frequencies, the frequency-dependence of inverters results in different $J_{i,i+1}$ values for each tuning state. As a result, the filter phase noise is different from the ideal values calculated in Fig. 104(c). Inverter values from (4.43)—(4.45) are first used to calculate terminating admittances $Y_{01}(\omega, V^-)$ and $Y_{01}(\omega, V^+)$ from (4.52) and (4.53), respectively. Phase noise is then calculated using (4.54), (4.37) and (4.38). Figs. 106(a) and (b) show the variation of phase noise with tuning state for different inverter implementations in Butterworth filters with fractional bandwidths of 1% and 8%, respectively. If the inverters are made tunable using RF MEMS switches, then the time-dependence of J-inverters must be

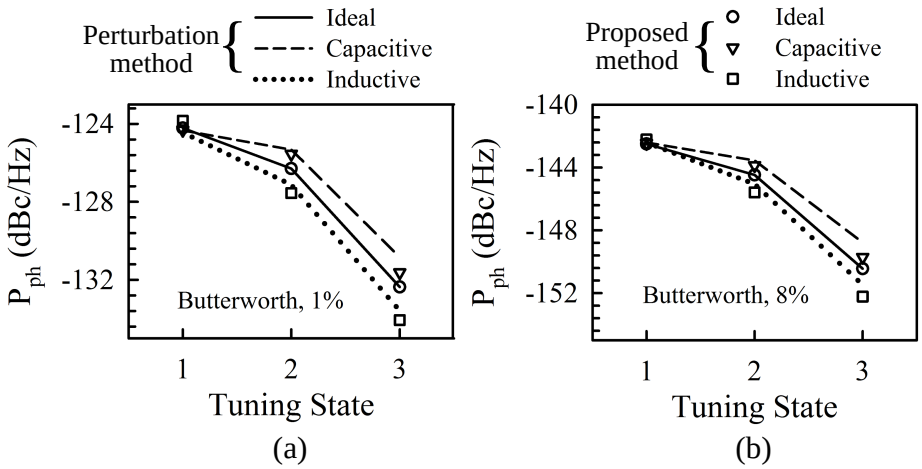

Fig. 106. Comparison of phase noise in Butterworth filters versus tuning state for different inverter configurations for fractional bandwidths of (a) 1% and (b) 8%. Phase noise is calculated at an offset of $2\pi \times 9$ kHz at filter center frequency for $P_{in} = -20$ dBm.

considered in the calculation of Y_{01} and Y_{02}, and the phase noise is then calculated accordingly.

5. Conclusion

In this study, a simple method to calculate nonlinear noise in Butterworth and Chebyshev RF MEMS tunable filters has been presented. By representing noise and nonlinearity as variations of resonator admittance in the bandpass domain, changes in the phase of the filter transfer function are calculated directly. This method is also employed to successfully predict the effect of filter nonidealities on phase noise. Results of the proposed approach are in excellent agreement with those in Section D of this chapter.

CHAPTER V

A SELF-SUSTAINED MICROWAVE PLATFORM FOR DETECTION OF ORGANIC LIQUIDS*

A. Introduction

Development of systems for accurate measurement of material properties is essential for a number of applications in industry, medicine, and pharmaceuticals [98]. One important application of microwave sensors is in the field of 'microwave-aquametry' where the moisture content of various materials is measured [99]. In many biological and agricultural products, the presence of moisture affects the physical properties of the material, resistance to microbes, and weight. For example, over-drying of grain costs money for the producer and reduces the weight of the product, which further reduces profits. On the other hand, if the moisture is too high, the buyer pays too much and the product may soon be ruined. Several published works have focused on the measurement of moisture content in grain [100], [101]. Moisture content of soil samples is another important application in the agricultural industry because it affects the growth and overall yield of crops [102]. Also, moisture content in paper or plywood determines its strength and quality, and must be accurately estimated in many industrial environments. Since the dielectric constant (real-part of the complex permittivity) of most dry materials is < 10, and that of water is ≈ 80, the dielectric constant of a water-containing material is strongly dependent on its moisture content at microwave frequencies. Thus, developing microwave systems that can accurately detect changes in dielectric constant of a material finds extensive application in a

---

variety of industries.

In the pharmaceutical industry, it is often important to be able to study properties of chemicals such as their structural composition and purity. Dielectric relaxation spectroscopy (DRS) provides a noninvasive and sensitive method to detect the structural properties of the material by studying the complex permittivity of chemicals at microwave frequencies [103]. In DRS, the molecular properties of a chemical are studied by observing changes in complex permittivity, which essentially depends on the bulk dielectric properties of the material-under-test (MUT). At low frequencies, the molecules of the MUT reorient according to the direction of the applied time-varying electric field, and hence exhibit relatively high values of dielectric constant. However, at microwave frequencies, the molecules of the MUT are unable to reorient to the rapidly varying electric field due to frictional forces between adjacent molecules. As a result, the dielectric constant of the MUT decreases from its low-frequency value and the loss of the MUT increases due to energy dissipated in overcoming frictional forces. Hence, detection of complex permittivity of chemicals at microwave frequencies gives valuable information regarding the structural properties of many organic and inorganic substances [104].

For this purpose, several broadband techniques have been developed that enable measurement of complex permittivity from MHz-frequencies up to 30 GHz, using guided-wave structures such as strip-lines or dielectric waveguides [105], [106]. However, such devices are often bulky or expensive, which limits their use when low-cost, in-situ measurements need to be made. Recently, several resonant techniques have been developed for permittivity characterization of unknown materials at a single microwave frequency. For many applications, detecting the complex permittivity at a single frequency provides sufficient information to distinguish between several dissimilar materials because the complex permittivity is unique to each material at a

particular microwave frequency. Shift in resonant frequency of waveguide, dielectric or coaxial resonators have been used for material characterization due to their high sensitivity [107]. Recently, substrate-integrated-waveguide-based sensors have been proposed as a low-cost alternative with high sensitivity and medium size [108]. However, to overcome the issue of cost and size, microwave sensors using planar resonant structures have also been implemented [109].

In general, resonator based sensors can be divided into two classes; (1) those whose electromagnetic fields are completely exposed the MUT, and (2) those whose electromagnetic fields are only partially exposed the MUT. Resonant techniques rely on measuring the relative shift of the magnitude of S-parameters due to the MUT. Resonant sensors whose electromagnetic fields are completely exposed the MUT have inherent limitations when materials with high dielectric loss at microwave frequencies (such as organic liquids) need to be characterized. The degradation of quality factor of the resonator due to a high-loss MUT results in a $|S_{21}|$ (or $|S_{11}|$) response that does not have a distinguishable peak (or notch) at any frequency. This makes it impossible to extract the dielectric constant of the MUT. To be able to detect high-loss materials using this technique, a reasonably high resonator quality factor must be maintained by reducing the sample volume of the high-loss MUT. As a result, the electromagnetic field of the sensor is only partially exposed to the MUT which makes it hard to accurately calibrate the measurement system. Also, since the MUT is not completely exposed to the electromagnetic field of the sensor, the resulting frequency shift in S-parameters is much smaller, making the detection process harder and less accurate.

Another aspect of microwave sensor design for complex permittivity detection involves its portability for in-situ measurements, and the ability to accurately detect MUTs without the need for expensive laboratory equipment. Several approaches

have been used in literature to achieve this goal. In [110], a scalar network analyzer is emulated using discrete broadband microwave sweep generators and power detectors to digitally obtain the shift in $|S_{21}|$ response of a planar resonator. Although such a system is relatively low-cost and portable, it is limited to detection of MUTs with low loss, since high-loss materials make the resonance completely disappear. Recently, a free-space measurement system employing reflectometers has been proposed for permittivity determination of lossy liquid materials [111]. However, this system requires a focused horn-lens antenna for accurate measurements and is typically much bulkier than a measurement system employing planar resonators.

In this chapter, a novel approach to measure dielectric constant based on a C-band planar oscillator is presented. Dielectric constant is detected based on shifts of oscillation frequency caused by the phase change of the sensing element when the MUT is applied. The proposed detection method is independent of the sample volume and loss of the MUT as long as oscillation conditions are satisfied and the frequency shift is detectable. The planar sensor embedded within the oscillator is completely exposed to the MUT and thus produces large shifts in frequency that can be accurately detected. Also, the proposed sensor can easily detect the dielectric constant of a high-loss material because the sensor operation is based on the phase response ($\angle S_{11}$) of the planar sensor and not its magnitude response ($|S_{11}|$). To eliminate expensive laboratory measurement equipment and make the sensor completely self-sustained, the C-band voltage-controlled oscillator is embedded in a discrete frequency synthesizer system. By doing so, any changes in oscillation frequency due to the MUT is negated by changing the control voltage of the oscillator. The change in control voltage can be easily stored digitally using an analog-to-digital converter, and mapped into changes in the dielectric constant of the MUT using a simple calculation process. Such a system is completely self-sustained and requires only a DC power supply, and

is very useful where portability and size is important.

B. Fundamental Theory

In this section, a brief review on the fundamentals of dielectric properties of materials will be presented from a molecular perspective, and serves as the underlying theory for the microwave system presented in this chapter for the detection of organic liquids.

The permittivity of a material, $\epsilon^* = \epsilon'_r - j\epsilon''_r$, is a property that describes the ability of a material to store charge. Here, ϵ'_r and ϵ''_r represent the real and imaginary parts of complex permittivity, respectively. In practice, materials are commonly specified by their dielectric constant (ϵ'_r) and loss tangent ($\tan\delta = \epsilon''_r/\epsilon'_r$). Since dielectric polarization of a material depends on the ability of its constituent dipoles to reorient in an applied electric field, materials that have large dipole moments also have large dielectric constants. Especially in liquids, the molecules reorient with the applied electric field at relatively low frequencies, and hence exhibit a large dielectric constant. However, at microwave frequencies, molecules are no longer able to rotate a significant amount before the electric field is reversed, and the permittivity decreases as a consequence of reduced dipole moment. Also, at microwave frequencies, the frictional forces between molecules dissipate energy in the form of heat due to fast reorientations under the influence of a rapidly varying electric field, and results in an increase in ϵ''_r.

For most organic liquids, the frequency dependence of complex permittivity is commonly represented by the Debye model expressed as [104]

$$\epsilon^* = \epsilon_\infty + \frac{\epsilon_s - \epsilon_\infty}{1 + j\omega\tau} \tag{5.1}$$

where τ is the relaxation time, and ϵ_s and ϵ_∞ are the values of permittivity at fre-

Table XIII. Debye-Model Parameters for Organic Solvents @ 20°C [112].

Material	ϵ_s	ϵ_∞	τ (ps)
Ethanol	25.07	4.5	143.24
Methanol	33.64	5.7	53.04
2-Butyl Alcohol	15.8	3.5	504
Xylene	2.53	2.27	9.55
Ethyl Acetate	6.04	2.48	4.34
Acetic Acid	6.15	2.48	32.74

quencies $<< \tau^{-1}$ and $>> \tau^{-1}$, respectively. Using (5.1) and separating into real and imaginary parts gives

$$\epsilon_r' = \epsilon_\infty + \frac{\epsilon_s - \epsilon_\infty}{1 + \omega^2\tau^2}; \qquad \epsilon_r'' = \frac{(\epsilon_s - \epsilon_\infty)\omega\tau}{1 + \omega^2\tau^2} \tag{5.2}$$

The relaxation time τ is a measure of the time taken for the molecules to adopt random orientations upon removal of the external field, and is generally a function of temperature. At a frequency $\omega = \omega_\tau$, when ϵ_r' reaches half its value between ϵ_s and ϵ_∞, the value of ϵ_r'' is maximum and $\tau = 1/\omega_\tau$. Also, the relaxation time may be related to the volume of a spherical molecule of radius r rotating in a viscous medium with viscosity η using [104]

$$\tau = 4\pi r^3 \frac{\eta}{k_B T} \tag{5.3}$$

where k_B is the Boltzmann constant and T is the temperature in Kelvin. Hence, knowledge of the dielectric properties of a material, and especially its relaxation time constant, gives important information regarding its molecular structure. The Debye model parameters for several organic solvents are shown in Table XIII. Fig. 107 shows

the real and imaginary components of permittivity for the organic liquids listed in Table XIII obtained from (5.2).

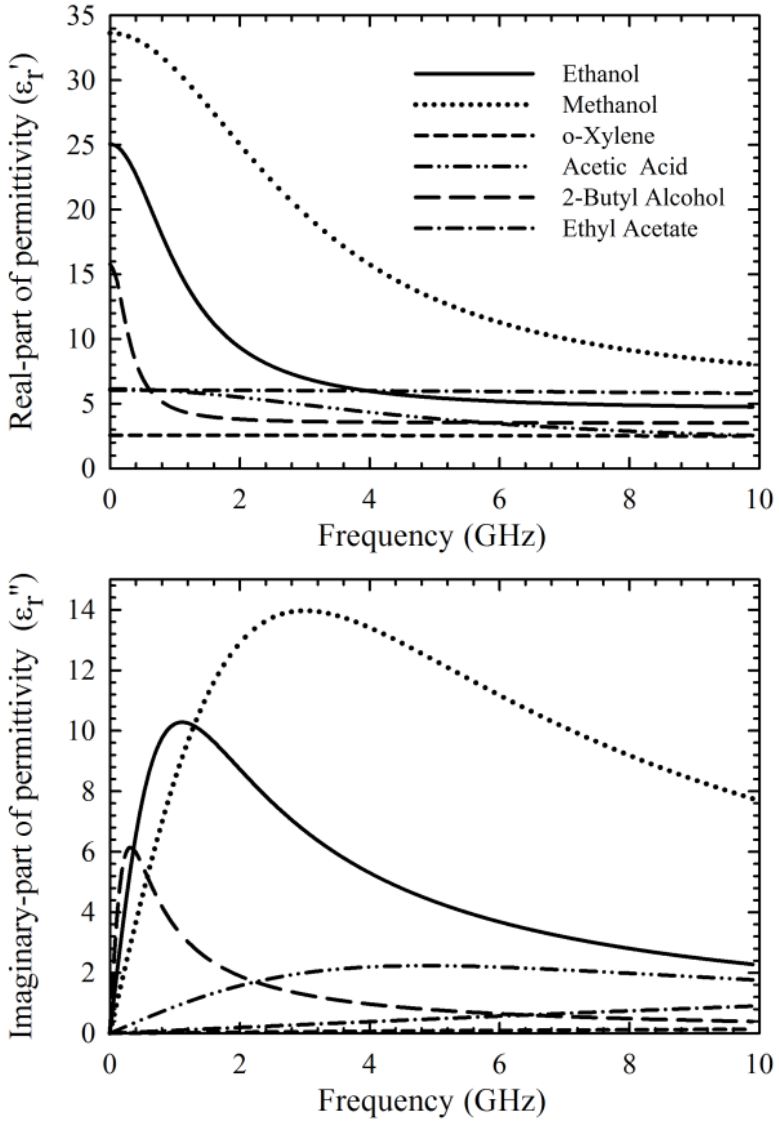

Fig. 107. Real and imaginary components of complex permittivity for common organic liquids as predicted by the Debye model.

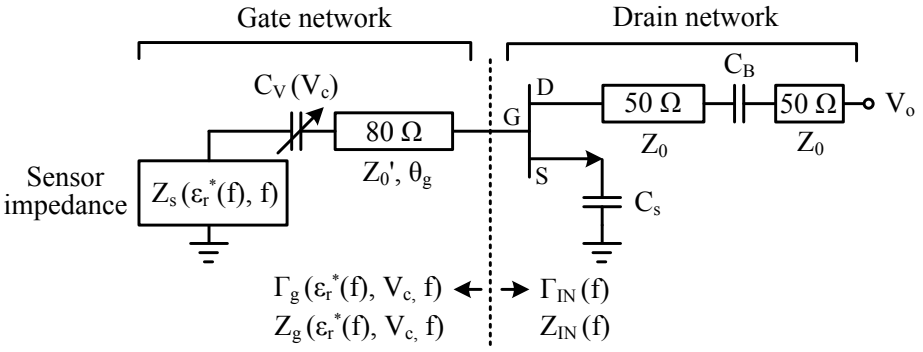

Fig. 108. Simplified schematic of the negative resistance oscillator used for permittivity measurement.

C. Oscillators for Dielectric Constant Measurement

1. Oscillator Design

Fig. 108 shows the schematic of a negative resistance oscillator employing a source series feedback capacitance (C_s) to generate negative resistance. The gate network has a transmission line with characteristic impedance $Z_0' = 80\ \Omega$ and electrical length θ_g in series with a voltage-controlled varactor $C_v(V_c)$ and a sensing element with complex impedance $Z_s(f)$. When an MUT with complex, frequency-dependent relative permittivity $\epsilon_r^*(f) = \epsilon_r'(f) - j\epsilon_r''(f)$ is applied to the sensor, its impedance changes as $Z_s(\epsilon_r^*(f), f)$. Here, $\epsilon_r'(f)$ and $\epsilon_r''(f)$ depict the dielectric constant and loss of the MUT, respectively. In general, the oscillation frequency depends on the variable loads in the gate network, which in this case are $C_v(V_s)$ and $Z_s(\epsilon_r^*(f), f)$ respectively. The purpose of the varactor is to negate any changes in oscillation frequency caused by the MUT. The oscillating signal is available at the output of the drain network which has two transmission lines of arbitrary electrical length (with characteristic impedance $Z_0 = 50\ \Omega$) with a DC blocking capacitor C_B between them.

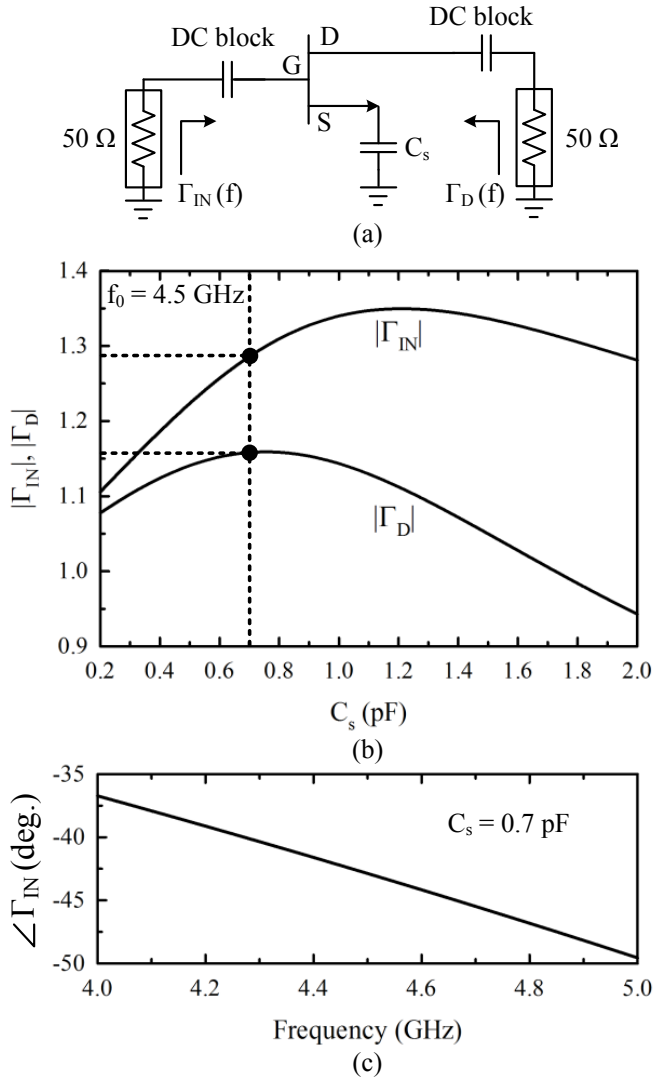

Fig. 109. (a) Simulation setup for the determination of C_s (DC biasing not shown), (b) variation of magnitude of reflection coefficients at gate and drain with C_s, and (c) phase variation of gate reflection coefficient with frequency.

a. Source Network

To design an oscillator with an output frequency of f_0, the value of C_s must be adjusted so that the transistor provides a negative resistance looking into the gate, implying $|\Gamma_{IN}(f_0)| > 1$. To determine the value of C_s, the S-parameters of a properly biased transistor, terminated by 50 Ω loads at the gate and drain as shown in Fig. 109(a), are simulated in Agilent ADS using the nonlinear model of the transistor from the ADS design library. The active device is an Avago Technologies' ATF-36077 pseudomorphic high electron mobility transistor (pHEMT) biased at a drain-source voltage (V_{DS}) of 1.5 V and gate-source voltage (V_{GS}) of -0.2 V with a drain current (I_D) of 10 mA.

Fig. 109(b) shows the variation of $|\Gamma_{IN}|$ and $|\Gamma_D|$ at $f_0 = 4.5$ GHz when different values of C_s are connected to the source terminal of the transistor. To measure high loss MUTs, the negative resistance generated must be maximum to ensure stable oscillations. Thus, the value of C_s must be chosen so that the magnitude of reflection coefficients at the gate and drain are maximum. Choosing $C_s = 0.7$ pF results in $|\Gamma_{IN}| = 1.29$ and $|\Gamma_D| = 1.16$. Fig. 109(c) shows the variation of $\angle\Gamma_{IN}$ with frequency for $C_s = 0.7$ pF. For stable oscillations at a frequency f_0, the gate network must be designed to meet the following conditions [113]

$$|\Gamma_{IN}(f_0)| \times |\Gamma_g(\epsilon_r^*, V_c, f_0)| > 1 \tag{5.4}$$

$$\angle\Gamma_g(\epsilon_r^*, V_c, f_0) = -\angle\Gamma_{IN}(f_0). \tag{5.5}$$

Since the overall network looking into the gate is capacitive, the gate network should be made inductive to satisfy the oscillation condition given by (5.5).

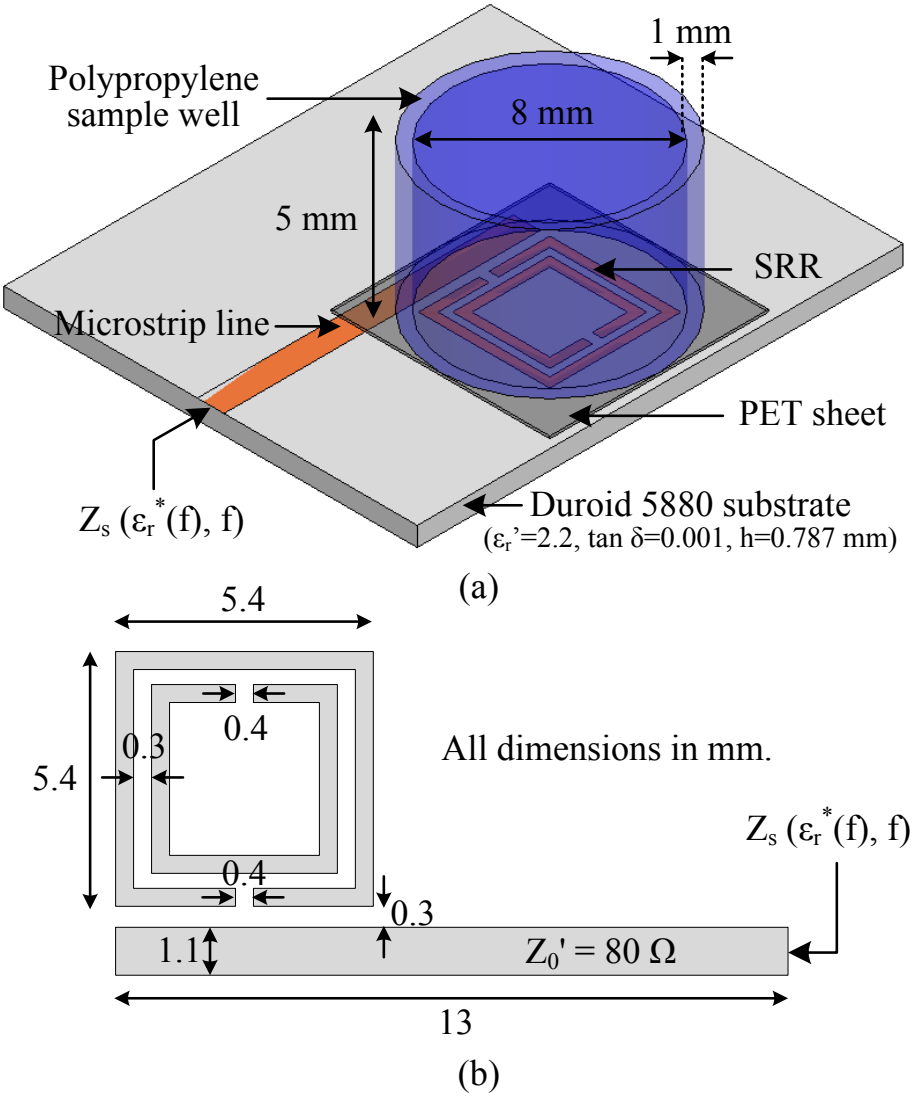

Fig. 110. (a) Three-dimensional view of the sensing element, and (b) dimensions of the split-ring resonator (SRR).

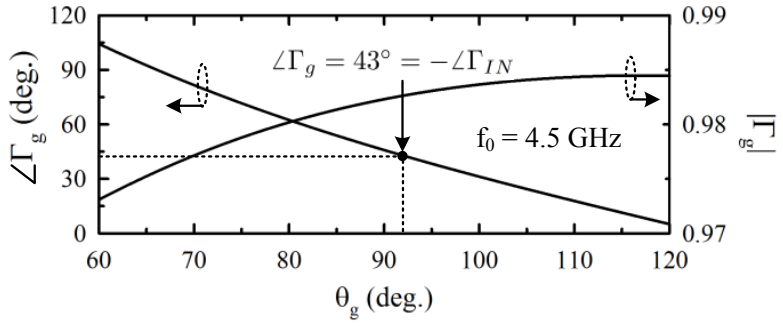

Fig. 111. Magnitude and phase variation of reflection coefficient of the gate network as a function of the electrical length of the gate transmission line.

b. Gate Network

The sensing element is a split-ring resonator (SRR) coupled to a microstrip line as shown in Fig. 110(a). The high confinement of electric fields at the open ends, and between the rings of the SRR makes it highly sensitive to permittivity changes in the dielectric layer above it [114]. The SRR is covered by a 100 μm thick sheet of Polyethylene Teraphalate (PET) with $\epsilon_r = 2.5$ and $\tan\delta = 0.025$, to prevent the sensor metalization from degrading when the MUT is applied. In order to contain the MUT, a sample well is constructed using a 5 mm long polypropylene tube ($\epsilon_r = 2.2$) with a wall thickness of 1 mm and inner diameter of 8 mm.

The dimensions of the SRR are shown in Fig. 110(b) and are chosen such that the SRR has an arbitrary resonant frequency that is above the desired oscillation frequency. This makes the SRR appear inductive at the oscillation frequency as required by the gate network. The sensing element is simulated using Ansoft HFSS to find the value of Z_s at $f_0 = 4.5$ GHz, when the MUT is absent. On account of the SRR-to-microstrip coupling and the 13 mm long transmission line with an 80 Ω characteristic impedance, the sensing element appears capacitive with an impedance $Z_s(\epsilon_r^* = 1, f_0) = 1.2 - j40\ \Omega$.

The varactor in Fig. 108 is a silicon-hyperabrupt tuning varactor from Aeroflex Metelics (MHV500) which provides a capacitance of $C_{v0} = C_v(V_c = 0\text{ V}) = 2.5$ pF. Neglecting varactor parasitics for simplicity, the equivalent input impedance of the gate network when $V_c = 0$ V, is given by

$$Z_g(f) = Z_0' \frac{Z_s(\epsilon_r^*(f), f) + j\left(Z_0' \tan\theta_g - \dfrac{1}{2\pi f C_{v0}}\right)}{\left(Z_0' + \dfrac{\tan\theta_g}{2\pi f C_{v0}}\right) + jZ_s(f)\tan\theta_g} \tag{5.6}$$

and the complex gate reflection coefficient is given by

$$\Gamma_g\left(\epsilon_r^*(f), V_c = 0, f\right) = \frac{Z_g(f) - Z_0}{Z_g(f) + Z_0}. \tag{5.7}$$

For an oscillation frequency of $f_0 = 4.5$ GHz in the absence of an MUT when $V_c = 0$ V, the electrical length θ_g of the transmission line in the gate network should be chosen so that (5.4) and (5.5) are satisfied. Assuming a sensor impedance of $Z_s(\epsilon_r^* = 1, f_0)$, $|\Gamma_g|$ and $\angle\Gamma_g$ can be calculated using (5.6) and (5.7). Fig. 111 shows the variation of $\angle\Gamma_g$ for different values of θ_g. Choosing $\theta_g = 92^\circ$ results in $\angle\Gamma_g = 43^\circ = -\angle\Gamma_{IN}$ at 4.5 GHz. The simulated values of $|\Gamma_g|$ are close to unity, and hence satisfy the condition in (5.4). The oscillator design is now complete. The following sections describe the response of the oscillator to MUT dielectric constant and effect of MUT loss.

2. Response to Material Dielectric Constant

To examine the effect of material dielectric constant (ϵ_r') on the oscillator, the impedance of the sensing element, $Z_s(\epsilon_r', f)$, is simulated in HFSS with lossless isotropic MUTs of various dielectric constants present in the sample well. It is assumed that the dielectric constant is frequency-independent and the sample well is completely filled with

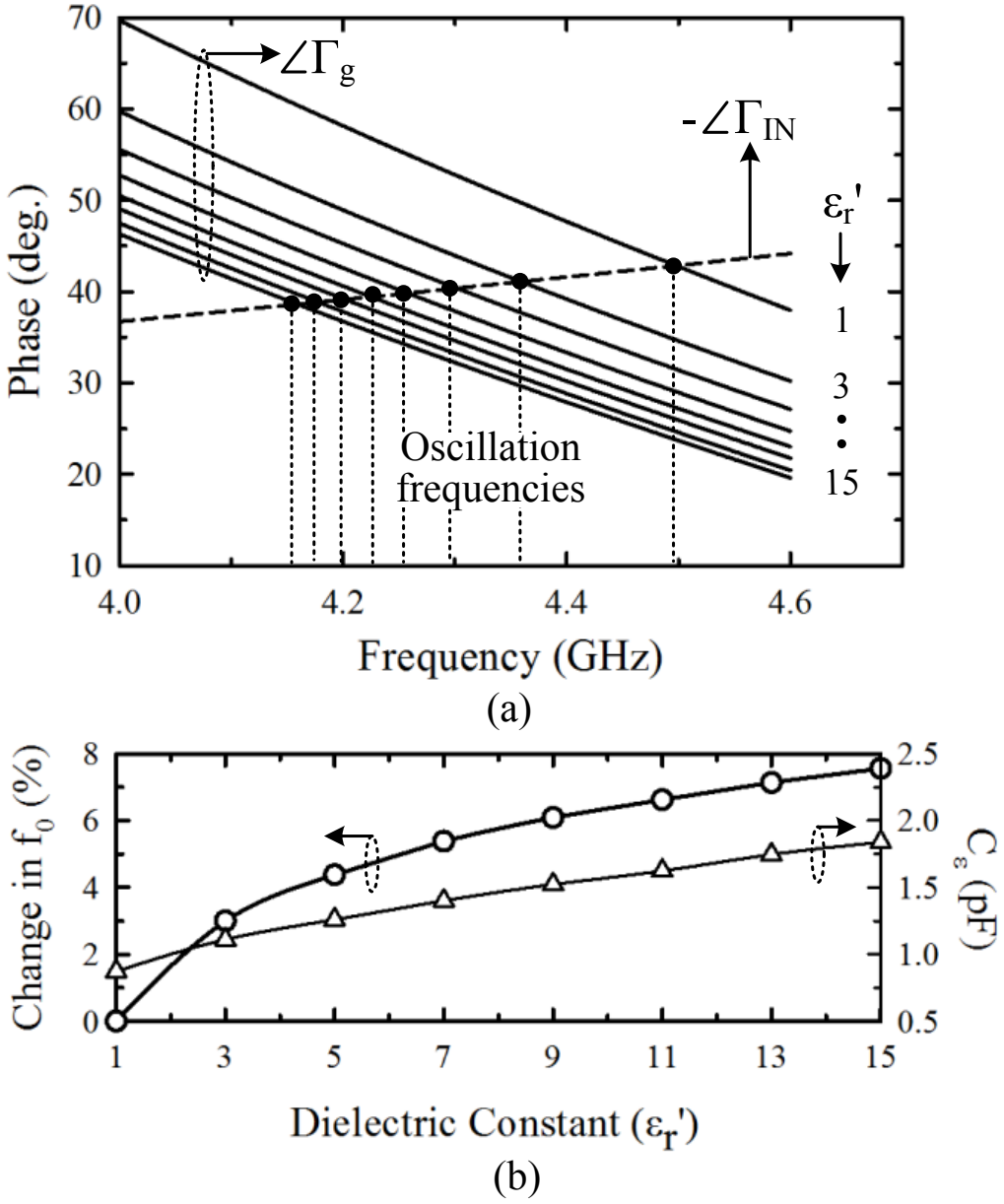

Fig. 112. Simulated: (a) phase of reflection coefficient of the gate network caused by the presence of MUTs, and (b) change in oscillation frequency and effective sensor capacitance versus dielectric constant.

the MUT, to a height of 5 mm above the SRR. From the simulated values of $Z_s(\epsilon_r', f)$, the phase variation of the gate reflection coefficient ($\angle\Gamma_g(\epsilon_r', V_c = 0, f)$) is calculated using (5.6) and (5.7), for each ϵ_r', as shown in Fig. 112(a). Negated phase variation of the reflection coefficient looking into the gate of the transistor [$\angle\Gamma_{IN}(f)$ from Fig. 109(c)] is also superimposed. The points of intersection between these curves are the frequencies at which the oscillation condition given by (5.5) is satisfied, and determine the oscillation frequencies for each value of ϵ_r'. The relative percentage change of the oscillation frequency as a function of MUT dielectric constant is shown in Fig. 112(b). The effective capacitance (C_ϵ) of the sensing element extracted from $Z_s(\epsilon_r', f)$ is also shown and has higher values as ϵ_r' of the MUT increases. Thus, determining the change in oscillation frequency is an effective means to estimate the dielectric constant of the MUT.

For lossless MUTs ($\epsilon_r'' = 0$), the real part of sensor impedance Z_s remains unchanged with a value of 1.2 Ω, which is mostly attributed to metallic losses in microstrip traces and dielectric losses in the duroid substrate, polyethylene sample well and PET sheet. Hence, the oscillation condition given by (5.4) is met for all values of ϵ_r' since $|\Gamma_g| \approx 1$ as shown in Fig. 111, ensuring sustained oscillations at frequencies that only depend on the MUT dielectric constant.

3. Effect of Material Loss

When an MUT with loss ($\epsilon_r'' \neq 0$) is present above the SRR, the sensing element is equivalently represented by a *lossy* capacitor whose admittance is given by

$$Y_s(\epsilon^*(f), f) = \frac{1}{Z_s(\epsilon^*(f), f)} = G_\epsilon + j\omega C_\epsilon. \tag{5.8}$$

where G_ϵ is a conductance that depends only on the ϵ_r'' of the MUT. Fig. 113(a) shows the relatively linear increase of G_ϵ with ϵ_r'' at $f_0 = 4.5$ GHz, obtained from full-wave

simulation of the sensing element in HFSS in the presence of lossy materials. Here, ϵ_r'' is assumed to be frequency independent and the lossy material is assumed to fill the sample well to a height of 5 mm. Simulations also verify that the extracted conductance values are independent of ϵ_r' and remain almost constant in a narrow bandwidth ($\approx 20\%$) of frequencies around f_0. Since ϵ_r' and ϵ_r'' affect the real and imaginary parts of the sensing admittance, respectively, measurement of ϵ_r' is completely independent of ϵ_r''. However, the conductance G_ϵ may impose restrictions on the capability for sustained oscillations.

To ensure sustained oscillations in the presence of a lossy material, the oscillation condition in (5.4) must be satisfied for all values of ϵ_r' and ϵ_r''. Figs. 113(b) and (c) show the simulated product of $|\Gamma_{IN}|$ and $|\Gamma_g|$ as a function of ϵ_r'' for different values of ϵ_r', for constant oscillation frequency and constant varactor voltage cases, respectively. It is important to maintain sustained oscillations for both these cases to ensure proper operation of the detection algorithm, and is explained in detail in Section E. In the constant frequency case, the varactor voltage V_c is adjusted to maintain a constant oscillation frequency of 4.5 GHz for each value of ϵ_r'. In the constant voltage case, the varactor voltage is constant ($V_c = 0$ V) and the oscillation condition is calculated at the frequency of oscillation corresponding to the value of ϵ_r' [Fig. 112(c)].

When $|\Gamma_{IN}| \times |\Gamma_g| < 1$, the oscillator enters a stable mode of operation and cannot maintain sustained oscillations. Thus, for a given ϵ_r', there is a maximum limit on the range of ϵ_r'' beyond which the oscillator does not oscillate. Fig. 113(b) shows that stable oscillations are supported for a wide range of ϵ_r'' values for high ϵ_r'. For low ϵ_r' values, the oscillator enters the stable region thereby limiting the range of ϵ_r'' that can be detected. This restriction occurs only when the low ϵ_r' materials have loss tangents ($\tan\delta = \epsilon_r''/\epsilon_r'$) in the range of 2.5–3, which is a very high value for most organic liquids in the GHz-range [112]. Material loss does not restrict oscillations for

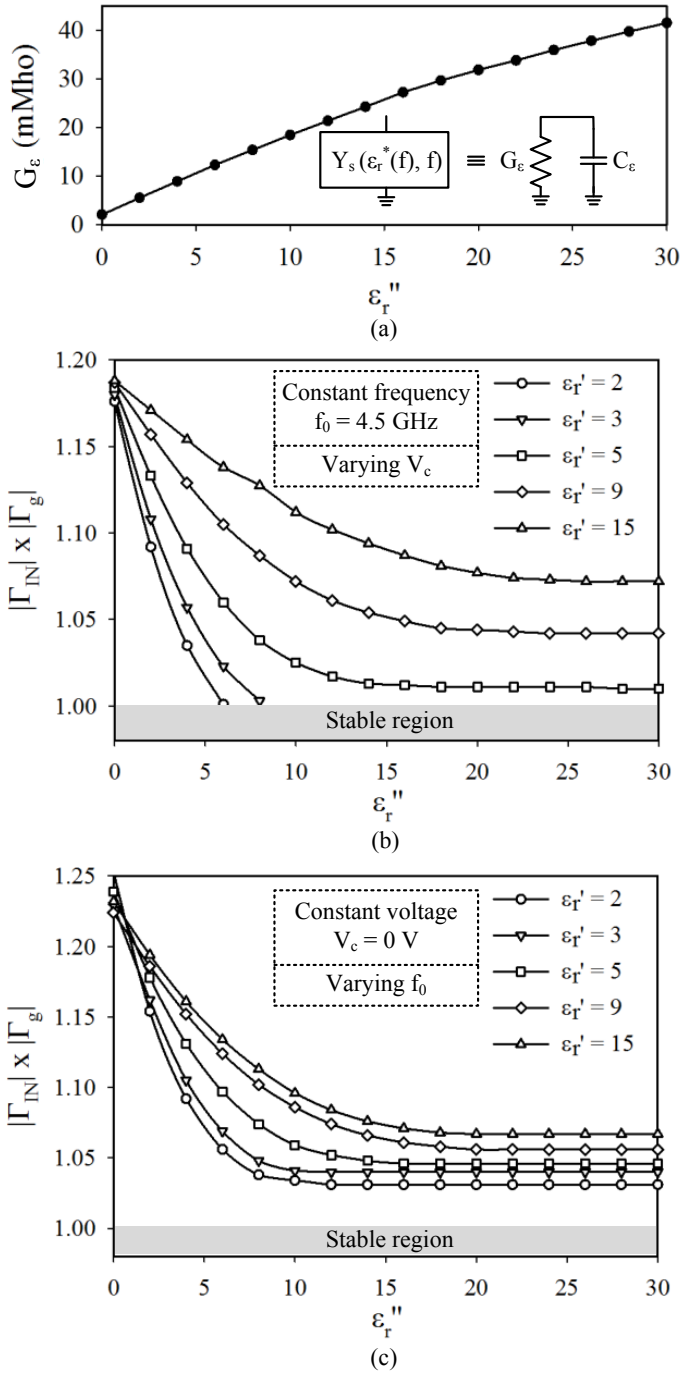

Fig. 113. Simulated: (a) Real part of sensor admittance when lossy, isotropic MUTs with arbitrary ϵ_r'-value and various ϵ_r''-values are placed in the sample well. Oscillation condition in (5.4) as a function of ϵ_r'' for the case of (b) constant oscillation frequency and (c) constant varactor voltage.

the constant voltage case as shown in Fig. 113(c). Hence, this oscillator guarantees sustained oscillations for a wide range of practical materials that need to be tested.

D. VCO Fabrication and Chemical Measurements

In this section, the VCO fabrication is explained and the chemical calibration of the sensor is presented in detail. Next, several MUTs are applied to the VCO and their corresponding dielectric constants (ϵ_r') are extracted. The results presented in this section are obtained from frequency measurements using a spectrum analyzer. Although, the sensor is not fully self-sustained, the results shown here prove the concept of permittivity detection using microwave oscillators.

The oscillator is fabricated on Rogers RT/Duroid 5880 with $\epsilon_r' = 2.2$ and thickness 0.787 mm using conventional PCB etching technology. Figs. 114(a) and (b) show the fabricated sensor prototype. In order to contain the MUT, a sample well is constructed using a 5 mm long polypropylene tube ($\epsilon_r' = 2.2$) with a wall thickness of 1 mm and inner diameter of 5 mm. To prevent sensor degradation due to interaction between the MUT and sensor surface, one end of the tube is closed by gluing a thin sheet of polyethylene teraphalate (PET) ($\epsilon_r' = 2.5$, $\tan\delta = 0.025$) with a thickness of 0.1 mm to the tube. The other end of the tube is open so that the MUT can be dispensed into the sample well. Fig. 114(c) shows the spectrum of the oscillator measured using an Agilent E4446A spectrum analyzer without the MUT and has a single tone at 4.4222 GHz with an output power of -5 dBm. The oscillation frequency of the VCO varies almost linearly with the control voltage (V_c) as shown in Fig. 114(d). The VCO exhibits a tuning range of 290 MHz with a K_{VCO} of 64.5 MHz/V. However, for the measurements that follow, the control voltage is fixed at $V_c = 0.5$ V. Choosing any other value of control voltage will result in equally valid results.

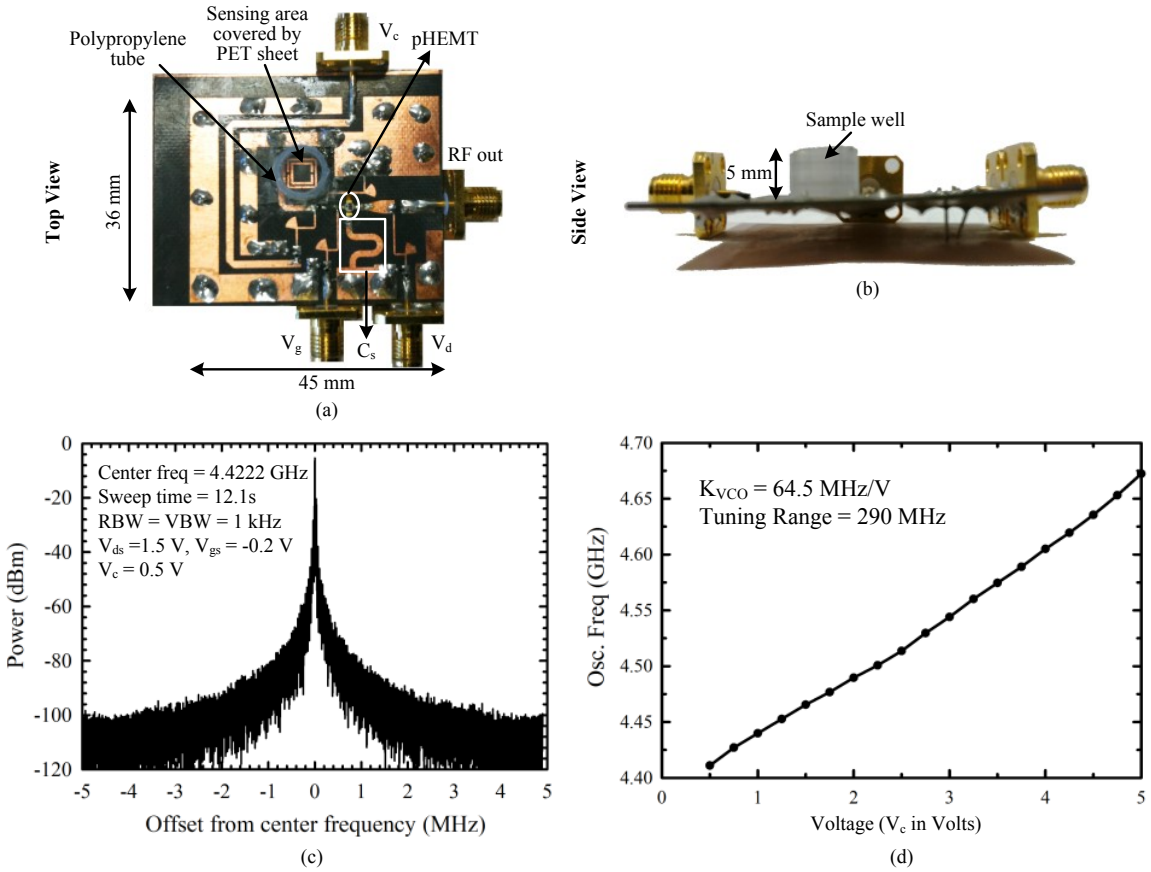

Fig. 114. (a) Top-view of the fabricated permittivity-sensing oscillator prototype, (b) side-view of the fabricated VCO, (c) measured oscillation spectrum without MUT, and (d) tuning characteristics of the VCO.

To calibrate the sensor, oscillation frequency shifts caused by well-known materials are measured for known sample volumes. Using the dielectric constant values of the calibration materials in [112] at ≈4.5 GHz, a 2nd-order polynomial is curve-fit to the frequency shifts. Figs. 115(a) and 116(a) show the curve-fit polynomial obtained from frequency shifts caused by 10 μL and 20 μL samples of ethanol and methanol (both with 99.8% purity), respectively. Frequency shift is measured by averaging the oscillator spectrum ten times to reduce the frequency error caused by drift. The oscillator drift is in the order of 150 kHz (over a 5 minute period) and does not significantly affect the sensor accuracy which typically shows shifts of > 5 MHz for the 10 μL and 20 μL samples of MUTs considered here. Five measurements are taken for each sample volume of each calibration material, and the average values are used for curve fitting. Using a larger sample volume results in lower error in the curve-fitting coefficients, and hence better detection accuracy because higher sample volumes cover the whole sensor area in a repeatable fashion.

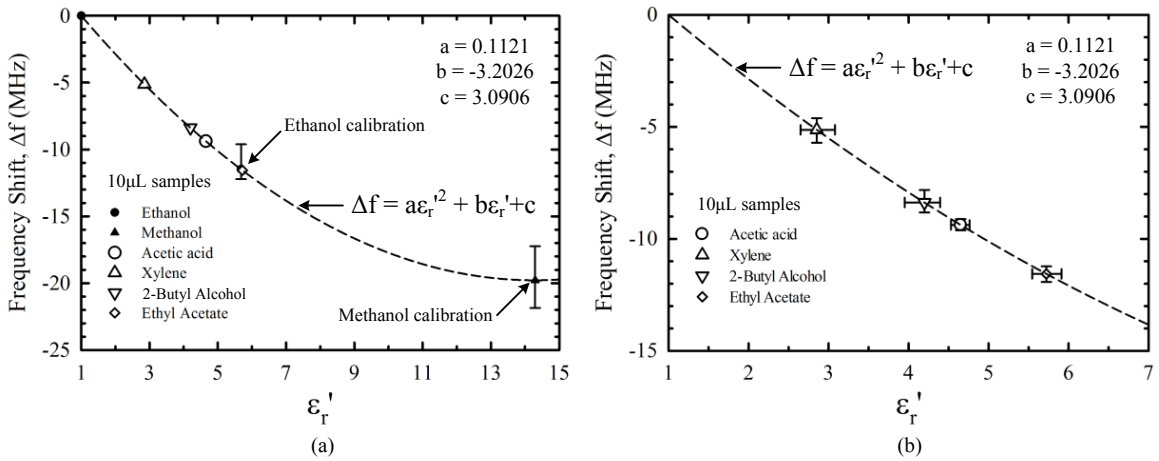

Fig. 115. (a) Measured oscillator frequency shift versus ϵ_r' for 10 μL MUT samples. Error bars are shown only for calibration materials. (b) Error bars in measurement of MUTs for 10 μL sample volumes. In both graphs, plotted symbols depict mean values.

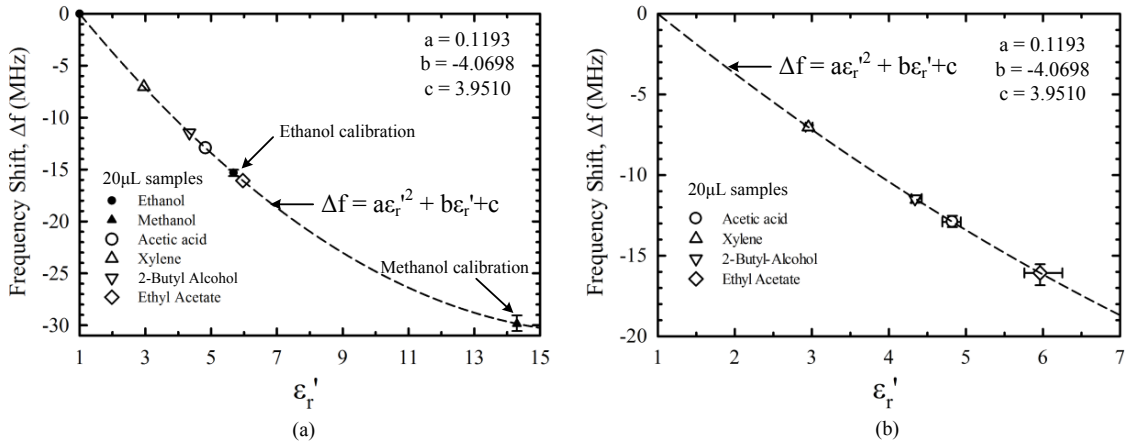

Fig. 116. (a) Measured oscillator frequency shift versus ϵ_r' for 20 μL MUT samples. Error bars are shown only for calibration materials. (b) Error bars in measurement of MUTs for 20 μL sample volumes. In both graphs, plotted symbols depict mean values.

Next, 10 μL and 20 μL samples of MUTs such as xylene, acetic acid, 2-butyl alcohol and ethyl acetate (all with $> 99.5\%$ purity) are applied to the oscillator and the frequency shifts for each material is obtained by averaging the oscillator spectrum ten times. Five measurements are taken for each sample volume of each MUT. Figs. 115(a) and 116(a) show the average frequency shifts obtained for different MUTs for 10 μL and 20 μL sample volumes, respectively. The dielectric constant of the MUT for a given volume is extracted by inverting the curve-fitted polynomial equation for that particular volume. Figs. 115(b) and 116(b) show the error bars in measured frequency shift and dielectric constant for 10 μL and 20 μL sample volumes of MUT, respectively. The error in the coefficients obtained by curve-fitting during calibration are not considered here. The extracted values of dielectric constant for each MUT is summarized in Table XIV, and show good agreement with the values predicted by the Debye model [see (5.1)] using the parameters shown in Table XIII [112].

Differences in extracted ϵ_r' values and those predicted by the Debye model are

Table XIV. Comparison of the Extracted ϵ'_r Values with the Debye Model at 4.5 GHz

Material	ϵ'_r (Debye)	Extracted ϵ'_r (10 μL)	Extracted ϵ'_r (20 μL)
Ethanol	5.17	-	-
Methanol	13.53	-	-
o-Xylene	2.55	2.85 $\pm$ 0.17	2.95 $\pm$ 0.05
Acetic Acid	4.1	4.65 $\pm$ 0.11	4.82 $\pm$ 0.08
2-Butyl Alcohol	3.56	4.19 $\pm$ 0.20	4.33 $\pm$ 0.08
Ethyl Acetate	5.98	5.72 $\pm$ 0.18	5.96 $\pm$ 0.20

attributed to inaccuracies in measurement such as insufficient sensor coverage by the MUT, temporary drifts in oscillation frequency and temperature fluctuations. Adding higher volumes of MUT such that the sensor area is fully covered would result in more accurate results. Large short-term frequency shifts during chemical measurement results in erroneous values of extracted ϵ'_r, and is most likely the cause of drastically different extracted dielectric constants of acetic acid and 2-butyl alcohol compared to the theoretical values. Also, errors caused by oscillation frequency drift over the measurement period can be reduced by taking digital averages of the control voltage if the sensing VCO is included as part of a frequency synthesizer architecture. This is discussed in the next section.

E. Development of the Frequency Synthesizer System

To extract the dielectric constant of organic liquids without using a spectrum analyzer, the VCO used for detection is included in a frequency synthesizer system. This section discusses the design and operation of such a self-sustained detection system in detail.

1. System Overview

Fig. 117 shows the basic block diagram of the frequency synthesizer system [115]. The RF output of the sensing VCO designed earlier is connected to a programmable frequency divider which converts the C-band oscillation frequency generated by the VCO to a baseband frequency (in the MHz range). The output of the programmable frequency divider is compared to a reference frequency using a phase-frequency detector (PFD). The PFD generates an error signal which depends on the difference between the reference frequency and frequency divider output, that drives a charge pump. The charge pump generates a series of current spikes that are proportional to the error signal provided by the PFD which are then filtered out by the lowpass loop filter so that a DC control voltage is provided to the VCO, thereby changing its oscillation frequency. When the error signal generated by the PFD is nearly zero, the system achieves locked state and the frequency of oscillation f_0 is given by $f_0 = Nf_{ref}$, where N is the frequency division value and f_{ref} is the reference frequency. By changing the value of N (integer or fractional), a stable oscillation signal can be synthesized over a discrete set of frequencies using this architecture. The proposed system is digitally interfaced to a microcontroller unit (MCU) for programmability. The MCU serves two primary functions; (1) to digitally store the control voltage (V_c) obtained at the output of the loop filter using an internal analog-to-digital converter (ADC), and (2) to provide the frequency division ratio N to the programmable frequency divider.

2. Functionality

The main idea behind chemical detection using a frequency synthesizer architecture is to convert changes in the oscillation frequency due to the presence of the MUT into equivalent changes of the digital control voltage at the output of the loop filter.

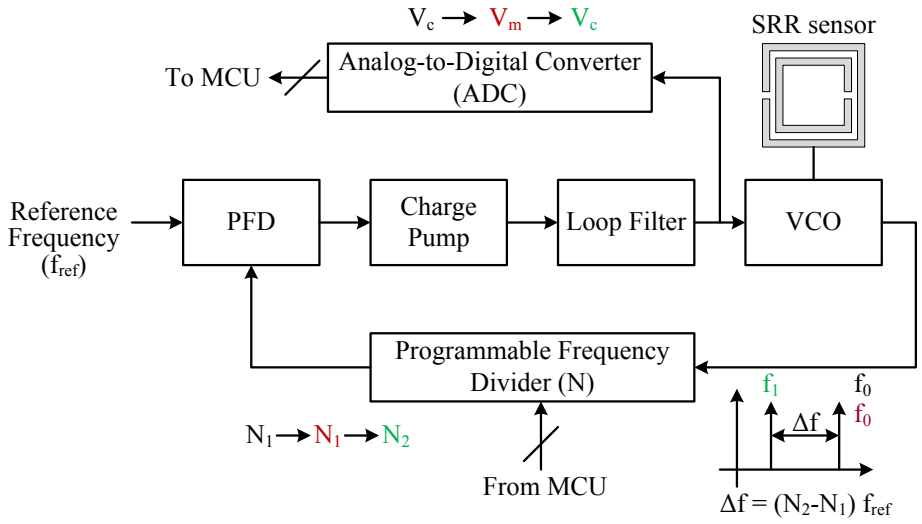

Fig. 117. Block diagram of a frequency synthesizer system digitally interfaced to a microcontroller unit.

The frequency shift caused by the MUT is then digitally recovered using a simple calculation process.

When a MUT is applied to the sensing VCO, the presence of an organic liquid layer above the SRR causes a shift in the oscillation frequency as described in Section C of this chapter. As a result, the closed loop system deviates from its locked state due to different signal frequencies present at the input of the PFD. Since the division ratio N is unchanged, the error signal generated by the PFD causes a change in the control voltage at the output of the loop filter in an effort to achieve locked state. In this way, change in oscillation frequency is simply converted to a change in DC level of the control voltage. The change in DC voltage level can be easily stored in the MCU using an ADC, and later on be used to digitally calculate the frequency shift caused by the MUT. Thus, the proposed architecture provides a self-sustained mechanism for chemical detection.

As shown in Fig. 118, the detection process using a frequency synthesizer architecture consists of the initialization, detection and calculation phases. The process

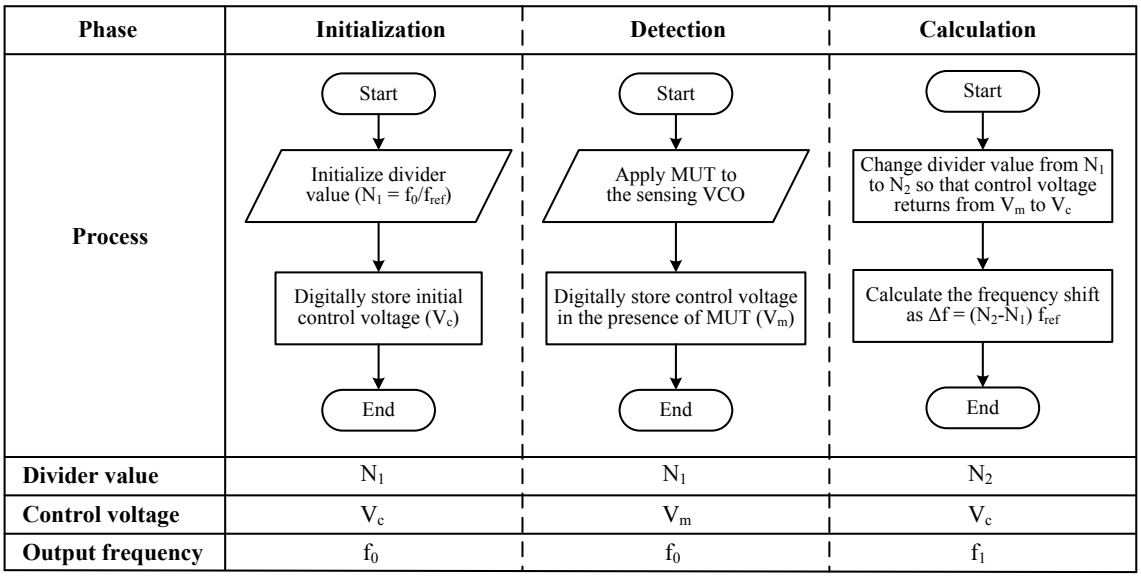

Fig. 118. Different phases of chemical detection using the frequency synthesizer system.

involved in each phase is discussed in detail as follows.

1. *Initialization*: The frequency divider is programmed using the MCU to have a value $N_1 = f_0/f_{ref}$. Here, f_0 is the frequency at which the electrical properties of the MUT need to be extracted. Once the loop is locked to provide an output frequency f_0, the control voltage at the output of the loop filter (V_c) is digitally stored in the MCU.

2. *Detection*: The MUT is dispensed into the sample well causing the oscillation frequency of the VCO to change. However, the closed loop system adjusts itself to maintain a constant output frequency f_0 and as a result, the control voltage at the output of the loop filter changes from V_c to V_m in the presence of the MUT. The voltage V_m is then digitally stored in the MCU.

3. *Calculation*: To return the control voltage at the output of the loop filter from V_m in the presence of the MUT, to its original value V_c, the divider value is

changed from N_1 to N_2 by the MCU, using a binary search algorithm. As a result, the frequency at the output of the synthesizer system decreases from f_0 to f_1. The change in output frequency due to the MUT is calculated as $|\Delta f| = |f_0 - f_1| = |(N_2 - N_1)|f_{ref}$.

Here, a couple of important points are worth mentioning regarding the detection process. First, the frequency shift caused by the MUT only depends on the dielectric constant ϵ_r' (real part of complex permittivity) and the sample volume. The loss of the MUT (depicted by ϵ_r''–the imaginary part of complex permittivity) only affects the power of oscillation. While detection of MUT loss is important for many applications, it is beyond the scope of this work. However, it can be argued that the output power variation due to the MUT is directly indicative of the material loss, and can be mapped into ϵ_r'' of the MUT. This is discussed is Chapter VI.

Second, there is some ambiguity regarding the exact frequency at which ϵ_r' of the MUT is extracted. This is because the output frequency varies from f_0 to f_1 during the calculation phase. Assuming that f_0 and f_1 lie within the tuning range of the VCO[1], the variation of ϵ_r' for most organic liquids over this narrow frequency range is small. For example, for the VCO designed in Section C of this chapter, the tuning range is 290 MHz which is a 6.5% bandwidth with respect to $f_0 = 4.5$ GHz. Over this small frequency range, ϵ_r' has a very small variation (see Fig. 107).

3. Implementation

The detailed block diagram of the frequency synthesizer system using discrete components is shown in Fig. 119. The PFD, charge pump, and programmable frequency

[1]It will be shown in Section F of this chapter that the frequency shift values Δf for a wide range of ϵ_r' values (from 1 to 13) lies well within the tuning range of most practical discrete microwave VCOs such as the one designed in Section C of this chapter.

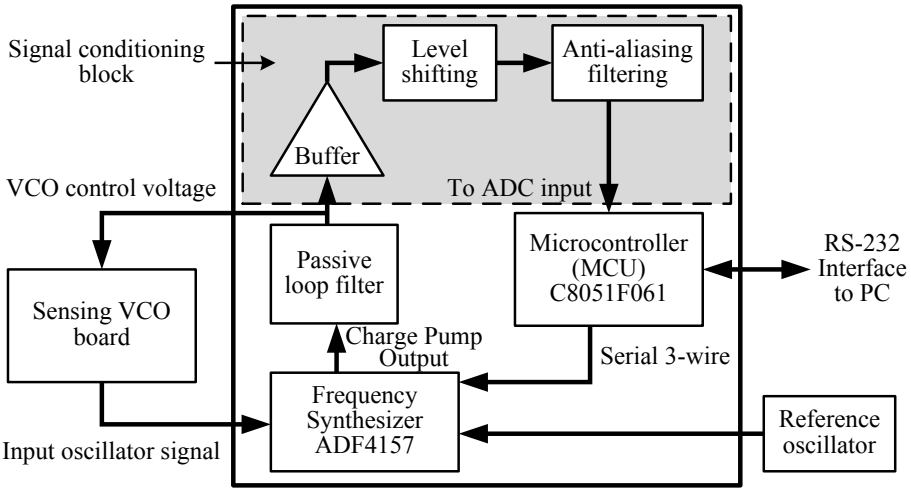

Fig. 119. Detailed implementation of the frequency synthesizer system with a digital interface.

divider are implemented using an Analog Devices ADF4157 fractional-N frequency synthesizer [116], with a 25-bit fixed modulus and 0.5 Hz output frequency resolution. The RF output power from the sensing VCO provided to the frequency synthesizer chip must be limited between -10 and 0 dBm for proper operation. Since the VCO designed in Section C provides an output power of -5 dBm, it can be directly connected to the frequency synthesizer chip. Directional couplers may be used if required to provide the appropriate power level to the RF input pin of the ADF4157 chip. A reference signal with a frequency of 14.86086 MHz and peak-to-peak amplitude of 0.65 V is provided to the ADF4157 chip using an Agilent 33120A waveform generator. This can also be replaced by a surface mount crystal oscillator for greater system portability. The ADF4157 chip is easily programmable using a serial 3-wire interface from the MCU. The charge pump output from the chip is applied to a passive loop filter implemented using discrete surface-mount components on the board.

To design the passive loop filter, important trade-offs involved in determination of loop bandwidth must be considered. Choosing a high loop bandwidth implies

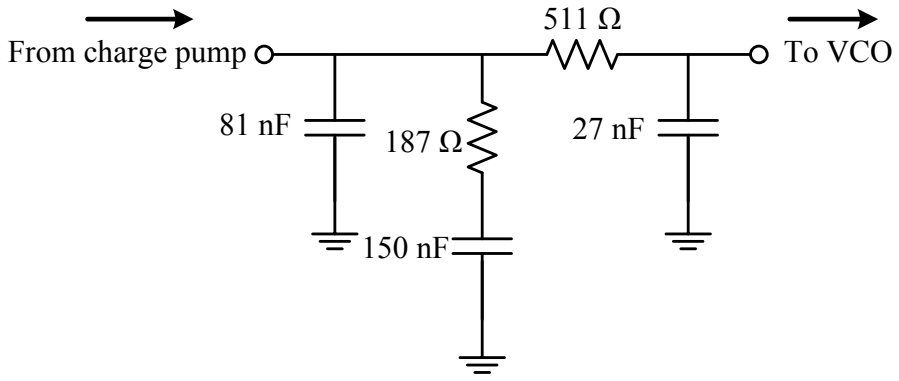

Fig. 120. Schematic of the passive lowpass loop filter.

a fast locking time, while choosing a low loop bandwidth helps reduce the level of reference spurs that appear at the output of the frequency synthesizer. Also, as a rule of thumb, the loop bandwidth must be at least ten times lower than the frequency of the reference signal for loop stability [115]. Since locking time is not a critical factor in detection of material permittivity, the loop bandwidth in the proposed system is chosen as 20 kHz, and is in the range of recommended values for the ADF4157 frequency synthesizer [116]. Also, for guaranteed system stability, the phase margin is selected to be 60°. Fig. 120 shows the schematic of a second-order passive loop filter designed and optimized for these specifications using the ADIsimPLL software developed by Analog Devices for ADF4157 frequency synthesizer design. Since the supply voltage for the charge pump inside the ADF4157 chip is set to $V_{CP} = 5$ V, the DC voltage at the output of the loop filter varies between 0.5 and 5V for output frequencies from 4.5 to 4.8 GHz.

Before the loop filter output is digitally stored in the MCU, the DC voltage level must be buffered, level-shifted and filtered as shown in Fig. 119. The buffering stage is used to provide a high input impedance at the loop filter output and effectively isolate the DC level-shifting and filtering blocks from the phase-locked-loop system.

Fig. 121 shows the circuit-level implementation of the signal conditioning blocks. An opamp (Analog Devices OP275) is used as a buffer stage. Since the ADC input pin on the MCU chip can tolerate a maximum of 3.3V, the 0.5–5V DC level at the loop filter output must be level shifted to be below 3.3V. For this purpose, a resistive

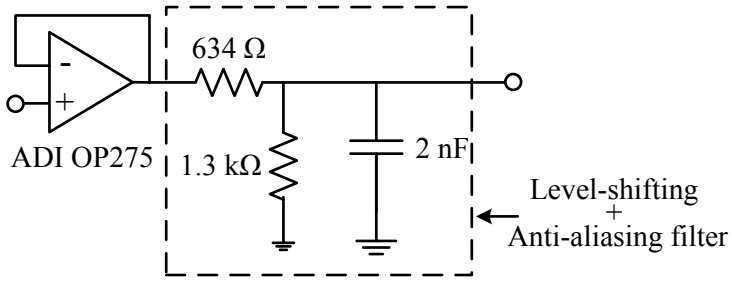

Fig. 121. Schematic of the signal conditioning block.

divider is employed to reduce the voltage level at the output of the voltage follower by a factor of $1300/(1300 + 634) = 3.3/5 = 0.67$, as shown in Fig. 121. Also, before the signal is sampled by the ADC present inside the MCU chip, the bandwidth of the signal must be restricted to approximately satisfy the Nyquist sampling theorem to avoid signal corruption due to aliasing. Thus, since the sampling rate of the ADC within the MCU is $f_s = 250$ kHz [117], the anti-aliasing filter must have a lowpass response with corner frequency $f_c = f_s/2 = 125$ kHz. In Fig. 121, the lowpass response is obtained using a single-stage RC filter where the capacitor value is given by $C = 1/2\pi(125 \times 10^3)(634\Omega) = 2$ nF.

The MCU used in the system is a Silicon Laboratories' C8051F06 8051 microcontroller with an in-built 16-bit ADC [117]. The microcontroller is interfaced to a PC using an RS-232 serial interface. The primary functions of the MCU are: (1) to store digital data obtained from the in-built ADC, and (2) issue commands to the ADF4157 frequency synthesizer to perform the initialization, detection and calculation phases described in Fig. 118. The MCU is initialized and subsequently

programmed to serially communicate with the PC using a virtual instrument (VI) interface designed in National Instruements' LabView software. Fig. 122 shows the fabricated frequency synthesizer system for detection of organic liquids. Excluding the VCO, the frequency synthesizer system is implemented on standard 62-mil thick FR4 substrate. The VCO control voltage, RF signal from VCO and reference frequency are provided using Subminiature-A (SMA) connectors. All power supplies are provided through banana connectors located at various points on the board. The RS-232 interface to the PC requires a RS-232 driver chip located on the top right hand corner of the board. In addition, a TTL driver IC is included if the board needs to be interfaced with TTL-compatible circuitry in the future. A possible scenario where it may be required is when an array of sensing VCOs is used for detection and the RF outputs from the VCO array needs to be multiplexed to the RF input connector on the frequency synthesizer board. In this case, the TTL driver is needed to drive the control pins of the multiplexer. In sensing applications, an array of sensors is typically used to obtain more accurate detection results by averaging the results of each sensing element.

F. Fully Self-Sustained Chemical Measurements

To verify the validity of the proposed self-sustained measurement system, the dielectric constants of the organic liquids listed in Table XIII are extracted and compared to the theoretical values predicted by the Debye model. The measurement procedure, chemical calibration and dielectric constant extraction are described in detail in the sections that follow.

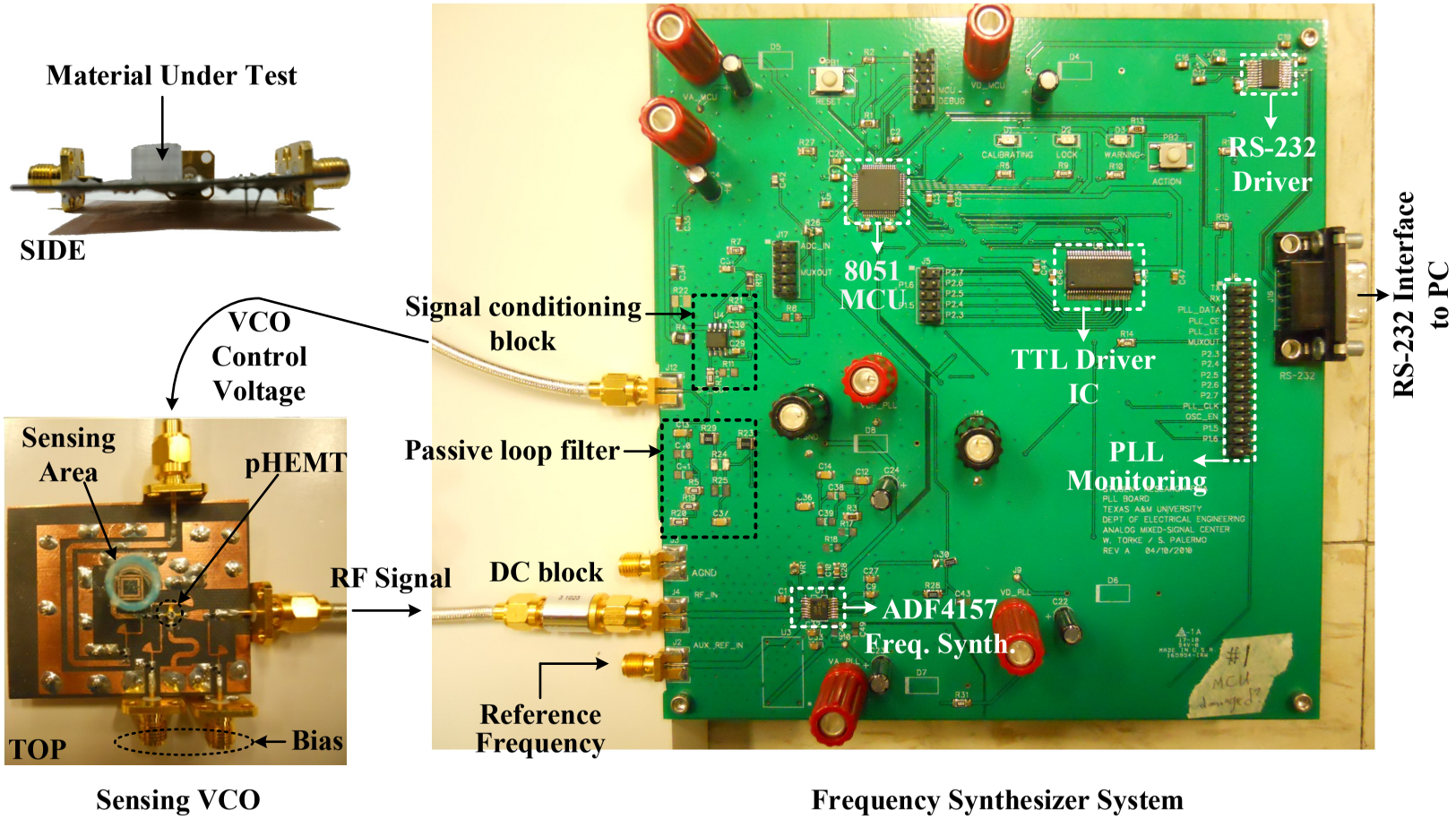

Fig. 122. Fabricated frequency synthesizer system for detection of organic liquid materials.

1. Measurement Procedure

First, the frequency synthesizer system is powered up and the MCU registers, ADC settings, and RS-232 serial communication protocols are initialized. Communication between the MCU and PC interface is verified by a sequence of read/write commands issued to the MCU. The ADF4157 frequency synthesizer chip is then programmed by the MCU by entering the detection frequency ($f_0 = 4.5$ GHz) and reference frequency ($f_{ref} = 14.86086$ MHz) into the LabView VI. When the frequency divider value is set to $N_1 = f_0/f_{ref} = 4.5 \times 10^9/14.86086 \times 10^6 \approx 303$, the system locks to the output frequency of f_0. To verify that the system is indeed in the locked state, the 'lock-detect' output of the ADF4157 chip must be at a logic-high state. When the system is locked, the output of the loop filter has a voltage of $V_c \approx 0.5 - 0.7$ V. V_c is then digitized by the ADC and the mean initialization voltage $\overline{V}_c$ is obtained by digitally averaging the ADC output 65536 times, and is finally stored in the MCU memory. At this time, system initialization is complete.

Second, a known sample volume of organic liquid to be analyzed is dispensed into the sample well using a Finnpipette II single-channel pipetter[2] with adjustable volumes between 10 μL and 200 μL (accuracy $> 99\%$). The addition of a dielectric layer above the sensor shifts the oscillation to lower frequencies. To maintain locked state at a frequency f_0, the loop filter output voltage changes from V_c to a higher value V_m. The voltage V_m is digitally averaged 65536 times to obtain the mean value of control voltage $\overline{V}_m$, that is stored in the MCU memory. The detection process is now complete.

Finally, to estimate the frequency shift caused due to the organic liquid under test, the calculation phase is executed. In this stage, the MCU attempts to change the

[2]Available [online]: http://www.thermoscientific.com.

divider value so that the loop filter output $\overline{V}_m$ approaches the value $\overline{V}_c$ that is stored in the memory. When the loop filter output has a DC level that is within a few mV of $\overline{V}_c$, the divider has a new value N_2 that depends on the MUT. Consequently, the output of the frequency synthesizer moves to a lower frequency f_1, and the frequency shift is obtained as $|\Delta f| = |(N_2 - N_1)|f_{ref}$, and displayed on the PC monitor.

2. Sensitivity Analysis

To characterize the frequency synthesizer system as a self-sustained platform for chemical detection, it is important to study the dependence of frequency shift provided by the system as a function of the MUT and sample volume. To do this, the MUTs used for analysis are divided into two main classes: (1) calibration materials such as ethanol and methanol, which have been well characterized in literature with respect to frequency and temperature, and (2) test materials, which are unknown organic liquids whose dielectric constants must be determined. In addition, in the absence of any calibration materials, air is also treated as a calibration point which provides zero frequency shift for $\epsilon'_r = 1$.

Sample volumes from 10 μL to 200 μL of calibration and test materials are dispensed into the sample well and frequency shifts are measured. For each sample volume of each material, five frequency measurements are taken and the average frequency shift is computed. Fig. 123 shows the average frequency shifts and error bars obtained for each volume and calibration and test materials. The dielectric constants of the calibration materials (ethanol and methanol) at 4.5 GHz and 20°C are indicated. For a given sample volume, it is observed that the frequency shifts obtained for test materials are all lower than those obtained for methanol, indicating that their dielectric constants must be lower than that of methanol.

For any material, at low sample volumes ($< 50\mu$L), the frequency shift is an

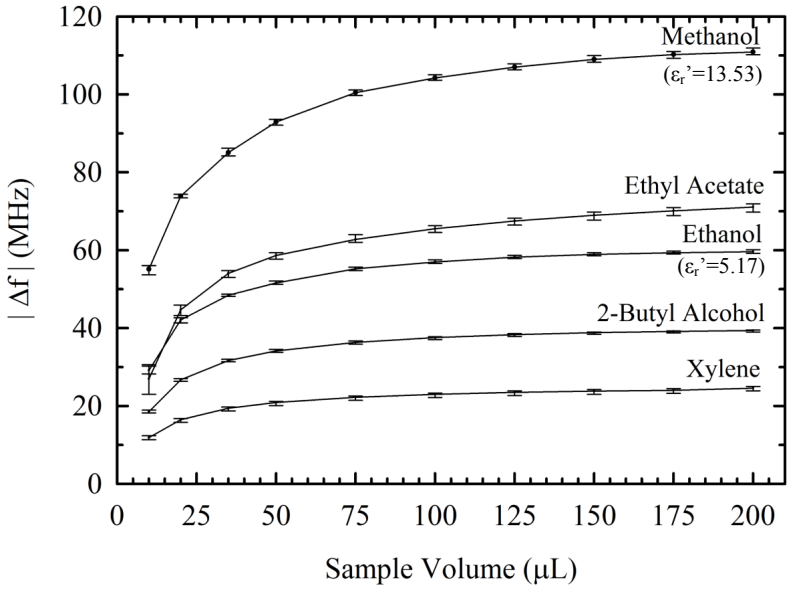

Fig. 123. Measured frequency shift versus sample volumes for several MUTs.

increasing function of sample volume because a considerable part of the electromagnetic field of the SRR lies outside the MUT. Consequently, the frequency shift keeps increasing as more liquid volume is added due to greater interaction between the electromagnetic field of the sensor and MUT. Dielectric constant measurements made for such low sample volumes tend to be very sensitive to actual liquid volumes, and often result in erroneous calibrations and dielectric constant values primarily due to insufficient sensor coverage by the MUT and partial interactions of the MUT with the electromagnetic field of the sensor.

However, the frequency shifts almost stop increasing beyond a threshold volume for a particular material. In this case, the electromagnetic field that extends into the space above the SRR sensor is completely filled with the MUT. As a result, increasing liquid volume provides a negligible increase in frequency shift. At high sample volumes, calibrations and dielectric constant extractions tend to have greater accuracy because of large frequency shifts which can be precisely detected, and relative

insensitivity to the dispensed sample volume.

3. Chemical Calibration and Detection

Using the frequency shift obtained for ethanol and methanol for a given volume, a calibration curve that maps frequency shift into dielectric constant (ϵ'_r) can be obtained for that particular volume. In general, this mapping is represented by a 2nd-order curve-fit polynomial equation obtained from measurements of calibration materials as

$$|\Delta f|(S_v) = a(S_v)\epsilon'^2_r + b(S_v)\epsilon'_r + c(S_v) \tag{5.9}$$

where S_v is the sample volume of calibration materials used, and $|\Delta f|$ is the average frequency shift for that particular sample volume. Fig. 124 shows the curve-fit calibration curves obtained using frequency shift measurements in air, ethanol and methanol. Table XV shows the chemical calibration coefficients $a(S_v)$, $b(S_v)$ and $c(S_v)$ for different sample volumes S_v. The calibration coefficients are based on the measured mean values of frequency shift and have a certain degree of error associated with them. However, this has been ignored here because the error bars in the frequency shift measurement for ethanol and methanol in Fig. 123 are very small. For more exact error analysis, the errors in calibration coefficients must also be considered.

To extract the dielectric constant of an unknown organic liquid, a sample volume S_v of the unknown liquid material is dispensed into the sample well of the VCO. Next, frequency shift is measured using the frequency synthesizer system and the dielectric constant of the unknown material is extracted by finding the roots of the quadratic equation in (5.9) as

$$\epsilon'_r = \frac{-b(S_v) + \sqrt{b(S_v)^2 - 4a(S_v)[c(S_v) - |\Delta f|(S_v)]}}{2a(S_v)} \tag{5.10}$$

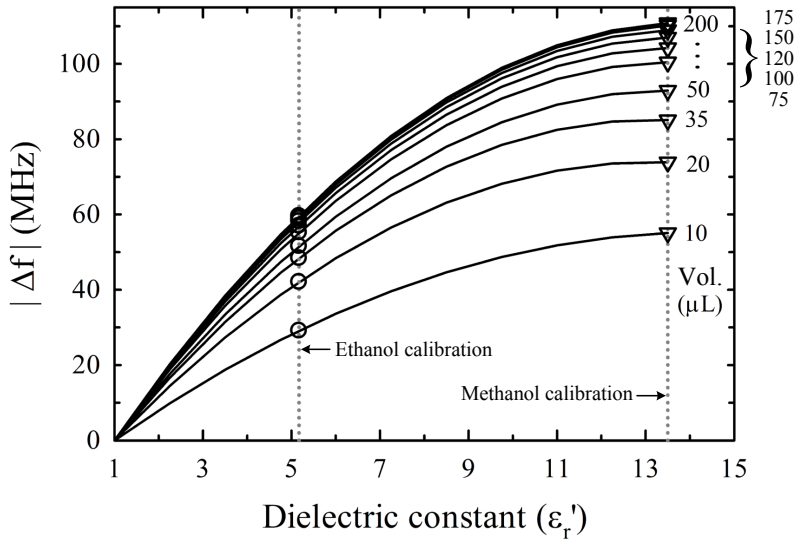

Fig. 124. Chemical calibration curves for different sample volumes using air, ethanol and methanol as reference materials.

Table XV. Chemical Calibration Coefficients for the Frequency Synthesizer-Based Measurement System

Sample Vol. (S_v)	$a(S_v)$	$b(S_v)$	$c(S_v)$
10	-0.3092	8.8904	-8.5812
20	-0.5017	13.185	-12.683
35	-0.5772	15.175	-14.598
50	-0.5932	16.033	-15.440
75	-0.6248	17.094	-16.469
100	-0.6395	17.610	-16.970
125	-0.6478	17.952	-17.304
150	-0.6498	18.138	-17.489
175	-0.6501	18.242	-17.592
200	-0.6511	18.307	-17.656

Table XVI. Comparison between Theoretical and Measured Values of Dielectric Constant for a Sample Volume $S_v = 100\mu$L, at 4.5 GHz

MUT	Theoretical	Measured
2-Butyl Alcohol	3.56	3.555 $\pm$0.030
o-Xylene	2.51	2.473 $\pm$0.035
Ethyl Acetate	5.98	5.982 $\pm$0.085

Fig. 125 shows the extracted dielectric constants of 2-butyl alcohol, o-xylene and ethyl acetate for sample volumes between 10 μL and 200 μL. For sample volumes between 50 μL and 200 μL, the extracted dielectric constant is in excellent agreement with the Debye model in (5.1), and is almost independent of the sample volume. The high detection accuracy obtained is attributed to the MUT being completely exposed to the electromagnetic field of the SRR sensor. In other words, the liquid layer above the SRR is entirely penetrated by the electromagnetic field lines of the SRR. However, for sample volumes lower than 50 μL, the detection accuracy is noticeably lower and is due to the MUT not covering the entire surface of the SRR and/or the MUT not occupying the entire volume in which electromagnetic fields are present above the SRR. In both cases, the calibration and detection accuracy is significantly degraded. Table XVI shows the theoretical and extracted values of dielectric constant for test materials at 4.5 GHz, when a sample volume of 100 μL is used. At this sample volume, the measured dielectric constant has a variation of $< \pm 1.5\%$ about its mean value, and thus provides very accurate detection compared to the results obtained in Section D using the oscillator alone.

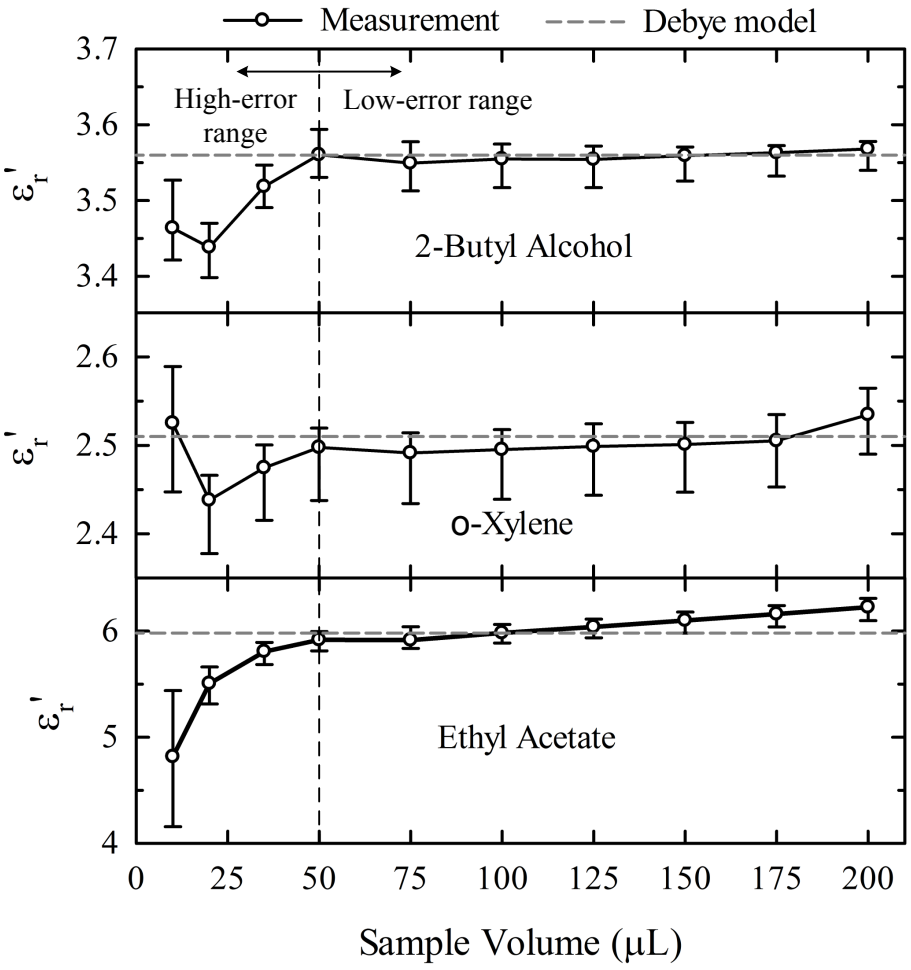

Fig. 125. Extracted dielectric constant values for 2-butyl alcohol, o-xylene and ethyl acetate for sample volumes between 10 μL and 200 μL.

G. Conclusion

In this chapter, a self-sustained, microwave platform for detection of dielectric constant of organic liquids has been developed. Since the entire system only requires DC power supplies for operation, it can be easily run with the help of batteries and is very useful where portability is of prime importance. The novelty of the system developed in this chapter lies in the use of microwave oscillators in a frequency synthesizer architecture, which allows the system to be digitally interfaced with a PC. The ability of digital post-processing such as taking large number of averages greatly improves the accuracy of the measurement system. The dielectric constant of several organic liquids has been extracted and is in excellent agreement with reported values. The system designed, implemented and measured in this work has diverse applications in the field of agriculture, pharmaceuticals and medicine.

CHAPTER VI

CONCLUSION AND FUTURE WORK

A. Conclusion

The major topics in this dissertation are the development of novel miniaturization techniques for single-band, dual-band, ultrawideband and tunable RF filters, the design and implementation of hybrid RF MEMS tunable filters using substrate-integrated-waveguides, and detailed analysis of nonlinear noise phenomena in all-pole RF MEMS tunable filters. In addition, a fully self-sustained microwave platform for the detection of dielectric constant of lossy organic liquids has been demonstrated.

A variety of miniaturization techniques are developed in this thesis, all of which result in considerable size reduction of the filter structure. For UWB filters employing the composite microstrip-CPW topology, slow-wave capacitively-loaded CPW lines are used to reduce the multiple-mode resonator size by 40%. Stub-loaded microstrip-CPW transitions are used to improve the rejection skirt at the upper passband edge while defected ground structures are used to obtain an upper stopband rejection better than 22 dB from 11 to 16 GHz. A novel bridge structure is utilized to generate an interference rejection notch at 5.6 GHz in the filter response. The measured insertion loss is 0.9 dB over the 3.1-10.6 GHz passband, and the UWB filter with improved rejection and frequency notch is only $0.32\lambda_0$-long at mid-band frequency. For filters at K-band, a lumped element filter has been implemented on 90-nm CMOS technology and is approximately 10 times smaller than its thin-film microstrip equivalent. Special attention is given to the effect of automatic metal-filling processes during fabrication. The filter has an insertion loss of approximately 5 dB and occupies a total area of 0.315 mm^2 on-chip. For single-band substrate integrated waveguide filters, half-mode

operation and cross-shaped fractal structures proves to be effective in reducing the filter area by up to 37% (for the 2nd fractal iteration), while simultaneously improving the filter quality factor. For dual-band substrate integrated waveguide filters, using half-mode structures drastically reduces the filter size by a factor of six, compared to their full-mode equivalents. The measured filter response has center frequencies of 1.05 and 1.3 GHz, and insertion losses of 1.7 and 1.8 dB at each band, respectively. A rejection level of approximately 50 dB is achieved between filter passbands, and >40 dB is achieved between 1.45 and 2.71 GHz. The rejection level in close vicinity of the upper passband (at 1.681 GHz) is around 70 dB.

Another major emphasis of this dissertation is the development of hybrid substrate-integrated-waveguide (SIW) RF MEMS tunable filters. Tunable filters based on full-mode and half-mode operation have been designed, fabricated and tested for the 1.2-1.6 GHz range. Over this tuning range, the filters have 13 or 14 distinct frequency states, providing almost contiguous frequency coverage. Packaged, surface-mount RF MEMS switches from Omron Inc. have been used to implement tunability because they have excellent RF performance and are easily soldered onto the filter structure. As a result, the hybrid approach to RF MEMS tunable filter design greatly reduces fabrication complexity while still providing high performance. In the full-mode SIW tunable filter, the resonator is tuned by perturbing the cavity fields using metallic posts. The measured filter response shows an insertion loss variation between 2.2 and 4.1 dB, and quality factors between 93-132, over all tuning states. By appropriate placement of the tuning posts, constant fractional bandwidth tuning (3.7% $\pm$ 0.5%) is obtained. A spurious suppression better than 28 dB is obtained up to 4 GHz using dissimilar elliptic lowpass filters at the tunable filter input and output. In comparison to the current state-of-the-art, this filter has the highest quality factor using off-the-shelf RF MEMS switches on conventional PCB substrates. In the half-mode

SIW tunable filter, the resonator is tuned using an inductive network of via-holes and short lengths of transmission line. The filter is approximately 2.5 times smaller than its full-mode equivalent and exhibits excellent stopband performance due to absence of even-order spurious resonances. The measured filter response shows an insertion loss variation between 1.2 and 3.4 dB, and quality factors between 75-140, over all tuning states. By appropriately designing the inverters, constant absolute bandwidth tuning (1 dB-bandwidth=85±10 MHz) is obtained.

This dissertation also deals with the detailed analysis of nonlinear noise in all-pole RF MEMS tunable filters. The objective of this study is to calculate the effect of phase noise in RF MEMS tunable filters induced by Brownian noise in MEMS switches, and the impact on the SNR at the filter output. In addition, the nonlinearity of the RF MEMS switches is considered during noise calculations. Initially, the CAD model of the RF MEMS switch is used to estimate nonlinear noise using harmonic balance simulation. To provide better insight into the nature of noise in tunable filters, a complete mathematical treatment for nonlinearity and noise is presented. Nonlinear effects in tunable filters is studied using an iterative method to extract the large-signal S-parameters of the filter. Next, two independent analytical approaches based on pole-perturbation and admittance variation are presented, and compared with the CAD-based method for validation. In summary, this study proves that the output SNR degradation in an RF MEMS tunable filter is most significant in filters with low fractional bandwidth, high order and high quality factor.

Finally, a self-sustained microwave platform for the detection of organic liquids is implemented and tested. The main idea here is to detect the dielectric constant of an unknown organic liquid based on oscillation frequency changes of a microwave voltage-controlled oscillator. The sensing element is a split ring resonator due to its high field confinement. To make the system self-sustained, the oscillator is included as

part of a frequency synthesizer architecture, and digitally interfaced to a computer. As a result, very accurate dielectric constant measurements are made without the requirement for expensive laboratory test equipment. It is also used to detect the properties of chemical mixtures. The entire detection system only requires DC power supplies and is very useful for portable, in-situ measurement of dielectric properties.

B. Future Work

1. Half-Mode Substrate Integrated Waveguide Diplexer

In dual-band communication systems, a diplexer is often an essential component that splits the incoming signal into its respective frequency bands as shown in Fig. 126. However, to effectively separate the incoming signal into its constitutive frequencies, diplexers often require high stopband rejection and isolation. Recently, substrate integrated waveguides loaded with complementary split ring resonators (CSRRs) have been used for diplexer design in [118] and shows excellent performance. The half-mode substrate integrated waveguide structure utilized in Chapters II and III is an ideal candidate for the design of high performance diplexers primarily due to its low-loss properties, good rejection performance due to absence of spurious modes and compact size. Thus, a half-mode substrate integrated waveguide diplexer will be a very useful component in modern compact dual-band transceivers.

2. Ku-Band Half-Mode Substrate Integrated Waveguide RF MEMS Tunable Filter

Several planar RF MEMS tunable filters have been reported in literature for Ku-band (12-18 GHz) applications in [74] and [119], primarily for applications in military wide-band tracking receivers. Half-mode substrate integrated waveguide tunable filters in the 12-18 GHz range (like the one developed in Chapter III for the 1.2-1.6 GHz range)

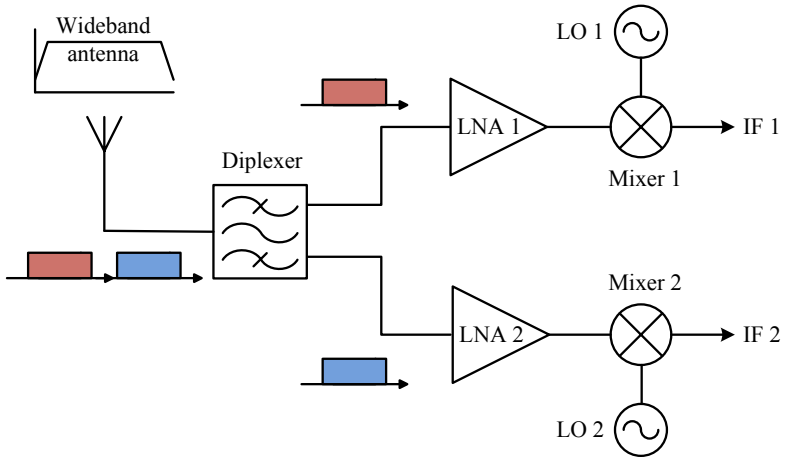

Fig. 126. Block diagram of a dual-band receiver which uses a diplexer to separate the received signal into appropriate frequency bands.

would provide much higher quality factors, compact size and low insertion losses compared to planar filters. However, the parasitics of packaged RF MEMS switches make them unusable at this frequency range. Instead, the filters must employ monolithically fabricated metal-contact RF MEMS switches which have much lower parasitics at high frequencies. For improved performance, capacitive RF MEMS switches in the tuning network of the filter since they have better low-loss characteristics than metal-contact switches, in the down-state position.

3. Experimental Verification of Nonlinear Noise in RF MEMS Tunable Filters

Majority of the treatment of nonlinear noise in RF MEMS tunable filters in Chapter IV of this dissertation is purely mathematical. Although the values of phase noise in all-pole RF MEMS tunable filters obtained from theory is validated using harmonic balance analysis techniques, it is still vital to verify the theories of phase noise experimentally. This is a very challenging task considering that phase noise values for a practical RF MEMS tunable filter with reasonable fractional bandwidth and order

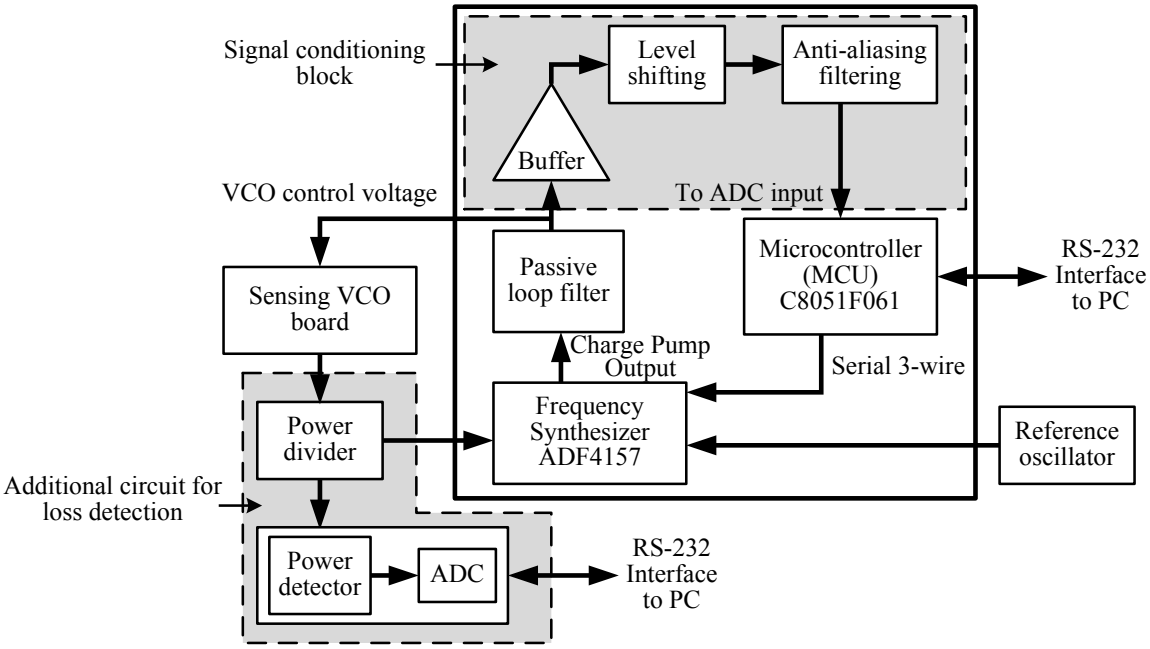

Fig. 127. Frequency synthesizer architecture for organic liquid detection including power detector circuitry for detection of material loss.

are still very low to measure using even the best spectrum analyzers available today. However, special techniques have been developed to measure phase noise values close to the noise floor using interferometric techniques in [120]. Using such a custom phase noise measurement setup, the phase noise levels in RF MEMS tunable filters can be measured, and will be very useful in validating the results reported in this dissertation.

4. Self-Sustained Platform for Detection of Material Loss

Material loss is represented by the imaginary part (ϵ_r'') of the complex permittivity of a material, and is a quantity that must be determined for an unknown material in addition to its dielectric constant (ϵ_r'). Since the complex permittivity of a material is a unique property, determining ϵ_r' and ϵ_r'' is of utmost importance. In the measurement system proposed in Chapter V, the ϵ_r' of the material only produces frequency shifts

in oscillation. By utilizing a power detector with an integrated analog-to-digital converter, changes in oscillation power can be digitally stored in a computer and used to estimate ϵ_r'' of the material under test. Such a system is shown in Fig. 127 and can be easily implemented by adding a power detector unit at the output of the oscillator. In practice, the mapping of oscillation power to loss of the MUT is not simple since the dielectric constant of the MUT also changes power of oscillation. Thus, appropriate power calibration methods must be developed to decouple the oscillation power change caused by the MUT dielectric constant from that caused by the MUT loss.

REFERENCES

[1] G. L. Matthaei, E. Young, and E. M. T. Jones, *Microwave Filters, Impedance-Matching Networks, and Coupling Structures.* Norwood, MA: Artech House, 1980.

[2] I. C. Hunter, *Theory and Design of Microwave Filters.* London, U.K.: IEE, 2001.

[3] G. Macchiarella and S. Tamiazzo, "Design techniques for dual-passband filters," *IEEE Transactions on Microwave Theory and Techniques*, vol. 53, no. 11, pp. 3265-3271, Nov. 2005.

[4] J. Lee and K. Sarabandi, "A synthesis method for dual-band microwave filters," *IEEE Transactions on Microwave Theory and Techniques*, vol. 55, no. 6, pp. 1163-1170, Jun. 2007.

[5] Federal Communications Commission (FCC), Revision of Part 15 of the Commission's Rules Regarding Ultra-Wideband Transmission Systems, First Report and Order, Washington DC, FCC 02-48, 2002.

[6] R. Gomez-Garcia and J. I. Alonso, "Systematic method for the exact synthesis of ultra-wideband filtering responses using high-pass and low-pass sections," *IEEE Transactions on Microwave Theory and Techniques*, vol. 54, no. 10, pp. 3751-3764, Oct. 2006.

[7] L. Zhu, S. Sun and W. Menzel, "Ultra-Wideband (UWB) bandpass filters using multiple-mode resonator," *IEEE Microwave and Wireless Components Letters*, vol. 15, no. 11, pp. 796-798, Nov. 2005.

[8] Z.-C. Hai, J.-S. Hong, J. P. Parry and D. P. Hand, "Ultra-wideband bandpass filter with multiple notch bands using nonuniform periodical slotted ground structure," *IEEE Transactions on Microwave Theory and Techniques*, vol. 57, no. 12, pp. 3080-3088, Dec. 2009.

[9] Z.-C. Hai and J.-S. Hong, "UWB bandpass filter using cascaded high-pass and low-pass filters with multilayer liquid crystal polymer technology," *IEEE Transactions on Microwave Theory and Techniques*, vol. 58, no. 4, pp. 941-948, Apr. 2010.

[10] Z.-C. Hao and J.-S. Hong, "Ultrawideband filter technologies," *IEEE Microw. Mag.*, vol. 11, no. 4, pp. 56-68, Jun. 2010.

[11] A. Tasic, A. Serdijn and J. R. Long, "Adaptive multi-standard circuits and systems for wireless communications," *IEEE Circuits and Systems Magazine*, vol. 6, no. 1, pp. 29-37, 2006.

[12] W. J. Keane, "YIG filters aid wide open receivers," *Microwave Journal*, vol. 17, no. 8, Sept. 1980.

[13] K. Entesari and G. M. Rebeiz, "RF MEMS, BST, and GaAs varactor system-level response in complex modulation systems," *Int. Journal of RF and Microwave CAE*, vol. 18, no. 1, pp. 86-98, Sept. 2007.

[14] J. Lee, M. S. Uhm and I-.B Yom, "A dual-passband filter of canonical structure for satellite applications," *IEEE Microwave and Wireless Components Letters*, vol. 14, no. 6, pp. 271-273, June 2004.

[15] J. S. Hong and M. J. Lancaster, *Microstrip Filters for RF/Microwave Applications* New York: Wiley, 2001.

[16] C.-H. Lee, C.-I.G. Hsu and C.-C. Hsu, "Balanced dual-band BPF with stub-loaded SIRs for common-mode suppression," *IEEE Microwave and Wireless Components Letters*, vol. 20, no. 2, pp. 70-72, Feb. 2010.

[17] Y.-H. Cho, H.-I. Baek, H.-S. Lee and S.-W. Yun, "A dual-band combline band-pass filter loaded by lumped series resonators," *IEEE Microwave and Wireless Components Letters*, vol. 19, no. 10, pp. 626-628, Oct. 2009.

[18] S. lee and Y. Lee, "A planar dual-band filter based on reduced-length parallel coupled lines," *IEEE Microwave and Wireless Components Letters*, vol. 20, no. 1, pp. 16-18, Jan. 2010.

[19] D. Deslandes and K. Wu, "Single-substrate integration technique of planar circuits and waveguide filters," *IEEE Trans. Microwave Theory Tech.*, vol. 51, no. 2, pp. 593-596, Feb. 2003.

[20] X.-P Chen and K. Wu, "Substrate integrated waveguide cross coupled filter with negative coupling structure," *IEEE Trans. Microwave Theory Tech.*, vol. 56, no. 1, pp. 142-149, Jan. 2008.

[21] X.-P Chen, K. Wu and D. Drolet, "Substrate integrated waveguide filter with improved stopband performance for satellite ground terminal," *IEEE Trans. Microwave Theory Tech.*, vol. 57, no. 3, pp. 674-683, Mar. 2009.

[22] X.-P. Chen, K. Wu and Z.-L. Li, "Dual-band and triple-band substrate integrated waveguide filters with chebyshev and quasi-elliptic responses," *IEEE Transactions on Microwave Theory and Techniques*, vol. 55, no. 12, pp. 2569-2578, December 2007.

[23] Y. Ding and K. Wu, "Miniaturization techniques of substrate integrated waveguide circuits," in *IEEE MTT-S Workshop Series on Art of Miniaturizing RF and Microwave Passive Components*, Chengdu, China, 14-15 Dec. 2008, pp. 63-66.

[24] L.-S. Wu, X.-L. Zhou and W.-Y. Yin, "A novel multilayer partial H-plane filter implemented with folded substrate integrated waveguide (FSIW)," *IEEE Microwave and Wireless Components Letters*, vol. 19, no. 8, pp. 494-496, Aug. 2009.

[25] H.-Y. Chien, T.-M. Shen, T.-Y. Huang, W.-H. Wang and R.-B. Wu, "Miniaturized bandpass filters with double-folded substrate integrated waveguide resonators in LTCC," *IEEE Transactions on Microwave Theory and Techniques*, vol. 57, no. 7, pp. 1774-1782, Jul. 2009.

[26] H. Wang, L. Zhu and W. Menzel, "Ultra-wideband bandpass filter with hybrid microstrip/CPW structure," *IEEE Microwave and Wireless Components Letters*, vol. 15, no. 12, pp. 844- 846, Dec. 2005.

[27] S. W. Wong and L. Zhu, "Implementation of compact UWB bandpass filter with a notch-band," *IEEE Microwave and Wireless Components Letters*, vol. 18, no. 1, pp. 10-12, Jan. 2008.

[28] Z.-C. Hao and J.-S. Hong, "Compact UWB filter with double notch-bands using multilayer LCP technology," *IEEE Microwave and Wireless Components Letters*, vol. 19, no. 8, pp. 500- 502, Aug. 2009.

[29] L. Nan, K. Mouthaan, Y.-Z. Xiong, J. Shi, S. C. Rustagi, *et al.*, "Design of 60- and 77-GHz narrow-bandpass filters in CMOS technology," *IEEE Trans. on Circuits and Systems-II*, vol. 55, no. 8, pp. 738-742, Aug. 2008.

[30] S. Sun, J. Shi, L. Zhu, S. C. Rustagi, and K. Mouthaan, "Millimeter-wave bandpass filters by standard 0.18-um CMOS technology," *IEEE Electron Device Letters*, vol. 28, no. 3, pp. 220-222, Mar. 2007.

[31] C.-L. Yang, S.-Y. Shu and Y.-C. Chiang, "Analysis and design of a chip filter with low insertion loss and two adjustable transmission zeros using 0.18-μm CMOS technology," *IEEE Transactions on Microwave Theory and Techniques*, vol. 58, no. 1, pp. 176-184, Jan. 2010.

[32] S.-C. Chang, Y.-M. Chen, S.-F. Chang, Y.-H. Jeng, C.-L. Wei, *et al.,* "Compact millimeter wave CMOS bandpass filters using grounded pedestal stepped-impedance technique," *IEEE Transactions on Microwave Theory and Techniques*, vol. 58, no. 12, pp. 3850-3858, Dec. 2010.

[33] G. M. Rebeiz, *RF MEMS Theory, Design and Technology.* New York: Wiley, 2003.

[34] G. M. Rebeiz, K. Entesari, I. Reines, S.-J. Park, M. El-Tanani, A. Grichener and A. Brown, "Tuning in to RF MEMS," *IEEE Microw. Magazine*, vol. 10, issue 6, pp. 55-72, Oct. 2009.

[35] S.-J. Park, K.-Y Lee and G. M. Rebeiz, "Low-loss 5.15-5.70 GHz RF MEMS switchable filter for wireless WLAN applications," *IEEE Trans. Microwave Theory Tech.*, vol. 54, no. 11, pp. 3931-3939, Nov. 2006.

[36] S.-J. Park, I. Reines and G. M. Rebeiz, "Low-loss 4-6 GHz tunable filter with 3-bit high-Q orthogonal bias RF MEMS capacitance network," *IEEE Trans. Microwave Theory Tech.*, vol. 56, no. 10, pp. 2348-2355, Oct. 2008.

[37] M. A. El-Tanani and G. M. Rebeiz, "High-performance 1.5-2.5 GHz RF MEMS

tunable filters for wireless applications," *IEEE Trans. Microwave Theory Tech.*, vol. 58, no. 6, pp. 1629-1637, Jun. 2010.

[38] S.-J. Park, I. Reines, C. Patel and G. M. Rebeiz, "High-Q RF MEMS 4-6 GHz tunable evanescent-mode cavity filter," *IEEE Trans. Microwave Theory Tech.*, vol. 58, no. 2, pp. 381-389, Feb. 2010.

[39] K. Entesari, "Development of high performance 6-18 GHz tunable/switchable RF MEMS filters and their system implications," Ph.D Dissertation, University of Michigan, Ann Arbor, MI, 2006.

[40] S. Majumder, J. Lampen, R. Morrison and J. Maciel, "A packaged, high lifetime ohmic MEMS RF switch," in *IEEE MTT-S International Symposium Digest*, Philadelphia, PA, 8-13 Jun. 2003, vol. 3, pp. 1935-1938.

[41] Y. Uno, K. Narise, T. Masuda, K. Inoue, Y. Adachi, K. Hosoya, T. Seki and F. Sato, "Development of SPDT-structured RF MEMS switch," in *15th International Solid-State Sensors, Actuators and Microsystems Conference*, Denver, CO, 21-25 June 2009, pp. 541-544.

[42] J. Muldavin, C. Bozler and C. Keast, "Wafer-scale packaged RF-MEMS switches,"in *IEEE MTT-S International Symposium Digest*, San Francisco, CA, 11-16 Jun. 2006, vol. 3, pp. 267-270.

[43] G. M. Rebeiz, "Phase-noise analysis of MEMS-based circuits and phase shifters," *IEEE Trans. Microwave Theory Tech.*, vol. 50, no. 5, pp. 1316-1323, May 2002.

[44] L. Dussopt and G. M. Rebeiz, "Intermodulation distortion and power handling in RF MEMS switches, varactors and tunable filters," *IEEE Trans. Microwave Theory Tech.*, vol. 51, no. 4, pp. 1247-1256, April 2003.

[45] T.-N. Kuo, S.-C. Lin and C. H. Chen, "Compact ultra-wideband bandpass filters using composite microstrip-coplanar-waveguide structure," *IEEE Transactions on Microwave and Theory Techniques*, vol. 54, no. 10, pp. 3772-3778, Oct. 2006.

[46] J.-W. Baik, T.-H. Lee and Y.-S. Kim, "UWB bandpass filter using microstrip to CPW transition with broadband balun," *IEEE Microwave and Wireless Components Letters*, vol. 17, no.12, pp.846-848, Dec. 2007.

[47] J.-K. Lee and Y.-S. Kim, "Ultra-wideband bandpass filter with improved upper stopband performance using defected ground structure," *IEEE Microwave and Wireless Components Letters*, vol. 20, no.6, pp.316-318, Jun. 2010.

[48] S. W. Wong and L. Zhu, "EBG-embedded multiple-mode resonator for UWB bandpass filter with improved stopband performance," *IEEE Microwave and Wireless Components Letters*, vol. 17, no.6, pp.421-423, Jun. 2007.

[49] F. Aryanfar and K. Sarabandi, "Compact millimeter-wave filters using distributed capacitively loaded CPW resonators," *IEEE Transactions on Microwave Theory and Techniques*, vol. 54, no. 3, pp. 1161-1165, Mar. 2006.

[50] D. M. Pozar, *Microwave and RF Design of Wireless Systems*, New York: Wiley, 2001.

[51] C. H. Doan, S. Emami, A. M. Niknejad and R. W. Broderson, "Millimeter-wave CMOS design," *IEEE Journal of Solid State Circuits*, vol. 40, no. 1, pp. 144-155, Jan. 2005.

[52] P. Blondy, . R. Brown, D. Cros, and G. M.Rebeiz, "Low-loss micro-machined filters for millimeter-wave communication systems," *IEEE Trans. Microwave Theory Tech.*, vol. 54, no. 12, pp. 2283-2288, Dec. 1998.

[53] K. T. Chan, C. Y. Chen, A. Chin, J. C. Hsieh, J. Liu, *et al.*, "40-GHz coplanar waveguide bandpass filters on silicon substrate," *IEEE Microwave and Wireless Components Letters*, vol. 12, no. 11, pp. 429-431, Nov. 2002.

[54] S. B. Cohn, "Direct-coupled-resonator filters," *Proc. of Institute of Radio Engineers (IRE)*, vol. 45, no. 2, pp. 187-196, Feb. 1957.

[55] K. Wada, Y. Aihara, T. Kamiyama and O. Hashimoto, "3-pole bandpass filters using short-ended half-wavelength resonators and their applications to a duplexer," in *Proc. IEEE Wireless Commun. Technol. Top. Conf.*, Honolulu, HI, 15-17 Oct. 2003, pp. 160-163.

[56] S. Zhou, Z. Wang, X. Ruimin, D. Shen and M. Zhan, "A novel X-band half mode substrate integrated waveguide (HMSIW) bandpass filter," in *2009 Asia Pacific Microwave Conference*, Singapore, 7-10 Dec. 2009, pp. 1387-1389.

[57] W. Hong, B. Liu, Y. Wang, Q. Lai, H. Tang, *et al.*, "Half mode substrate integrated waveguide: A new guided wave structure for microwave and millimeter wave application," in *Joint 31st Intern. Conf. on Infrared Millimeter Waves*, Shanghai, China, 18-22 Sept. 2006, pp. 219-219.

[58] Y. Wang, W. Hong, Y. Dong, B. Liu, H. J. Tang, *et al.*, "Half-mode substrate integrated waveguide (HMSIW) bandpass filter," *IEEE Microwave and Wireless Components Letters*, vol.17, no.4, pp. 265-267, Apr. 2007.

[59] K. Falconer, *Fractal Geometry: Mathematical Foundations and Applications,* 2nd ed. New York: Wiley, 2003.

[60] C. P. Baliarda, J. Romeu, and A. Cardama, "The Koch monopole: A small fractal antenna," IEEE Trans. Antennas Propag., vol. 48, no. 11, pp. 17731781,

Nov. 2000.

[61] I. K. Kim, N. Kingslet, M. Morton, R. Bairavasubramanian, J. Papapolymerou, *et al.*, "Fractal-shaped microstrip coupled-line bandpass filters for suppression of second harmonic," *IEEE Trans. Microwave Theory Tech.*, vol. 53, no. 9, pp. 2943-2948, Sept. 2005.

[62] P. Jarry and J. Beneat, *Design and Realizations of Miniaturized Fractal RF and Microwave Filters,* New York: Wiley, 2009.

[63] Q. Lai, C. Fumeaux, W. Hong and R. Vahldieck, "Characterization of the propagation properties of the half-mode substrate integrated waveguide," *IEEE Transactions on Microwave Theory and Techniques*, vol. 57, no. 18, pp. 1996-2004, August 2007.

[64] K. Entesari and G. M. Rebeiz, "A 25-75 MHz RF MEMS tunable filter," *IEEE Trans. Microwave Theory Tech.*, vol. 55, no. 11, pp. 2399-2405, Nov. 2007.

[65] V. Sekar and K. Entesari, "Inductively-loaded RF MEMS reconfigurable filters," *Int. Journal of RF and Microwave CAE*, vol. 19, no. 6, pp. 692-700, Dec. 2009.

[66] J. C. Bohorquez, B. Potelon, C. Person, E. Rius, C. Quendo, G. Tanne and E. Fourn, "Reconfigurable Planar SIW Cavity Resonator and Filter," in *2006 IEEE MTT-S International Microwave Symposium Digest*, San Francisco, CA, 11-16 Jun. 2006, pp. 947-950.

[67] M. Armendariz, V. Sekar and K. Entesari "Tunable SIW Bandpass Filters with PIN Diodes," in *Proceedings of 40th European Microwave Conference*, Paris, France, 28-30 Sept. 2010, pp. 830-833.

[68] W. Gautier, A. Stehle, B. Schoenlinner, V. Ziegler, U. Prechtel and W. Menzel, "RF MEMS tunable filters on low-loss LTCC substrate for UAV data-link," in *Proceedings of 4th European Microwave Integrated Circuits Conference*, Rome, Italy, 28-29 Sept. 2009, pp. 347-350.

[69] K. Wu, D. Deslandes and Y. Cassivi, "The substrate integrated circuits - a new concept for high-frequency electronics and optoelectronics," in *6th International Conference on Telecommunications in Modern Satellite, Cable and Broadcasting Service*, Serbia and Montenegro, 1-3 Oct. 2003, vol. 1, pp. P-III–P-X.

[70] S. Amari and U. Rosenberg, "Characteristics of cross (bypass) coupling through higher/lower order modes and their applications in elliptic filter design," *IEEE Trans. Microwave Theory Tech.*, vol. 53, no. 10, pp. 3135-3141, Oct. 2005.

[71] T. Seki, F. Sato, T. Masuda, I. Kimura and K. Imanaka, "Low-loss RF MEMS metal-to-metal contact switch with CSP structure," in *12th International Conference on Solid-State Sensors, Actuators and Microsystems*, Boston, MA, 9-12 Jun. 2003, vol. 1, pp. 340-341.

[72] N. Marcuvitz, *Waveguide Handbook.* New York: Dover Publications Inc., 1951.

[73] T.-S. Yun, H. Nam, J.-Y. Kim, B. Lee, J.-J. Choi, K.-B. Kim, T.-J. Ha and J.-C. Lee, "Harmonics suppressed substrate-integrated-waveguide filter with integration of low-pass filter, *Microwave and Optical Tech. Letters*, vol. 50, pp. 447-450, Jan. 2008.

[74] K. Entesari and G. M. Rebeiz, "A 12-18 GHz three pole RF MEMS tunable filter," *IEEE Trans. Microwave Theory Tech.*, vol. 53, no. 8, pp. 2566-2571, Aug. 2005.

[75] J. Johnson, G. G. Adams and N. E. McGruer, "Determination of intermodulation distortion in a contact-type MEMS microswitch," *IEEE Trans. Microwave Theory Tech.*, vol. 53, no. 8, pp. 2566-2571, Aug. 2005.

[76] K. Gong, W. Hong, H. Tang and J. Chen, "C-band bandpass filter based on half mode substrate integrated waveguide (HMSIW) cavities," in *2009 Asia Pacific Microwave Conference*, Singapore, 7-10 Dec. 2009, pp. 2591-2594.

[77] A. A. Oliner, "Scannable millimeter wave arrays, volume II," Final Technical Report, pp. 304-315, Polytechnic University, Farmingdale, NY, April 1989.

[78] J. Liu, D. R. Jackson, P. Liu, J. Wang and Y. Long, "The propagation wavenumber for microstrip line in the first higher-order mode," in *2010 International Conference on Microwave and Millimeter Wave Technology*, Chengdu, China, 8-11 May 2010, pp. 965-968.

[79] G. F. Craven and C. K. Mok, "The design of evanescent mode waveguide bandpass filters for a prescribed insertion loss characteristic," *IEEE Trans. Microwave Theory Tech.*, vol.19, no.3, pp. 295- 308, Mar. 1971.

[80] "Omron RF MEMS Switch 2SMES-01 datasheet," Schaumburg, IL, Omron Electronic Components LLC, 2009.

[81] E. Mehrshahi, M. Salehi and R. Rezaiesarlak, "Substrate integrated waveguide filters with stopband performance improvement," in *2010 International Conference on Microwave and Millimeter Wave Technology (ICMMT)*, Chengdu, China, 8-11 May 2010, pp. 2018-2020.

[82] T. B. Gabrielson, "Mechanical-thermal noise in micromachined acoustic and vibration sensors," *IEEE Trans. on Electron Devices*, vol. 40, no. 5, pp. 903-909,

May 1993.

[83] K. Entesari and G. M. Rebeiz, "A Differential 4-bit 6.5–10-GHz RF MEMS Tunable Filter," *IEEE Trans. Microwave Theory Tech.*, vol. 53, no. 3, pp. 1103-1110, Mar. 2005.

[84] A. Sivadas, M. Yu and R. Cameron, "A simplified analysis for high power microwave bandpass filter structures," in *IEEE MTT-S International Microwave Symposium Digest*, vol. 3, pp. 1771-1774, 2000.

[85] A. A. Tamijani, "Novel components for integrated millimeter-wave front-ends," Ph.D Dissertation, University of Michigan, Ann Arbor, MI, 2004.

[86] S.-J. Park, I. Reines, C. Patel and G. M. Rebeiz, "High-Q RF-MEMS 4—6-GHz Tunable Evanescent-Mode Cavity Filter," *IEEE Trans. Microwave Theory Tech.*, vol. 58, no. 2, pp. 381-389, Feb. 2010.

[87] A. R. Brown, G. M. Rebeiz, "A varactor-tuned RF filter," *IEEE Trans. on Microwave Theory and Tech.*, vol. 48, no. 7, pp. 1157-1160, July 2000.

[88] I. Bahl and P. Bhartia, *Microwave Solid State Circuit Design.* New York: Wiley, 1988.

[89] F. Kouril and K. Vrba, *Nonlinear and Parametric Circuits: Principles, Theory and Applications.* New York: Wiley, 1988.

[90] C. Ernst and V. Postoyalko, "Prediction of peak internal fields in direct coupled cavity filters," *IEEE Trans. on Microwave Theory and Tech.*, vol. 51, no. 1, pp. 64-73, Jan. 2003.

[91] A. G. Place and G. H. Allen, "Generalized pole sensitivity analysis due to parameter perturbation," *IEEE Trans. on Circuits and Systems—II:Analog and Digital Signal Processing*, vol. 44, no. 10, pp. 869-873, Oct. 1997.

[92] D. Deschrijver and T. Dhaene, "Fast passivity enforcement of s-parameter macromodels by pole perturbation," *IEEE Trans. Microwave Theory Tech.*, vol. 57, no. 3, pp. 620-626, Mar. 2009.

[93] M. E. Van Valkenberg, *Modern Network Synthesis.* New York: Wiley, 1960.

[94] M. Koochakzadeh and A. Abbaspour-Tamijani, "Closed-form formulas for predicting the nonlinear behavior of all-pole bandpass filters," *IEEE Trans. Microwave Theory Tech.*, vol. 56, no. 3, pp. 575-586, Mar. 2008.

[95] C. L. Goldsmith, Z. Yao, S. Eshelman, and D. Denniston, "Performance of low-loss RF MEMS capacitive switches," *IEEE Microwave Guided Wave Lett.*, vol. 8, pp. 269–271, Aug. 1998.

[96] R. J. Cameron, C. M. Kudsia and R. R. Mansour, *Microwave Filters for Communication Systems: Fundamentals, Design and Applications.* New York: Wiley, 2007.

[97] V. Miraftab and M. Yu, "Advanced coupling matrix and admittance function synthesis techniques for dissipative microwave filters," *IEEE Trans. Microwave Theory Tech.*, vol. 57, no. 10, pp. 2429-2438, Oct. 2009.

[98] E. Nyfors and P. Vainikainen, *Industrial Microwave Sensors.* Norwood, MA: Artech House, 1989.

[99] A. Kraszewski, ed., *Microwave Aquametry: Electromagnetic Wave Interaction With Water-Containing Materials.* Piscataway, NJ: IEEE Press, 1996.

[100] K. C. Lawrence, D. B. Funk, and W. R. Windham, "Swept-frequency grain moisture sensor," in *Proceedings Third Workshop on Electromagnetic Wave Interaction with Water and Moist Substances*, Athens, Georgia, 1999, pp. 128-132.

[101] M. Stacheder, "Grain moisture measurements with time domain reflectometry," in *Proceedings Third Workshop on Electromagnetic Wave Interaction with Water and Moist Substances*, Athens, Georgia, 1999, pp. 133-137.

[102] M. A. Hillhorst, "Dielectric characterization of soil," Ph.D Dissertation, Wageningen Agricultural University, The Netherlands, 1998.

[103] G. Smith, A. P. Duffy, J. Shen and C. J. Olliff, "Dielectric relaxation spectroscopy and some applications in the pharmaceutical sciences," *Journal of Pharmaceutical Sciences*, vol. 84, no. 9, pp. 1029-1044, Sept. 1995.

[104] C. Gabriel, S. Gabriel, E. H. Grant, B. S. J. Halstead and D. M. P. Mingos, "Dielectric parameters relevant to microwave dielectric heating," *Chemical Society Reviews*, vol. 27, pp. 213-223, 1998.

[105] J.-M. Kim, D. H. Oh, J.-H. Park, T.-W. Cho, Y. Kwon, *et al.*, "Permittivity measurements up to 30 GHz using micromachined probe," *Journal of Micromechanics and Microengineering*, vol. 15, pp. 543-550, 2005.

[106] K. Z. Rajab, K.-F. Fuh, R. Mittra and M. Lanagan, " Dielectric property measurement using a resonant nonradiative dielectric waveguide structure," *IEEE Microwave and Wireless Components Letters*, vol. 15, no. 2, pp. 104-106, Feb. 2005.

[107] L. F. Chen, C. K. Ong, C. P. Neo, V. V. Varadan and V. K. Varadan, *Microwave Electronics: Measurement and Materials Characterization.* New York: Wiley,

2004.

[108] K. Saeed, R. D. Pollard and I. C. Hunter, "Substrate integrated waveguide cavity resonators for complex permittivity characterization of materials," *IEEE Trans. on Microw. Theory and Tech.*, vol. 56, no. 10, pp. 2340-2347, October 2008.

[109] K. Saeed, A. C. Guyette, I. C. Hunter and R. D. Pollard, "Microstrip resonator technique for measuring dielectric permittivity of liquid solvents and for solution sensing," in *IEEE MTT-S International. Microwave Symposium Digest*, Honolulu, HI, 3-8 Jun. 2007, pp. 1185-1188.

[110] E. Fratticcioli, M. Dionigi and R. Sorrentino, "A simple and low-cost measurement system for the complex permittivity characterization of materials," *IEEE Trans. on Instrumentation and Measurement*, vol. 53, no. 4, pp. 1071-1077, Aug. 2004.

[111] U. C. Hasar, "A microcontroller-based microwave free-space measurement system for permittivity determination of lossy liquid materials," *Review of Scientific Instruments*, 80, 056103, 2009.

[112] F. Buckley and A. A. Maryott, "Tables of Dielectric Dispersion Data for Pure Liquids and Dilute Solutions," NBS circular 589, Boulder, CO, National Institute of Standards and Technology (NIST), 1958.

[113] P. G. Wilson and R. D. Carver, "An easy-to-use FET DRO design procedure suited to most CAD programs," in *IEEE MTT-S Microwave Symp. Dig.*, Anaheim, CA, 13-19 Jun. 1999, vol. 3, pp. 1033-1036.

[114] H-.J. Lee and J-.G. Yook, "Biosensing using split-ring resonators at microwave regime," *Applied Phys. Lett.*, 92, 254103, 2008.

[115] F. M. Gardner, *Phaselock Techniques*, 3rd ed., New York: Wiley, 2005.

[116] "High Resolution 6 GHz Fractional N Frequency Synthesizer – ADF4157 (Rev. A) – Datasheet," Norwood, MA, Analog Devices Inc., 2007.

[117] "Fully Integrated Mixed-Signal System-on-Chip Microcontroller – C8051F06x series (Rev. 1.2) – Datasheet," Austin, TX, Silicon Laboratories, 2004.

[118] Y. Dong and T. Itoh, "Substrate integrated waveguide loaded by complementary split ring resonators for miniaturized diplexer design," *IEEE Microw. and Wireless Comp. Lett.*, vol. 21, no. 1, Jan. 2011.

[119] I. Reines, C. L. Goldsmith, C. D. Nordquist, C. W. Dyck, G. M. Kraus, *et al.,* "A low-loss RF MEMS Ku-band switched capacitor bank," *IEEE Microw. and Wireless Comp. Lett.,* vol. 15, no.2, pp. 74-76, Feb. 2005.

[120] E. Rubiola, V. Giordano and J. Groslambert, "Very high frequency and microwave interferometric phase and amplitude noise measurements," *Review of Scientific Instruments,* vol. 70, no. 1, pp. 220-225, Jan. 1999.

APPENDIX A

DERIVATION OF PROTOTYPE PERTURBATION

For synchronously tuned filters [Fig. 84(a)], the susceptance slope of resonators are equal and are expressed as $b = b_1 = \ldots, b_N$. The shunt capacitance of the i^{th} resonator is obtained from the low-pass prototype element value (g_i) of the ladder network in Fig. 84(b) as $C_{ui} = g_i/(\overline{\omega}\omega_0\gamma_{0i})$, where γ_{0i} is an impedance normalization factor which may be rewritten in terms of g_i as

$$g_i = \overline{\omega} b \gamma_{0i} \tag{A.1}$$

where $b = \omega_0 C_{ui}$ is the susceptance slope of the resonator. The expressions in (4.19) may be rewritten in terms of prototype element values as

$$g_1 = \overline{\omega} b \left(\frac{Y_0}{g_0 J_{01}^2} \right), \quad g_2 = \overline{\omega} b \left(\frac{g_0 J_{01}^2}{Y_0 J_{12}^2} \right), \ldots \tag{A.2}$$

and so on. Comparing (A.1) and (A.2), a generalized expression for γ_{0i} is given by (4.21), and (4.20) is obtained from $\overline{g}_i = g_i/2$.

APPENDIX B

DERIVATION OF POLE PERTURBATIONS IN A CHEBYSHEV FILTER

The general expressions for lowpass prototype values of a Chebyshev filter are given by [15]

$$g_1 = (2/\gamma)\sin\theta_1, \quad g_i = \frac{1}{g_{i-1}}\frac{4\sin\theta_i \sin\theta_{i-1}}{A(k-1)} \tag{B.1}$$

where $A(k)$ and γ are given by (4.29). Using $\overline{g}_1 = g_1/2$, the above equation may be rearranged to obtain $\sin\theta_1 = \overline{g}_1\gamma$, and comparison with (4.27) results in

$$G_1 = \gamma \tag{B.2}$$

Case 1: i is odd

The recurring relation for g_i in (B.1) is used to calculate a general expression for g_i by considering the ratio of the product of prototype values expressed as

$$\frac{(g_i g_{i-1})\ldots(g_3 g_2)}{(g_{i-1}g_{i-2})\ldots(g_2 g_1)} = \frac{g_i}{g_1} = \frac{\sin\theta_i}{\sin\theta_1}\frac{\prod_{k=1}^{(i-1)/2} A(2k-1)}{\prod_{k=1}^{(i-1)/2} A(2k)} \tag{B.3}$$

Substituting for g_1 in (B.3) using (B.1) and subsequent rearrangement gives

$$\sin\theta_i = \overline{g}_i\gamma\frac{\prod_{k=1}^{(i-1)/2} A(2k)}{\prod_{k=1}^{(i-1)/2} A(2k-1)} \tag{B.4}$$

and comparison of (B.4) with (4.27) results in

$$G_i = \gamma\frac{\prod_{k=1}^{(i-1)/2} A(2k)}{\prod_{k=1}^{(i-1)/2} A(2k-1)} \tag{B.5}$$

Case 2: i is even

Similarly, a general expression for g_i may be calculated as

$$\frac{(g_i g_{i-1}) \ldots (g_2 g_1)}{(g_{i-1} g_{i-2}) \ldots (g_3 g_2)} = g_i g_1 = 4 \sin\theta_i \sin\theta_1 \times \frac{\prod_{k=1}^{(i-1)/2} A(2k-2)}{\prod_{k=1}^{(i-1)/2} A(2k-1)} \tag{B.6}$$

Substituting for g_1 and subsequent rearrangement gives

$$G_i = \frac{1}{\gamma} \frac{\prod_{k=1}^{(i-1)/2} A(2k-1)}{\prod_{k=1}^{(i-1)/2} A(2k-2)} \tag{B.7}$$

Using (B.2), (B.5) and (B.7), a generalized expression for G_i is given by (4.28) so that the angular pole locations θ_i in a Chebyshev filter satisfy (4.27).

VITA

Vikram Sekar received his Bachelors degree in telecommunication from Visveswariah Technological University, Belgaum, India, in 2006, his M.S. degree in electrical engineering from Texas A&M University in 2008, and his Ph.D. in electrical engineering from Texas A&M University in 2011 under the supervision of Prof. Kamran Entesari. In the summers of 2007 and 2008, he was a radio frequency design intern at Texas Instruments, Dallas, where he worked on printed circuit board modeling and signal integrity.

He has authored and co-authored over a dozen peer-reviewed articles in leading journals and conferences. From 2008 to 2011, he was also a teaching and research assistant in the Department of Electrical Engineering at Texas A&M University. He was awarded third place in the student paper competition held as part of the 2011 IEEE MTT-S International Microwave Symposium in Baltimore, MD, for his work on dual-band half-mode substrate-integrated-waveguide filters.

Mailing/contact address:
Department of Electrical and Computer Engineering
Texas A&M University
214 Zachary Engineering Center
TAMU 3128
College Station, TX 77843-3128